

UC Santa Barbara

UC Santa Barbara Electronic Theses and Dissertations

Title

2D Steep Transistor Technology: Overcoming Fundamental Barriers in Low-Power Electronics and Ultra-Sensitive Biosensors

Permalink

<https://escholarship.org/uc/item/4jz748s1>

Author

Sarkar, Deblina

Publication Date

2015

Peer reviewed|Thesis/dissertation

UNIVERSITY OF CALIFORNIA

Santa Barbara

2D Steep Transistor Technology: Overcoming
Fundamental Barriers in Low-Power Electronics and
Ultra-Sensitive Biosensors

A dissertation submitted in partial satisfaction
of the requirements for the degree of

Doctor of Philosophy

in

Electrical and Computer Engineering

by

Deblina Sarkar

Committee in charge:

Professor Kaustav Banerjee, Chair
Professor Samir Mitragotri
Professor David Awschalom
Professor Chris Palmstrom
Professor Chris G. Van de Walle

September 2015

The dissertation of Deblina Sarkar is approved.

Samir Mitragotri

David Awschalom

Chris Palmstrom

Chris G. Van de Walle

Kaustav Banerjee, Committee Chair

July 2015

2D Steep Transistor Technology: Overcoming
Fundamental Barriers in Low-Power Electronics and
Ultra-Sensitive Biosensors

Copyright © 2015

by

Deblina Sarkar

Dedicated to my dad (Barid Baran Sarkar) and mom (Asima Sarkar) who have made immense sacrifices throughout their lives for me and to my brother (Biswajit Sarkar) who has always supported me through unconditional love.

ACKNOWLEDGEMENTS

The past few years at UCSB has been an important phase in my life which contributed immensely to my growth as a researcher and overall as a person. During this period, I met and worked with some fantastic people who have influenced very positively my research as well as my life and this acknowledgement is a humble try to express my gratitude towards them.

I am indebted to my advisor Professor Kaustav Banerjee who has always been a great source of motivation and support for me. He never clipped my wings or confined me to a narrow research stream. Instead, he provided opportunities for me to broaden my sphere of knowledge and inspired me to spread my wings and traverse the distant realms of science. He taught me to think 'out of the box', to execute the research meticulously as well as the art of effective presentation. He has always been there to support me whenever I needed any help. I do not know how to thank him enough !

I am grateful to Professor Samir Mitragotri, whom I had the opportunity of collaborating with and having as my dissertation committee member. He provided priceless suggestions for research as well as for deciding future directions, which helped me immensely. He also allowed me to use his bio-engineering lab while we were setting up the bio-facilities in our group. I am thankful to Professor Chris Palmstrom, who has been a collaborator as well as a committee member, for his insightful discussions, which led to the strengthening of my dissertation. The III-V

samples used for my research were provided by his highly efficient MBE group. I would also like to thank Professor David Awschalom and Professor Chris Van de Walle for being in my committee and providing useful suggestions and advice. Though not in my committee, I had the opportunity to work with Professor Art Gossard and Professor Martin Moskovits and am thankful to them for their valuable inputs.

I had also been fortunate enough to work with some of the greatest scientists and researchers worldwide. I am grateful to Dr. Harald Gossner, Dr. Christian Ross, Professor Walter Hansch, Dr. Dimitri Linten, Dr. Steven Thijs and Dr. Navab Singh who provided me very useful training as well as insights. I would also like to thank Professor Pulickel Ajayan for his valuable suggestions for research. The high quality CVD-grown MoS₂ samples used in my research were provided by his expert group.

I am thankful to my fellow labmates at the Nanoelectronics Research Lab for providing their support in research and beyond : Navin Srivastava, Hamed Dadgour, Hong Li, Chuan Xu, Hadi Rasouli, Yasin Khatami, Wei Liu, Michael Krall, Jiahao Kang, Xuejun Xie, Wei Cao, Junkai Jiang, Xiang Li, and Haojun Zhang. I would also like to thank the lab members from collaborating groups : Aaron Anselmo, Rachel Koltun, Peter Burke, Jose Navarrete (from UCSB) and Yongji Gong (from Rice University) for their help and fruitful discussions.

The experimental work presented in this dissertation was made possible by the excellent nanofabrication facilities at UCSB and I am grateful to the nanofab staff for their support : Don Freeborn, Brian Lingg, Tom Reynolds, Bill Mitchell, Brian

Thibeault, Aidan Hopkins, Mike Silva, Ning Cao, Luis Zuzunaga, Adam Abrahamsen and Tony Bosch. I would also like to express my gratitude towards Tom Mates, Stephan Kraemer and Mark Cornish for helping me with the material characterization. Thanks also to all the administrative staff at UCSB for making my graduate life so smooth.

During my graduate days, I came across the works of Dr. Sunitha Krishnan and Anuradha Koirala who have dedicated their lives for the betterment of trafficked women and children. Their selfless work motivated me to do something for the 'children of lesser god' and made me realize what Martin Luther King, Jr. had put beautifully " Life's most persistent and urgent question is, 'What are you doing for others?' "

Lastly, yet most importantly, what I am today is because of my family. My parents have taught me to be strong and be courageous even when life hits with the worst hurdles. They have supported me through the highs and lows of life with unconditional love. My brother has always been my best friend and has contributed most to my intellectual and spiritual growth and I know that even if the whole world walks out someday, he will still be there for me.

"The powers of the mind
are like the rays of the sun
when they are concentrated
they illumine."

—Swami Vivekananda

"Every great advance
in science has issued from a
new audacity of imagination."

—John Dewey

"Thus, the task is, not so much to see
what no one has seen; but to think
what nobody has yet thought,
about that which everybody sees."

—Edwin Schrodinger

"Dream is not what
you see in sleep;
Dream is that which
doesn't let you sleep."

— A.P.J. Abdul Kalam

"Life's most persistent
and urgent question is,
'What are you doing
for others?'"

— Martin Luther King, Jr

Deblina Sarkar

Harold Frank Hall, Dept. of ECE, University of California, Santa Barbara, CA 93106

E-mail: deblina.ism@gmail.com, Tel: (805)-680-0476

EDUCATION:

- ❖ **PhD** (2008 –2015) University of California, Santa Barbara, CA
Electrical and Computer Engineering

Advisor: Prof. Kaustav Banerjee

AWARDS AND HONORS

- ❖ Selected for the "**Rising Stars in EECS**" workshop hosted by MIT (2015)
- ❖ One of the 3 winners of **Falling Walls Lab Young Innovator's competition** at UC San Diego (2015)
- ❖ One of the 4 young researchers from USA honored as "**Bright Mind**" and invited to speak at the KAUST-NSF Conference (2015)
- ❖ Department of Electrical and Computer Engineering **Dissertation Fellowship**, UCSB (2014)
- ❖ Work on ultra-sensitive electrical biosensor highlighted in **Nature Nanotechnology** (2012)
- ❖ Only researcher from the Americas and **one of the 3 students worldwide** to receive the prestigious 2011 IEEE Electron Devices Society's **PhD Fellowship Award** (2011) (<http://engineering.ucsb.edu/news/522>)
- ❖ **Best Student Paper Award** in All India Paper Presentation Competition "Vyakhan" (2008)
- ❖ **Best Female Student Award** by Undergraduate University (2008)
- ❖ Fellowship in 20th IEEE International Conference on VLSI Design (2007)
- ❖ Scholarship from Undergraduate University for outstanding academic performance (2005- 2008)
- ❖ **National scholarship** for outstanding performance in the high-school examination (2003)

SELECT RESEARCH ACCOMPLISHMENTS

- ❖ First experimental 2D quantum transistor to overcome the fundamental limitations in switching steepness of conventional transistors
Record subthreshold swing at ultra-low supply voltage
World's thinnest channel Tunnel Field Effect Transistor [Nature \(in press\)](#)
- ❖ First demonstration of the dependence of doping of transition metal dichalcogenides on work-function of metallic nanoparticles
Highest doping using nanoparticles [Nano Letters 2015](#)
- ❖ Highest sensitivity 2D biosensor
First electrical biosensor based on MoS₂ working in subthreshold region
Thinnest Field Effect Transistor based biosensor with bandgap
First MoS₂ based pH sensor [ACS Nano 2014](#)
- ❖ Introduction of concept of quantum-mechanical transducer for gas sensing
[APL 2013](#)
- ❖ First concept of Impact Ionization based biosensor for ultra-high sensitivity
[APL 2013 imos](#)
- ❖ First concept for beating the fundamental limitation in sensitivity of Field Effect Transistor based biosensor
Proposal for Tunnel Field Effect Transistor based biosensors [APL 2012](#)
[DRC 2012](#)
- ❖ First insights into high frequency behavior of graphene interconnects
First theoretical investigation of anomalous skin effect in graphene
First design of graphene based inductors [TED 2011 part1](#), [TED 2011 part2](#)
- ❖ First investigation of tunnel junction with embedded semi-metallic nanoparticles for transistor applications [APL 2011](#)
- ❖ In-depth insights into electron-hole duality during band-to-band tunneling process [APL 2010](#)
- ❖ First experimental analysis of impact of strain on electrostatic discharge of planar bulk protection devices
First concept of modulation of snapback region and its impact on stability
[IEDM 2010](#)
- ❖ Proposal for a novel hetero-junction Impact-Ionization transistor for lowering breakdown voltage [EDL 2010](#)

SELECT ARTICLES IN POPULAR PRESS AND JOURNALS HIGHLIGHTING MY RESEARCH

- ❖ "Biomolecular turn-ons"
[Nature Nanotechnology](#)
- ❖ "Ultrasensitive biosensor from molybdenite semiconductor outshines graphene"
[R&D Magazine](#), [Phys Org](#)
- ❖ "Ultra-sensitive electrical biosensor based on Tunnel-FET design beats conventional field effect transistors"
[EE Times](#), [R&D Magazine](#), [Science Newsline](#)

OTHER PRESS RELEASES ON GROUP RESEARCH WORK WHERE I AM A COAUTHOR

- ❖ "Two-dimensional atomically-flat transistors show promise for next generation green electronics"
[ScienceDaily](#)
- ❖ "Let's Make the Entire Chip from Graphene"
[IEEE Spectrum](#)
- ❖ "New rapid synthesis developed for bilayer graphene and high-performance transistors"
[Phys Org](#), [ScienceDaily](#)

RESEARCH PROJECTS

- ❖ **Graduate Research**
 - Design and fabrication of novel quantum transistors for obtaining high energy efficiency and ultra-scalability which includes exploration of tunnel-FETs (TFETs) as well as novel 2D materials (MoS₂, WSe₂ etc); Physics based modeling of quantum transport and band-to-band tunneling phenomenon including analytical modeling as well as development of own numerical device simulator based on Non-Equilibrium Green's Function Formalism. [Nature 2015 (in press), Nano Lett. 2015, APL 2011, APL 2010, EDL 2010]

- Design and fabrication of ultra-sensitive electrical biosensors; Demonstration of FET biosensor based on atomically layered structures (such a 2D graphene and transition metal dichalcogenides) which not only provide ultra-high sensitivity and easy patternability but are also ultra-flexible and hence highly promising for wearable and implantable bio-devices; I also proposed the idea of leveraging the phenomenon of interband tunneling for breaking the fundamental limits of conventional FET based biosensors. (this work is **highlighted in Nature Nanotechnology**) [**ACS Nano 2014, APL 2013, APL 2013, APL 2012, DRC 2012**]
- Experimental and theoretical exploration of novel methodology for increasing band to band tunneling current by embedding semi-metallic nanoparticles in the tunnel junction; Experimental investigation of Fermi level pinning and interface characteristics of InGaAs tunnel junction with semi-metallic ErAs nanoparticles embedded within through MBE. [**APL 2011**].
- Accurate physical modeling of ultra-high frequency conductance of graphene ribbons (GRs); rigorous analysis of the intricate processes occurring at high frequencies in GRs, such as anomalous skin effect (ASE), high-frequency resistance and inductance saturation, intercoupled relation between edge specularly and ASE; investigation of the implications for designing interconnects and energy efficient passive devices. [**TED 2011, TED 2011, IITC 2010**]
- Detailed theoretical and experimental analysis of the impact of strain on ESD performance in nanoscale devices (Gated diodes, NMOS devices in gate-grounded (GG) and gate-tied-high (GH) configurations) in both bulk as well as SOI technologies. [**IEDM 2010, ESD FORUM 2009**]

❖ **Under-graduate Research**

- Modeling and analysis of the major sources of leakages in nanoscale MOSFETs namely the subthreshold current, gate leakage and band to band tunneling leakage, design of novel device structures based on bandgap and gate engineering techniques for minimizing total leakage power dissipation and device-circuit co-design for demonstration of low

power 6 T SRAM cell. [**Jnl. Comp 2008, IEEE Si Nanotech. Workshop 2006, IEEE Intl. Conf. VLSI Design 2007, Intl. Conf. Low Dimen. Struc. Dev. 2007**]

- Investigation into novel alternative techniques based on spintronics for power reduction in nanoscale devices, implementation of spin filter using double barrier structures with magnetic quantum well and design of novel spin based logic gates. [**Workshop Recent Adv. Low Dimen. Struc. Dev. (WRA-LDSD) 2008, European Conf. Phys. Magnetism 2008**]

❖ **Internships and Industrial Experience**

- **Institute of Microelectronics, Singapore** (May-Aug. 2012)
Biomolecule conjugation and performance improvement of nanowire based FET biosensors.
- **Institute of Microelectronics, Singapore** (July-Sept. 2011)
Fabrication of novel FET based on silicon nanowire with twin gates for improved performance.
- **Infineon Technologies AG, Germany and IMEC, Belgium** (Nov. 2009-Jan. 2010)
Experimental and theoretical investigation of strain effects on ESD robustness.
- **Wuerzburg University, Germany** (May-July 2007)
Modeling and analysis of spin polarized current through a gated vertical double barrier structure.
- **Indian Institute of Technology, Kharagpur** (May-July 2006)
Modeling and analysis of the Effect of Dopant Position on Drain Current in 10nm Device considering quantum mechanical scattering.

TEACHING EXPERIENCE

- ❖ **Teaching Assistant**, Department of Electrical and Computer Engineering, UCSB
Course: Integrated Circuit Design & Fabrication (*Graduate Course, Prof. F.Brewer, Winter 2009*)

PUBLICATIONS

1. **D. Sarkar**, X. Xie, W. Liu, W. Cao, J. Kang, Y. Gong, S. Kraemer, P. M. Ajayan and K. Banerjee, "A subthermionic tunnel field-effect transistor with an atomically thin channel," *Nature*, 2015, DOI: 10.1038/nature15387 (in press)
2. W. Cao, J. Kang, **D. Sarkar**, W. Liu and K. Banerjee, "2D Semiconductor FETs-Projections and Design for Sub-10 nm VLSI," *IEEE Transactions on Electron Devices, Special Issue to commemorate the 60th anniversary of the IEDM*, Vol. 62, 2015 (in press).
3. **D. Sarkar**, X. Xie, J. Kang, H. Zhang, W. Liu, J. Navarrete, M. Moskovits and K. Banerjee, "Functionalization of Transition Metal Dichalcogenides with Metallic Nanoparticles: Implications for Doping and Gas-Sensing," *Nano Lett.*, Vol. 15, No. 5, pp. 2852, 2015.
4. W. Cao, J. Kang, **D. Sarkar**, W. Liu and K. Banerjee, "Performance Evaluation and Design Considerations of 2D Semiconductor Based FETs for Sub-10 nm VLSI," *IEDM Tech. Digest*, pp. 729, 2014.
5. X. Li, J. Kang, X. Xie, W. Liu, **D. Sarkar**, J. Mao and K. Banerjee, "Graphene Inductors for High -Frequency Applications – Design, Fabrication, Characterization , and Study of Skin Effect," *IEDM Tech. Digest*, pp. 120, 2014.
6. **D. Sarkar**, W. Liu, X. Xie, A. Anselmo, S. Mitragotri and K. Banerjee, "Molybdenum Disulphide Based Field Effect Transistors for Next-Generation Label-free Biosensors," *ACS Nano*. Vol. 8, No. 4, pp. 3992, 2014.
7. X. Xie, **D. Sarkar**, W. Liu, J. Kang, O. Marinov, M. J. Deen, and K. Banerjee, "Low-Frequency Noise in Bilayer MoS₂ Transistor," *ACS Nano*. Vol. 8, No. 6, pp. 5633, 2014.
8. J. Kang, W. Liu, **D. Sarkar**, D. Jena and K. Banerjee, "A Computational Study of Metal-Contacts to Monolayer Transition-Metal Dichalcogenide Semiconductors," *Phys. Rev. X*. Vol. 4, No. 3, pp. 031005, 2014.
9. W. Cao, **D. Sarkar**, Y. Khatami, J. Kang and K. Banerjee, "Subthreshold-Swing Physics Of Tunnel Field-Effect Transistors," *AIP Advances*. Vol. 4, pp. 067141, 2014.
10. J. Kang, W. Cao, X. Xie, D. Sarkar, W. Liu and K. Banerjee, "Graphene and beyond-graphene 2D crystals for next-generation green electronics.," *Proc. SPIE*

- 9083, Micro- and Nanotechnology Sensors, Systems, and Applications VI, pp. 908305, 2014.
11. W. Liu, S. Krämer, **D. Sarkar**, H. Li, P. M. Ajayan, and K. Banerjee, “Controllable and Rapid Synthesis of High-Quality and Large-Area Bernal Stacked Bilayer Graphene using Chemical Vapor Deposition” *ACS Chemistry of Materials*, Vol. 26, No. 2, pp. 907, 2014.
 12. J. Kang, **D. Sarkar**, Y. Khatami, and K. Banerjee, “Proposal for All-Graphene Monolithic Logic Circuits,” *Appl. Phys. Lett.*, Vol. 103, No. 8, pp. 083113, 2013.
 13. W. Liu, J. Kang, W. Cao, **D. Sarkar**, Y. Khatami, D. Jena and K. Banerjee, “High-Performance Few-Layer-MoS₂ Field-Effect-Transistor with Record Low Contact-Resistance” *IEDM Tech. Digest*, pp. 808, 2013.
 14. **D. Sarkar** and K. Banerjee, “Impact-Ionization Field-Effect-Transistor Based Biosensors for Ultra-Sensitive Detection of Biomolecules,” *Appl. Phys. Lett.*, Vol. 102, No. 20, pp. 203110, 2013.
 15. **D. Sarkar**, H. Gossner, W. Hansch and K. Banerjee, “Tunnel-Field-Effect-Transistor Based Gas-Sensor: Introducing Gas Detection with A Quantum-Mechanical Transducer,” *Appl. Phys. Lett.*, Vol. 102, No. 14, pp. 023110, 2013.
 16. W. Liu, J. Kang, **D. Sarkar**, Y. Khatami, D. Jena and K. Banerjee, “Role of Metal Contacts in Designing High-Performance Monolayer n-Type WSe₂ Field-Effect-Transistors,” *Nano Letters*, Vol. 13, no. 5, pp. 1983, 2013.
 17. **D. Sarkar** and K. Banerjee, “Proposal for Tunnel-Field-Effect-Transistor as Ultra-Sensitive and Label-Free Biosensor,” *Appl. Phys. Lett.* Vol. 100, No. 14, pp. 143108, 2012. (**highlighted in Nature Nanotechnology** <http://www.nature.com/nnano/reshigh/2012/0512/full/nnano.2012.78.html>)
 18. **D. Sarkar** and K. Banerjee, “Fundamental Limitations of Conventional-FET Biosensors: Quantum-Mechanical-Tunneling to the Rescue,” *Device Research Conference Tech. Digest*, 2012.
 19. J. Kang, **D. Sarkar**, W. Liu, D. Jena and K. Banerjee, “A Computational Study of Metal-Contacts to Beyond-Graphene 2D Semiconductor Materials,” *IEDM Tech. Digest*, pp. 808, 2012.
 20. **D. Sarkar** and K. Banerjee, “Metallic-Nanoparticle Assisted Enhanced Band-To-Band Tunneling Current,” *Appl. Phys. Lett.*, Vol. 99, No. 13, pp. 133116, 2011.
 21. X. Li, Z. Chen, N. Shen, **D. Sarkar**, N. Singh, K. Banerjee, Guo-Qiang Lo, Dim-Lee Kwong, “Vertically Stacked and Independently Controlled Twin-Gate MOSFETs on a Single Si Nanowire,” *IEEE Elec. Dev. Lett.*, Vol. 32, No. 11, pp. 1492, 2011.

22. **D. Sarkar**, C. Xu, H. Li, and K. Banerjee, "High-Frequency Behavior of Graphene-Based Interconnects – Part I: Impedance Modeling," *IEEE Trans. Elec. Dev.*, Vol. 58, No. 3, pp. 843, 2011.
23. **D. Sarkar**, C. Xu, H. Li, and K. Banerjee, "High-Frequency Behavior of Graphene-Based Interconnects – Part II: Impedance Analysis and Implications for Inductor Design," *IEEE Trans. Elec. Dev.*, Vol. 58, No. 3, pp. 853, 2011.
24. **D. Sarkar**, M. Krall, and K. Banerjee, "Electron-hole Duality During Band-to-Band Tunneling Process in Graphene-Nanoribbon Tunnel-Field-Effect Transistors," *Appl. Phys. Lett.*, Vol. 97, No. 26, pp. 263109, 2010.
25. **D. Sarkar**, N. Singh and K. Banerjee, "A Novel Enhanced Electric-Field Impact-Ionization MOS Transistor," *IEEE Elec. Dev. Lett.*, Vol. 31, No. 11, pp. 1175, 2010.
26. **D. Sarkar**, S. Thijs, D. Linten, C. Russ, H. Gossner and K. Banerjee, "A Quantitative Inquisition into ESD Sensitivity to Strain in Nanoscale CMOS Protection Devices," *IEDM Tech. Digest*, pp. 808, 2010.
27. **D. Sarkar**, C. Xu, H. Li, and K. Banerjee, "AC Conductance Modeling and Analysis of Graphene Nanoribbon Interconnects," *IEEE Intl. Interconnect Tech. Conf. (IITC)*, pp.1, 2010.
28. K. Banerjee, H. Li, C. Xu, Y. Khatami, H.F. Dadgour, **D. Sarkar**, W. Liu, "Prospects of Carbon Nanomaterials For Next-Generation Green Electronics," *IEEE Conf. Nanotech. (IEEE-NANO)*, pp. 56, 2010.
29. **D. Sarkar**, H. Gossner and K. Banerjee, "Experimental Investigation of ESD Performance for Strained Silicon Nano-Devices," *ESD Forum*, pp. 36, 2009.
30. **D. Sarkar**, D. Datta, and S. Dasgupta, "Modelling of Leakage Current Mechanisms in nanoscale DG MOSFET and its application to low power SRAM design" *Jnl. Comp.*, Vol. 3, No. 2, pp. 37, 2008.
31. **D. Sarkar**, "Spin Selection in Resonant Tunneling Diode using Dilute Magnetic Semiconductors," *Workshop Recent Adv. Low Dimen. Struc. Dev. (WRA-LDSD)*, Nottingham, UK, 2008.
32. **D. Sarkar**, "Implementation Of A Spintronics Full Adder," *European Conf. Phys. Magnetism*, Poland, June 2008.
33. **D. Sarkar**, "A Novel Technique for Reduction of Gate Leakage Current Using Double Gate SiGe/Si/SiGe Heterostructure n-Channel Mosfet," *Intl. Conf. Low Dimen. Struc. Dev.*, Columbia, 2007.

34. **D. Sarkar**, S. Ganguly, D. Datta, A.A.P. Sarab and S. Dasgupta, “Modeling of Leakages in Nanoscale DG MOSFET to Implement Low Power SRAM: a Device/Circuit Co-Design,” *IEEE Intl. Conf. VLSI Design*, Bangalore, India, 2007.
35. D. Datta, A. A. Sarab, S. Ganguly, **D. Sarkar** and S. Dasgupta, “A New Design Architecture of Novel Nanoscale Device to Reduce Leakage Currents,” *IEEE Silicon Nanotech. Workshop*, HI, USA, 2006.

BOOK CHAPTER

Carbon Integrated Electronics, H. Li, Y. Khatami, **D. Sarkar**, J. Kang, C. Xu, W. Liu, and K. Banerjee, in *Intelligent Integrated Systems: Technologies, Devices and Architectures*. Ed: S. Deleonibus, WSPC-Pan Stanford (Singapore) Publishers, 2014.

TECHNICAL REVIEWER

Journal Of Applied Physics, IEEE Transactions on Electron Devices, IEEE Transactions on Nanotechnology, IEEE Electron Device Letters, Nano-Micro Letters, Microelectronics Journal, Journal of Photochemistry and Photobiology A: Chemistry, Superlattices and Microstructures, Journal of Computational Electronics

SKILLS

❖ **Computational Skills :**

- developed own nano-scale device simulator based on Non-Equilibrium Green's Function Formalism
- proficient in C, Matlab, Mathematica, Maple, Medici, Sentaurus, Silvaco

❖ **Experimental Skills:**

- device processing and characterization
- biosensor development and characterization, surface functionalization
- 2D technology (processing and characterization of nanomaterials such as graphene, MoS₂, WSe₂)
- processing structures based on III-V material with embedded semi-metallic nanoparticles

ABSTRACT

2D Steep Transistor Technology: Overcoming Fundamental Barriers in Low-Power Electronics and Ultra-Sensitive Biosensors

by

Deblina Sarkar

In order to sustain the unprecedented growth of the Information Technology, it is necessary to achieve dimensional scalability along with power reduction, which is a daunting challenge. In this dissertation, two-dimensional (2D) materials are explored as promising materials for future electronics since they can, not only enable dimensional scaling without degradation of device electrostatics but it is also shown here, that they are highly potential candidate for interconnects and passive devices. 2D semiconductors are investigated for transistor applications, and novel approach for doping using nanoparticle functionalization is developed. It is also demonstrated that these materials can lead to ideal transfer characteristics. Aimed towards on-chip interconnect and inductor applications, the first detailed methodology for the accurate evaluation of high-frequency impedance of graphene is presented. Using the developed method the intricate high-frequency effects in graphene such as Anomalous Skin Effect (ASE), high-frequency resistance and inductance saturation, intercoupled relation between edge specularity and ASE and the influence of linear dimensions on impedance are investigated in detail for the first time.

While 2D materials can address the issue of dimensional scalability, power reduction requires scaling of power supply voltage, which is difficult due to the fundamental thermionic limitation in the steepness of turn-ON characteristics or subthreshold swing (SS) of conventional Field-Effect-Transistors (FETs). To address this issue, a detailed theoretical and experimental analysis of fundamentally different carrier transport mechanism, based on quantum mechanical band-to-band tunneling (BTBT) is presented. This dissertation elucidates an underlying physical concept behind the BTBT process and provides clear insight into the interplay between electron and hole characteristics of carriers within the forbidden gap during tunneling. Moreover, a novel methodology for increasing the BTBT current through incorporation of metallic nanoparticles at the tunnel junction is proposed and theoretically analyzed, followed by experimental demonstration as proof of concept, which can open up new avenues for enhancing the performance of Tunneling-Field-Effect-Transistors (TFETs).

This dissertation, also establishes, for the first time, that the material and device technology which have evolved mainly with an aim of sustaining the glorious scaling trend of Information Technology, can also revolutionize a completely diverse field of bio/gas-sensor technology. The unique advantages of 2D semiconductor for electrical sensors is demonstrated and it is shown that they lead to ultra-high sensitivity, and also provide an attractive pathway for single molecular detectability- the holy grail for all biosensing research. Moreover, it is theoretically illustrated that steep turn-ON characteristics, obtained through novel technology such as BTBT, can result in

unprecedented performance improvement compared to that of conventional electrical biosensors, with around 4 orders of magnitude higher sensitivity and 10-fold lower detection time.

With a view to building ultra-scaled low power electronics as well as highly efficient sensors, new generation of van-der Waal's BTBT junctions combining 2D with 3D materials is proposed and experimentally demonstrated, which not only retain the advantages of 2D films but also leverages the matured doping technology of 3D materials, thus harnessing the best of both worlds. These attributes are instrumental in the achievement of unprecedented BTBT current, which is more than 3 orders of magnitude higher than that of best reported 2D heterojunctions till date.

Finally, with the optimization of the novel heterojunctions, this dissertation also achieves a significant milestone, furnishing the first experimental demonstration of TFETs based on 2D channel material to beat the fundamental limitation in subthreshold swing (SS). This device is the first ever TFET, in a planar architecture to achieve sub-thermionic SS over 4 decades of drain current, a necessary characteristic prescribed by the International Technology Roadmap for Semiconductors and in fact, the only TFET to date, to achieve so, in any architecture and in any material platform, at a low power-supply voltage of 0.1 V. It also represents the world's thinnest channel sub-thermionic transistor, thus, cracking the long-standing issue of simultaneous dimensional and power supply scalability and hence, can lead to a paradigm shift in information technology as well as healthcare.

TABLE OF CONTENTS

Chapter 1:	Introduction.....	1
1.1.	Scaling Issue and Power Crisis	1
1.1.1.	Dimensional Scaling and 2D Materials.....	1
1.1.2.	Supply Voltage Scaling and Steep Transistors.....	3
1.2.	Beyond Low Power Computation	7
1.3.	Synopsis of Dissertation.....	8
Chapter 2:	2D Materials: from Transistors To Interconnects.....	10
2.1.	Introduction	10
2.2.	Properties of 2D Materials : Graphene and Beyond	12
2.3.	Transistors : 2D Semiconducting Transition Metal Dichalcogenides.....	18
2.3.1.	Doping.....	18
2.3.2.	Gate control.....	37
2.3.3.	Contacts.....	40
2.4.	Interconnects : 2D Semi-Metallic Graphene	45
2.4.1.	Anomalous High-Frequency Effects in Graphene.....	46
2.4.2.	Impedance Modeling : Semi Infinite Slab.....	55
2.4.3.	Impedance Modeling : Finite Structure.....	60
2.4.4.	Summary of Impedance Extraction Methodology.....	69
2.4.5.	High Frequency Analysis of Graphene Interconnects.....	72

2.4.6. High Frequency Analysis of Graphene Inductors.....	80
2.5. Summary	85
Appendix A	87
Appendix B	88
Chapter 3: Steep Transistors.....	90
3.1. Introduction	90
3.2. Impact Ionization MOSFET (I-MOS).....	91
3.2.1. General Device Structure and Working Principle	91
3.2.2. Novel Enhanced Electric Field I-MOS (E2I-MOS).....	92
3.2.3. Challenges.....	98
3.3. Tunnel Field Effect Transistors (TFETs).....	98
3.3.1. Device Structure and Working Principle	98
3.3.2. Understanding Band-to-Band Tunneling.....	104
3.3.3. Analytical Modeling of TFETs.....	111
3.3.4. Development of Numerical Quantum Mechanical Simulator	119
3.3.5. Performance Improvement : Nanoparticle Assisted Tunneling.....	125
3.4. Summary	139
Chapter 4: Beyond Low Power Computation.....	140
4.1. Introduction	140

4.2.	2D Material for Sensing	142
4.2.1.	FET based Biosensor	142
4.2.2.	Work-Function Modulated Gas-sensor.....	168
4.3.	Fundamental Limitation of Electrical Sensors and the Solutions	170
4.3.1.	TFET based Biosensor	171
4.3.2.	I-MOS based Biosensor	182
4.3.3.	TFET Based Gas-Sensor.....	193
4.4.	Summary	204
Chapter 5:	Atomically-Thin Channel Subthermionic Transistor.....	206
5.1.	Introduction	206
5.2.	Challenges and Novel Solution through 3D-2D Hetero-TFET.....	208
5.3.	Exploration of 3D-2D Tunnel-Junctions.....	212
5.3.1.	Junction with Highly P-doped 3D Material	214
5.3.2.	Junction with Highly N-doped 3D Material	218
5.3.3.	Comparison with Experimental 2D Tunnel-Junctions.....	220
5.3.4.	Analytical Modeling	221
5.4.	Steep TFET with 2D Channel	225
5.4.1.	Device Design and Fabrication.....	225
5.4.2.	Material Characterization.....	230

5.4.3.	Proof of Band-to-Band Tunneling	234
5.4.4.	Beating the Fundamental Thermionic Limitation.....	238
5.4.5.	Control Experiments	243
5.4.6.	Repeatability and Hysteresis.....	245
5.4.7.	Comparison with Previous Experimental TFETs	247
5.4.8.	Potential for High Performance	248
5.4.9.	Note on 1D TFETs and 2D-2D Tunnel Junctions	252
5.5.	Summary	254
Chapter 6:	Conclusions and Future Work.....	256
6.1.	Ultra-Scalable Low Power Switches.....	256
6.2.	Extremely Sensitive and Fast Sensors.....	262
6.3.	Future Work	265
6.3.1.	Drain Current Improvement.....	265
6.3.2.	Experimental Demonstration of TFET based Sensors.....	269
References.....		271

Chapter 1: Introduction

1.1. Scaling Issue and Power Crisis

Electronic Integrated Circuits (ICs) are ubiquitous in today's society and forms the workhorse for the growing industry of Information Technology. To sustain this growth, there has been an increasing demand for higher performance and enhanced functionality, which historically, has been met by scaling of the Field-Effect-Transistors (FETs) which form the building blocks of the ICs. The scaling rules dictate the reduction of the critical dimensions of the FET and the operating voltage by the same factor, so that transistor density is increased without the rise in the power density.

While, aggressive scaling has continued for more than past four decades, the current technology faces issues in both dimensional and voltage scaling, which pose serious challenges for further scaling and hence, growth of Information Technology. The two issues along with the potential directions for addressing them, are discussed below.

1.1.1. Dimensional Scaling and 2D Materials

In a Field-Effect-Transistor (**Figure 1.1(a)**), current flows through a semiconducting channel between the source and drain electrodes. The current flow is controlled by a

third electrode called gate, which is capacitively connected to the channel and hence, the gate can turn the device ON or OFF. However, as the channel length is scaled to deep sub-micron regime, electric fields from the source and drain begin to influence the potential of the channel and the gate can no longer effectively control the channel potential, resulting in degradation of device electrostatics. The electric field from the drain lowers the barrier in the channel close to the source-channel junction and this phenomenon is called Drain Induced Barrier Lowering (DIBL) (**Figure 1.1(b)**). DIBL can lead to significant current flow even when the device is supposed to be OFF. This increase in OFF-current (or leakage) leads to increase in undesirable static power dissipation, which is a burning issue for the IT Industry. Hence, it is of absolute necessity to improve the gate control over the channel.

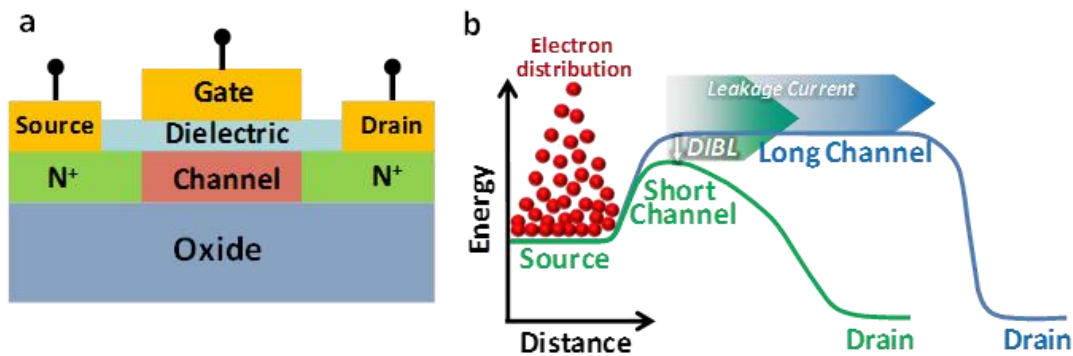


Figure 1.1 (a) The schematic diagram of a conventional FET (CFET). (b) Conduction band profile of a conventional FET for both long and short channel lengths.

A parameter that indicates how efficiently the gate controls the channel is the natural length scale (λ), [1] which depends on the gate capacitance as well as the permittivity and thickness of the semiconducting channel. A rule of thumb is that in order for the gate to maintain efficient electrostatics, λ should be 5-10 times smaller than the

channel length (L_g)[2]. The expressions for λ for Silicon-ON-Insulator (SOI) MOSFET structure is given by

$$\lambda_{SOI} = \sqrt{\frac{\epsilon_s}{C_g} t_s} \quad (1.1)$$

where t_s and ϵ_s are the thickness and permittivity of the semiconducting channel respectively, C_g is the gate capacitance. It is evident from equation (1.1), that reducing the channel thickness can help in reducing the λ and hence, improve the device electrostatics. 2D layered materials are highly promising in this respect. Since the adjacent layers of the 2D materials have van der Waal's bonding, it is relatively easy to obtain as thin as a single atomic layer of these materials and thus, λ can be very small. Moreover, they are characterized by pristine, dangling-bond free interfaces. In addition, they offer easy patternability due to their planar nature compared to 1D structures such as nanowires and nanotubes. Thus, 2D materials are considered as highly potential candidates as channel material for beyond-Si scaling era.

1.1.2. Supply Voltage Scaling and Steep Transistors

Even if excellent electrostatics can be achieved with atomically-thin 2D Materials, the second and most severe challenge for MOSFETs still remains, which is the increase in dynamic power density due to inability to scale down the supply voltage. Lowering the power in electronic components is of critical importance for energy-efficiency leading to reduction in Green House Gases, increasing battery life

of portable electronics and implanted medical devices as well as solving heat dissipation issues in mobile and non-portable systems. The most effective way to control the power density is to scale down the supply voltage (V_{DD}) as the dynamic power displays a quadratic dependence on V_{DD} . Ideally we would prefer a transistor with very abrupt step like transfer characteristics (**Figure 1.2(a)**) such that with the application of an infinitesimally small gate voltage, the device can be turned ON from the OFF state. However, in conventional FETs (CFETs) there is a fundamental limitation of the steepness of the turn-ON characteristics (**Figure 1.2(b)**) and they need the gate voltage to be changed by at least 60 mV to cause a corresponding change of the drain current by one decade (or 10X). This implies that in order to achieve an ON-OFF ratio of 4 decades, supply voltage of at least 240 mV (4*60 mV) is required. Hence, in case of CFETs, it is not possible to reduce the supply voltage and still maintain reasonable ON-OFF ratio.

The reason behind this fundamental limitation is discussed below. The steepness of the turn-ON behavior of the FET is characterized by a parameter called the Subthreshold Swing (SS), which is defined as the inverse of the subthreshold slope and is given by $SS = (d \log_{10} I_{DS} / dV_{GS})^{-1}$ where I_{DS} : drain current, V_{GS} : gate to source voltage. The SS is dependent on two factors as shown by the two terms in equation (1.2).

$$SS = \frac{\partial V_{GS}}{\partial \psi} \frac{\partial \psi}{\partial (\log_{10} I_{DS})} \quad (1.2)$$

First term is determined by the device electrostatics, or in other words, how well the surface potential of the semiconductor (ψ) at the interface of the semiconductor and gate-dielectric is modulated by the gate voltage and is given by the ratio of the change in V_{GS} to the change in ψ . Even in case of perfect electrostatics, the lowest possible value of the first factor is 1, which means a particular change in gate voltage (ΔV_{GS}) leads to almost similar change in surface potential of the semiconductor channel ($\Delta\psi$) such that $\Delta\psi = \Delta V_{GS}$. The second term affecting SS , is determined by how efficiently the current is modulated by the change in the surface potential. The lowest possible value of the second factor is 60 mV/dec at room temperature for conventional FETs as explained below. The transport mechanism (**Figure 1.2(c)**) of the conventional FETs is based on thermionic emission over the barrier, which implies only electrons having energy higher than the barrier height can transport to the drain and contribute to current. Hence, current can be increased (or decreased) by decreasing (or increasing) the barrier height H . Since the electrons in the source is distributed according to the Fermi-Dirac distribution, which can be approximated as Boltzmann distribution for energies much higher than the Fermi level, the occupied density of states, or equivalently the electron density per unit energy (n) decreases exponentially with increase in energy (E) ($n \propto e^{-E/k_B T}$). Thus, with a decrease in surface potential by $\Delta\psi$, and hence, decrease in barrier by the same amount, current will increase following the trend $I_{DS} \propto e^{\Delta\psi/k_B T}$. Hence, the minimum value for the second factor, can be calculated as $[K_B T/q \ln(10)]$, which has the value of 60 mV/dec at room temperature. Thus, combining the minimum values for the first and second term, the

limitation of SS in case of conventional FETs comes out to be 60 mV/decade. Note that this minimum value of 60 mV/dec for SS , is obtained even in presence of perfect electrostatics. Degradation of device electrostatics, will degrade (increase) the SS further.

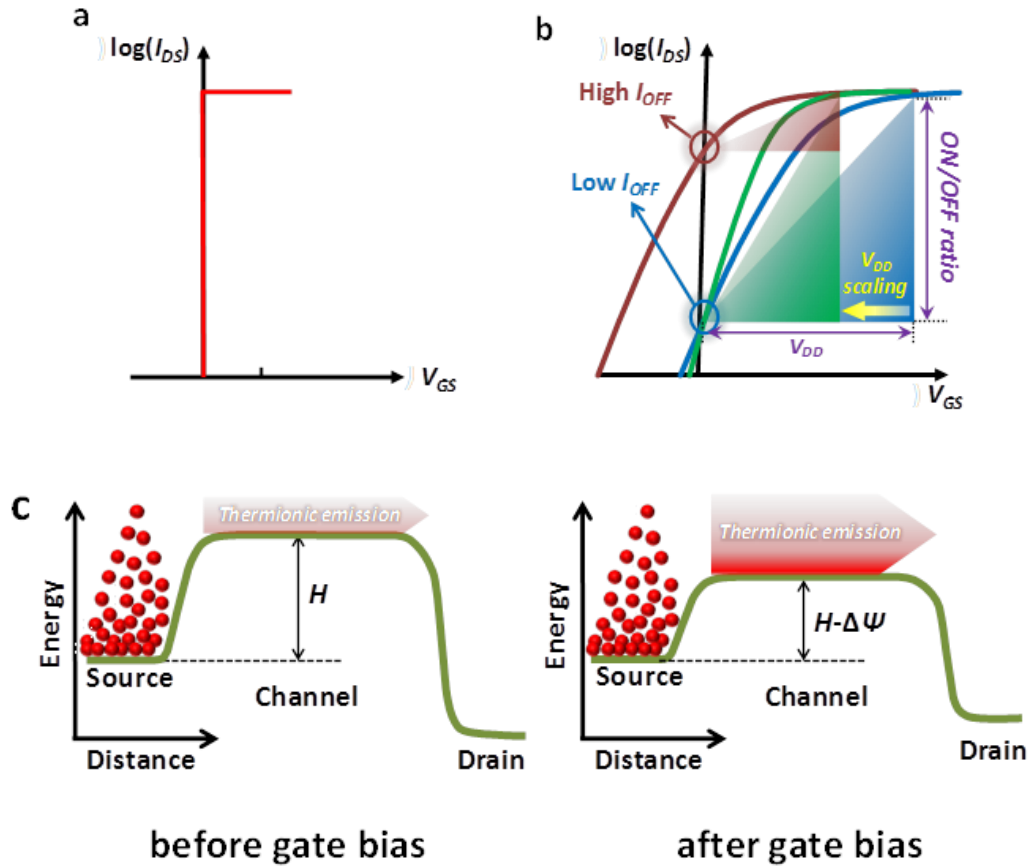


Figure 1.2 (a) Ideal step-like $\log(I_{DS})$ - V_{GS} characteristics. (b) In reality, I_{DS} - V_{GS} characteristics have finite slopes and look like the blue curve. If we try to scale down the supply voltage (V_{DD}) and hence, make the device turn on with a lower V_{GS} , the characteristics will look like the brown curve leading to significantly higher leakage current and low ON-OFF current ratio. In order to reduce V_{DD} , and at the same time achieve high ON-OFF current ratio, it is necessary to make the slope of the I_{DS} - V_{GS} curve steeper or the inverse of the slope (defined as the Subthreshold Swing) smaller, as illustrated by the green curve. (c) Band diagrams before and after application of gate potential illustrating the transport mechanism in conventional FETs. Only electrons with energy higher than the barrier height can transport to the drain. H is the height of the barrier before application of gate potential and $\Delta\psi$ is change in surface potential of the semiconductor channel after application of gate potential.

In order to scale the supply voltage for tackling the dynamic power, it is necessary to build transistors with steep turn-ON characteristics or in other words, transistors with SS lower than 60 mV/dec at room temperature (which can be called steep transistors, in short). Since the fundamental limitation in SS arises from the thermionic emission based carrier transport mechanism, achievement of steeper turn-ON will require employment of fundamentally different carrier transport mechanisms. Details of the steep transistors will be discussed in Chapter 2.

1.2. Beyond Low Power Computation

The present dissertation shows that beyond low power computation, FETs based on 2D semiconductors and with steep turn-ON characteristics, can also be very advantageous for a diverse field of gas/bio-sensor technology. Sensors, specially biosensors based on FETs have been gaining momentum and attention as a viable technology for the medical, forensic, and security industries since they are very cost-effective compared to optical detection procedures. Such biosensors allow for scalability and label-free detection of biomolecules – removing the step and expense of labeling target molecules with fluorescent dye. The principle of action of an FET biosensor is similar to the FETs used in digital circuit applications, except that the physical gate is removed and the work of the gate is carried out by the charged biomolecules that are to be detected. For immobilizing these biomolecules, the dielectric surface enclosing the semiconductor is coated with specific receptors, which can bind to the target biomolecules (a process called conjugation). However,

the current FET based biosensors suffer from severe limitations either in terms of practical implementation or for achievement of high sensitivity and low detection limit. This dissertation points out that achievement of dimensional scalability as well as reduction of SS , which can alleviate the power crisis of digital electronics, can also help in addressing the limitations of biosensing technology.

1.3. Synopsis of the Dissertation

The scalability issues discussed above, can usher in the dead end of the glorious scaling trend of Information Technology. While use of 2D materials can improve dimensional scalability, building of 2D material based transistors itself faces several problems. Moreover, simultaneous achievement of dimensional and supply voltage scaling is a daunting challenge. In the following chapters, we will carry out detailed analysis of these issues and we will propose and demonstrate solutions to address them. It is also illustrated in this dissertation, that the novel approaches proposed here, can be leveraged to address the critical problems in a completely diverse field of gas/bio sensing technology. In chapter 2, 2D materials are explored. In order to improve device performance, important factors such as doping, high capacitance gating and contacts are investigated and critical strategies are demonstrated for fabrication of highly efficient transistors. The first detailed methodology for the accurate evaluation of high-frequency impedance of 2D layered structures relevant to on-chip interconnect and inductor applications is also presented with view to building of all 2D integrated circuits. Chapter 3 explores steep transistors which are relatively

less disruptive compared to present CMOS technology, for choosing the best option. The chapter provides in-depth physical understanding of the fundamentally different transport mechanism which can lead to subthermionic SS . Novel approaches are also demonstrated for improving the performance of the steep devices. Chapter 4 demonstrates, how the use of 2D semiconductor platform as channel can help in the design of ultra-sensitive bio/gas-sensors with extremely low detection limits. The concept of fundamental limitation in sensitivity for electrical sensors have been elucidated for the first time and the approach to overcome it using steep transistors, has been theoretically illustrated. With the detailed understanding of 2D material systems as well as physics of steep turn-ON behavior obtained from Chapters 2 and 3, Chapter 5 furnishes the first demonstration of a 2D material based transistor to break the fundamental limitation in SS of conventional FETs. This transistor with atomically thin channel and exhibiting a record average SS of 31.1 mV/dec can enable dimensional scalability without power penalty and hence, can open up new avenues for ultra-dense and low-power integrated circuits as well as ultra-sensitive bio/gas-sensors. Chapter 6 provides the conclusions and directions for future work.

Chapter 2: 2D Materials: From Transistors to Interconnects

2.1. Introduction

Graphene, the first demonstrated thermodynamically stable 2D material, with its fascinating properties and rich physics has harbingered a new era of 2D technology, intriguing research in graphene and beyond graphene 2D materials. These materials are highly versatile and combine excellent electronic, optical, mechanical and magnetic properties, which make these materials potential candidates for variety of novel applications. 2D semiconductors, due to their ultra-thin nature, provides excellent electrostatics, which, not only make them attractive materials for highly scalable digital Field-Effect Transistors (FETs) [3] but also for designing ultra-sensitive FET based biosensors.[4] These materials are also very attractive for optical applications since they can lead to strong light emission, as demonstrated in photoluminescence experiments.[5] They also offer valley polarization through optical pumping and hence are promising for the recently developed field of Valleytronics.[6] Moreover, they possess unique edge effects and magnetic properties [7][8] which can be leveraged for novel Spintronics applications.

2D materials also offer a broad range of choices among insulators, semiconductors and metals. While graphene, a 2D semi-metal material with outstanding electrical, thermal, and mechanical properties, is a highly potent candidate for next-generation interconnects and passive devices, hexagonal boron nitride (h-BN), with a large band gap (> 5 eV) can be used as an extremely thin dielectric layer with high dielectric strength (7.94 MV/cm). On the other hand, 2D Transition Metal Dichalcogenides (TMDs) can have considerable band gaps (1 eV - 2 eV) and can be used as channel materials to potentially reduce leakage power (thereby achieving high ON/OFF ratio) for digital applications.[9] This leads to unique potential for fabrication of all-2D integrated circuits [10] for flexible electronics with wide-spread applications starting from displays and personal entertainment products to exercise monitors, prosthetic devices and computers. 2D materials are a natural choice for flexible electronics due to their atomically-thin and layered nature which provides excellent mechanical flexibility, high transparency as well as ability to sensitively interact with the environmental perturbations.

In this chapter, we first discuss the band structure and properties of the 2D materials. Next, 2D semiconducting TMDs are explored for transistor applications. Three important factors for designing efficient transistors namely doping, high capacitance gating and formation of good contacts have been studied. Finally, ultrahigh-frequency behavior of semi-metallic graphene ribbons (GRs) is investigated and their consequences in designing interconnects and low-loss on-chip inductors are analyzed.

2.2. Properties of 2D Materials : Graphene and Beyond

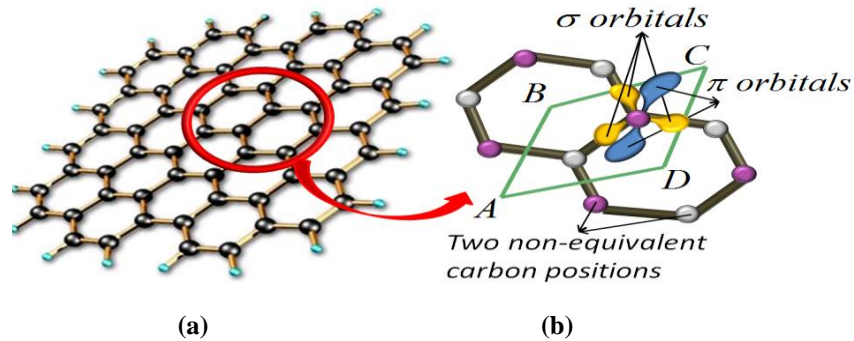


Figure 2.1(a) The basic honeycomb structure of graphene. **(b)** An enlarged view showing the two non-equivalent carbon positions of graphene. ABCD represents the unit cell which contains the two types of atoms. The three in-plane σ orbitals and π orbitals perpendicular to the sheet are shown.

2D materials consist of vertically stacked layers held together by relatively weak van der Waals force and each layer is formed of covalently bonded atoms. The weak inter-layer bonding allows them to be mechanically exfoliated from bulk to form atomically thin flakes, for example, graphene can be exfoliated from bulk graphite. Graphene[11] is the most widely known 2D material consisting of single layer of carbon atoms packed into a two-dimensional honeycomb lattice structure (**Figure 2.1(a)**). It has two non-equivalent carbon positions as shown in **Figure 2.1(b)** and the unit cell which contains two types of atoms. Carbon has four valence orbitals ($2s$, $2p_x$, $2p_y$, $2p_z$). The $2s$, $2p_x$ and $2p_y$ orbitals form the three in-plane σ bonds in graphene and a fourth bond is formed by the overlap of p_z (or π) orbitals perpendicular to the sheet.

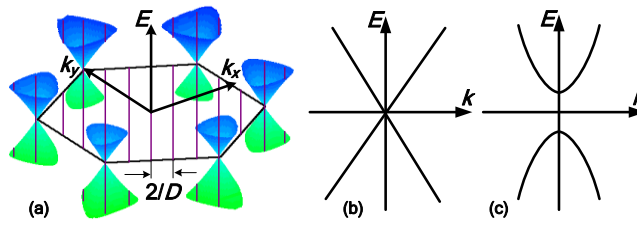


Figure 2.2(a) The band structure of graphene forms hexagonal cones in the vicinity of the Fermi energy. The apexes of the six cones are called Dirac points. The formation of a nanotube cuts the energy landscape into slices of allowed states (wave vector is quantized). The locations of the cross section of the cut lines in k -space with the cones determine whether the resulting band structure is **(b)** metallic or **(c)** semiconducting.

It is the π orbitals which determine the conduction properties of graphene, a simple physical explanation of which is as follows. Considering only two carbon atoms, when they are brought closer to each other, their individual energy levels split into bonding and antibonding levels. Since the overlapping of the in-plane $2s$, $2p_x$ and $2p_y$ orbitals of one carbon atom with those of the other is much stronger than that between the two $2p_z$ orbitals. Hence, the $2s$, $2p_x$ and $2p_y$ orbitals split much more compared to the $2p_z$ orbitals. Hence, the states near the chemical potential are formed by the $2p_z$ orbitals and thus they determine the current flow.[12] The Brillouin zone of graphene is shown in **Figure 2.2(a)** where the cones represent the electron energy dispersion of graphene close to the Fermi energy. It can be calculated by a simple tight-binding approach[13]. The bandgap of graphene as can be observed from **Figure 2.2(b)** is zero. The band structure of graphene is unique in the sense that the E - k relation is linear for lowest energies near the six corners of the two-dimensional hexagonal Brillouin zone, leading to zero effective mass for electrons and holes[14]. The well-known relativistic energy-momentum equation can be expressed as:

$$E_{tot} = \sqrt{P^2 c^2 + m_0^2 c^4} \quad (2.1)$$

where E_{tot} is the total energy of a particle; P is the momentum; c is the speed of light; m_0 is the rest mass. The kinetic energy E_{kin} is the difference between total energy (E_{tot}) of a particle and the rest energy ($m_0 c^2$) of the particle:

$$E_{kin} = E_{tot} - m_0 c^2 = \sqrt{P^2 c^2 + m_0^2 c^4} - m_0 c^2. \quad (2.2)$$

When $P \ll m_0 c$, equation (2.2) reduces to

$$E_{kin} = P^2 / 2m_0, \quad (2.3)$$

which implies the non-relativistic case. In this case, E_{kin} is proportional to P^2 . When $m_0 = 0$ or the particle is massless, equation (2.3) is reduced to

$$E_{kin} = P c. \quad (2.4)$$

In such case, E_{kin} is proportional to P .

In graphene, since the E - k relation is linear at low energies:

$$|E| = \hbar v_F |\vec{k} - \vec{k}_0| = |\vec{P}| v_F. \quad (2.5)$$

Therefore, the electrons and holes in graphene can be considered as massless particles with a “speed of light” of v_F , the Fermi velocity. Due to this linear “dispersion” relation at low energies, electrons and holes near these six points behave like relativistic particles described by the Dirac equation for spin 1/2 particles [15]. Hence, the electrons and holes are called Dirac fermions, and the six corners of the Brillouin zone (the apexes of the six cones shown in **Figure 2.2(b)**) are called the Dirac points. The lack of an intrinsic bandgap in graphene and the extreme difficulties

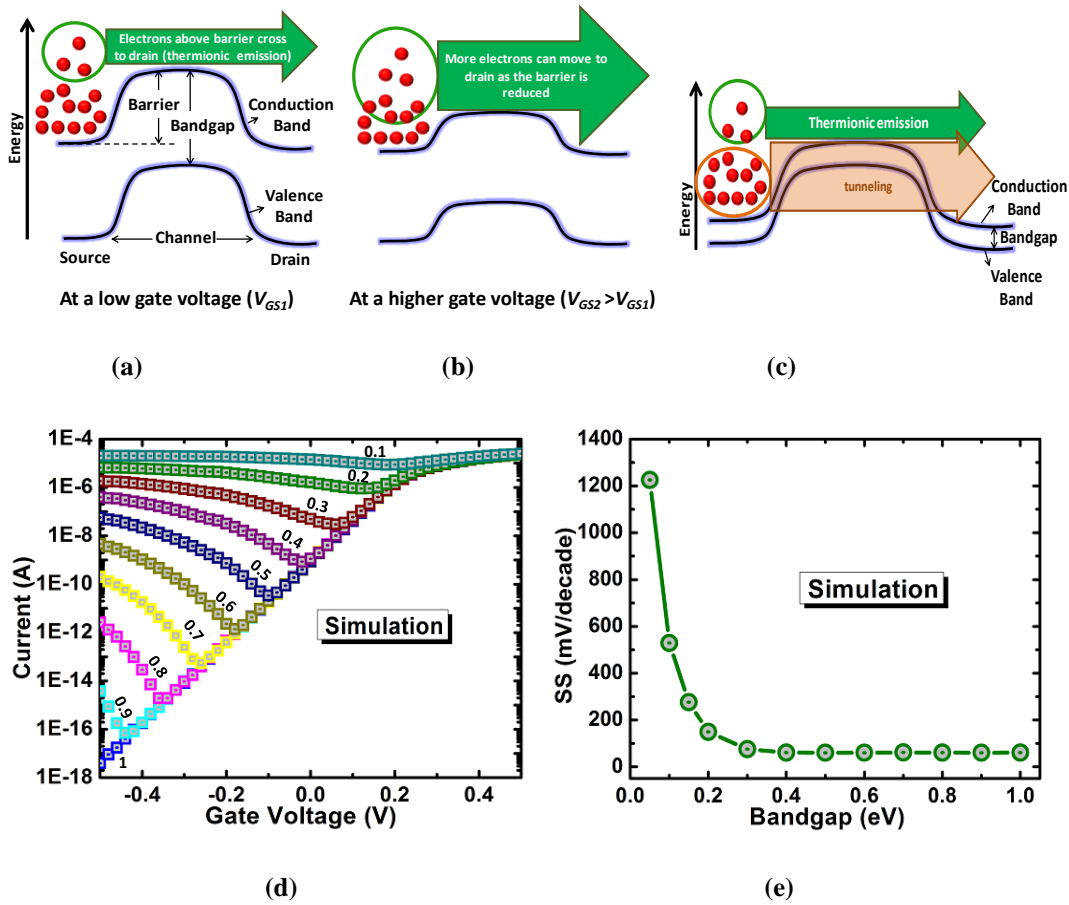


Figure 2.3(a) Schematic band diagram illustrating current flow mechanism in (n-type) FETs with the semiconducting layer having considerable bandgap. Only electrons having energy greater than the barrier height can cross the barrier and contribute to current as shown by the green arrow. At low gate voltage (V_{GS1}), few electrons (within the green circle) can cross the barrier. **(b)** After the application of higher gate voltage (V_{GS2}), more electrons (within the green circle) can cross the barrier. **(c)** In case the semiconducting channel has very small bandgap, electrons can not only flow above the top of the barrier, but electrons with lower energies can also tunnel through the barrier, which can increase the leakage current. **(d)** Current as a function of gate voltage for different bandgaps of the semiconducting channel material varying from 1eV to 0.1 eV. Corresponding bandgap for each curve is shown in the figure. **(e)** Subthreshold swing as a function of bandgap of the semiconducting channel material.

in engineering the same [16]–[20] makes it unsuitable for building transistors. The reason is explained as follows. In transistors, where semiconducting materials with a band gap serve as a channel, only electrons having energy higher than the source-to-channel barrier can transport from source to drain, as illustrated in **Figure 2.3(a)**. Hence, with lowering of the barrier more electrons can flow to the drain (**Figure**

2.3(b)), and since electrons occupy the energy levels according to the Boltzmann distribution at the source, the SS obtained can be as low as 60 mV/dec at room temperature as explained in Chapter 1. However, if the band gap of the semiconducting material is extremely small, the barrier is extremely thin and even electrons having energies lower than the barrier height begin to flow via direct tunneling, as illustrated in **Figure 2.3(c)**. This leads to an increase in off-state leakage current, as shown in **Figure 2.3(d)**, and hence in the degradation of SS , as clear from **Figure 2.3(e)**, even though the simulation parameters related to channel thickness and dielectric properties have been chosen to achieve almost perfect electrostatics, i.e., near-ideal change of potential at the interface of the semiconductor and the gate dielectric with a change in gate voltage.[4] Though, graphene is not suitable material for digital transistors, it is considered as a potential material for VLSI interconnects [21]–[26] due to their unique properties such as capability to conduct high current densities, high thermal conductivity [27] and long mean free path (MFP) that leads to large electrical conductance[28].

For building transistors, another class of 2D layered materials in the form of Transition-Metal-Dichalcogenides (TMDs) as shown in **Figure 2.4(a)**, which possess finite bandgap (**Figure 2.4(b)**) are highly attractive. TMDs consist of a family of 2D semiconductor layers of covalently bonded transition metal and dichalcogenide atoms arranged in hexagonal lattice (**Figure 2.4(a)**) where adjacent layers are held together by weak Van der Waal's forces. MoS₂ and WSe₂ are the most commonly explored TMDs.

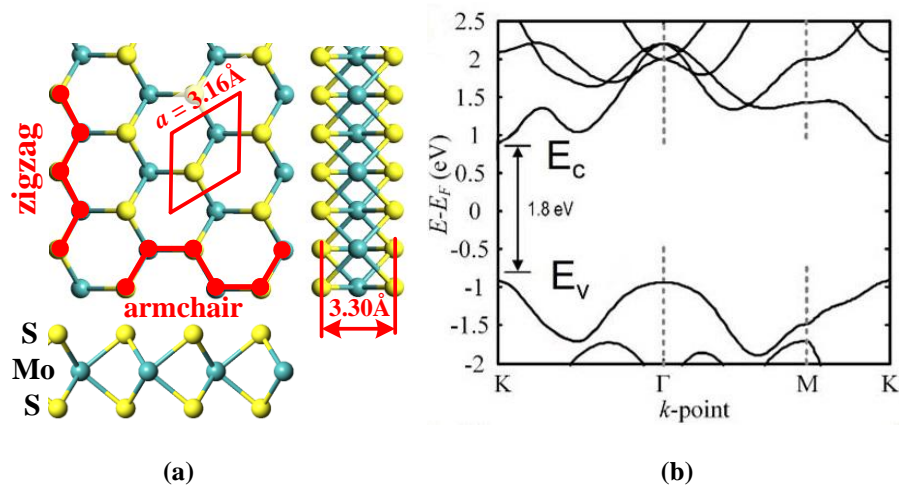


Figure 2.4 (a) Schematic diagram showing the 3 views of MoS₂ which belongs to the class of TMDs (b) Energy dispersion of monolayer MoS₂. Monolayer MoS₂ has a direct band gap of 1.8 eV.

TMDs offer excellent electrostatics due to ultra-thin nature and lack of dangling bonds and at the same time, are also easily patternable due to their planar structure. On the other hand, thinning down conventional 3D materials to nanometer-scale dimensions is not only process-wise challenging; such structures suffer from interfaces with trap states and worse mobility degradation (**Figure 2.5**). Hence, the 2D semiconducting TMDs are highly promising for ultra-scaled transistors.[29][30]

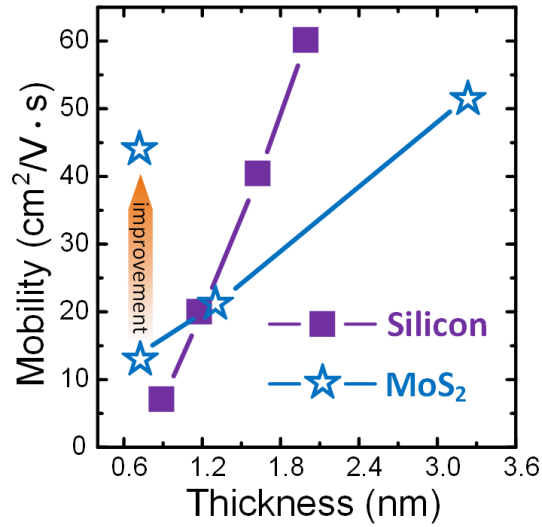


Figure 2.5. This figure shows how mobility degrades with material thickness. The mobility of Si[31] degrades much faster than that of MoS₂[32]. At 0.9 nm, it is only around 6-7 cm²/V·s. While the 0.65 nm thick 1L MoS₂ has a mobility of around 12. Recently, this value has been boosted to 44 by W. Liu et al.[33] In general, 2D materials pay much less for being thin compared to bulk materials.

2.3. Transistors : 2D Semiconducting Transition Metal Dichalcogenides

2.3.1. Doping

For various applications including FETs and photovoltaics, it is necessary to tune the electronic properties of TMDs through modulation of the mobile charge concentrations, or, in other words, doping. Both p and n type doping can be achieved electrostatically[34],[35] by application of gate voltage, but, it requires extra electrodes (gates) that can increase power dissipation and increase area. Another way of doping is through substitution of the transition metal[36],[37] or the chalcogenide[38] of TMDs with appropriate elements. However, substitutional doping disturbs the structure of the TMDs through defect formation. Though,

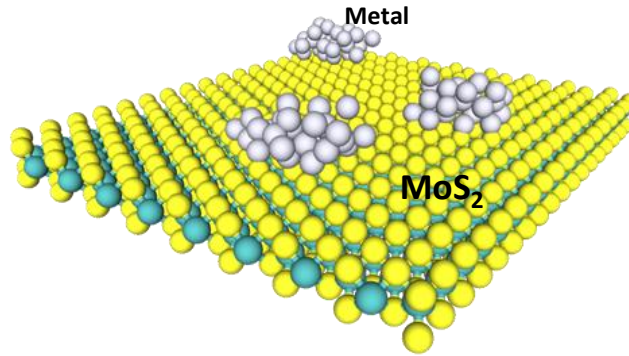
physisorption[39][40] of molecules can also lead to doping effect, they are unstable in nature. Solution based functionalization of TMD flakes have also been reported to achieve doping,[41]–[43] but the functionalization process is generally complicated and time-consuming. Plasma based doping[44][45] leads to formation of defects and significant reduction in mobility. Hence, exploration of efficient doping methodologies are required, which would be stable, easy to implement and would not lead to significant defects in the TMDs. In case of WSe₂, efficient n-type doping using Potassium[46] as well as silicon carbide thin films[47] have been shown. Cs₂CO₃[48] and 1,2 dichloroethane (DCE)[49] have been reported to lead to n-type doping of MoS₂. P-type doping of WSe₂ using NO_x chemisorption has been recently reported[50]. Also, p-type doping of MoS₂ using MoO₃ has been explored[51]. However, MoO₃ is very sensitive to the contaminants in the air leading to variations in its work-function[52].

The large surface-to-volume ratio offered by 2D TMD semiconductors offer unique opportunities for efficient surface functionalization/treatment to enable charge transfer to and from the atomically-thin layered materials. Especially, incorporation of surface adatoms such as nanoparticles (NPs) of noble metals can be an effective way of doping 2D TMD materials, as these metals are resistant to environmental corrosion and oxidation. Moreover, functionalization using noble metallic NPs can also open up new avenues for gas sensing[53]–[55] as well as biosensing[56] applications, as has been demonstrated in case of nanotubes/nanowires or graphene oxide. In this dissertation we investigate the doping effect in TMDs caused by NPs of

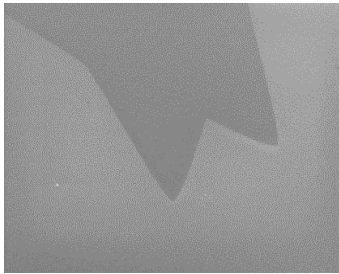
noble metals (Au, Ag, Pd, Pt) and show that all these metallic NPs lead to p-type doping of MoS₂.^[57] The low work function metals such as Scandium (Sc) and Yttrium (Y) are also studied to demonstrate the relationship between metal work function and doping effect in MoS₂. While Sc leads to p-type doping, n-type doping can be obtained from Y. Moreover, it is shown that for MoS₂, Pt NPs can lead to as high as 2X higher p-type doping effect compared to that of the most commonly used Au NPs^{[58],[59]}. While most experiments are performed using MoS₂, which is a typical representative of the TMD family, the doping effect of Pt NPs on WSe₂, another commonly used TMD material, is also explored.

Results and Discussion

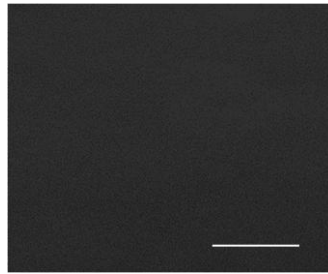
The TMD flakes are obtained on 280 nm SiO₂/Si substrates using the micromechanical exfoliation technique, which is an efficient way for prototyping experiments on various 2D materials.^{[3], [32], [39], [46], [60]–[64]} However, large area synthesis of MoS₂ is also made possible by the recent developments in liquid-scale exfoliation^{[65],[66]} and chemical vapor deposition growth.^{[67],[68]} The metallic nanoparticles are incorporated on the TMD sheet using ebeam deposition. The schematic diagram of a MoS₂ flake with NPs is shown in **Figure 2.6(a)**. **Figure 2.6(b)** shows the Scanning Electron Microscopy (SEM) image of a MoS₂ flake while **Figure 2.6(c)** and **(d)** show the magnified images of a portion of the flake, without and with the NPs, respectively. The Atomic Force Microscopy (AFM) characterization of the NPs is shown in **Figure 2.6(e)** and **(f)**.



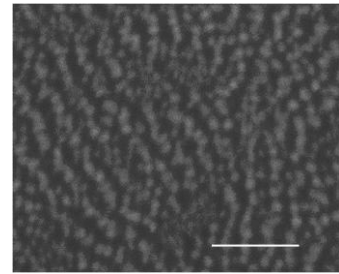
(a)



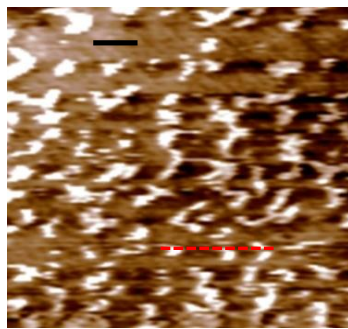
(b)



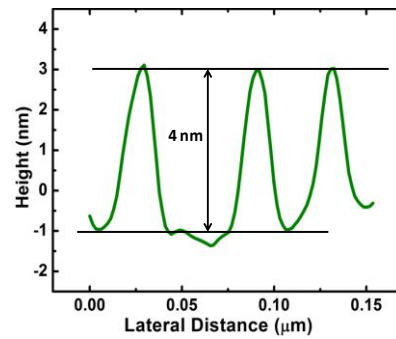
(c)



(d)



(e)



(f)

Figure 2.6 (a) Schematic diagram of an MoS₂ flake with metallic nanoparticles. (b) Scanning Electron Microscopy (SEM) micrograph of a MoS₂ flake on SiO₂/Si substrate. Magnified SEM image of the portion of the flake before any nanoparticle deposition which is basically featureless as shown in (c) and after Pt NPs are deposited as shown in (d). Scale bar, 50 nm. The deposition rate used is 0.5A/s for 100s. (e) Atomic Force Microscopy (AFM) image showing NPs on MoS₂ flake. Scale bar (black line), 50 nm. (f) Height profile of the NPs along the red dotted line shown in (e).

Electrical measurements are an efficient way of characterizing the doping effect on semiconducting materials. Hence, Field-Effect Transistors (schematic diagrams are shown in **Figure 2.7(a)** and **(b)**) are fabricated on the MoS₂ flakes (**Figure 2.7(c)**) with 20nm/100nm Ni/Au as source and drain metal contacts (**Figure 2.7(d)**). The underlying SiO₂ and the highly doped Si substrate are used as the gate dielectric and gate contact respectively. The thickness of the flake is characterized using AFM (**Figure 2.7(e)** and **(f)**). To explore the effect of metallic NPs on MoS₂, the MoS₂ FET was measured first without the NPs and then the same device was measured again immediately after the deposition of NPs. Note that the metallic NPs do not form a continuous film and the current essentially flows through the MoS₂ channel. This is obvious since if a continuous metallic film would have formed, then current between the source and drain would essentially flow through the metallic film due to its lower resistance compared to semiconducting MoS₂ and therefore, the current could not have been modulated by the gate. **Figure 2.8(a)** and **(b)** shows the Id-V_g and Id-V_d curves respectively before and after incorporation of the Ag NPs. The MoS₂ FET exhibits n-type transistor characteristics as the current increases with the increase in gate voltage. On incorporation of Ag NPs, the Id-V_g curve shifts towards the right compared to that without the NPs, indicating that more positive gate voltage is required to turn on the FET with NPs, implying p-type doping by the Ag NPs. The doping effect of other noble metallic NPs such as Au, Pd and Pt are also explored as shown in **Figure 2.8(c) - (h)**. All these metals also lead to p-type doping as is clear from the shift of the Id-V_g curves. It is observed that Pt, which has the

highest WF (about 5.9) among these metals, results in the highest shift in Id-Vg curve and thereby, highest p-type doping.

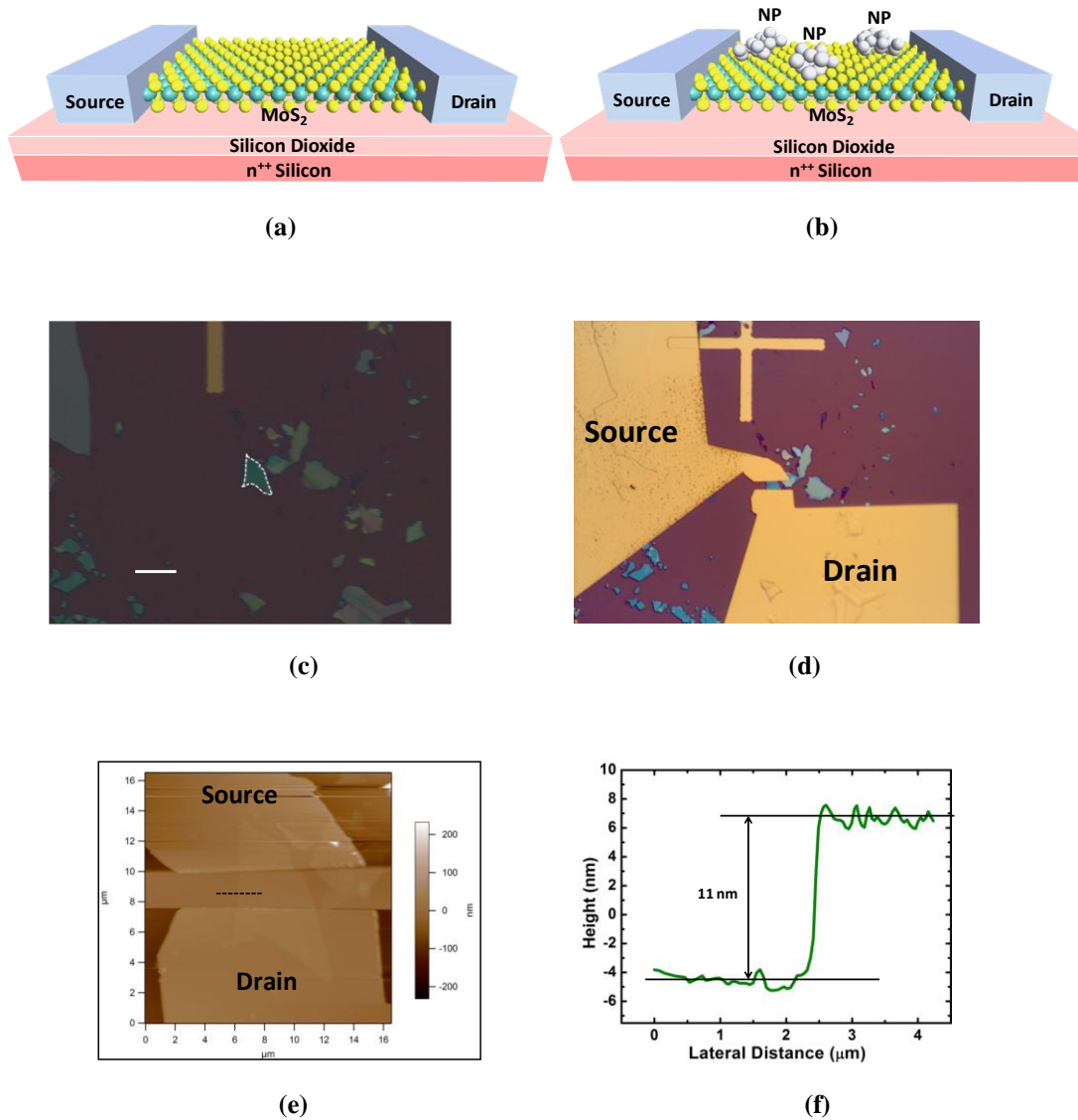


Figure 2.7(a) without NPs and (b) with NPs. (c) Optical image of a MoS₂ flake (highlighted by white dotted line) mechanically exfoliated on 280 nm SiO₂ grown thermally on Si. Scale bar is 10 μm. (d) Optical image of the FET fabricated on the MoS₂ flake shown in (c). The source and drain regions were defined by e-beam lithography followed by e-beam deposition of 20nm/100nm Ni/Au. (e) AFM image of the MoS₂ FET. (f) Height profile of the MoS₂ flake along the black dotted line shown in (e).

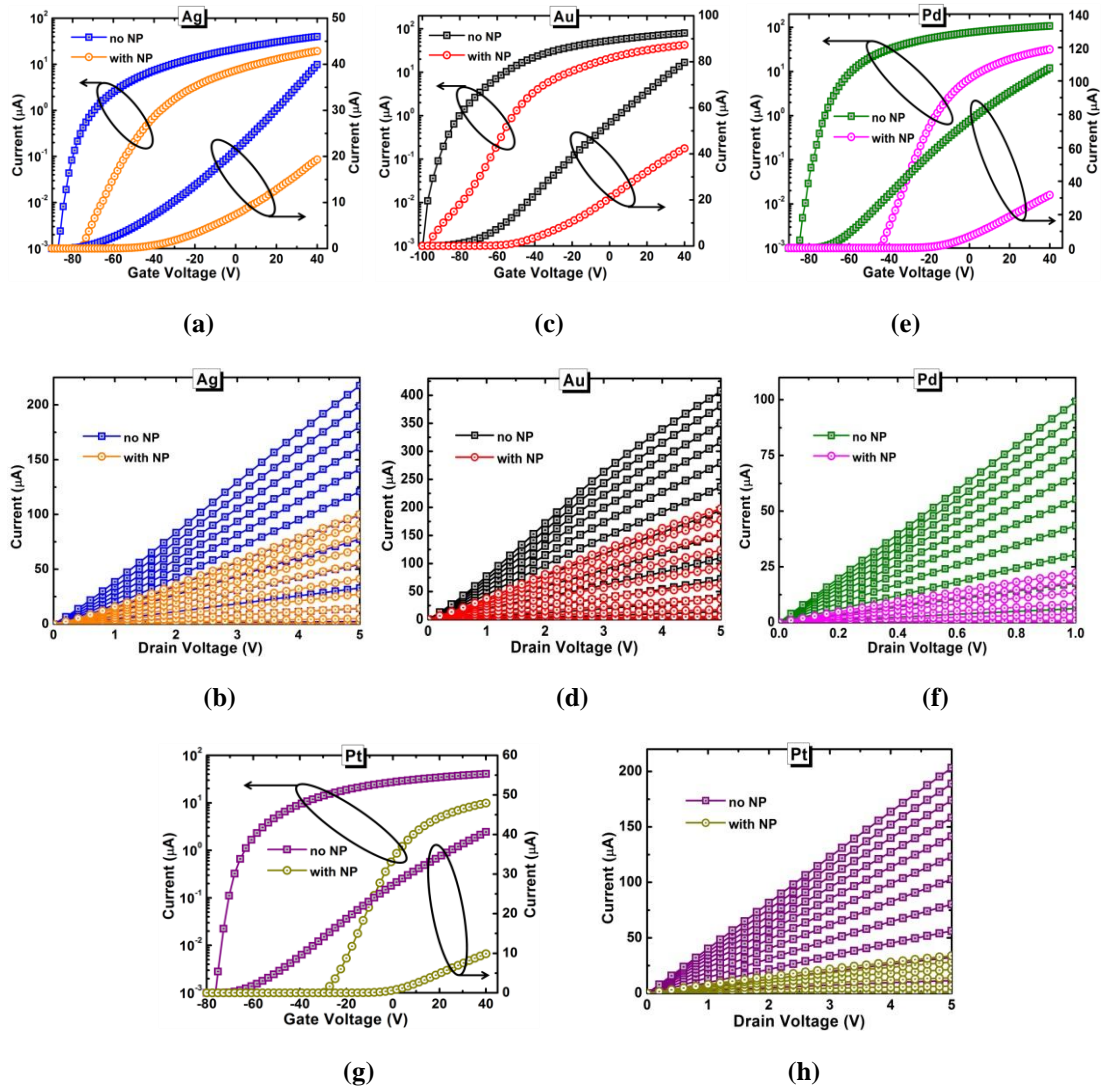


Figure 2.8. Drain current as a function of gate voltage (I_d - V_g) for MoS₂ FETs before and after incorporation of nanoparticles of (a) Ag, (c) Au, (e) Pd, (g) Pt. The left axes show values in logarithmic scale while the right axes show values in linear scale. The drain current vs drain voltage (I_d - V_d) curves before and after incorporation of nanoparticles of (b) Ag, (d) Au, (f) Pd, (h) Pt where V_g is varied from -80V to 40V in steps of 10V. The thickness of the MoS₂ used in all the 4 cases is around 8nm. All metals are deposited at the rate of 0.5A/s for 100s. As can be observed from the I_d - V_g curves, V_{TH} is negative for all cases since the MoS₂ is naturally n-doped. All the metallic NPs lead to p-type doping as is evident from the shift of the I_d - V_g curves with NPs towards the right. Pt is observed to lead to the highest shift and hence to highest doping.

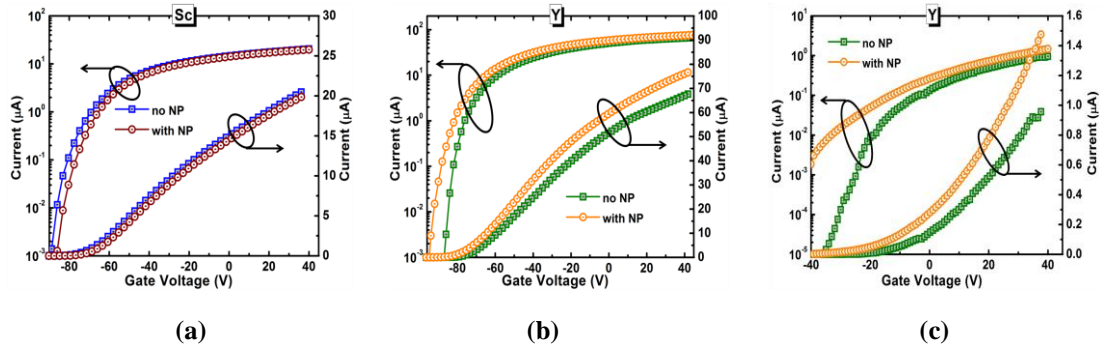


Figure 2.9(a) Drain current as a function of gate voltage for MoS₂ FETs before and after incorporation of Sc nanoparticles. The left axis shows values in logarithmic scale while the right axis shows values in linear scale. The thickness of the MoS₂ used is around 8 nm. Sc NPs are found to shift the Id-Vg curves slightly to the right indicating slight p-type doping. **(b)** The drain current vs gate voltage curves MoS₂ FET before and after incorporation of Y nanoparticles. Y NPs are found to shift the Id-Vg curves slightly to the left indicating n-type doping. The thickness of the MoS₂ used is around 8 nm. **(c)** Significant n-type doping is obtained in case of a mono-layer MoS₂ FET after incorporation of Y NPs. Both Sc and Y are deposited at the rate of 0.5A/s for 100s.

To investigate the effect of incorporation of metallic NPs with very low WF, experiments are carried out with Scandium (Sc) with a WF of 3.5 and Yttrium (Y) with a WF of 3.1. Sc NPs are found to result in slight p-type doping as shown in **Figure 2.9(a)**. N-type doping can be obtained by using Y NPs as illustrated in **Figure 2.9(b)** and **(c)**. While in case of multi-layer MoS₂ FET, Y NPs can lead to only slight n-type doping (**Figure 2.9(b)**), the doping effect increased significantly when a mono-layer MoS₂ is used (**Figure 2.9(c)**) as is evident from the higher shift of the Id-Vg curves.

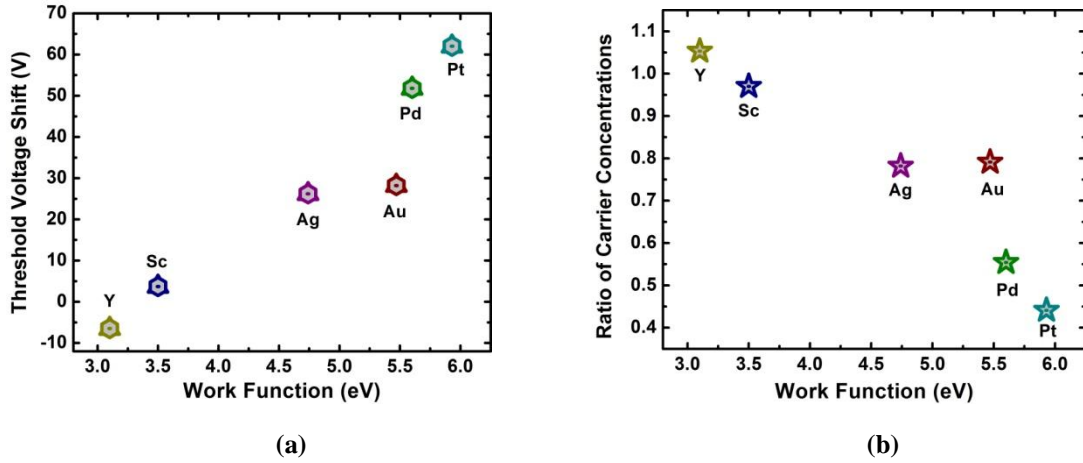


Figure 2.10 (a) Shift of threshold voltage (ΔV_{TH}) due to incorporation of NPs as a function of the workfunction (WF) of different metals. In case of Y, ΔV_{TH} is negative due to n-type doping. In case of all other metals, ΔV_{TH} is positive as they lead to p-type doping and an increasing trend is observed with increasing WF due to higher p-type doping by NPs of metals with higher WFs. (b) Ratio of carrier concentrations (R_{ξ}) after NPs incorporation to those before. R_{ξ} is higher than 1 for Y, as n-type doping by Y increases the effective carrier (electron) concentration. For all other metals, R_{ξ} is less than 1 and a decreasing trend is observed with increasing WF due to the decrease in the effective carrier (electron) concentrations with more p-type doping. The thickness of MoS₂ is similar in all the cases and is around 8 nm.

The shift in threshold voltage (given by $\Delta V_{TH} = V_{TH_NP} - V_{TH}$ where V_{TH} and V_{TH_NP} are the threshold voltages before and after the incorporation of NPs, respectively) as a function of WF of different metals is shown in **Figure 2.10(a)**. Since n-type doping means lower gate voltage is required to turn on the n-type devices and hence lower threshold voltage, the ΔV_{TH} is negative for Y as is clear from the figure. For the other metals, ΔV_{TH} is positive as they lead to p-type doping and with the increase in the metal WF, the ΔV_{TH} shows an increasing trend corroborating the increase in the p-type doping with the increase in the metal WF. The ratio of carrier concentrations with and without the NPs (given by $R_{\xi} = \xi_{NP}/\xi$ where ξ and ξ_{NP} are the carrier concentrations before and after incorporation of NPs, respectively) at a gate voltage of 40V, is illustrated in **Figure 2.10(b)**. Due to the capacitive coupling of

the gate, at positive gate voltage, 2D carrier (electron) density is formed at the semiconductor-dielectric interface. Since n-type doping leads to an increase in the effective carrier (electron) density, $R_{\xi} > 1$ for Y. However, in the case of the other metals, the effective carrier (electron) density is reduced due to the p-type doping, leading to $R_{\xi} < 1$. Higher the p-type doping, lower will be the R_{ξ} . As shown in **Figure 2.10(b)**, R_{ξ} exhibits a decreasing trend with the increase in WF due to the increase in p-type doping. From **Figure 2.10** it can be observed that Pt NPs can lead to a 2-fold higher doping effect compared to that of Au NPs, which has been commonly used to dope 2D materials.

As n type doping can be obtained by using Y NPs, which, however, is not a noble metal, it is necessary to investigate its stability. Doping with Y NPs is found to be unstable and degraded on exposure to air due to the oxidation of Y. **Figure 2.11(a)** shows the drain current vs. gate voltage curves of a MoS₂ FET without any NPs and after incorporation of Y NPs measured at two different times. N-type doping is observed when the device is measured immediately after Y NP incorporation as the threshold voltage shifted towards the left and hence current increased. However, after about 10 hrs, the doping degraded as indicated by the increase in threshold voltage and decrease in current levels, which became similar to those without any NPs.

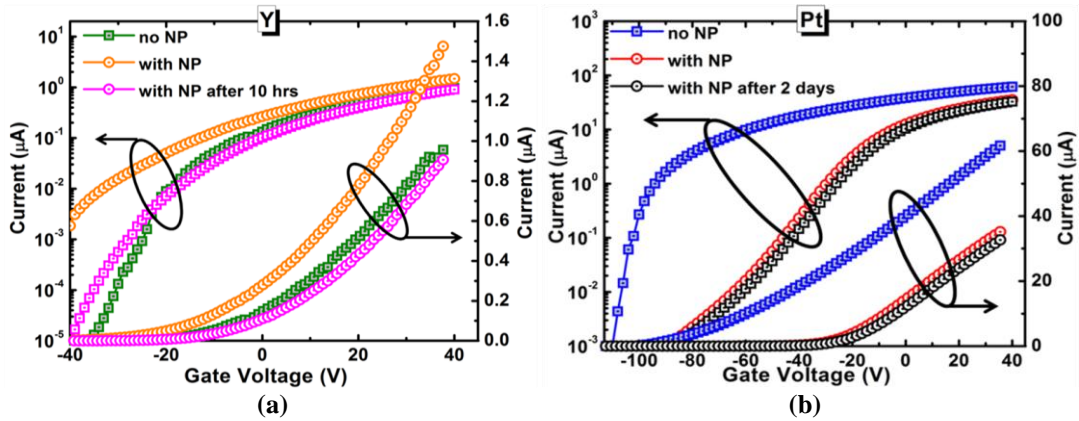


Figure 2.11(a) Drain current as a function of gate voltage for MoS₂ FETs without any NPs (green curve), after incorporation of Y nanoparticles and measured immediately (orange) and measured after 10hrs (magenta curve). The left axis shows values in logarithmic scale while the right axis shows values in linear scale. **(b)** Drain current as a function of gate voltage for MoS₂ FETs without any NPs (green curve), after incorporation of Pt nanoparticles and measured immediately (orange) and measured after 2 days (magenta curve). The left axis shows values in logarithmic scale while the right axis shows values in linear scale.

On the other hand, noble metals are resistant to environmental attack and hence, lead to stable doping as shown in the case of Pt NPs (**Figure 2.11(b)**).

Since Pt NPs lead to the highest doping and at the same time is stable, the rest of this section focuses on exploration of Pt NPs in more detail. Raman Spectroscopy is used to analyze the effect of Pt NPs. The Raman spectra excited by 632.8 nm line for a MoS₂ sheet before and after Pt NP incorporation is shown in **Figure 2.12**. For both the cases of with and without nanoparticles, apart from the E¹_{2g} and A_{1g} peaks, a peak is also visible around 455 cm⁻¹, which is typical for MoS₂ for excitation at 632.8 nm.[69] For MoS₂ with NPs, the features are shifted towards the right, indicating p-type doping.[70]

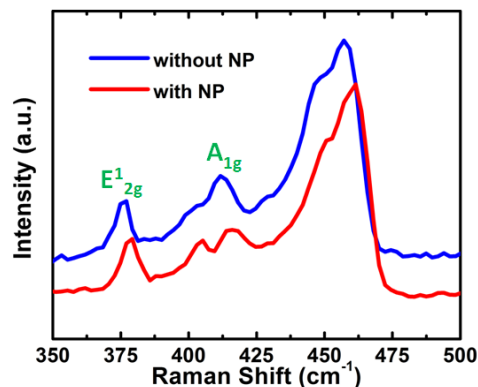


Figure 2.12. The Raman spectra excited for a MoS₂ sheet before and after incorporation of Pt NPs shown by blue and red lines respectively. The red line is shifted towards the right compared to the blue line, indicating p-type doping by the Pt NPs.

Raman spectroscopy measurements were done at various points on the sample surface to take into account the effect of variations. For all the measurements, in case of MoS₂ with NPs, the features are shifted towards the right (**Figure 2.13**) compared to those without the nanoparticles, confirming p-type doping.

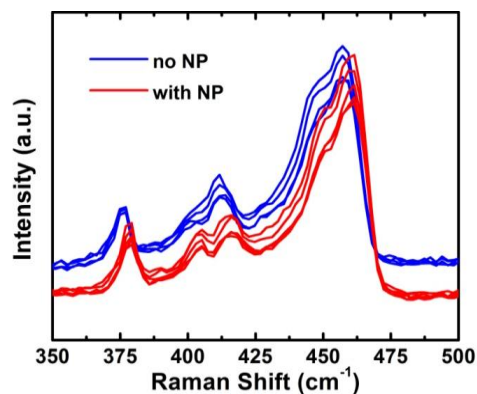


Figure 2.13. The Raman spectra excited for a MoS₂ sheet before and after incorporation of Pt NPs shown by blue and red lines respectively. The red lines are shifted towards the right compared to the blue lines, indicating p-type doping by the Pt NPs.

To better understand the doping effect of Pt NPs, ab initio density functional theory (DFT) calculations were performed. Since, MoS₂ in general is naturally doped n-type, this n-type doping is simulated by using Cl atoms. Since DFT only utilizes periodic boundary conditions with mono-crystalline materials, metal-MoS₂-Cl system is modeled by a unit cell, which is periodic along lattice vector a and b and separated by vacuum in the c direction, as shown in **Figure 2.14(a)**. The unit cell contains a doped MoS₂ layer with Cl atoms as dopants, topped by a thin film of Pt to emulate the Pt island. The mean absolute strain is 1.35% due to a slight lattice mismatch. All the atoms are allowed to relax.

It is important to note that the study of the metal-2D material interfaces (**Figure 2.14(b)**) requires careful treatment of the van der Waals (vdW) interaction between them. In order to reproduce such nonlocal dispersive force, which are important in weakly bonded systems, DFT-D2 approach[71] is used, where a semi-empirical dispersion potential described by a simple pair-wise force field is added to the conventional Kohn-Sham DFT energy.

Local density approximation (LDA)[72] is adopted for the exchange correlations, together with either the double- ζ polarized basis set for expanding electronic density. The calculations are performed using Atomistix ToolKit (ATK).[73] $8 \times 8 \times 1$ k-points are sampled in the Brillouin zone (BZ). The temperature is set to be 300 K. The density mesh cut-off is 200 Rydberg and the maximum force is 0.05 eV/Å for geometry optimizations.

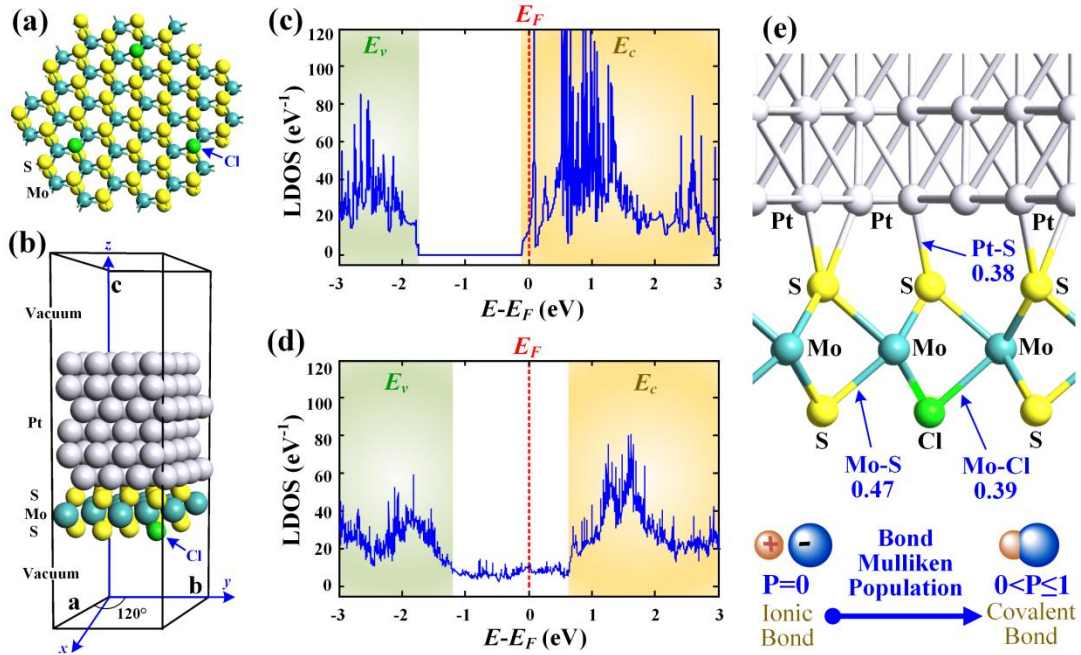


Figure 2.14(a) The top view of MoS₂ with incorporated Cl atoms in order to simulate the n-type doping in MoS₂. (b) The schematic view of MoS₂-Cl-Pt system. (c) The local density of states diagram of MoS₂-Cl. The orange shaded region denotes the conduction band while the green shaded region denotes the valence band and the white region in between is the bandgap. The Fermi-level, denoted by the red dashed line lies in the conduction band clearly indicating an n-doped MoS₂. (d) After incorporation of Pt, the Fermi-level moves away from the conduction band indicating p-type doping by the Pt. (e) Schematic showing the Mulliken Population (P) for Mo-S bond (0.47), Mo-Cl bond (0.39) and Pt-S bond (0.38). P=0 denotes ionic bond while P > 0 denote covalent bond. Thus, the positive value of P for Pt-S bond signifies that Pt forms covalent bond with the S of MoS₂.

The density of state diagrams before and after the incorporation of Pt NPs are shown in **Figure 2.14**(c) and (d) respectively. As is clear from the figures, after the incorporation of Pt NPs the Fermi level (denoted by the dashed line) shifts below the conduction band indicating p-type doping by the Pt NPs. Mulliken population analysis (**Figure 2.14**(e)) is also performed to understand the nature of bonding between Pt and MoS₂. Bond Mulliken population (P) represents the electronic charge

distribution in a molecule and the nature of the molecular orbitals for a pair of atoms.[74] The value of P varies from 0 to 1, where $P = 0$ and $0 < P \leq 1$ indicate ionic and covalent bonds, respectively. For covalent bonding, the numerical value of P indicates the strength of the bond. From **Figure 2.14(e)** it is clear that Pt forms covalent bonds with the Sulfur of MoS_2 and the value of P for Pt-S bond is found to be 0.38.

DFT simulations can also be used to calculate the phonon spectra for physical explanation of the shift obtained due to p-doping.[57] Taking the example of important Raman modes A_{1g} and E_{2g}^1 , it is shown in **Figure 2.15** that the energy of both A_{1g} and E_{2g}^1 (Polar Longitudinal Optical (LO) mode) increase slightly upon p-doping, consistent with the experimental observation. Note, that the energy of Polar Transverse Optical (TO) mode decreases but this mode is not Raman active. Physically, the shifts of Raman modes can be explained in terms of the *born effective charges* of Mo and S atoms in the MoS_2 molecule. Born effective charge is defined as the change in polarization divided by the amount an ion is displaced, so it is not zero even in the undoped cases. In intrinsic MoS_2 , it is 1.11 electrons (positive charge) for Mo atom, and it is -0.52 electrons for each S atom.

In A_{1g} mode, sulfur atoms vibrate in opposite direction, perpendicular to the basal plane. When the MoS_2 is p-doped, the negative charge on the S atom will be less and hence, the repulsive Coulomb interaction of S atoms with the adjacent S atoms in another layer will be smaller. Consequently, the binding interaction of a MoS_2 molecule in a particular layer with that in the adjacent layers will be stronger, which

will make the stiffness constant of the A_{1g} mode larger, and thus, the vibration frequency will be higher according to the classical oscillator model.

For E_{2g}^1 LO mode, the Mo and S atoms vibrate in the basal plane and the displacement of the charges is accompanied by an extra force due to the electric field, parallel to the displacement. When we p-dope the MoS_2 , the polarization field will be stronger, so the restoring forces will be larger, thereby increasing the stiffness constant. Thus, the LO frequency will be higher as is observed experimentally and through simulations.

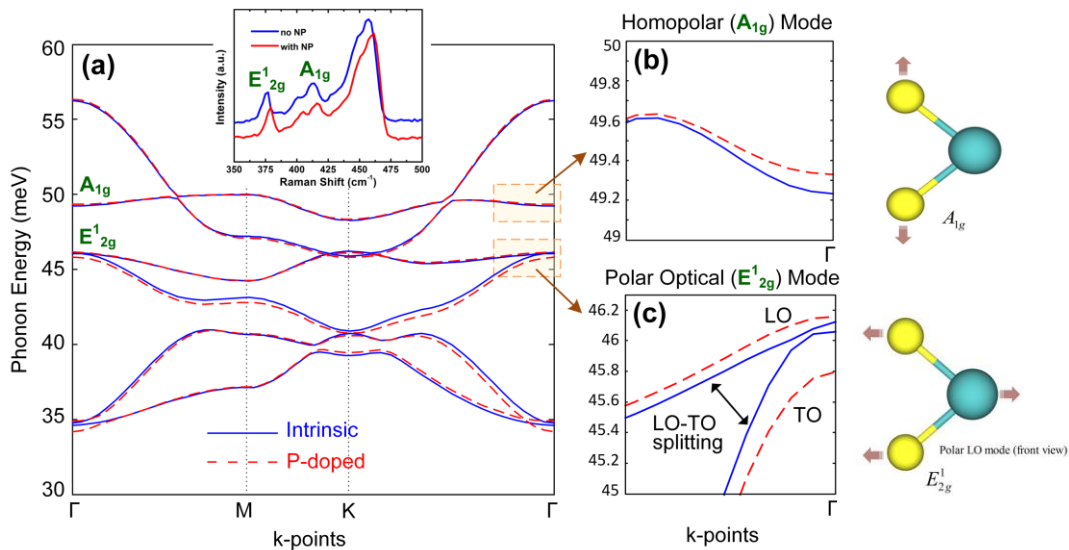


Figure 2.15 (a) Phonon spectra of intrinsic and p-doped MoS_2 (molar fraction 0.1%) calculated by DFT. Inset shows Raman spectra of intrinsic and p-doped MoS_2 measured in experiments. (b,c) Zoom of A_{1g} mode and E_{2g}^1 mode at Γ point. The schematic showing the direction of the atomic vibrations in A_{1g} mode and E_{2g}^1 mode are also shown on the right of (b) and (c) respectively. In (b), doping increases the phonon energy of homopolar mode (A_{1g}), and hence, the Raman peak corresponding to the A_{1g} mode shifts to the right, as shown in the inset of (a). In (c), doping increases macroscopic polarization and thus increases the polar LO phonon energy of the E_{2g}^1 mode.

The effect of different doses of Pt NPs on the MoS_2 FET is shown in **Figure 2.16**. First, the FET was measured without the NPs as shown by the blue curves in the

Id-Vg and Id-Vd plots in **Figure 2.16(a)** and **(b)**, respectively. Then, the device was measured after deposition of Pt NPs at the rate of 0.2A/s for 30s, as shown by the red curves. The same device was measured again after another 30s (total 60s) of deposition as shown by the green curves and yet again after another 30s (total 90s) of deposition as shown by the black curves and finally after another 60s (total 150s) of deposition as shown by the magenta curves, all at the same deposition rate. It is observed that by increasing the dose of Pt NPs in steps it is possible to gradually shift the transfer characteristics and dope the MoS₂.

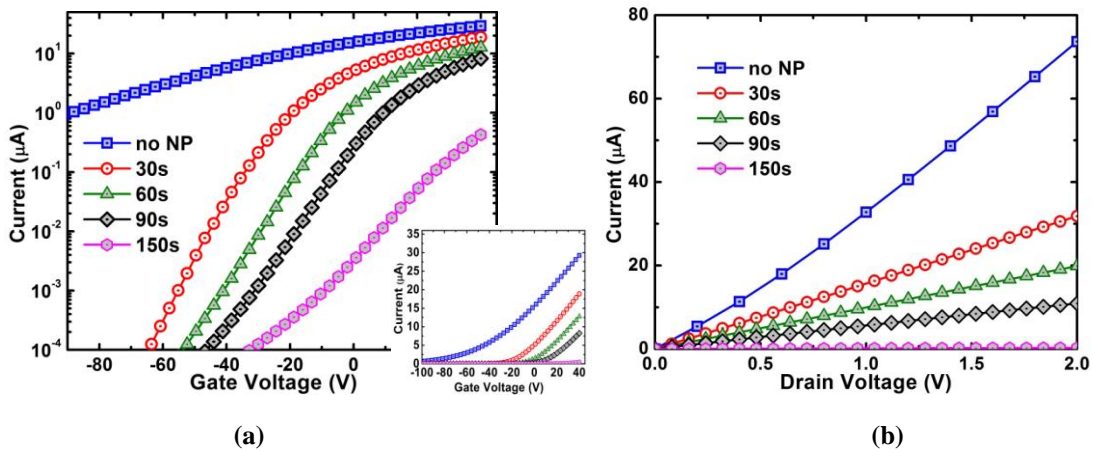


Figure 2.16(a) Drain current as a function of gate voltage (Id-Vg) curves for MoS₂ FET for different doses of Pt NPs. The Id-Vg curve before the incorporation of Pt nanoparticles is shown by the blue curve. The MoS₂ flake used to fabricate this device is exfoliated from a bulk sample having higher intrinsic n-doping compared to that in previous figures, which allows observation of the effect of different Pt NP doses more prominently. The red, green, black and magenta curves show Id-Vg characteristics after deposition of Pt NPs at the rate of 0.2A/s for 30s, 60s, 90s and 150s, respectively. The y-axis shows the values of current in logarithmic scale. The inset figure shows the curves in linear scale. The corresponding Id-Vd curves at Vg = 40V are shown in **(b)**.

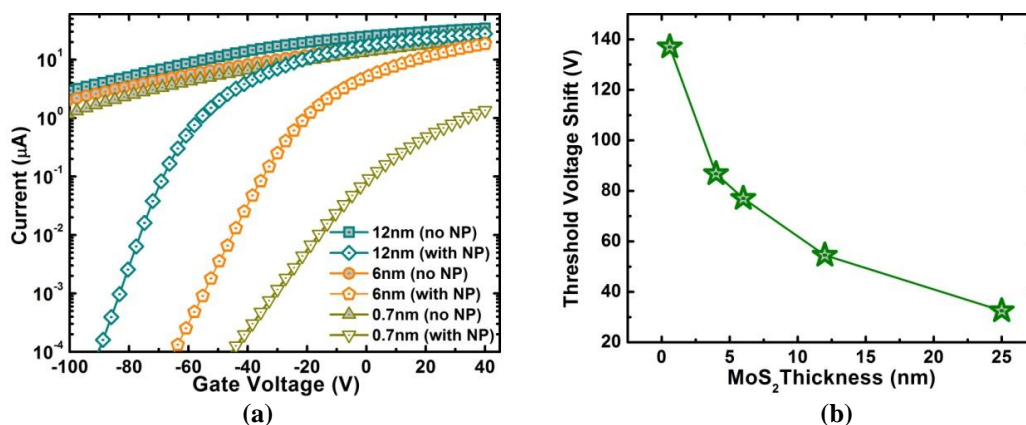


Figure 2.17. Effect of different thicknesses of MoS₂ on the doping characteristics. (a) Id-Vg curves (with the current multiplied by their respective ratios of length to width) before and after incorporation of Pt NPs for different MoS₂ thicknesses. Thinner the MoS₂, higher is the shift in curve with NPs to the right compared to that without the NPs. (b) The threshold voltage shift decreases with increase in MoS₂ thickness indicating lower doping effect.

Next, the effect of MoS₂ thickness on the doping characteristics is investigated. For this purpose MoS₂ flakes with different thicknesses are identified using optical contrast and the accurate thicknesses are measured using AFM. Subsequently, FETs are fabricated on the selected flakes. After initial measurements of the FET transfer characteristics, Pt NPs are deposited on the flakes at the same time, followed by another set of measurement with the NPs. To eliminate the effect of different lengths and widths of the FETs with different thicknesses, the currents of the devices are multiplied by their respective ratios of length to width and plotted in **Figure 2.17(a)**. It is observed that for almost similar levels of initial current, on incorporation of Pt NPs, the shift of the Id-Vg curve for the monolayered MoS₂ device is the highest (137 V) followed by those of the thicker MoS₂ devices. The threshold voltage shift is plotted as a function of the MoS₂ thickness in **Figure 2.17(b)**. It can be observed that the shift and hence the doping decreases with the

increase in the thickness. This is because of the screening of the doping effect by the top MoS₂ layers.

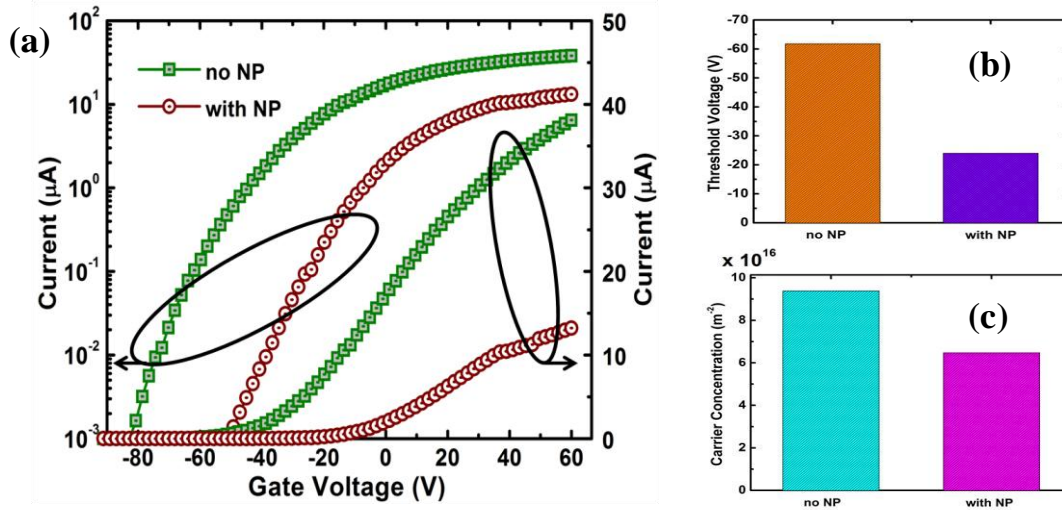


Figure 2.18(a) Drain current as a function of gate voltage for WSe₂ FETs before and after incorporation of Pt NPs. The left axis shows values in logarithmic scale while the right axis shows values in linear scale. The thickness of the WSe₂ used is around 9 nm. Pt is deposited at the rate of 0.5A/s for 100s. Similar to the case for MoS₂, Pt NPs are found to shift the Id-Vg curves to the right indicating p-type doping of WSe₂. **(b)** Threshold voltages before and after incorporation of Pt NPs showing shift towards more positive values in the presence of Pt NPs. **(c)** Carrier Concentrations before and after incorporation of Pt NPs. Effective decrease in carrier (electron) concentration is observed due to the p-type doping by Pt NPs.

Apart from MoS₂, another TMD material most commonly used is WSe₂[39], [46], [63]. The doping effect of Pt NPs on WSe₂ is also explored by fabricating FETs and carrying out measurements in the same way as that of the MoS₂ experiments. The Id-Vg curves before and after incorporation of Pt NPs are shown in **Figure 2.18(a)**. P-type doping by the metallic NPs is evident from the shift of Id-Vg curve for FET with NPs towards the right. The threshold voltage and carrier concentration without and with the NPs are shown through the bar diagrams in **Figure 2.18(b)** and **(c)**,

respectively, illustrating the increase in the threshold voltage and decrease in effective carrier (electron) concentration after NP incorporation.

Compared to the MoS₂ devices, the effective mobility (which includes the influence of contacts) of WSe₂ devices are found to be lower. This is because, due to the lower electron affinity of WSe₂, Ni forms higher Schottky barrier for n-type conduction with WSe₂ compared to MoS₂. Mobility can be improved by choosing proper contact metals, [75][76] which, however, is not the focus of this work. Effective mobility is calculated as $\mu = (L/W)dG/dV_g C_{ox}^{-1}$ in the linear region, where C_{ox} is the capacitance of the 280 nm-thick bottom SiO₂ dielectric; G is the conductance; L and W are the length and width of the channel, respectively. For both MoS₂ and WSe₂ FETs, the mobility decreased slightly after incorporation of NPs. The mobility for WSe₂ before and after Pt NP incorporation are found to be 16.8 cm²V⁻¹s¹ and 10.23 cm²V⁻¹s¹ respectively while those for MoS₂ FET are 32 cm²V⁻¹s¹ and 26 cm²V⁻¹s¹ respectively.

2.3.2. Gate Control

Till now back gated MoS₂ FETs have been discussed. As the back gate dielectric is very thick (300 nm SiO₂), the SS obtained from this devices is much above the thermionic limit and very high back gate voltages need to be applied in order to turn the devices ON (**Figure 2.19(a)**). For practical application, top gated FETs with thinner high-k dielectrics are necessary. Currently, the TMD technology is still undergoing development and formation of scaled and high quality gate dielectrics remains a challenge. Due to the lack of dangling bonds the initial dielectric layers are

formed through physical absorption which leads to degraded quality and pinholes in case of thinner dielectric layer[77] which causes high gate leakage current. Increasing the dielectric thickness decreases gate leakage but compromises the gate capacitance and hence, device electrostatics. High-k dielectric HfO_2 formed through Atomic Layer Deposition, as gate dielectric is investigated. Thickness of the HfO_2 film has to be around 30 nm for reducing leakage and the SS obtained is around 200 mV/dec (Figure 2.19(b)).

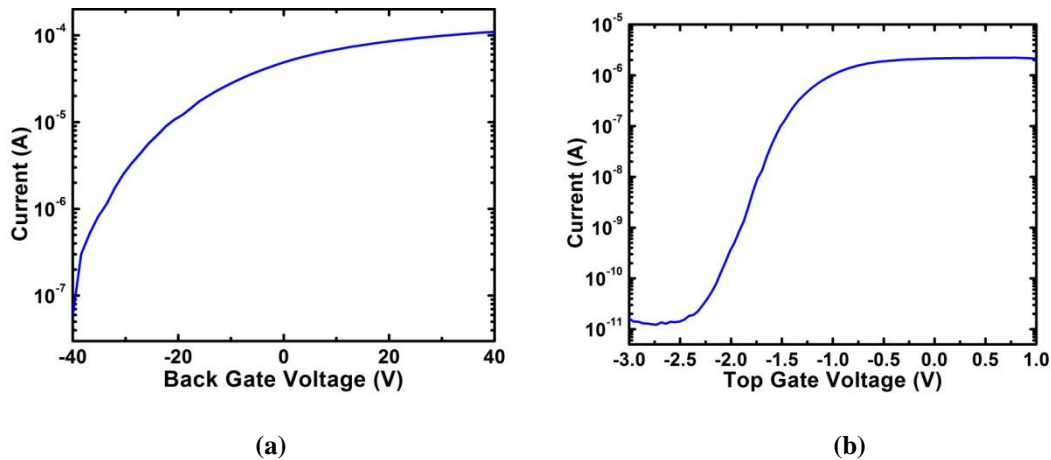


Figure 2.19 (a) Drain current as a function of back gate bias. (b) Drain current as a function of top gate bias. The thickness of ALD HfO_2 is around 30 nm.

In order to increase gate coupling and improve SS , instead of using the conventional high-k dielectric, a solid polymer electrolyte (PE) consisting of poly(ethylene oxide) (PEO) and lithium perchlorate (LiClO_4) is explored in this work for forming the gate capacitor, which can lead to high gate capacitance due to the formation of electrical double layer[78]. For polymer electrolyte gating, the gate electrode does not need to be directly above the channel and is formed on the side as

shown in **Figure 2.20**. The PE is formed by mixing PEO and LiClO₄ in 8:1 ratio in methanol and it can be drop casted or even lithographically patterned[79]. The dielectric constant for the PEO matrix has been reported in literature as 5.[80] The drain electrode is covered with SiO₂ to prevent the drain voltage from influencing the electric double layer[78] formed in the polymer. The measured transfer and output characteristics of the conventional FET with polymer gating is shown in **Figure 2.21**. [81] The *SS* obtained is near to the ideal value of 60 mV/dec for all the drain voltages. This corroborates to the highly efficient gate control by PE gating.

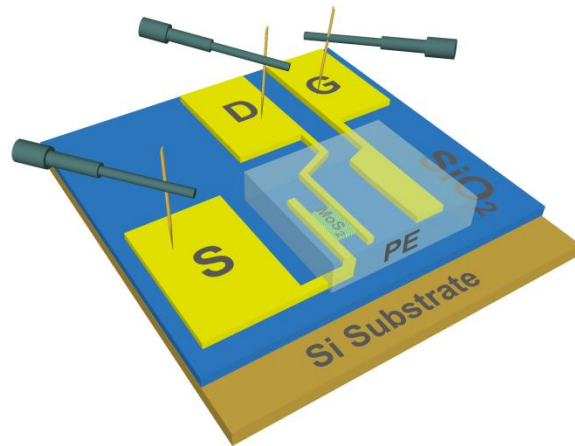


Figure 2.20. Schematic diagram of a MoS₂ FET with as the polymer electrolyte gating.

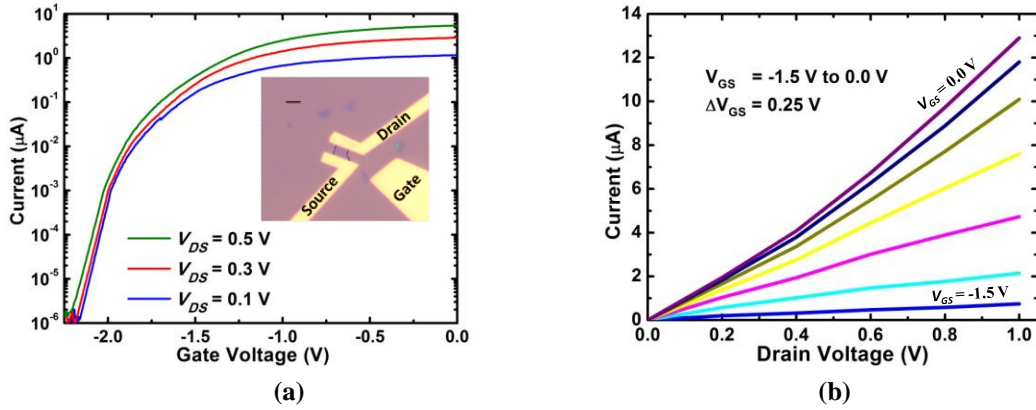


Figure 2.21(a) The I_{DS} - V_{GS} characteristics of the conventional-FET based on bilayer MoS₂ (as shown in **Figure 2.20**) for different V_{DS} . The inset figure shows the optical image of the device. Scale bar: 5 μm . Length and average width of the device are 3.6 μm and 5.8 μm , respectively. **(b)** The I_{DS} - V_{DS} characteristics of the same device measured in (a).

2.3.3. Contacts

To understand the contact effect on MoS₂ FET operation, it is necessary to measure the Schottky barrier between metal contact and the MoS₂. The slope of the Arrhenius plot in the high-temperature region can be used to analyze the Schottky barrier from the thermionic emission theory[82].

For extracting the Schottky barrier height, first the analytical equation for thermionic current in 2D materials is derived.[33] We start from the basic current equation given by $I = 2qn v_x / L_x$, where q is the electronic charge, n is the electron number, v_x the electron velocity and L_x the length along x direction. Here, we assumed current direction to be along x and transverse direction to be along y . Expressing n in terms of density of states and putting $v_x = 1/\hbar dE/d\kappa_x$ (where E is the energy, \hbar is the reduced Planck's constant and k_x the wave-vector along x direction) we can write,

$$I = \frac{2g_v q}{2\pi h} W \int_0^\infty (f_s - f_d) dE \int_{-\sqrt{\frac{2mE}{\hbar^2}}}^{\sqrt{\frac{2mE}{\hbar^2}}} dk_y \quad (2.6)$$

Here g_v is the valley degeneracy and W the width. The energy reference point or $E=0$ is considered to be the bottom of the conduction band in the semiconductor at source-channel junction at flat-band. The maximum value of transverse wave vector k_y is given by the equation $\frac{\hbar^2 k_y^2}{2m} \leq E$ (where m is the effective mass, which is similar in x and y direction for MoS₂) and thereby the integration limits for dk_y are derived in equation (2.6). In the above equation f_s and f_d represent the distribution of electrons in the source and drain respectively and can be approximated as Boltzmann distribution function when $(E-E_f)$ is $\gg K_B T$, where E_f is the Fermi level, K_B is the Boltzmann constant and T is the temperature. Thus equation (2.6) becomes

$$I = \frac{4\sqrt{2}g_v q \sqrt{m}}{h^2} W \int_0^\infty \sqrt{E} \left[e^{-\frac{E-E_{fs}}{K_B T}} - e^{-\frac{E-E_{fd}}{K_B T}} \right] \quad (2.7)$$

Solving the above integral we get,

$$I = \frac{4\sqrt{2\pi}g_v q \sqrt{m}}{h^2} W (K_B T)^{3/2} \left(e^{-\frac{E-E_{fs}}{K_B T}} - e^{-\frac{E-E_{fd}}{K_B T}} \right) \quad (2.8)$$

E_{fs} equals $-\phi_b$ and since the applied source-drain voltage is V_{ds} , E_{fd} equals $-\phi_b - V_{ds}$. Inserting these values in equation (2.8), the final expression for thermionic emission current for 2D material can be derived as:

$$I = A_{2D} WT^{3/2} e^{-\frac{q\phi_b}{K_B T}} \left(1 - e^{-\frac{qV_{ds}}{K_B T}} \right) \quad (2.9)$$

where A_{2D} is the Richardson's constant for 2D materials and is derived to be:

$$A_{2D} = \frac{2\sqrt{2\pi} g_v q \sqrt{m}}{h^2} K_B^{3/2} \quad (2.10)$$

By comparing the thermionic emission equations of 2D material and bulk material, one can find that temperature dependence is lower for 2D material compared to that of 3D material. In addition, the Richardson's constant is also different for 2D material and 3D material (with different unit). Schottky barrier height as a function of V_{bg} is shown in **Figure 2.22**. As mentioned in [82], it is necessary to evaluate the flat-band gate voltage because it is a benchmark to identify the transition point between the tunneling current and thermionic emission current. When the gate voltage is below the flat-band gate voltage, the thermionic emission solely contributes to the current. Hence, using the thermionic emission equation for 2D materials, the Schottky barrier between MoS₂ and Ti can be accurately extracted. The extracted Schottky barrier between monolayer MoS₂ and Ti varies from 0.3-0.35 eV measured from 6 monolayer devices. The Schottky barrier between monolayer MoS₂ and Ti is

significant larger than the Schottky barrier between multilayer MoS₂ (bandgap: 1.2 eV) and Ti, which is around 50 meV.[82] Considering the large bandgap of monolayer MoS₂ (1.8 eV), the extracted Schottky barrier between monolayer MoS₂ and Ti is quite reasonable.

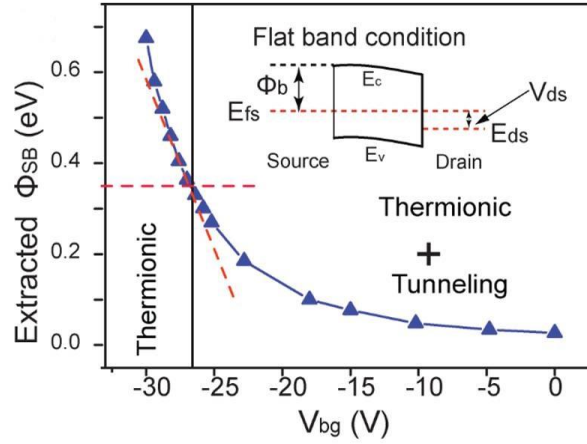


Figure 2.22. Extracted effective barrier height (Φ_{SB}) as a function of V_{bg} for monolayer MoS₂ FET with Ti contact. Inset shows the band diagram at flat band condition, which is defined as the bias condition at which there is zero band bending in the channel.

It has been shown that metals with d-orbitals form good contacts with TMDs due to the possible overlap with d-orbitals in TMDs, which improves electron injection[75][76][63]. MoS₂ is naturally n-doped and exhibits n-FET characteristics. Thus, using low WF metals can reduce the Schottky barrier height for contacting the conduction band of MoS₂ and hence improve n-FET performance. Hence, Yttrium (Y) which has d-orbitals and at the same time exhibits a very low WF of 3.1 eV, is investigated as a contact to MoS₂. Moreover, as it has been shown in previous section, Y can dope the MoS₂ n-type, making it more attractive as a contact to MoS₂ n-FET. The oxidation of Y can be prevented by using noble metal such as Au on the top of Y. The transfer and output characteristics of back gated MoS₂ FET with 20 nm/

50 nm thick Y/Au as source and drain contacts are shown in **Figure 2.23**. It is observed that Y can lead to good contact with MoS₂.

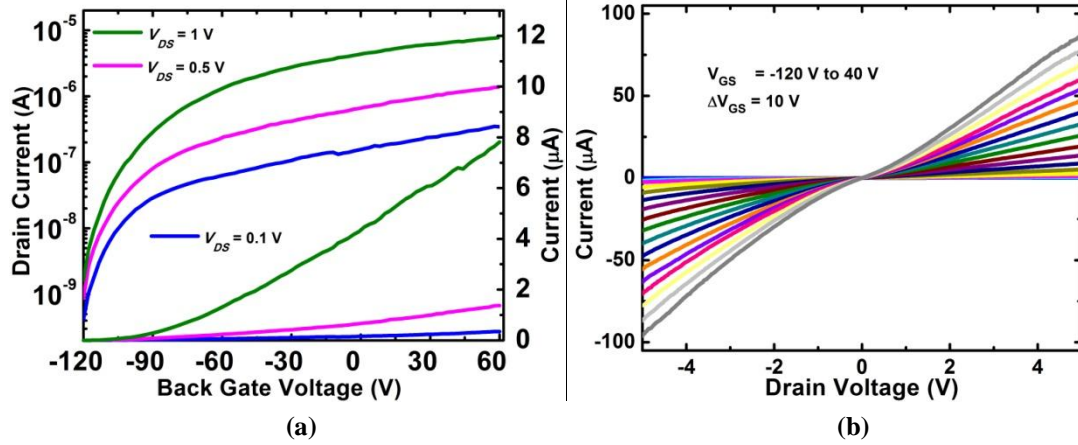


Figure 2.23. (a) The I_{DS} - V_{GS} characteristics of a FET based on mono-layer MoS₂ with Y/Au contact, for different V_{DS} . (b) The I_{DS} - V_{DS} characteristics of the same device measured in (a).

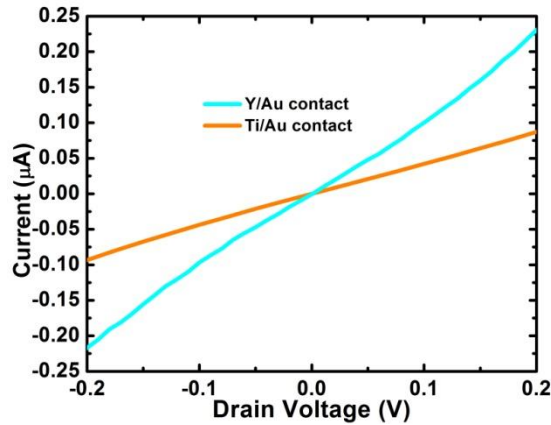


Figure 2.24. Comparison of source to drain currents with the gate floating obtained from MoS₂ FETs with Y/Au and Ti/Au contacts. For proper comparison, monolayer MoS₂ is used and current has been normalized by multiplying by the ratio of length to width, in both cases. The thickness of Y and Ti used are 20 nm while that of Au is 50 nm, in both cases.

For comparison, the source to drain current with the gate floating of a MoS₂ FET with Y/Au contact is plotted along with that of a MoS₂ FET with the most commonly

used Ti/Au contact (**Figure 2.24**). It is observed that the current obtained from Y/Au contact is more than 2x higher than that obtained using Ti/Au contacts.

2.4. Interconnects : 2D Semi-Metallic Graphene

Graphene is a promising material for VLSI including 3-D heterogeneous integration with Silicon due to their outstanding properties. Since Graphene based FETs have already been shown to be attractive for analog/RF devices [83] and graphene ribbons can be designed to outperform Cu interconnects [21], graphene could be the material of choice for realizing horizontal interconnects (including RF-interconnects [84]) as well as low-loss on-chip inductors[23], [85]that form a critical component in RF circuits. As a prospective interconnect material, besides performance analysis in terms of d.c. conductance and delay, a thorough investigation of the high-frequency effects of GRs is equally compelling. It is important to note that the significant frequency is already > 60 GHz for 45 nm technology [86]. It has been shown that carbon nanotubes (CNTs) can be very attractive for high-frequency application such as on-chip inductor design due to their large momentum relaxation time [87]. GRs not only enjoy a large momentum relaxation time but at the same time are more controllable from the fabrication point of view due to their planar nature. Thus, detailed analysis and modeling of the high-frequency behavior of GRs is highly desirable. To this end, first we investigate and provide insights into the intricate processes occurring at high frequencies in GR.[22] Then, based on the understanding, we develop an accurate model for calculating the impedance of GRs using the

Boltzmann equation with magnetic vector potential Green's function approach.[22]
Based on the developed methodology, we carry out a rigorous investigation of the high-frequency effects in GR interconnects and inductors.[23][24]

2.4.1. Anomalous High-Frequency Effects in Graphene

The focus of our work will be on doped multilayer GRs, which are interesting for practical high-frequency applications such as interconnect and inductor design. The monolayer and undoped multilayer GRs have very high resistivity and are not of much interest for such applications [21]. The stage-2 AsF_5 intercalated GR (**Figure 2.25**) has been shown to have in-plane conductivity greater than that of Cu [21] [88] and hence it is chosen as a representative case of doped GRs. Our methodology is applicable to any other type of doping as well.

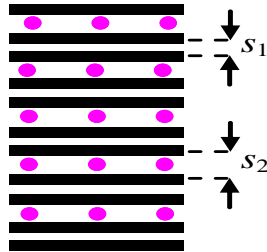


Figure 2.25. Schematic view of a stage-2 intercalation doped multi-layer GR. The solid lines indicate graphene layers, while the dots indicate intercalation dopant layers. s_1 and s_2 are the layer spacing between two adjacent graphene layers.

Anomalous Skin Effect and Ohm's Law

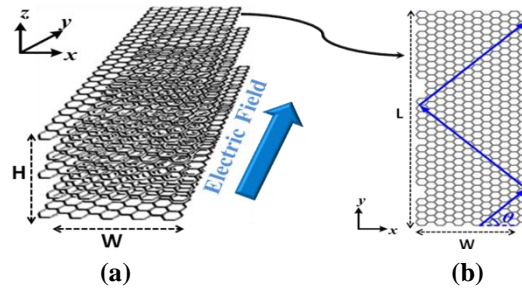


Figure 2.26(a) Multi-layer GR structure showing the selection of axis and the direction of electric field. **(b)** Carrier transport elaborated on a single layer. Carrier transport in GR is confined within each 2D layer. Inter-layer transport is negligible. Thus carriers can only move in the x and y directions, get scattered by the edges and finally contribute to current along y .

The high-frequency effects in doped multi-layer GRs as shown in **Figure 2.25** [21], are very complicated and require serious consideration of various intricate processes as discussed below. For high-frequency investigation, each GR layer cannot be treated as a single element with uniform electric-field and current because of the current density redistribution within a GR layer due to skin effect. Moreover, because of its large mean free path (MFP) GR is susceptible to anomalous skin effect (ASE). ASE occurs when the MFP becomes comparable to the skin depth [89]. When the MFP is much smaller compared to the skin depth, electric field can be assumed to be constant within the MFP. This results in current density being directly proportional to the electric field, with the constant of proportionality being the conductivity and thus the Ohm's law is satisfied. However, when the skin depth becomes comparable to the MFP the carriers can no longer be considered to be moving under the influence of a constant field between collisions and the current at any point will also be influenced by values of electric field at other points. This renders the simplifying assumptions of

Ohm's law invalid and necessitates a more generic approach based on the Boltzmann equation.

For illustrating the arguments made above let us first consider a simplified structure of a semi-infinite slab of GRs. The height is taken to be infinite so that the z dimensionality can be safely excluded from any consideration while the width is kept semi-infinite to simplify the explanations yet not miss the vital points. In **Figure 2.26** the carrier transport mechanism in GR is explained.

In the following paragraphs, we start from the basic Boltzmann equation and highlight the condition under which Ohm's Law is valid and subsequently, in the next sub-section, prove that this condition is not satisfied by GRs at high frequencies. It is to be noted that all equations that will be developed correspond to the electrons. However, since holes involve only sign changes and the final result remains unaltered, the model is equally valid irrespective of whether electrons or holes are the majority carriers. Now, the distribution function for carriers is given by:

$$f = f_0 + f_1(\mathbf{v}, \mathbf{r}); \quad f_0 = \left(1 + \exp \frac{E - E_f}{K_B T} \right)^{-1} \quad (2.11)$$

where f_0 and f_1 are the equilibrium and non-equilibrium distribution functions respectively, v is the velocity vector, r is the space vector, E_f is the Fermi Level, K_B is Boltzmann's constant and T is the temperature. The Boltzmann equation for the distribution function of the conduction electrons is given by

$$\mathbf{v} \cdot \nabla_r f + \frac{(1 + i\omega\tau)}{\tau} f_1 = \frac{e}{\hbar} \boldsymbol{\varepsilon} \cdot \nabla_k f \quad (2.12a)$$

Here $\boldsymbol{\varepsilon}$ and k are the electric field vector and wave vector respectively, τ is the

momentum relaxation time, ω is the angular frequency, e is the electronic charge and $\hbar = h/2\pi$ where h is the Planck's constant. The electric field and the distribution function does not vary along the transport direction i.e., y . Hence $\frac{\partial f}{\partial y}$ reduces to zero.

Moreover, since the dimension along z direction is considered infinite, $\frac{\partial f}{\partial z}$ is negligible. Thus $\mathbf{v} \cdot \nabla_r f$ term in equation (2.12a) reduces to $v_x \frac{\partial f}{\partial x}$. As electric field is applied along the y direction, only the y directed term remains in the RHS of equation (2.12a). Hence the 3D Boltzmann equation reduces to equation (2.12b).

$$v_x \frac{\partial f}{\partial x} + \frac{(1+i\omega\tau)}{\tau} f_1 = \frac{e}{\hbar} \varepsilon(x) \frac{\partial f}{\partial k_y} \quad (2.12b)$$

Here v_x represents the component of velocity along x axis and $\varepsilon(x)$ is the y directed electric field, which is a function of x . If we assume that the first term in equation (2.12b) can be neglected, we obtain the well known Ohm's law and the equation for current density is given by equation (2.13). Readers are referred to [90] for details of the derivation method.

$$J(x) = \frac{\sigma_{dc} \varepsilon(x)}{1+i\omega\tau} \quad (2.13)$$

where σ_{dc} is the d.c. conductivity.

Now, before we discuss the condition under which the assumption made to derive Ohm's law is valid, we require a small discussion on the skin depth. For calculating the skin depth, first the Maxwell's equations given by equation (2.14a) can be used to relate the electric field to the current density equation (2.14b) by eliminating

magnetic field terms and neglecting the displacement current.

$$\nabla \times \mathbf{H}_0 = \mathbf{J} + \frac{\partial \mathbf{D}}{\partial t}; \quad \nabla \times \boldsymbol{\varepsilon} = -\mu \frac{\partial \mathbf{H}_0}{\partial t} \quad (2.14a)$$

$$\frac{\partial^2 \boldsymbol{\varepsilon}(x)}{\partial x^2} = i\mu_0 \omega \mathbf{J}(x), \quad \mu_0 = 4\pi \times 10^{-7} \quad (2.14b)$$

where J is the current density and D is the electric displacement field and μ is the permeability. The magnetic field intensity is denoted by H_0 in order to distinguish it from the height of the GR structure, which is represented by H .

From equations (2.13) and (2.14b), we can eliminate the current density term and the electric field can be solved as:

$$\boldsymbol{\varepsilon}(x) = \boldsymbol{\varepsilon}(0) \exp\left\{-\frac{(1+i)x}{\delta' \sqrt{1+i\omega\tau}}\right\} \quad \text{where } \delta' = \sqrt{\frac{2}{\omega\mu_0\sigma}} \quad (2.15)$$

Then, the skin depth can be derived from equation (2.15) as:

$$\delta = \delta' \sqrt{[1+(\omega\tau)^2] * [\sqrt{1+(\omega\tau)^2} - \omega\tau]} \quad (2.16)$$

At low frequencies the kinetic inductance (KI) term $\omega\tau$ can be neglected and hence,

$$\delta \approx \delta'.$$

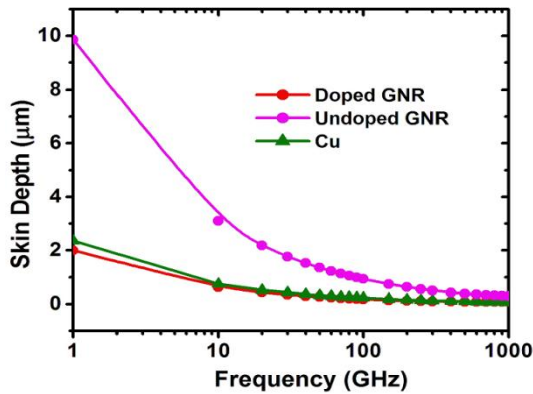


Figure 2.27. Variation of skin depth with frequency for Cu, undoped and doped GR.

Figure 2.27 shows the variation of skin depth with frequency. Skin depth decreases as frequency is increased. Due to its lower conductivity value, skin depth of undoped GR is found to be much larger compared to that of Cu or doped GR.

It can be proved that the first term in equation (2.12b) can be neglected when the condition $l/\delta' \ll (1 + \omega^2 \tau^2)^{3/4}$ is satisfied [91]. Here l is the mean free path given by $l = v_f \tau$ where v_f is the Fermi velocity. Now when the condition is not satisfied, Ohm's Law becomes invalid and ASE creeps in. We call the ratio $l/\delta' * (1 + \omega^2 \tau^2)^{3/4}$ the critical ratio (CR). If the kinetic inductance is neglected the CR becomes simply l/δ' . We can say that ASE becomes important when CR approaches unity.

ASE: GR Vs Cu and CNT

In the following discussion, we show why ASE is an issue at high-frequencies in GRs but it is not so critical for other interconnect materials like Cu or CNTs.

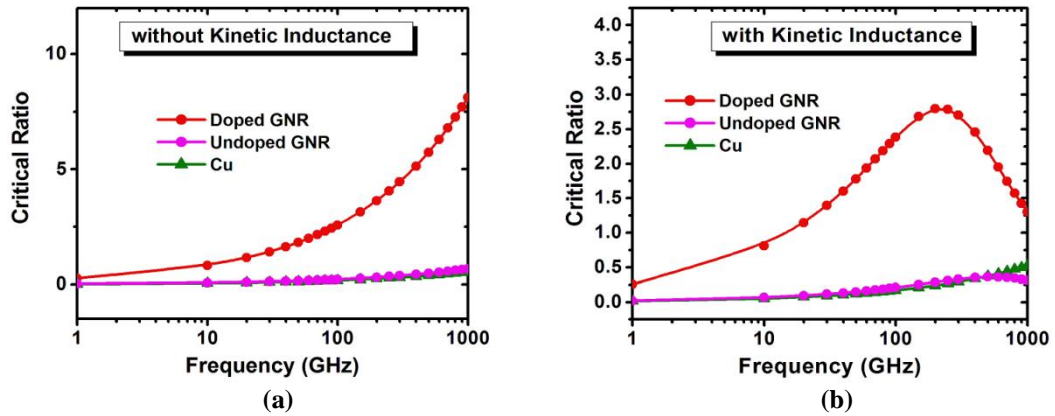


Figure 2.28. Variation of critical ratio with frequency for Cu, undoped and doped GR without (a) and with (b) consideration of kinetic inductance.

In **Figure 2.28(a)** and **(b)** the critical ratio without and with the kinetic inductance is plotted for undoped, doped GR and Cu. VLSI Cu is considered since even for the wide global wires the conductivity corresponds to that of the VLSI Cu, which is $0.4545(\mu\Omega\cdot\text{cm})^{-1}$ [92]. The lower conductivity of VLSI Cu compared to that of bulk Cu is mainly due to grain boundary scattering and impurity scattering. The values of v_f and τ for Cu are $1.57\text{e}6$ m/s and $2.5477\text{e-}14$ s respectively [93]. The Fermi velocity of GR is given as $v_f = \sqrt{3}\pi\gamma a/h$, where $\gamma = 3\text{eV}$ is the overlap integral between nearest neighbor π -orbitals, $a = 0.246$ nm is the lattice constant [94]. For obtaining the value of τ we use the values of MFP that has been extracted from experimental results of bulk graphite in [21] which takes into account the impact of layer to layer interactions that reduce the conductivity in multi-layered GRs. For neutral GR with in-plane conductivity of $0.026 (\mu\Omega\cdot\text{cm})^{-1}$ [95], layer spacing of 0.34 nm and $E_f = 0$, the MFP is extracted to be 419 nm while for the stage-2 AsF_5 intercalated graphite with a hole volume concentration (n_p) of $4.6\times 10^{20} \text{ cm}^{-3}$, in-plane conductivity of $0.63 (\mu\Omega\cdot\text{cm})^{-1}$, average layer spacing (s) between two adjacent graphene layers of 0.575 nm, $|E_f| = 0.60$ eV, MFP is extracted to be $1.03\mu\text{m}$. In [21], MFP is defined as $l_d = v_f\tau_b$ where τ_b is the backscattering time, which corresponds to relaxation of momentum from P to $-P$ and can be related to the momentum relaxation time τ (corresponding to relaxation from P to 0) as $\tau_b = 2\tau$. Thus τ can be written as $\tau = l_d/2v_f$.

The curves with KI show a peak with decay at both ends but no such effect is seen in the plot without KI. The increase in CR at lower frequencies can be attributed to the decrease in skin depth as shown in **Figure 2.27**. However, at very high frequencies

the kinetic inductance dominates and causes the CR to reduce again due to the increase in the $\omega\tau$ term. It is seen that the CR in GR increases much more rapidly compared to that of Cu and this is because of the large MFP of GR. It is clear from the graphs that CR in Cu tends to unity only at very high frequencies, while in GR, it cannot be neglected compared to one even around 1GHz. Thus ASE needs to be considered for GR even at much lower frequency ranges while it will not be an issue in traditional metals like Cu except at very high frequencies (> 100 GHz). As we move towards even higher frequencies, the CR in GR is seen to decay rapidly due to its larger KI (**Figure 2.28(b)**). ASE will not be a serious issue in undoped GR because of its smaller MFP and higher resistivity. Since mono-layer GR has extremely high resistance, it will also not be susceptible to ASE.

Readers may be inclined to think that CNT structures, which also enjoy a large MFP, are also susceptible to ASE. However it is not the case as explained below. In CNT bundles (**Figure 2.29**) the transport is one dimensional i.e., along the axis of the CNT, which is direction y in the figure and only the MFP along this direction is large. The impedance from one CNT to another i.e., the impedance in both x and z direction is very high and thus the MFP in those two directions is very small. Thus any electric field and current distributions that take place have length scales much larger than the MFP within the frequency range of interest and hence anomalous skin effect is not an issue in CNTs. Graphene, on the other hand, has large MFP not only in the transport direction i.e., y but also along x (**Figure 2.26**) and hence the distributions along the x

direction will be influenced by ASE. The layer to layer impedance in multilayer GRs is very high and hence there is no ASE in the z direction.

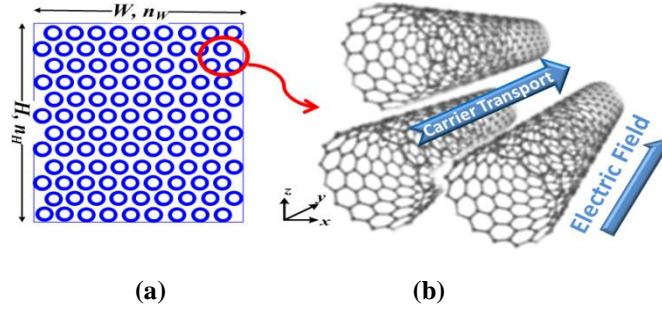


Figure 2.29(a) Cross-sectional view of CNT bundles with width W and height H . n_w and n_H are the number of CNTs along the width and height, respectively. **(b)** Carrier transport in CNT. In CNT bundles, the carriers move only in one direction i.e., along y , which is the direction of axis of the CNTs. Carrier transport from one tube to another i.e., along x and z directions is negligible because of the high impedance between the tubes. Thus the MFPs along these two directions are also small.

Thus the high-frequency analysis of GRs is much more involving compared to CNTs or traditional metals. The impedance extraction method developed for CNTs [87] is not applicable to GRs. A thorough quantitative analysis is required to accurately evaluate the high-frequency effects in GRs with detailed investigation into the skin effects but to the best of our knowledge there is no report in the literature to this end. In this work, for the first time, a rigorous investigation is carried out into the intricate high-frequency processes in GR structures and an accurate methodology is developed by taking into consideration all important effects. The developed model not only gives accurate evaluation of impedance at high frequencies but is equally efficient at lower frequencies as well as in the calculation of exact values of the d.c. resistance.

2.4.2. Impedance Modeling : Semi Infinite Slab

Since the condition for Ohm's Law is not valid for GRs at high frequencies, we need to derive the current density for GRs without the simplifying assumption of Ohm's Law. That is what we do in this sub-section for a semi-infinite slab of GRs and subsequently, using the derived current density we show the calculation of the surface impedance.

Derivation of Current Density

As has been explained in the previous section, the x derivative of f cannot be neglected in the case of GR. Hence in order to extract the impedance accurately, we solve equation (2.12b) retaining all the terms. We can write:

$$\frac{\partial f}{\partial k_y} \approx \frac{\partial f_0}{\partial E} \frac{\partial E}{\partial k} \frac{\partial k}{\partial k_y}$$

We use the linear dispersion relation of graphene [96]

$$E = \hbar v_f k \quad (2.17a)$$

$$v_x = v_f \cos \theta \quad (2.17b)$$

$$v_y = v_f \sin \theta \quad (2.17c)$$

The angle θ is as shown in **Figure 2.26(b)**. Now assuming $\frac{\partial f}{\partial x} \approx \frac{\partial f_1}{\partial x}$ and using

equation (2.17), we finally obtain the following equation:

$$v_x \frac{\partial f_1}{\partial x} + \frac{(1+i\omega\tau)}{\tau} f_1 = e v_y \mathcal{E}(x) \frac{\partial f_0}{\partial E} \quad (2.18)$$

The general solution to the differential equation given by equation (2.18) is:

$$f_1 = \exp\left(-\frac{(1+i\omega\tau)x}{\tau v_x}\right) \left\{ F(v) + \frac{e}{v_x} \frac{\partial f_0}{\partial E} \int_0^x v_y \varepsilon(t) \exp\left(\frac{(1+i\omega\tau)t}{\tau v_x}\right) dt \right\} \quad (2.19)$$

where $F(v)$ is a function of velocity v , which can be solved from the boundary conditions. The inclusion of electric field within the integral takes into account that the distribution function at any point is not a local function of the electric field at that point but includes other points as well, which is absolutely essential for the treatment of anomalous skin effect. The boundary condition for $v_x < 0$ can be derived from the fact that f_1 should not become exponentially large as $x \rightarrow \infty$ and hence we get:

$$f_1^- = -\frac{e}{v_x} \frac{\partial f_0}{\partial E} \int_x^\infty v_y \varepsilon(t, z) \exp\left(-\frac{(1+i\omega\tau)(x-t)}{\tau v_x}\right) dt \quad (2.20)$$

f_1^- is the distribution function for $v_x < 0$. The boundary condition for $v_x > 0$ depends on the edge scattering. For our analysis, we have considered the two extreme cases of perfectly diffuse ($p=0$) and perfectly specular ($p=1$) reflection, where p is the fraction of carriers scattered elastically at the edges. For diffuse reflection, the drift velocity is reduced to zero after scattering at the edge while in the case of specular reflection, complete reversal of drift velocity occurs. Thus the boundary conditions for the two cases are given by:

$$f_1^+(v, x=0) = 0 \quad \text{for } p=0 \quad (2.21a)$$

$$f_1^+(v_x, v_y, v_z, x=0) = f_1^-(-v_x, v_y, v_z, x=0) \quad \text{for } p=1 \quad (2.21b)$$

where f_1^+ is the distribution function for $v_x > 0$ and $x=0$ denotes an edge of the GR structure. From the above boundary conditions we get:

$$f_1^+ = \frac{e}{v_x} \frac{\partial f_0}{\partial E} \int_0^x v_y \varepsilon(t, z) \exp\left(-\frac{(1+i\omega\tau)(x-t)}{\tau v_x}\right) dt \quad \text{for } p=0 \quad (2.22a)$$

$$= \frac{e}{v_x} \frac{\partial f_0}{\partial E} \int_{-\infty}^x v_y \varepsilon(t, z) \exp\left(-\frac{(1+i\omega\tau)(x-t)}{\tau v_x}\right) dt \quad \text{for } p=1 \quad (2.22b)$$

In graphene, current transport is two dimensional within a layer. The 2D current density is given by:

$$J_{2D} = -\sum_i en \langle v_y \rangle \quad (2.23a)$$

where n is the 2D density of carriers, $\langle v_y \rangle$ is the ensemble average over the distribution function f , and the summation is over all the valleys indexed by i in the Brillouin zone. Expanding the expression for $\langle v_y \rangle$ equation (2.23a) becomes:

$$J_{2D} = -\frac{2en \int v_y f d\mathbf{k} 2(L/2\pi)^2}{\int f d\mathbf{k} 2(L/2\pi)^2} \quad (2.23b)$$

The pre-factor of 2 in the above equation corresponds to the two equivalent valleys of graphene which has a hexagonal brillouin zone with each vertex contributing $1/3^{\text{rd}}$ of a valley. The 3D current density can be obtained by multiplying by the number of layers (N_l) and dividing by the height. Thus we get:

$$J = J_{2D} * N_l / H = J_{2D} / s \quad (2.23c)$$

where s is the average spacing between the layers. Equation (2.23c) can be simplified and written as:

$$J(x) = -\frac{e}{\pi^2 s} \int v_y f_1 d\mathbf{k} \quad (2.23d)$$

Substituting the expression for f_l from equation (2.20) and (2.22) and solving

equation (2.23d) using equation (2.17), the current density can be expressed as:

$$J(x) = \frac{2e^2 E_f}{\pi^2 \hbar^2 v_f s} \int_0^\infty g\left(\frac{x-t}{l}\right) \varepsilon(t) dt \quad \text{for } p=0 \quad (2.24a)$$

$$= \frac{2e^2 E_f}{\pi^2 \hbar^2 v_f s} \int_{-\infty}^\infty g\left(\frac{x-t}{l}\right) \varepsilon(t) dt \quad \text{for } p=1 \quad (2.24b)$$

where $g(u) = \int_0^{\pi/2} \frac{\sin^2 \theta}{\cos \theta} \exp\left\{\frac{(1+i\omega\tau)|u|}{l \cos \theta}\right\} d\theta$

Detailed derivation of equation (2.24) from equation (2.23d) is shown in the Appendix A.

Calculation of the Surface Impedance

Now, using equation (2.24b) and substituting $u_1=x/l$, $u_2=t/l$ and defining the function

$\xi(u_1) = \varepsilon(lu_1)$ we get:

$$\xi''(u_1) = i\alpha \left\{ p \int_{-\infty}^\infty g(u_1 - u_2) \xi(u_2) du_2 + (1-p) \int_0^\infty g(u_1 - u_2) \xi(u_2) du_2 \right\} \quad (2.25)$$

where $\alpha = \frac{2e^2 E_f l^3 \mu_0 \omega}{\pi^2 \hbar^2 v_f s}$

Now the surface impedance can be calculated as:

$$Z_s = \frac{\varepsilon(0)}{\int_0^\infty J(x) dx} \quad \text{and using equation (2.14b) we get:}$$

$$Z_s = -i\mu_0 \omega \frac{\varepsilon(0)}{\varepsilon'(0)} \quad (2.26)$$

which can also be written as:

$$Z_s = -i\mu_0\omega l \frac{\xi(0)}{\xi'(0)} \quad (2.27)$$

$\frac{\xi(0)}{\xi'(0)}$ can be calculated from equation (2.25) by standard methods based on the theory of Fourier integrals. The readers are referred to [91] for details of the calculation method.

If NSE and Ohm's law were valid, the surface impedance could be calculated from equation (2.15) and equation (2.26) as:

$$Z_s = \sqrt{\frac{\omega\mu_0}{2\sigma}} \left\{ \sqrt{\sqrt{(\omega\tau)^2 + 1} - \omega\tau} + i\sqrt{\sqrt{(\omega\tau)^2 + 1} + \omega\tau} \right\} \quad (2.28)$$

Figure 2.30(a) shows the variation of surface resistance with frequency for both $p=0$ and $p=1$ where ASE is taken into account and the results are compared with the case of NSE. Kinetic Inductance is neglected here for simplifying the problem at present, since here we are mainly interested in comparing NSE and ASE. We show the effect of KI in the more rigorous analysis of finite GR structures [23] in the next sections. It can be observed that at lower frequencies all the curves merge together. However at higher frequencies, the increase in resistance with ASE taken into account (for both $p=0$ and $p=1$) is greater than the case where ASE is neglected (i.e., NSE) and the difference increases with frequency. Another important point to note is that the resistance for $p=0$ is higher than that at $p=1$ and the difference between the two also increases as frequency is increased. Variation of surface inductance with frequency is plotted in **Figure 2.30(b)**. Surface inductance decreases as frequency is increased because with the increase in frequency the current gets confined more and

more towards the edges. Also the effect of ASE for $p=0$ is found to be more compared to that for $p=1$. Detailed discussion on these effects is presented in the following sections.

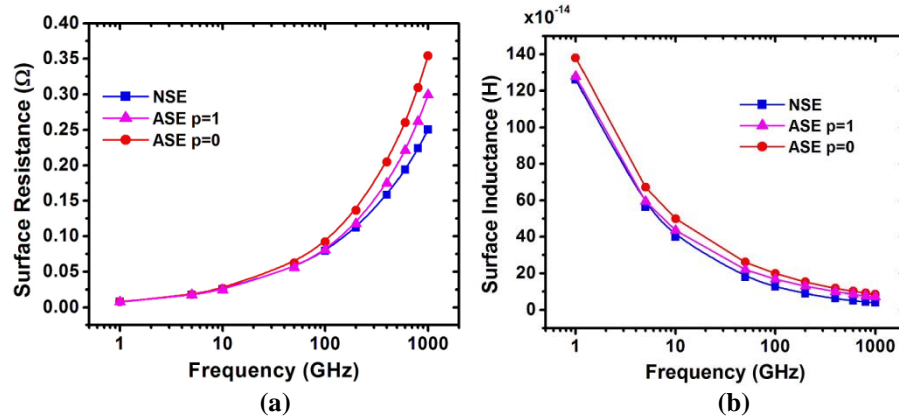


Figure 2.30. Surface resistance (a) and surface inductance (b) of a semi-infinite slab of GR as a function of frequency.

2.4.3. Impedance Modeling : Finite Structure

The GR structures relevant for high-frequency interconnect and inductor designs have finite rectangular cross-sections. The dimensions chosen here are relevant for top global interconnects and high frequency inductor design. Very small dimensions ($W < 10\text{nm}$) will show worse performance as already has been pointed out in [21] and hence is not considered in this dissertation. Secondly, there is no impact of skin effect when the dimensions are very small. Hence the effective conductivity at high frequencies would be the same as the d.c. conductivity, analysis of which has already been done in previous literature [21]. Since now the electric field and current distribution will be a function of both x and z directions, equation (2.25) and the standard procedure described above for calculation of the impedance will not be valid

here. Therefore, in this section, we present a model for calculating impedance of finite GR structures. First, we present a generic approach, which is valid at all frequencies followed by a simplified model, which may be adopted at relatively lower frequencies.

Generic Approach

Though now the height is finite, $v_z \frac{\partial f}{\partial z}$ can still be neglected since the velocity along the z direction is negligible. Hence the 3D Boltzmann equation basically reduces to the same form as equation (2.18) and the distribution function can be expressed by equation (2.19) with the only exception that in both the equations and in all subsequent equations, the electric field is a function of both x and z . The boundary conditions for solving $F(v)$ are given by:

$$\begin{aligned} &\text{for } p = 0 \\ &f_1^+(v, x = 0) = 0 \end{aligned} \quad (2.29a)$$

$$f_1^-(v, x = W) = 0 \quad (2.29b)$$

$$\begin{aligned} &\text{for } p = 1 \\ &f_1^+(v_x, v_y, v_z, x = 0) = f_1^-(-v_x, v_y, v_z, x = 0) \end{aligned} \quad (2.29c)$$

$$f_1^+(-v_x, v_y, v_z, x = W) = f_1^-(v_x, v_y, v_z, x = W) \quad (2.29d)$$

From the above boundary conditions f_l can be solved as:

for $p = 0$

$$f_1^+ = \frac{e}{v_x} \frac{\partial f_0}{\partial E} \int_0^x v_y \varepsilon(t, z) \exp\left(-\frac{(1+i\omega\tau)(x-t)}{\tau v_x}\right) dt \quad (2.30a)$$

$$f_1^- = -\frac{e}{v_x} \frac{\partial f_0}{\partial E} \int_x^W v_y \varepsilon(t, z) \exp\left(-\frac{(1+i\omega\tau)(x-t)}{\tau v_x}\right) dt \quad (2.30b)$$

for $p = 1$

$$\begin{aligned} f_1^+ = f_1^- = & \frac{e}{v_x} \frac{\partial f_0}{\partial E} \int_0^W \frac{v_y \varepsilon(t, z)}{\exp\left(\frac{(1+i\omega\tau)W}{\tau v_x}\right) - \exp\left(-\frac{(1+i\omega\tau)W}{\tau v_x}\right)} \\ & * \left[\exp\left(-\frac{(1+i\omega\tau)(-W+x+t)}{\tau v_x}\right) + \exp\left(-\frac{(1+i\omega\tau)(W+x-t)}{\tau v_x}\right) \right] dt \\ & + \frac{e}{v_x} \frac{\partial f_0}{\partial E} \int_0^x v_y \varepsilon(t, z) \exp\left(-\frac{(1+i\omega\tau)(x-t)}{\tau v_x}\right) dt \end{aligned} \quad (2.30c)$$

Now incorporating the expression for f_l from equation (2.30) in equation (2.23d), the current density $J(x, z)$ across the GR structure is calculated through numerical integration with an initial guess of the electric field. Then the Green's function approach is used to calculate the new electric field distribution as is explained below. For this purpose, the GR structure is divided into several small filaments as shown in **Figure 2.31**. Self and mutual inductances are calculated for the filaments from which the Green's function is derived. Self inductance per unit length (L_{Self} in uH/m) of a filament is given by [97]:

$$L_{Self} = 0.2[\ln(2L/GMD) - 1.25 + AMD/L + (\mu/4)T] \quad (2.31)$$

Here L is the length, GMD and AMD are the geometric and arithmetic mean distances respectively for a single filament, μ is the permeability and T is the frequency correction parameter, which equals 1 for near-direct-current condition. The division of the GR structure is done in such a way that each filament has a square

cross-section and GMD for each single filament is given by 0.44705 times the side of a filament [97]. AMD in this case is defined as the average of all possible distances within a cross-section of a filament and it is calculated numerically.

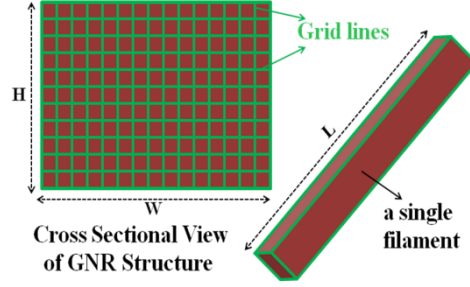


Figure 2.31. Division of the GR structure into small filaments for applying the Green's function.

Mutual inductance between different filaments can be calculated from the following equations:

$$Q_{jk} = \ln \left\{ \left(\frac{L}{d_{jk}} \right) + \left[1 + \left(\frac{L^2}{d_{jk}^2} \right) \right]^{1/2} \right\} - \left[1 + \left(\frac{d_{jk}^2}{L^2} \right) \right]^{1/2} + \left(\frac{d_{jk}}{L} \right) \quad (2.32a)$$

$$M_{jk} = 0.2Q_{jk} \quad (2.32b)$$

Here Q_{jk} is the mutual inductance parameter, M_{jk} is the mutual inductance per unit length ($\mu\text{H}/\text{m}$) and d_{jk} is the distance between the centers of the two filaments considered, respectively. It should be noted that the more accurate equation requires d_{jk} substituted by GMD_{jk} , the geometric mean distance between the j^{th} and k^{th} filament. However, since GMD_{jk} is almost equal to d_{jk} , we will use d_{jk} , for simplicity.

The Green's function is given by:

$$\begin{aligned} G_{jk} &= L_{Self} && \text{if } j = k \\ &= M_{jk} && \text{otherwise} \end{aligned} \quad (2.33)$$

The vector potential is calculated as:

$$A_j = a_f \sum_k G_{jk} J_k \quad (2.34)$$

Here a_f is the cross-sectional area of a filament. The current and electric field in each filament is approximated by the values at the centre of the respective filament and J_k represents the current density at the centre of the k^{th} filament.

The voltage drop across a filament can be given by:

$$V_j = (\varepsilon_j + i\omega A_j)L \quad (2.35)$$

Since we are working with an initial guessed value of electric field, the voltage drop across different filaments may be different. The average voltage drop V_{avg} is calculated and a new value of electric field distribution is obtained from it. All the steps are then repeated again with the new values of electric field and iterations are continued till convergence is achieved separately for both the real and imaginary parts of the electric field. Finally, from this self-consistent procedure, the impedance is obtained as:

$$Z = \frac{V_{avg}}{a_f \sum_k J_k} \quad (2.36)$$

Simplified Methodology

The methodology described above is a very generic approach. However when the MFP is much smaller compared to the skin depth or at lower frequencies, only normal skin effect occurs and some simplifying assumptions can be adopted for such cases.

Ohm's law remains valid and the current density at any point can be assumed to depend only on the value of the electric field at that same point. Thus, in the equation for non-equilibrium distribution function (equation (2.19)), the electric field can be taken out of the integration and this results in much simplified expressions for f_i .

$$f_1^+(v, x) = e\tau v_y \varepsilon \frac{\partial f_0}{\partial E} \left\{ 1 - (1-p) \left(1 - p \exp\left(-\frac{W}{\tau v_x}\right) \right)^{-1} \exp\left(-\frac{x}{\tau v_x}\right) \right\} \quad (2.37a)$$

$$f_1^-(v, x) = e\tau v_y \varepsilon \frac{\partial f_0}{\partial E} \left\{ 1 - (1-p) \left(1 - p \exp\left(\frac{W}{\tau v_x}\right) \right)^{-1} \exp\left(\frac{W-x}{\tau v_x}\right) \right\} \quad (2.37b)$$

The kinetic inductance term has been dropped intentionally in the above equations and it is taken into account at a later stage as would be clear from the explanations in the following passages. For taking into account the size effects, effective conductivity is extracted. For this purpose the dc current density (equation (2.38a)) is first calculated from the Boltzmann distribution function given by equation (2.37). Then the average current density is evaluated and is used to find the effective d.c conductivity σ_{eff_dc} as shown in equation (2.38b). It is to be noted that in equation (2.38a) the current density is only a function of the x direction and not z because the electric field is considered as a constant here. Since here we are interested only in the calculation of σ_{eff_dc} , the electric field has no actual role to play and it gets cancelled in equation (2.38b) and hence we could have effectively replaced it by 1 as well.

$$J_{d.c}(x) = -\frac{e}{\pi^2 S} \iint v_y f_1 k \partial k \partial \theta \quad (2.38a)$$

$$\sigma_{eff_d.c} = \frac{1}{W\epsilon_0} \int_0^w J(x) dx \quad (2.38b)$$

Now the momentum relaxation time is updated to include the size effects and we obtain the effective momentum relaxation time τ_{eff} as in equation (2.39a). Finally the kinetic inductance term is incorporated and the effective a.c conductivity σ_{eff} is obtained as in equation (2.39b).

$$\tau_{eff} = \frac{\sigma_{eff_d.c}}{\sigma_0} \tau \quad (2.39a)$$

$$\sigma_{eff} = \frac{\sigma_{eff_d.c}}{1 + i\omega\tau_{eff}} \quad (2.39b)$$

The current density can be expressed as:

$$J(x, z) = \sigma_{eff} \mathcal{E}(x, z) \quad (2.40)$$

The current density distribution within the GR structure can be calculated from equation (2.40) starting with an initial guess of electric field distribution. After that, the self consistent iteration method described for ASE is followed for calculation of the impedance.

High-Frequency Analysis

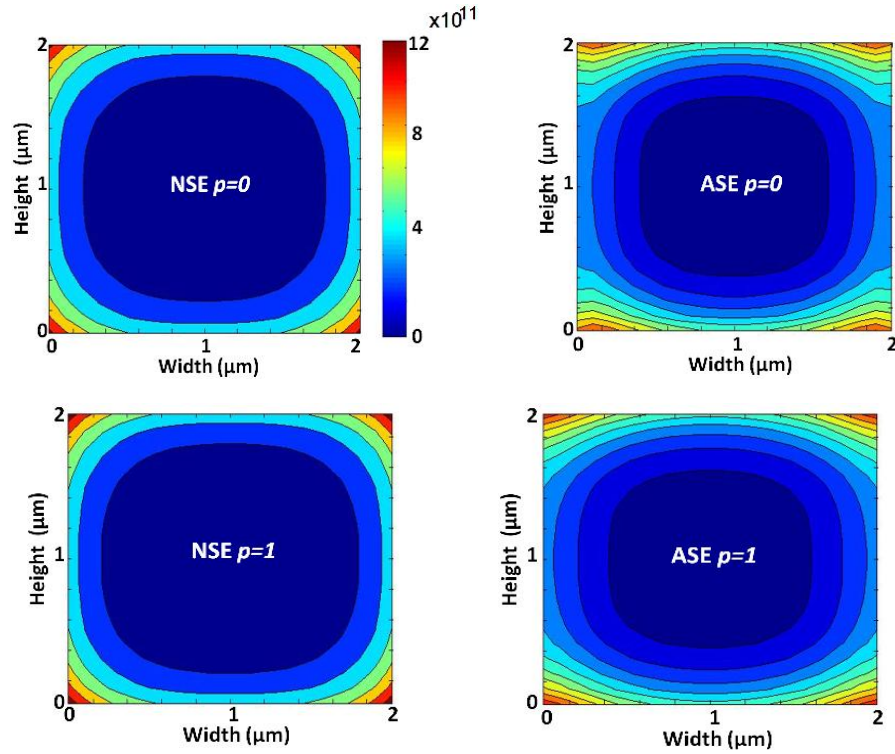


Figure 2.32. Normalized current density distribution graphs across the cross-section of a $2 \times 2 \mu\text{m}^2$ GR structure. The color scale shown is same for all the distribution plots.

The normalized current density distribution plots across the cross section of a $2 \times 2 \mu\text{m}^2$ GR structure are shown in **Figure 2.32**. It is observed that when only NSE is considered, current density J is symmetrical about x and z (the distribution remains the same if the plot is rotated by 90°), and no visible difference is obtained between $p=0$ and $p=1$. While in the case of ASE, the contours take on a different shape about x and z as well as between $p=0$ and $p=1$. For explaining the above results we need to take into account two important effects. Firstly, the skin effect tends to confine the current towards the boundaries. However near the boundaries $x=0$ and $x=W$ (which are the edges of the GR layers), the edge scattering effect causes reduction in the

current density compared to that at $z=0$ and $z=H$ (which are the bottom and top layers). Hence we get the asymmetrical distribution in case of ASE. On the other hand, NSE gives symmetrical contours since it is obtained using Ohm's law with an effective conductivity. Also, between the two edge specularities, $p=0$ results in the lowest current density since it is related to completely diffusive scattering and this effect can be observed only when ASE is taken into account. Thus the impact of edge scattering effect can only be appreciated when ASE is considered. It can also be noted that NSE leads to higher estimation of current density compared to ASE.

In **Figure 2.33**, resistance and inductance of the GR structure with consideration of ASE is plotted as a function of frequency for both $p=0$ and $p=1$. Edge specularity is found to have considerable impact on the resistance while its effect on the inductance is found to be almost negligible.

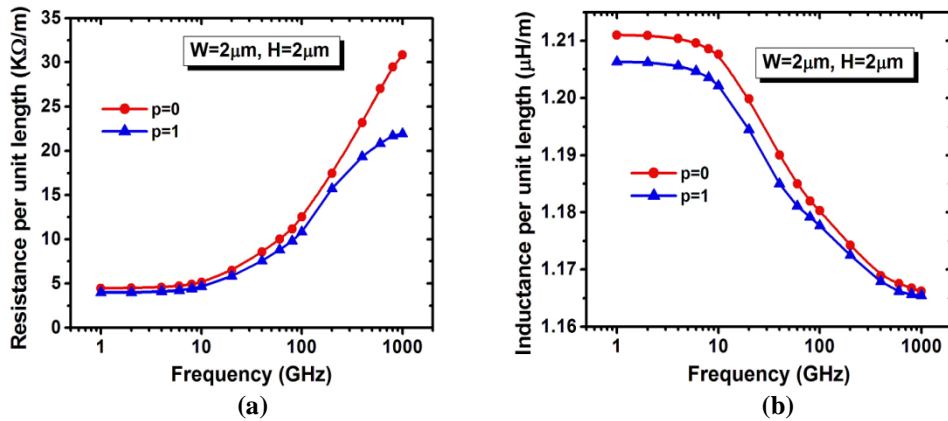


Figure 2.33. Variation of resistance (a) and inductance (b) of GR structure with frequency for both $p=0$ and $p=1$. L is taken to be $500\mu\text{m}$.

2.4.4. Summary of Impedance Extraction Methodology

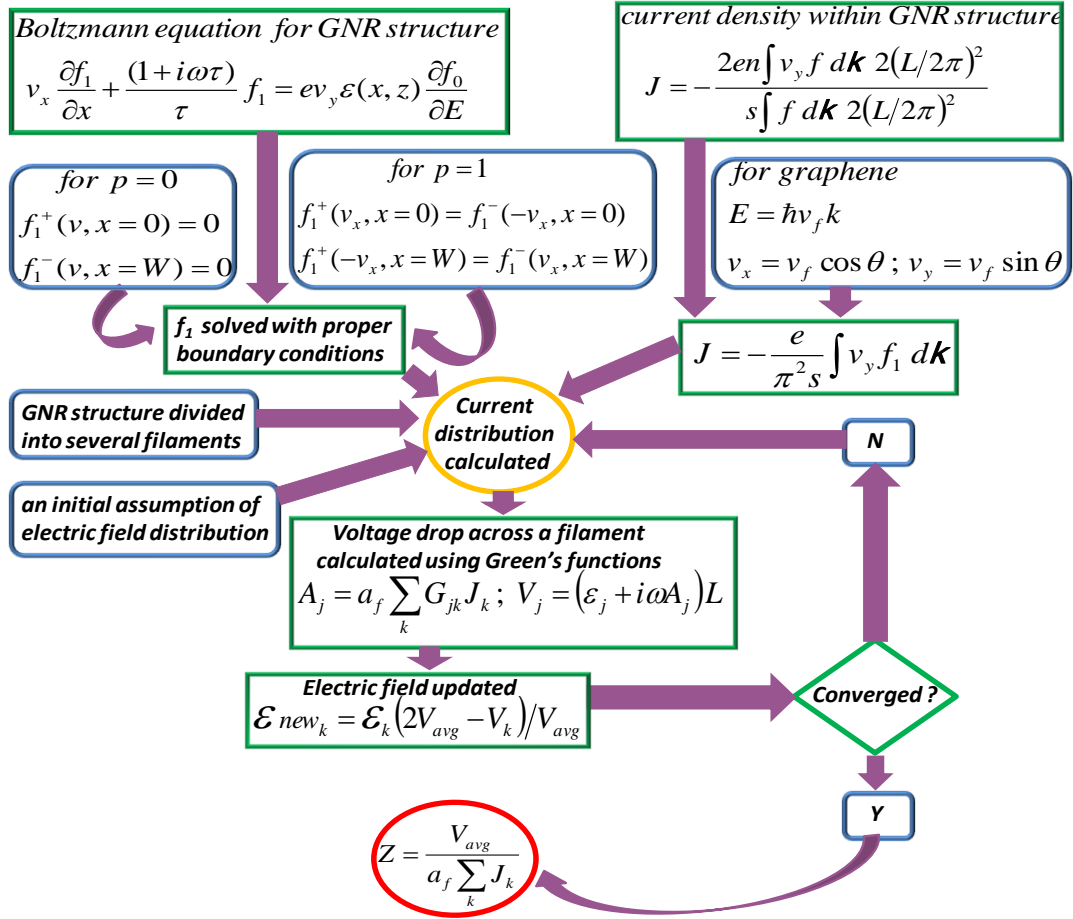


Figure 2.34. Outline of impedance extraction methodology. f_0 and f_1 are the equilibrium and non-equilibrium distribution function with $f = f_0 + f_1$. v_x and v_y represent the components of velocity along x and y axis, τ is the momentum relaxation time, ω is the angular frequency, ε is the electric field, E is the energy, f_1^+ and f_1^- are the distribution function for $v_x > 0$ and $v_x < 0$, n is the 2D carrier density, s is the average spacing between layers, v_f is the Fermi velocity, k is the wave vector, A_k and J_k are the vector potential and current density of the k^{th} filament, G_{jk} is the Green's function parameter between the j^{th} and k^{th} filament, a_f is the cross-sectional area of a filament, V_{avg} is the voltage drop averaged over all filaments and Z is the impedance.

To accurately capture the intricate processes occurring at high frequencies, we developed a modeling framework where starting from the basic Boltzmann equation and combining the unique E-k dispersion relation for graphene, the current density

across a GR structure is derived. This is followed by self-consistent numerical calculation of electric field distribution from magnetic vector potential Green's function approach. The outline of our method is presented in **Figure 2.34**. For gauging the impact of ASE, another simplified analysis is done where ASE is neglected and only NSE is considered by assuming an effective complex conductivity (considering kinetic inductance [87]).

Here is a side note for the benefit of the readers on the appropriateness of the use of Boltzmann equation for a.c conductance modeling of GR for interconnect and inductor applications, as opposed to full-fledged quantum-mechanical approach. For such applications, we are dealing with lengths of about hundreds of microns, width and height of few microns. At such large length scales and room temperature, the quantum interference effects get washed out and hence development of full-fledged quantum approach based on quantum kinetic equations is rendered unnecessary. The Boltzmann equation is well enough in that regime. In this connection, we should also mention that at such large widths, the configuration of the edges (i.e., whether the GR is armchair or zigzag) does not affect the conductance. The edge-specularity does affect the impedance and it has been incorporated in our calculations.

In [21], in which detailed analysis of the d.c performance of GRs was carried out, Matthiessen's Rule was used to obtain the conductance. It is interesting to compare the effective d.c conductance obtained from the method described above, which is based on the accurate solution of Boltzmann equation with the approximate solution given by Matthiessen's Rule for both the extreme cases of edge specularities i.e.,

completely diffusive ($p=0$) and completely elastic ($p=1$) scattering. Here p is the fraction of carriers scattered elastically at the edges. Derivation of the d.c. conductance from Matthiessen's Rule for $p=0$ can be found in [21] and that for $p=1$ is shown in the Appendix B. **Figure 2.35** shows the comparison of the d.c. conductance obtained using the two methods. Since the curves are found to match closely for both the cases, it can be concluded that the approximate method based on Matthiessen's Rule is quite reasonable for analysis of d.c. conductance.

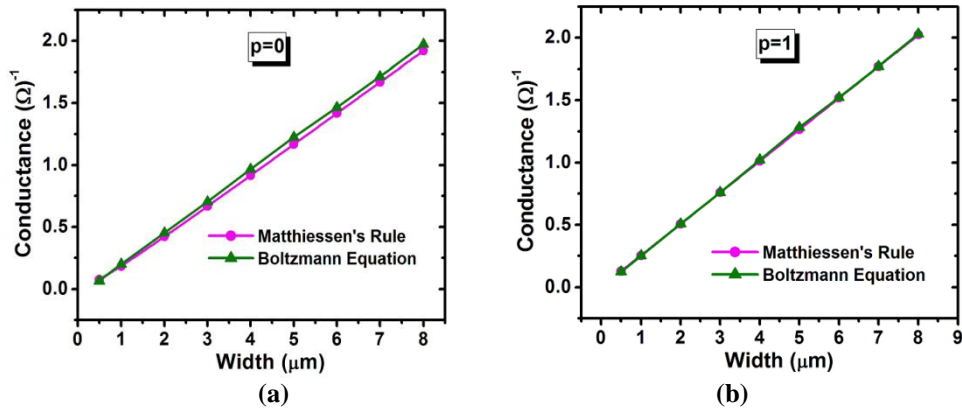


Figure 2.35. Comparison of conductance obtained from Matthiessen's rule with that extracted from Boltzmann equation as a function of width for (a) $p=0$ and (b) $p=1$, proves the validity of Matthiessen's rule for d.c. conductance analysis.

2.4.5. High Frequency Analysis of Graphene Interconnects

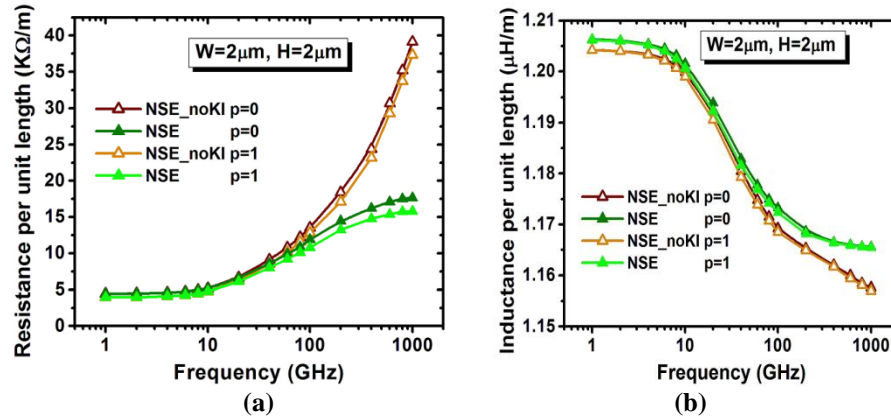


Figure 2.36. Effect of kinetic inductance on (a) resistance and (b) inductance for $p=0$ and $p=1$. The large KI of graphene leads to saturation of both resistance and inductance at high frequencies. W and H represent the width and height of the GR structure respectively. The length (L) is taken to be $500\ \mu\text{m}$.

Based on the method outlined in the previous section, a comparative study of the effect of ASE with respect to NSE is carried out and the impact of kinetic inductance (KI), edge specularity and the linear dimensions of the structure on impedance are investigated. All analysis results shown for GR pertain to the stage-2 AsF_5 intercalation doped multi-layer GR, which can have in-plane conductivity greater than that of Cu, and hence is interesting for high frequency applications. In **Figure 2.36(a)**, the effect of KI on the resistance is investigated. It is seen that when KI is neglected the resistance increases unboundedly with frequency, while in the actual case, the large KI of GR tends to saturate the resistance at higher values of frequency for both $p=0$ and $p=1$. Inductance also shows saturation at higher frequency ranges due to the kinetic inductance term while it keeps decreasing when it is neglected, as seen in **Figure 2.36(b)**.

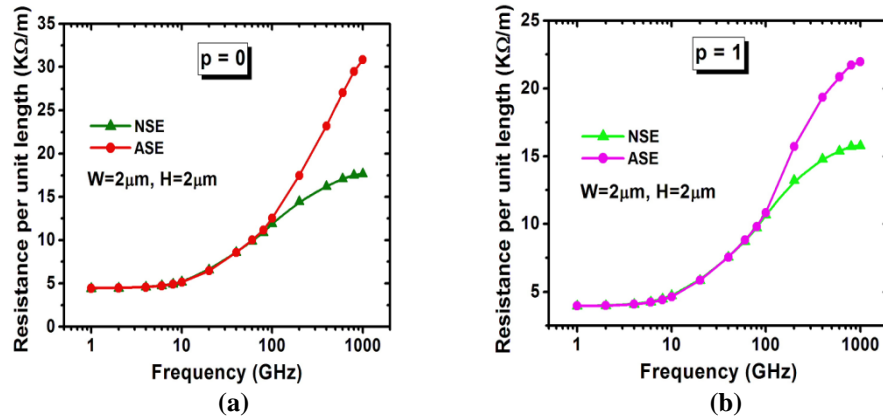


Figure 2.37. The variation in resistance of a $2\mu\text{m} \times 2\mu\text{m}$ GR structure with frequency for (a) $p=0$ and (b) $p=1$, for the two cases: with and without considering the anomalous skin effect. Difference in resistance due to ASE becomes apparent after about 100 GHz and this difference increases with increasing frequency. The length (L) is taken to be $500\mu\text{m}$.

In **Figure 2.37** the resistance at different frequencies is compared between the two cases: with and without considering the ASE. The increase in resistance due to ASE becomes apparent after about 100GHz and with increasing frequency this difference increases significantly. Also the impact of ASE for $p=0$ is found to be greater than that for $p=1$ as is clear from **Figure 2.38**. This effect is elaborately discussed here. Since $p=0$ is related to completely diffusive scattering, the corresponding resistance is always greater than that for $p=1$. However at low frequencies difference between the two is small and not seen in the graphs. As the frequency increases, the current gets confined more and more towards the edges and hence the effect of edge scattering becomes increasingly important and leads to significant increase in resistance for $p=0$ compared to $p=1$.

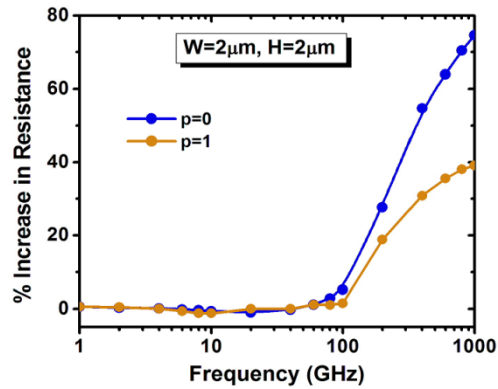


Figure 2.38. The percentage increase in the resistance of GR as a function of frequency for $p=0$ and $p=1$. The effect of ASE for $p=0$ is found to be much greater than that for $p=1$ and the effect of edge scattering becomes more prominent at higher frequencies.

Figure 2.39 shows the variation of inductance with frequency. For $p=1$, at lower frequencies, the inductance with and without ASE being considered match each other since ASE is not effective at low frequencies. As frequency is increased, inductance due to ASE becomes higher. However at very high frequencies they merge again. This is because at very high frequency the current will mainly be confined to the edges for both the cases and the difference in current distribution in the two cases causes negligible change in inductance. At lower frequencies, since edge scattering is more vigorous for completely diffuse reflection ($p=0$), current density in the center is higher than that near the edges, leading to slightly higher inductance considering ASE with $p=0$ than the NSE case. No such difference can be seen for $p=1$. At very high frequencies they match each other similar to the effect seen for $p=1$. Overall, the ASE has much less effect on the inductance compared to its effect on resistance.

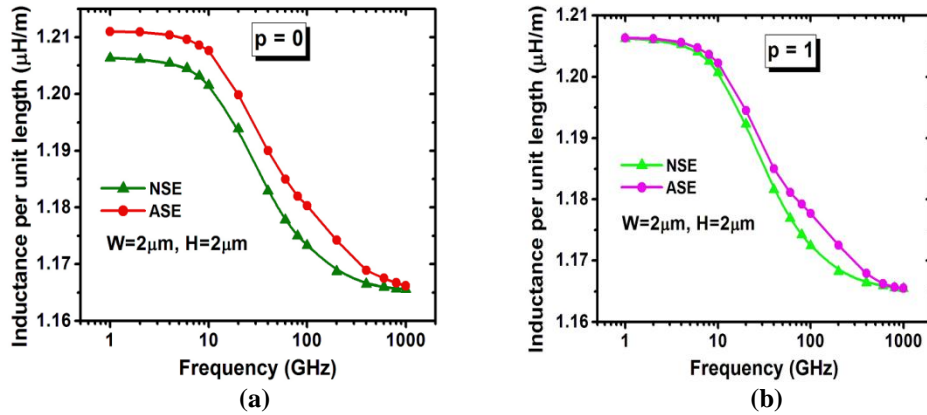


Figure 2.39. Variation of inductance of GR structure with frequency for (a) $p=0$ and (b) $p=1$. It is seen that for both $p=0$ and $p=1$, ASE has very little effect on inductance values. L is taken to be $500 \mu\text{m}$.

Variation of resistivity (ρ) with width, keeping the thickness fixed reveals some very important physics. From **Figure 2.40** it is clear that resistivity decreases as width is decreased and this is due to the reduction in skin effect. To elaborate the impact of ASE as a function of width, the percentage increase in resistivity due to ASE compared to the NSE case for various widths is shown in the inset figures. The curves for both $p=0$ and $p=1$, show a peak with decay at both ends. This can be explained as follows. At very small width, the percentage is low since the skin effect itself is weak. The percentage increases as the width is increased because the skin effect begins to play an important role. However, with further increase in width it decreases again. This is because at very large widths, the distribution function becomes much more dependent on z (along the height direction) than on x (along the width direction) and hence the term containing the derivative of f_l with respect to x in the Boltzmann equation (**Figure 2.34**) becomes less important. Thus the difference between ASE and NSE basically reduces.

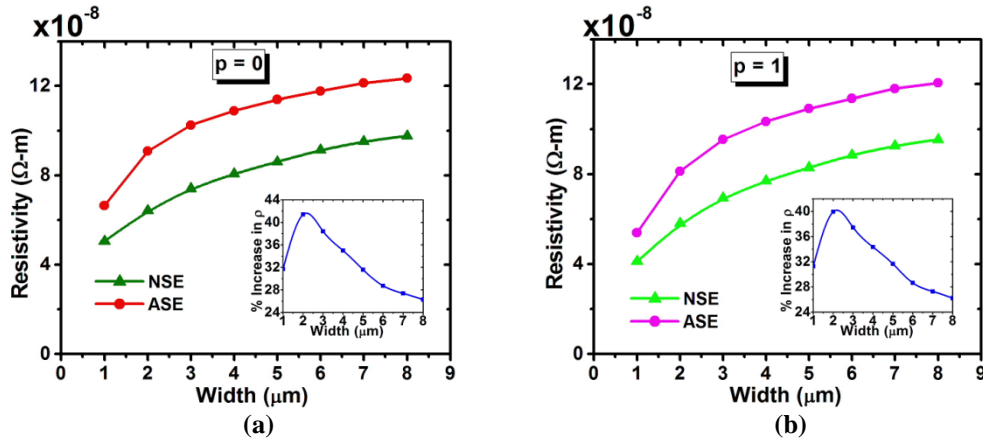


Figure 2.40. Variation of resistivity of GR structure with width while keeping thickness constant ($2\mu\text{m}$) at a frequency of 400GHz for (a) $p=0$ and (b) $p=1$. Resistivity increases with increasing width due to increase in skin effect. The inset figures show that the percentage increase in resistivity due to ASE with respect to the NSE case, for both $p=0$ and $p=1$, first increases with width and then decreases.

In **Figure 2.41** the percentage increase in resistivity for $p=0$ with respect to $p=1$ is plotted as a function of width. The curves show a decreasing trend indicating that the effect of edge specularity reduces with increasing width.

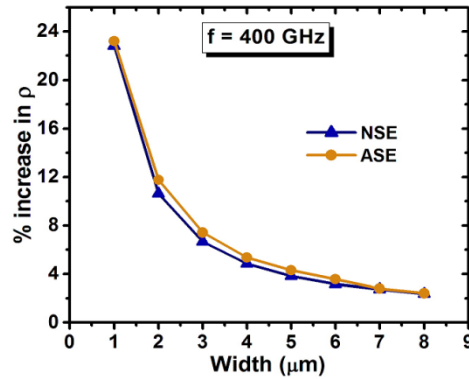


Figure 2.41. Percentage increase in resistivity (ρ) as a result of perfectly diffuse scattering ($p=0$) with respect to that of perfectly elastic scattering ($p=1$) for both NSE and ASE cases show a decreasing trend with width.

The variation of resistance with the height keeping the width fixed is shown in **Figure 2.42**. At very small heights, the difference in resistivity for NSE and ASE cases is very low as in the case of width variation. But with the increase in height, the

difference continues to increase and does not show any decreasing trend, which is obvious since the $\partial f_1/\partial x$ term in the Boltzmann equation (**Figure 2.34**) is not affected by the height variation.

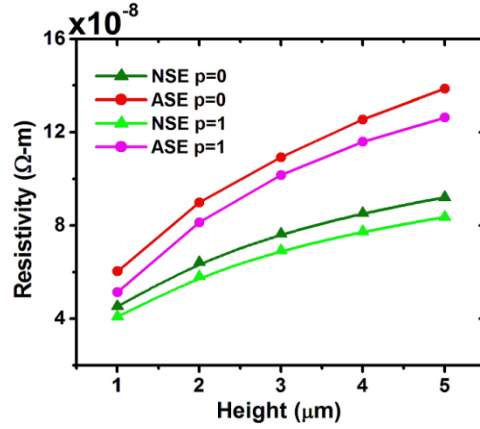


Figure 2.42. Variation of resistivity with height ($W=2\mu\text{m}$, $f=400\text{GHz}$). For both $p=0$ and $p=1$, the difference in resistivity between NSE and ASE cases increase with height.

The variation of inductance with width keeping the height constant for both $p=0$ and $p=1$ with and without consideration of ASE is shown in **Figure 2.43(a)**. ASE or edge scattering is found to have very little effect on the inductance. The variation of inductance with height for fixed width is shown in **Figure 2.43(b)**. Almost similar trend as in the case of width variation is observed.

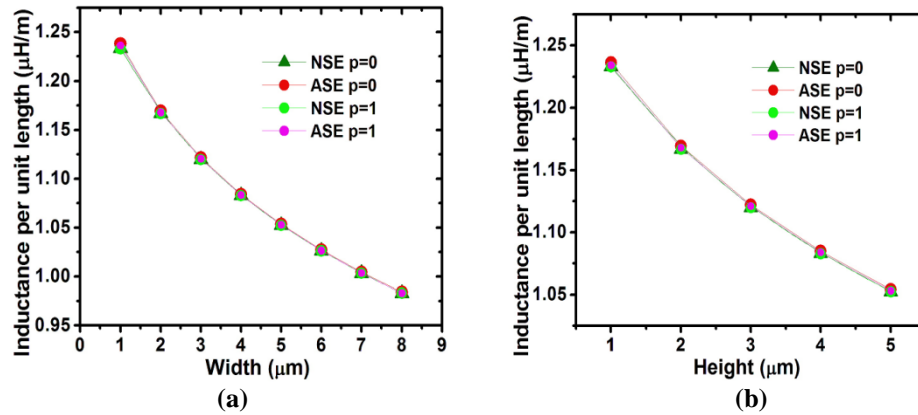


Figure 2.43. Variation of inductance at a frequency of 400GHz with: (a) width at fixed height ($H=2\mu\text{m}$) and (b) height at fixed width ($W=2\mu\text{m}$). Inductance decreases as width or height is increased. ASE or edge scattering is found to have negligible effect on the inductance values.

To gauge the potential of GR for high-frequency applications, a comparative analysis of the resistance and inductance of the GR interconnects is made with traditional metal Cu as well as other prospective interconnect materials like single-walled and multi-walled carbon nanotubes. A plot of the resistance as a function of frequency for these different materials is shown in **Figure 2.44**. The length, width and height of the interconnects are taken to be 500 μm , 2 μm , and 1 μm , respectively. The resistance of GR interconnects for both $p=0$ and $p=1$ is found to be lower than that of Cu and single-walled carbon nanotube (SWCNT) with 1/3 metallic fraction. GR has lower resistance than that of multi-walled carbon nanotube with a diameter of 10 nm till about 50 GHz for $p=0$ and 90 GHz for $p=1$. At higher frequencies, the resistance of GR is higher due to the increased skin effect. **Figure 2.45** shows the variation of the inductance of GR interconnects compared to that of Cu and CNTs. Inductance of GR is slightly higher than that of Cu and SWCNT with 1/3 metallic fraction, while the inductance of MWCNT with diameter of 10 nm is found to be highest.

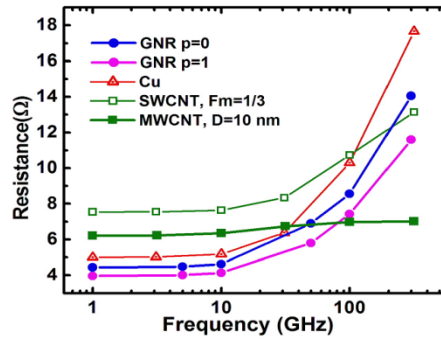


Figure 2.44. Variation of resistance with frequency for GR with $p=0$, $p=1$, Cu, SWCNT and MWCNT. The Cu wire is simulated using the field solver FastHenry. D indicates the diameter of the MWCNT and Fm indicates the fraction of metallic SWCNTs in the SWCNT bundle. The data for CNTs have been obtained from [87].

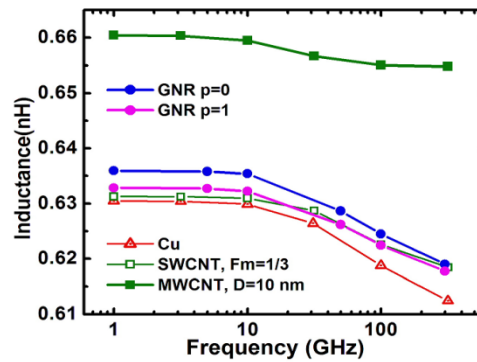


Figure 2.45. Variation of inductance with frequency for GR with $p=0$, $p=1$, Cu, SWCNT and MWCNT. The Cu wire is simulated using the field solver FastHenry. The data for CNTs have been obtained from [87].

The above detailed study can provide guidelines for the design of GR based interconnects and the frequency dependent resistance and inductance evaluated using our methodology can be easily employed for delay analysis of GR interconnects based on the model described in [21].

2.4.6. High Frequency Analysis of Graphene Inductors

For high-frequency applications such as high quality on-chip inductor design, GRs have a great advantage over CNTs since they are more controllable from the fabrication point of view. This is due to the planar nature of graphene, which can be patterned using high resolution lithography. Furthermore, for inductor design with CNTs, a metal contact is required at each corner to connect CNT bundles in different directions as shown in **Figure 2.46 (b)**, while no such contacts are required for GR based inductors (**Figure 2.46 (a)**). Hence, for GR based inductors, the contact resistance will be reduced significantly compared to that of CNTs. Thus GRs pose to be a very attractive candidate for high-quality inductor design and so it is interesting to study their performance.

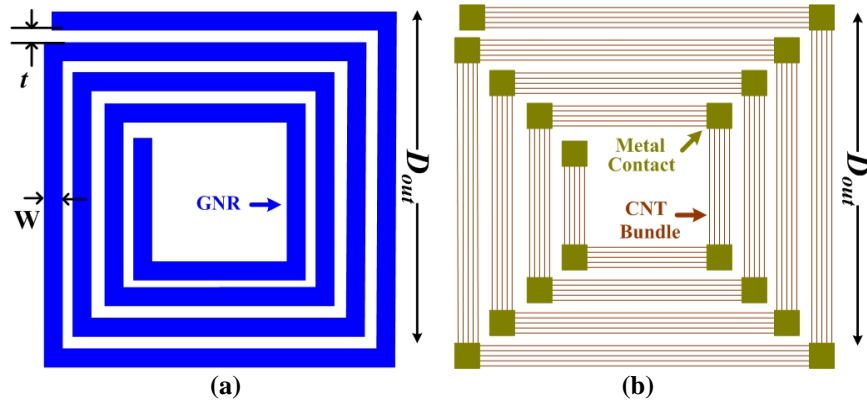


Figure 2.46. The schematic view of a 4-turn spiral (a) GR based and (b) CNT based inductor. At each corner, there is a metal contact to connect CNT bundles. However no such contacts are required for GR based inductors, which is a big advantage due to the reduction of contact resistance. W and t are the conductor width and the conductor spacing, respectively.

To analyze the performance of inductors, their quality factor (Q) needs to be calculated. Higher quality factor leads to lower loss and higher frequency stability

and hence is desirable for inductor design. In this dissertation, the modified π model of on-chip inductors [87] as shown in **Figure 2.47**, is used to calculate the Q-factor.

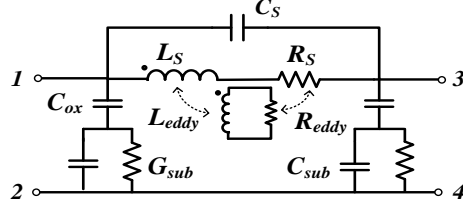


Figure 2.47. Equivalent 11-element π model for on-chip spiral inductors.

In this model, L_S and R_S are the series frequency-dependent inductance and resistance, respectively. L_{eddy} and R_{eddy} are the eddy current induced parameters and they capture the eddy current effects in the substrate [98]. C_S , C_{ox} , and C_{sub} represent the inter-turn conductor capacitance, oxide capacitance and substrate capacitance respectively [99]. Now, the Q-factor of the inductor can be calculated as:

$$Q = -\frac{imag(Y_{11})}{real(Y_{11})}$$

where Y_{11} is the input admittance of the inductor network (across ports 1 and 2 with ports 3 and 4 shorted, in **Figure 2.47** [87]).

Now, taking the Q-factor as the yard-stick for inductor performance, a comparative study of the GR based inductor with that of Cu and CNT inductors is carried out. First, we analyze the four-turn inductor shown in **Figure 2.46**, which is for low-frequency applications ($< 10\text{GHz}$). It has outermost diameter $D_{out} = 200 \mu\text{m}$, conductor width, $W = 8 \mu\text{m}$, conductor thickness, $H = 2 \mu\text{m}$, conductor spacing, $S = 1 \mu\text{m}$, and oxide and substrate thicknesses of $10 \mu\text{m}$ and $300 \mu\text{m}$, respectively. Different substrate resistivities ($\rho_{sub} = 10 \Omega \cdot \text{cm}$ and $\rho_{sub} = 0.01 \Omega \cdot \text{cm}$) are considered for our

analysis. **Figure 2.48** shows the Q-factor results for GR, Cu and different types of CNTs considering low-loss (high-resistivity; $10 \Omega\cdot\text{cm}$) substrate. The maximum Q-factor of GR-inductor shows an improvement of about 20% compared to that of Cu. On the other hand, 50% improvement is observed with respect to SWCNT (with 1/3 metallic fraction) inductors. GR inductors can achieve about 15% increase in maximum Q-factor compared to MWCNT based inductors with diameter of 10 nm.

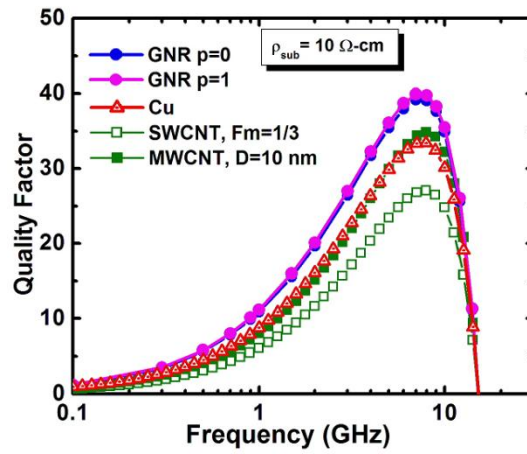


Figure 2.48. Q-factors of inductors based on GR, Cu, SWCNT, and MWCNT interconnects as a function of frequency, for low-loss ($\rho_{sub} = 10 \Omega\cdot\text{cm}$) substrate. All inductors have outermost diameter = $200 \mu\text{m}$, 4 turns, wire width $W = 8 \mu\text{m}$, wire thickness $H = 2 \mu\text{m}$, wire spacing $S = 1 \mu\text{m}$. Oxide and substrate thickness are assumed to be $10 \mu\text{m}$ and $300 \mu\text{m}$, respectively.

Figure 2.49 shows the Q-factor for inductors considering high-loss substrate ($\rho_{sub} = 0.01 \Omega\cdot\text{cm}$). With high-loss substrate, GR inductors can achieve about 14% improvement in maximum Q-factor compared to Cu. With respect to SWCNT (with 1/3 metallic fraction), 36% improvement is observed. While, a maximum Q-factor increase of 19% is achieved by GR-inductors compared to MWCNT inductor with diameter of 10 nm.

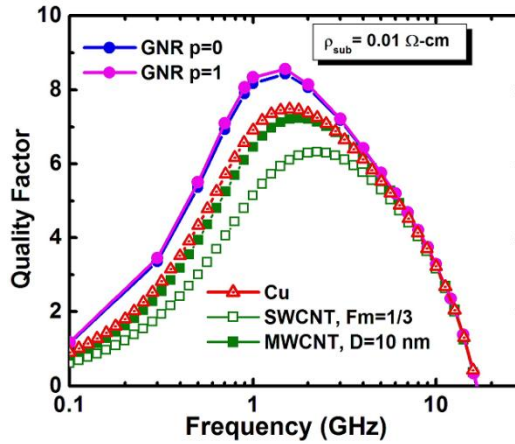


Figure 2.49. Q-factors of inductors based on GR, Cu, SWCNT, and MWCNT interconnects as a function of frequency, for high-loss ($\rho_{sub} = 0.01 \Omega\cdot cm$) substrate. All inductors have outermost diameter = $200 \mu m$, 4 turns, wire width $W = 8 \mu m$, wire thickness $H = 2 \mu m$, wire spacing $S = 1 \mu m$. Oxide and substrate thickness are assumed to be $10 \mu m$ and $300 \mu m$, respectively.

For ultra high-frequency RF circuits (tens of gigahertz), inductors are designed to have relatively small number of turns. **Figure 2.50(a)** shows one possible inductor design that has only 3/4 turn, an outer diameter of $100 \mu m$, and conductor width and thickness of $5 \mu m$ and $1 \mu m$, respectively. **Figure 2.50(b)** shows the comparative analysis of the Q-factor of such inductors at several tens of gigahertz application for GR, Cu wire and different types of CNT bundles for low-loss substrate. It is observed that improvement in maximum Q-factor of about 32% with respect to Cu can be achieved with GR inductors. As high as 40% improvement compared to SWCNT (with 1/3 metallic fraction) is seen. The comparative analysis for inductors considering high-loss substrate is shown in **Figure 2.51**. Improvement in maximum Q-factor of about 6.5% and 13% can be achieved with GR compared to Cu and SWCNT (1/3 metallic fraction), respectively.

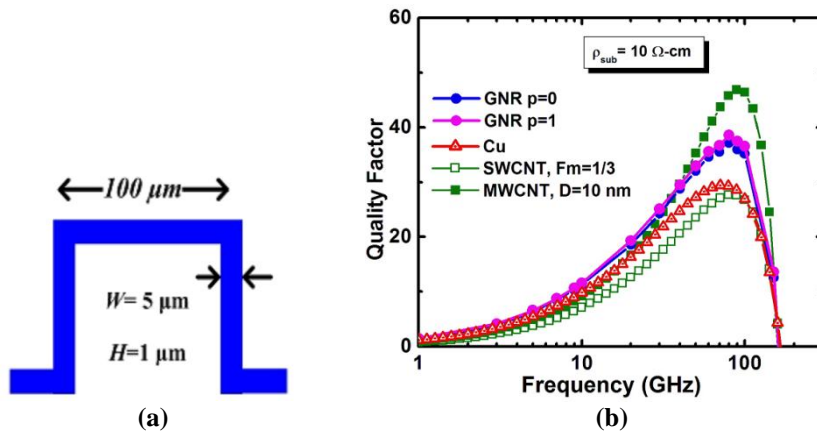


Figure 2.50(a) Structure of inductor for very high-frequency applications. (b) Q-factors of inductors based on GR, Cu, SWCNT, and MWCNT interconnects for low-loss ($\rho_{sub} = 10 \Omega\text{-cm}$) substrate. The thicknesses of oxide and substrate are 6 μm and 200 μm, respectively.

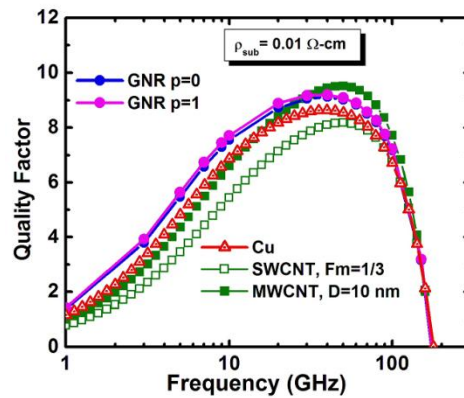


Figure 2.51. Comparison of the Q-factors of inductors for very high-frequency applications (structure shown in **Figure 2.50**(a)) based on GR, Cu, SWCNT, and MWCNT interconnects for high-loss ($\rho_{sub} = 0.01 \Omega\text{-cm}$) substrate. The thicknesses of oxide and substrate are 6 μm and 200 μm, respectively.

The improved performance of GR-inductor compared to Cu and SWCNT is due to its reduced d.c resistance. ASE tends to increase the resistance of GR with frequency but its effect is not significant in the frequency range of interest for designing the low frequency four-turn inductors or even the 3/4 turn inductors as can be deduced from **Figure 2.37**. Though MWCNT is found to exhibit better performance for ultra high-

frequency applications, fabrication of such inductor structures with long CNT bundles in the horizontal direction remains challenging. Hence, GR inductors could offer a more practical option for high-frequency interconnect and inductor applications.

2.5. Summary

In this chapter, we first provided a basic introduction to the properties of 2D materials. Then, we identified the issues namely doping, gate control and contacts, in realizing 2D semiconducting TMD based transistors and discussed approaches for addressing them. It is shown that incorporation of nanoparticles of noble metals can be an effective way to non-degenerately dope the TMDs. It is also illustrated that polymer-complex gate can lead to high capacitance gating resulting in near-ideal SS in MoS₂ FETs. For formation of efficient source and drain contacts, Y/Au stack is proposed and demonstrated to be superior to commonly used Ti/Au contacts. Apart from transistor applications, 2D semi-metallic graphene based interconnects and inductors are also investigated and their high frequency behavior is analyzed. An accurate model is developed in this project, for the extraction of high-frequency impedance of graphene interconnects. The methodology presented is generic in the sense that it can not only be used for the evaluation of high-frequency impedance, but also for accurate extraction of low-frequency as well as d.c impedance. Using the Boltzmann equation coupled with the E-k relation for graphene, the current density in a GR structure is derived taking into account the non-local values of electric field. Then the electric field and current density is calculated self-consistently using the

magnetic vector potential Green's function approach. It is shown that to accurately obtain the current density distribution and consequently the impedance, the anomalous skin effect should be taken into account. The proposed methodology is then used to analyze the high-frequency effects in graphene interconnects and investigate the important implications for high-frequency applications such as interconnect and inductor design.

Appendix A

From equations (2.20), (2.22a) and (2.23d) we can write for $p=0$:

$$J(x) = -\frac{e^2}{\pi^2 s} \left\{ \int_0^x dt \int_{v_x > 0} \frac{v_y^2}{v_x} \varepsilon(t) \exp\left(-\frac{(1+i\omega\tau)(x-t)}{\tau v_x}\right) \frac{\partial f_0}{\partial E} d\mathbf{k} \right. \\ \left. - \int_x^\infty dt \int_{v_x < 0} \frac{v_y^2}{v_x} \varepsilon(t) \exp\left(-\frac{(1+i\omega\tau)(x-t)}{\tau v_x}\right) \frac{\partial f_0}{\partial E} d\mathbf{k} \right\} \quad (A1)$$

Let us represent the integral over \mathbf{k} for $v_x > 0$ as I_1 , and that for $v_x < 0$ as I_2 . Thus equation (A1) can be written as:

$$J(x) = -\frac{e^2}{\pi^2 s} \left\{ \int_0^x dt I_1 - \int_x^\infty dt I_2 \right\} \quad (A2)$$

Now using equation (2.17b) and (2.17c) we get:

$$I_1 = \int_0^\infty \int_{-\pi/2}^{\pi/2} \frac{(v_f \sin \theta)^2}{v_f \cos \theta} \varepsilon(t) \exp\left(-\frac{(1+i\omega\tau)(x-t)}{\tau v_f \cos \theta}\right) \frac{\partial f_0}{\partial E} k dk d\theta \quad (A3)$$

For doped GR we can write $\frac{\partial f_0}{\partial E} \approx -\delta(E-E_f)$ and using equation (2.17a), we obtain:

$$I_1 = -\frac{2E_f}{\hbar^2 v_f} \int_0^{\pi/2} \frac{(\sin \theta)^2}{\cos \theta} \varepsilon(t) \exp\left(-\frac{(1+i\omega\tau)(x-t)}{\tau v_f \cos \theta}\right) d\theta \quad (A4)$$

Now I_2 has basically the same form as I_1 except that the θ integration is from $\pi/2$ to $3\pi/2$. Putting $\theta' = \pi - \theta$ and following similar steps described above for I_1 , we get:

$$I_2 = \frac{2E_f}{\hbar^2 v_f} \int_0^{\pi/2} \frac{(\sin \theta')^2}{\cos \theta'} \varepsilon(t) \exp\left(\frac{(1+i\omega\tau)(x-t)}{\tau v_f \cos \theta'}\right) d\theta' \quad (A5)$$

Combining equations (A2), (A4) and (A5) the current density can be expressed as:

$$J(x) = \frac{2e^2 E_f}{\pi^2 \hbar^2 v_f s} \int_0^\infty \varepsilon(t) dt \int_0^{\pi/2} \frac{(\sin \theta)^2}{\cos \theta} \exp\left(-\frac{(1+i\omega\tau)|x-t|}{\tau v_f \cos \theta}\right) d\theta \quad (\text{A6})$$

which is the same as equation (2.22a). Following a similar procedure, the current density for $p=1$ can also be derived.

Appendix B

The conductance per unit layer of GR is given by [21]

$$G_{total} \approx \frac{2}{\Delta E_n} \left[\int_0^\infty G_n(\text{electrons}) dE_n + \int_{-\infty}^0 G_n(\text{holes}) dE_n \right] \quad (\text{B1})$$

Here $\Delta E_n = \hbar v_f / 2W$, $E_n = \hbar v_f k_x$ and

$$\int_0^\infty G_n(\text{electrons}) dE_n = \frac{2q^2}{h} \int_0^\infty E \left(-\frac{\partial f_0}{\partial E} \right) dE \int_0^E \frac{1}{E} T_n(E) dE_n \quad (\text{B2})$$

The transmission coefficient is given by:

$$T_n(E) = \frac{1}{L} \left(\frac{1}{l_d \cos \phi} + \frac{1-p}{W \cot \phi} \right)^{-1} \quad (\text{B3})$$

where $\phi = \pi/2 - \theta$ The first integral in equation (B2) can be evaluated as in [21]. For

$p=1$ the second integral becomes:

$$\begin{aligned} \int_0^E \frac{1}{E} T_n(E) dE_n &= \int_0^{\pi/2} \frac{1}{L} \left(\frac{1}{l_d \cos \phi} \right)^{-1} \cos \phi d\phi \\ &= \frac{\pi l_d}{4L} \end{aligned} \quad (\text{B4})$$

Thus for $p=1$ we get:

$$G_{total} = \frac{1}{L} \frac{2q^2}{h} \frac{W}{hv_f} 2K_B T \ln \left[2 \cosh \left(\frac{E_f}{2K_B T} \right) \right] \pi d \quad (\text{B5})$$

The conductance is given by:

$$G = G_{total} H/s \quad (\text{B6})$$

Chapter 3: Steep Transistors

3.1. Introduction

Designing low-power and energy-efficient integrated circuits constitutes a key area for sustaining the irreversible growth of the global Information Technology industry. However, lowering of power using traditional techniques becomes increasingly difficult beyond the 22 nanometer technology node. This is due to the fact that in such nanoscale devices, the most effective “knob” used for lowering power, namely the power supply voltage, cannot be scaled as rapidly as in earlier technology generations without incurring significant performance penalty. This is due to the fundamental limitation in the steepness of turn-ON characteristics or Subthreshold Swing (SS) of conventional FETs (CFETs) as discussed in Chapter 1. Since this limitation arises from the thermionic emission based transport mechanism in CFETs, it is necessary to develop transistors with fundamentally different transport mechanism, in order to obtain subthermionic SS . Transistors with steep turn-ON characteristics (i.e. SS below the thermionic limit), which we call as the "steep transistors" can lead to the scalability of power supply voltage and hence, lower the power dissipation. Different approaches to achieve steep transistors have been proposed in the literature, such as impact-ionization based MOS (I-MOS) [100], Nano-Electro-Mechanical Switches (NEMS) [101], MOS-FETs with ferroelectric layer integrated in the gate stack (Fe-FET) [102] and Tunnel-FET (TFET) [103]. Fe-

FET suffer from complex material integration issues. On the other hand, NEMS devices exhibit significantly small ON currents [104]. Among the new generations of subthermionic transistors, I-MOS and TFETs are less disruptive and offer integrability with CMOS process and hence, will be discussed and evaluated in the next sections.

3.2. Impact Ionization MOSFET (I-MOS)

3.2.1. General Device Structure and Working Principle

Impact Ionization MOS (I-MOS) transistor [104]–[106], has been explored extensively [107]–[121], since its introduction due to its capability of providing ultra low SS . It is essentially a gated p-i-n diode structure employing avalanche breakdown mechanism where the gate covers only part of the channel as shown in **figure 3.1(a)**. The working principle is explained in **figure 3.1(b)**. The device works under reverse biased condition. In the OFF-state, the current comprises of reverse-biased p-n junction leakage current. When positive gate bias is applied, the electric field in the intrinsic ungated region increases and when the energy threshold for breakdown (ΔE) is reached, impact ionization starts. Due to the intrinsic carrier multiplication process associated with impact ionization, current increases abruptly with the increase in gate bias near the breakdown point. This abrupt change in current leads to SS below the thermionic limit.

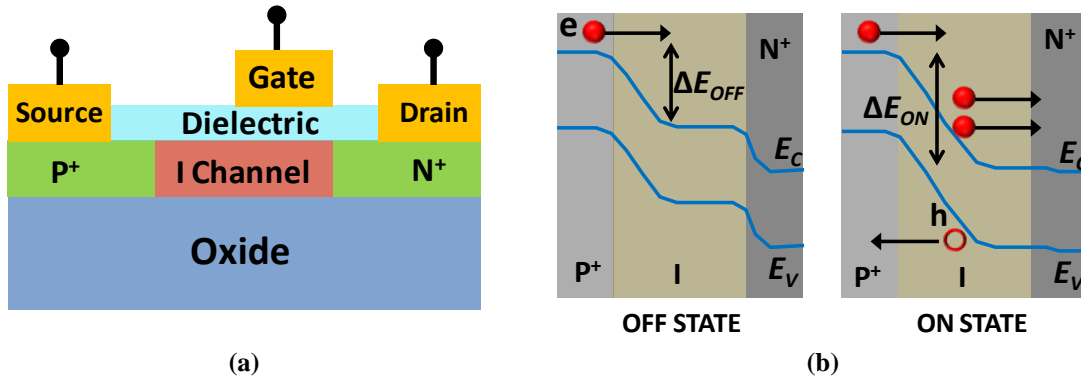


Figure 3.1(a) Schematic diagram of a I-MOS. (b) Band diagram of a I-MOS in OFF and ON state.

3.2.2. Novel Enhanced Electric Field I-MOS (E2I-MOS)

One of the major issues with I-MOS is its high breakdown voltage (V_{BD}) needed for normal operation. In this project, we propose a novel enhanced electric-field impact-ionization MOS (E2I-MOS) employing a heterostructure of two materials having different bandgaps.[122] It is shown that with proper tuning of band offset between the two materials in the heterostructure, low breakdown voltage even below that of the narrower bandgap material could be achieved.

Device Structure

The schematic of an n-type E2I-MOS is shown in **Figure 3.2**. Though equally feasible on bulk, heterostructure on insulator is used because it leads to reduced leakage currents due to elimination of drain-to-body and source-to-body leakage components [121]. The materials are chosen such that material 1 (M-1) has higher bandgap (E_g) than material 2 (M-2), and the difference in bandgap approximately equals the valence band offset $|\Delta E_g| \approx |\Delta E_V|$, while $\Delta E_C \approx 0$. Si and SiGe are very

good choices for the materials to be used as M-1 and M-2, respectively.

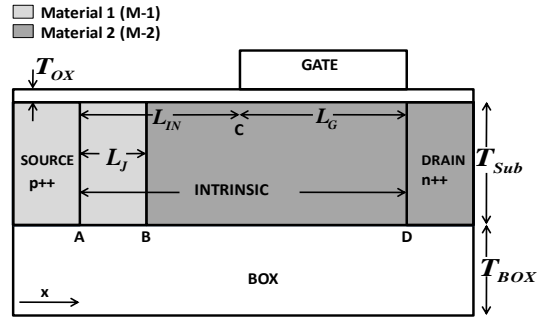


Figure 3.2. Basic device structure for n-type E2I-MOS. In all simulations, $L_G = L_{IN}$ and drain voltage $V_D=0$. Unless mentioned otherwise, the parameters used are: $L_G=L_{IN}=50$ nm, $L_J=10$ nm, $T_{OX}=3$ nm, $T_{Sub}=40$ nm, $T_{BOX}=350$ nm, gate work function $\Phi_M=4.17$ V.

Such heterostructure could be fabricated using selective epitaxy of SiGe inside recessed silicon. Ge condensation with cyclic annealing can be used to convert the Si seed layer (a layer of single crystal Si used to start SiGe epitaxy) into SiGe, which can also enhance the Ge concentration in deposited SiGe [123]. Fabrication process can be simplified by designing this device in vertical wire/pillar architecture where Si/SiGe can be a base wafer and the other material, SiGe/Si, is epitaxially deposited. Pillars can be formed through simple patterning and dry etching. This way we can get a source, channel, and drain in a single hetero-junction pillar without any intermixing of materials. As the gate can be defined using deposition and etch back, precise control on the gate edge is possible. Thus a structure close to self-aligned is possible without a self-aligned method. Furthermore, the obtained structure will be Gate-All-Around, providing even better electrostatic control over the channel and hence better electrical characteristics. For p-type E2I-MOS, the material requirement is such that $\Delta E_g \approx \Delta E_C$ with $\Delta E_V \approx 0$.

The device simulations were done using local-field impact-ionization model [124], which suffices since the non-local dead space effect is cancelled by the velocity overshoot effect in small p-i-n junctions (<100 nm) [125]. Previous experimental results [106] have proved the validity of the local-field model. Since the dimensions used (L_G , L_{IN} , L_J) are well above the threshold value (~ 5 nm), below which the quantum effects become important [118], this model is reasonably accurate in our case. To correctly model the transport across the abrupt heterojunction between M-1 and M-2, both the thermionic emission and tunneling have been taken into account.

Operation Principle

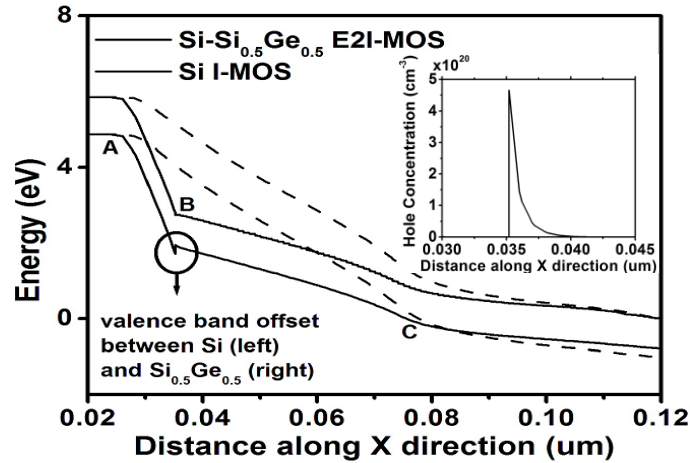


Figure 3.3. Band diagrams for n-type E2I-MOS and I-MOS ($V_S = -4.8V$, $V_G = 0V$ for both cases) during ON state. The points A, B and C correspond to those in Figure 3.2. Fermi-Dirac distribution function is employed. Temperature and mole-fraction dependent density of states and effective masses are used [124]. For the same applied bias, E2I-MOS ($|\Delta E_g| \approx |\Delta E_v| \approx 0.22eV$) has much sharper band bending and, hence, higher electric field near the source than that in I-MOS. The inset figure shows the accumulation of holes, which causes the band bending. From the simulations it is found that breakdown voltage has been reached for E2I-MOS but not for I-MOS at the biases shown.

The operation principle of an n-type E2I-MOS is discussed below. When negative bias is applied to source, with drain grounded, electron-hole pairs are generated due

to impact ionization in the intrinsic region. The electrons are swept away by the electric field towards the drain, however the holes created at $x > L_J$, are obstructed from moving towards the source due to the valence band offset, leading to accumulation of holes at the heterojunction. The accumulated holes pull the bands down increasing the electric field near the source (**Figure 3.3**). Since the impact ionization coefficient rises exponentially with the electric field [126], increase in electric field enhances the electron-hole pair generation. This leads to accumulation of more holes, which in turn, increases the electric field further. Thus the accumulation of holes acts as a positive feedback to impact ionization and the increased electric field near the source results in the reduction of the breakdown voltage. From **Figure 3.3** it is clear that the E2I-MOS has much sharper band-bending and hence, higher electric field near the source compared to that of the standard I-MOS for the same applied bias. Though reduction in V_{BD} through manipulation of electric field has been reported in some previous works [115][116], our structure is based on a completely different device design platform.

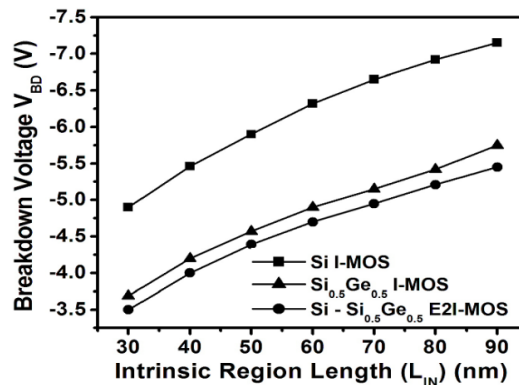


Figure 3.4. Comparison of V_{BD} of n-type Si- $Si_{0.5}Ge_{0.5}$ E2I-MOS with Si I-MOS and $Si_{0.5}Ge_{0.5}$ I-MOS at various L_{IN} . E2I-MOS exhibits lower V_{BD} due to the enhanced electric field near source.

In **Figure 3.4**, V_{BD} of Si-Si_{0.5}Ge_{0.5} E2I-MOS (M-1: Si, M-2: Si_{0.5}Ge_{0.5}) is compared with Si I-MOS and Si_{0.5}Ge_{0.5} I-MOS at various intrinsic region lengths (L_{IN} in **Figure 3.2**). For the Si-Si_{0.5}Ge_{0.5} E2I-MOS, V_{BD} reduction of about 1.8V compared to the Si I-MOS and 0.2V compared to the Si_{0.5}Ge_{0.5} I-MOS can be obtained. It is to be noted that the lowering of V_{BD} achieved in E2I-MOS is not due to strain effects, which when included could lead to further improvement due to strain induced bandgap reduction. The transfer characteristic of Si-Si_{0.5}Ge_{0.5} E2I-MOS is presented in **Figure 3.5**. Very low SS of about 6 mV/dec and high drive current of 1mA/ μ m have been obtained.

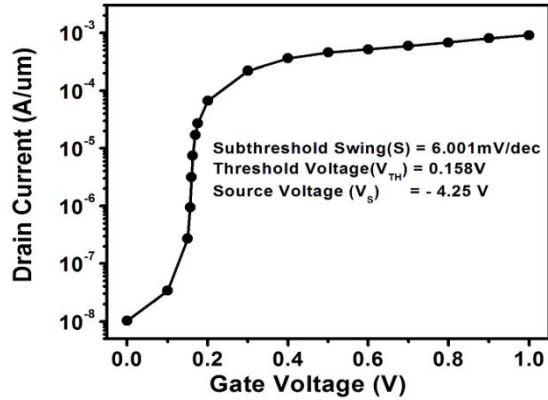


Figure 3.5. Simulated I_D - V_G characteristics of n-type Si-Si_{0.5}Ge_{0.5} E2I-MOS ($V_{BD} = - 4.4$ V). Subthreshold swing is measured at the inflection point.

Offstate Leakage and Reliability

As the device dimensions are scaled down, the OFF current of the I-MOS increases severely due to the band-to-band tunneling (BTBT) leakage. A solution to this problem would be to use wide bandgap materials. However, use of higher bandgap materials leads to higher breakdown voltage. Moreover, for the same $V_S - V_{BD}$ or V_{TH} ,

the I-MOS with wider bandgap material would have higher BTBT than that with narrower bandgap material. This is because the wider bandgap material requires higher V_S , which gives rise to higher electric field and hence enhanced BTBT. On the other hand, the uniqueness of E2I-MOS is that, it is designed to achieve substantial reduction in V_{BD} , even though the bandgap of the material (M-1) near the source is higher. Thus the leakage due to BTBT is significantly lowered. **Figure 3.6** illustrates that the Si-Si_{0.5}Ge_{0.5} E2I-MOS exhibits 10x reduction in OFF state leakage compared to the Si_{0.5}Ge_{0.5} I-MOS because of its higher tunneling barrier as well as lower V_{BD} . This leads to reduction in power dissipation and since the BTBT severely limits the scalability of the intrinsic region (L_{IN}), the E2I-MOS having a substantially lower BTBT, also allows a higher scalability.

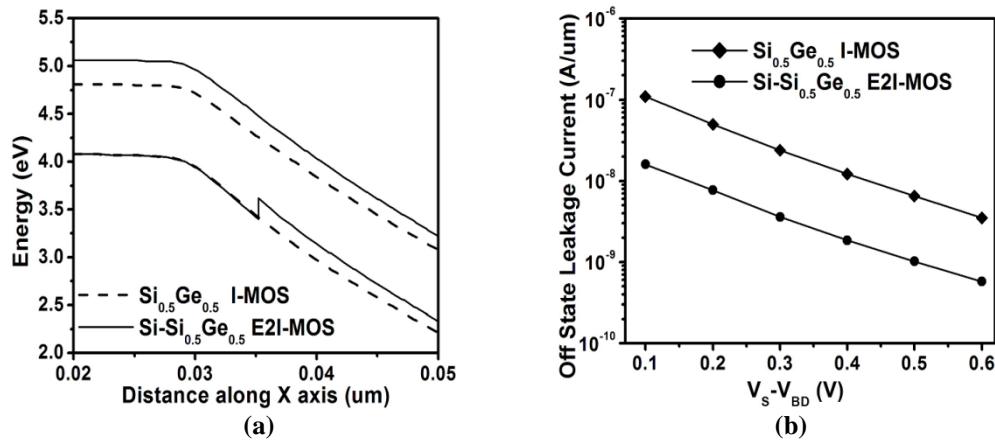


Figure 3.6(a). Band diagrams during OFF-state for n-type Si-Si_{0.5}Ge_{0.5} E2I-MOS and Si_{0.5}Ge_{0.5} I-MOS at same bias voltages. For the same applied bias, electric field for both devices is same in the OFF state, as there is no accumulation of holes in E2I-MOS. However, the tunneling barrier for E2I-MOS is higher than that in I-MOS because E2I-MOS has higher bandgap material near the source. **(b).** Leakage currents are compared for same values of $V_S - V_{BD}$ (Si_{0.5}Ge_{0.5} I-MOS having higher V_{BD} should be biased at higher negative source voltage than that of Si-Si_{0.5}Ge_{0.5} E2I-MOS to obtain the same V_{TH}). Leakage in E2I-MOS is much smaller than that in I-MOS due to the higher tunneling barrier and lower V_{BD} .

3.2.3. Challenges

In E2I-MOS, using a heterostructure composed of two materials having different bandgaps, breakdown voltage lower than that of both materials can be obtained. Thus, the breakdown voltage can be reduced. Another serious issue in I-MOS is the device reliability due to the generation of hot carriers in the vicinity of the gate dielectric [106]. For the E2I-MOS during the ON state, the electric field is increased near the source in the M-1 region, while the field in M-2 is reduced (**Figure 3.3**), thus the generation due to impact ionization can mostly be confined to M-1, which is away from the gate dielectric region. This is expected to reduce the V_{TH} instability and improve the reliability of the device. Though various other techniques have also been proposed for combating the reliability issues [112], [114], [119], significant improvements are still necessary and currently, the reliability issue is a serious drawback of I-MOS devices. In this respect, Tunnel-FETs which are also gated p-i-n diodes are more promising, as they do not suffer from such reliability issues.

3.3. Tunnel Field Effect Transistors (TFETs)

3.3.1. Device Structure and Working Principle

Tunnel-FET (TFET) [103], [127]–[133] has recently attracted a lot of attention as a highly potential candidate for obtaining steep turn-ON characteristics. The schematic diagram of a TFET is shown in **Figure 3.7**. TFET is also a gated p-i-n diode but unlike I-MOS, the gate covers the whole of the intrinsic region and the carrier

transport mechanism involves band-to-band tunneling (i.e. tunneling between valence and conduction bands). The band diagram illustrating the working principle of TFET is shown in **Figure 3.8**. In the OFF state, electrons below the source valence band cannot transport to the drain, as the width of tunneling barrier (as represented by the length of magenta arrow) between source and drain is large (**Figure 3.8(a)**). Above the source valence band and below the conduction band, i.e., within the bandgap, there are no available density of states and hence, no carrier transport occurs there as represented by the green arrow with cross. Above the source conduction band, electrons can flow to the drain as there is no barrier and this basically constitutes the reverse biased p-n junction leakage. However, the number of electrons available in the conduction band of source is very low as the source is p-doped with the Fermi level (green dashed line) in the valence band and electron concentration decreases exponentially with increase in energy above the Fermi level. There can be some channel to drain tunneling as shown by the yellow arrow but this can be reduced by using proper drain design such as low doping, higher bandgap near drain or underlap gate. In the ON state, after application of positive gate bias, the bands in the channel bend down, and the conduction band of channel comes below the valence band of the source, lowering the tunneling width (as represented by the length of red arrow in **Figure 3.8(b)**). Hence, electrons from below the source valence band can tunnel to the empty states of the channel conduction band, leading to increase in the tunneling current (**Figure 3.8(b)**). In case of TFET, particles tunnel through the barrier instead of going over the barrier. However, the forbidden gap has no density of states (DOS)

available. Hence, the electrons can no longer follow the Fermi-Dirac distribution within the forbidden gap and thus the tail of the Fermi distribution is said to be cut-off by the forbidden gap of the semiconductor. As illustrated in the figure, there are no electrons available within the green circle since it lies within the bandgap. This cutting of Fermi tail can lead to subthermionic SS .

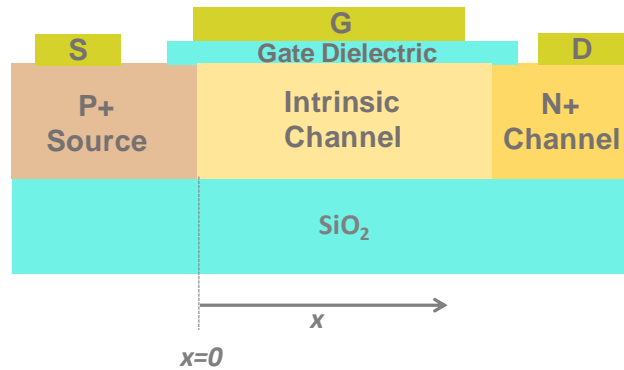


Figure 3.7. Schematic diagram of a TFET.

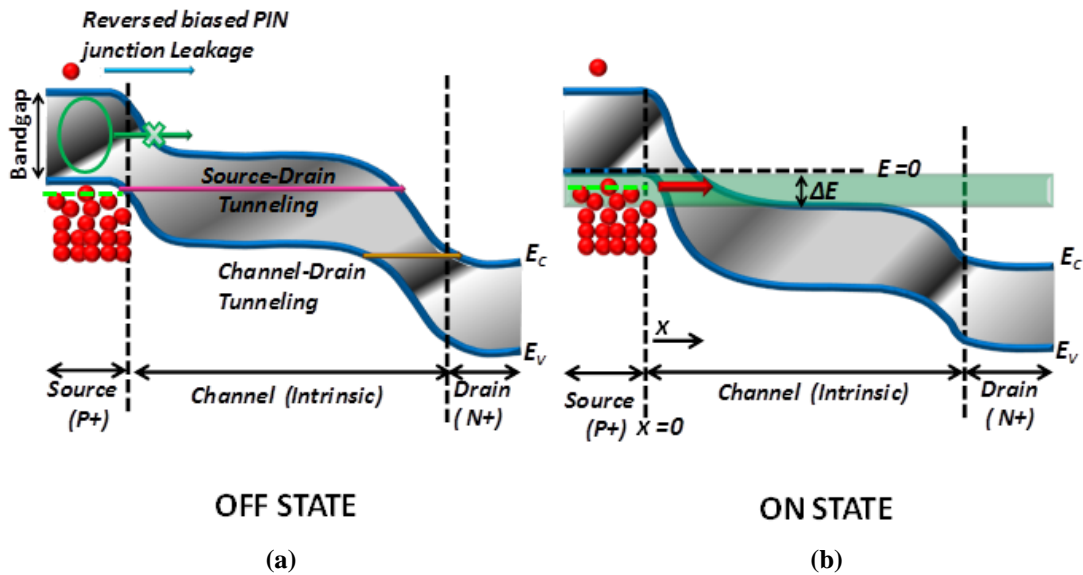


Figure 3.8. Band diagram of a TFET in OFF (a) and ON (b) state. E_C and E_V represent the conduction and valence band respectively.

Single Carrier Tunneling Barrier And Subthreshold Swing

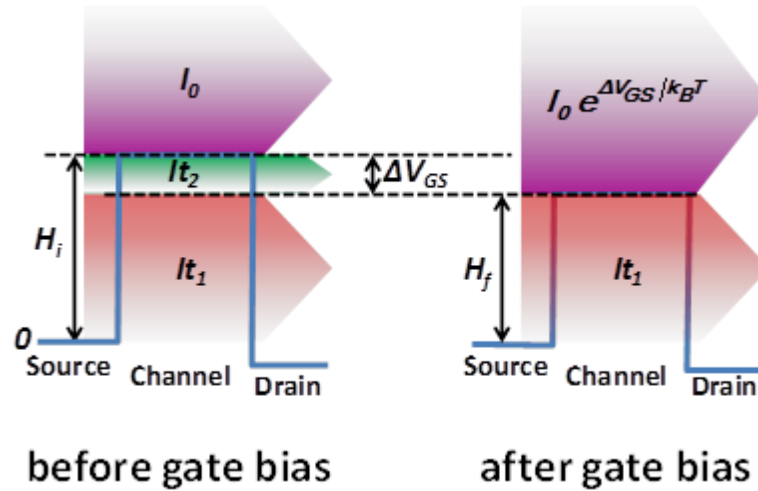


Figure 3.9. Band diagrams of a barrier in which carriers can transport not only through thermionic emission above the barrier but they can also tunnel through the barrier, before and after application of gate voltage (V_{GS}).

As discussed above, in case of band-to-band tunneling[134], where carriers tunnel from the valence to the conduction band, it is possible to achieve SS below thermionic limit. In Chapter 1, we discussed that for transport based on thermionic emission over the barrier, the minimum SS achievable is $K_B T/q \ln(10)$. Here, we show that, for any barriers, which involve combination of single carrier tunneling (but not Band-to-Band-tunneling) and thermionic emission, the SS is also limited by the thermionic limit.[81] By single carrier tunneling, we mean situations where either electrons or holes are involved in tunneling but not both. On the other hand, Band-to-Band-tunneling involves both electrons and holes[135]. A single carrier tunneling barrier is shown in **Figure 3.9**, which for example can be achieved by vertically stacking a 2D material (with non-zero bandgap) between two layers of graphene. This barrier can be

thought to be similar to that shown in **Figure 1.2(c)**, but the only difference is that the width of the barrier is small enough so that apart from transmission over the barrier through thermionic emission, electrons with energy lower than the barrier height, can also tunnel directly from source to drain. Initially, before application of gate voltage, let the barrier height be H_i , and after increasing the gate voltage by ΔV_{GS} , the height is reduced to H_f (where $H_f = H_i - \Delta V_{GS}$ in the best case assuming perfect electrostatics). Let us divide the initial current (I_i) into 3 components: let the current above the barrier through thermionic emission be I_0 , tunneling current through the barrier from energy 0 to H_f be I_{t1} and that from energy H_f to H_i be I_{t2} (**Figure 3.9**). After the application of gate voltage, the final current (I_f) can be thought to be comprised of two components, current above the barrier, which is increased compared to the initial thermionic emission current and is given by $I_0 e^{\Delta V_{GS}/k_B T}$ (as explained in previous section) and the tunneling current through the barrier given by I_{t1} . For small change in gate voltage, the SS can be written as

$$SS = \frac{\Delta V_{GS}}{\log_{10}\left(\frac{I_f}{I_i}\right)} = \frac{\ln(10)\Delta V_{GS}}{\ln\left(\frac{I_f}{I_i}\right)} \quad (3.1)$$

Now, inserting the current components for I_i and I_f in equation (3.1), we get

$$SS = \frac{\ln(10)\Delta V_{GS}}{\ln\left(\frac{I_0 e^{\Delta V_{GS}/k_B T} + I_{t1}}{I_0 + I_{t1} + I_{t2}}\right)} \quad (3.2)$$

Now, since

$$\frac{I_0 e^{\Delta V_{GS}/k_B T} + I_{t1}}{I_0 + I_{t1} + I_{t2}} < \frac{I_0 e^{\Delta V_{GS}/k_B T}}{I_0} \quad (3.3)$$

we get,

$$\frac{\ln(10)\Delta V_{GS}}{\ln\left(\frac{I_0 e^{q\Delta V_{GS}/k_B T} + I_{t1}}{I_0 + I_{t1} + I_{t2}}\right)} > \frac{\ln(10)\Delta V_{GS}}{\ln\left(\frac{I_0 e^{q\Delta V_{GS}/k_B T}}{I_0}\right)} = \ln(10) \frac{k_B T}{q} \quad (3.4)$$

This implies that, in the case when single carrier tunneling is present along with thermionic emission, not only it is fundamentally impossible to achieve SS lower than $K_B T/q \ln(10)$, but in fact, the SS is further degraded from this minimum value.

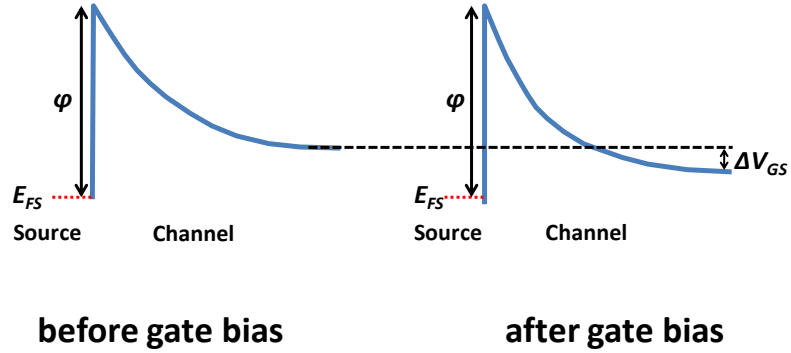


Figure 3.10. Band diagrams of Schottky barrier at the source-channel junction, before and after application of gate potential. ϕ denotes the Schottky barrier height and E_{FS} denotes the Fermi level of the source.

Even, in case of a Schottky barrier (**Figure 3.10**), it is not possible to achieve SS lower than the fundamental limit of MOSFET. Solomon has showed using simple mapping technique, that it is not possible to achieve lower SS than $K_B T/q \ln(10)$ when single carrier tunneling is involved. His methodology is valid for both Schottky

barriers as well as direct source-drain tunneling. Readers are referred to his paper [136] for further details of the methodology.

3.3.2. Understanding Band-to-Band Tunneling (BTBT)

Here, we highlight an underlying physical concept [135] behind the BTBT process that has been mostly overlooked in the literature. It is shown that the carriers exhibit dual nature of electrons and holes during the BTBT phenomenon and ignoring this duality can not only lead to substantially erroneous results but also to misleading conclusions.

Though rigorous quantum mechanical treatment of tunneling can be achieved through the *Non-Equilibrium Green's Function* (NEGF) formalism, computationally efficient models are required for fast calculations. WKB approximation provides such a tool, through which the transmission coefficient can be calculated from the wave vector, which is dependent on the type of barrier. Often the barrier for tunneling is considered to be $E_C - E$ [129][137][138][139][140], which is the barrier for electrons or $E - E_V$ [141], which is the barrier for holes. During the tunneling phenomenon, particles transit through a forbidden gap with imaginary wave vectors. If only electron (hole) tunneling and thereby only the barrier for electrons (holes) is considered, it implies that the electron (hole) faces a barrier at the valence (conduction) band edge, and hence, its wave-vector becomes imaginary there, which is unphysical because the wave-vector can be imaginary only within the bandgap and not on the valence/conduction band edge. Here, we illustrate the electron-hole duality (EHD)

within the forbidden gap during the BTBT process taking a graphene nano-ribbon (GNR) TFET as an example. While all the results here, are presented for GNRs, the EHD concept is inherent to the physics of the BTBT process and hence is applicable to any other material.

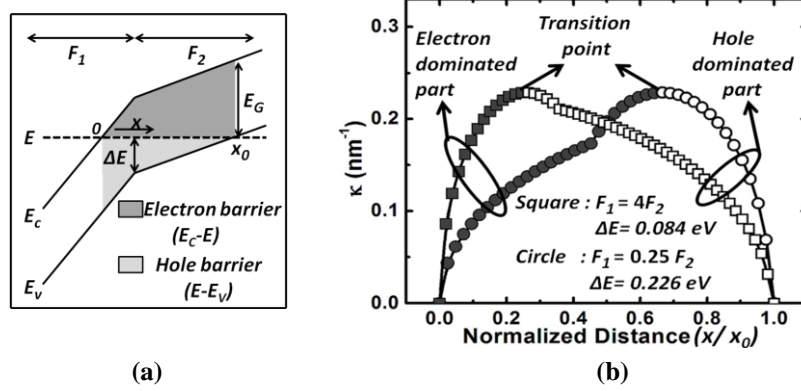


Figure 3.11(a) Band diagram of a graphene nano-ribbon under the influence of two different forces (F_1 and F_2). **(b)** Imaginary part of the wave vector (κ) as a function of normalized distance between the two turning points ($x=0$ and $x= x_0$). A GNR with 38 carbon atoms along the width, giving a bandgap of 0.27 eV is considered. Squares represent κ for $F_1=20$ MV/m, $F_2=5$ MV/m and $\Delta E=0.084$ eV, while circles represent that for $F_1=5$ MV/m, $F_2=20$ MV/m and $\Delta E=0.226$ eV. When $F_1>F_2$, the barrier for electrons increases steeply and hence reduces the electron dominated part of the wave-vector and the transition point shifts to the left. Reverse situation occurs for $F_1<F_2$.

The dispersion relation of GNRs can be derived from the mode

space Hamiltonian as [142]: $E = \sqrt{t_0^2 + t_n^2 - 2t_0t_n \cos(3k_x a/2)}$ where $t_0 = -2.77$ eV, a is

the C-C bond length and t_n is related to the quantized y directed wave-vector k_{yn} [143]

as $t_n = t_0 \left(1 + \exp(i\sqrt{3}k_{yn} a/2)\right)$ giving rise to a bandgap of $E_G = 2\sqrt{t_0^2 + t_n^2 - 2t_0t_n}$.

Under the influence of two different forces, as shown in **Figure 3.11(a)**, the barrier for electrons (E_C-E) and holes ($E-E_V$) is different and thus would lead to different tunneling probabilities. Let us first consider only electron tunneling, in which case we can write:

$$\sqrt{t_0^2 + t_n^2 - 2t_0t_n \cos\left(\frac{3k_e a}{2}\right)} - \frac{E_G}{2} = -(E_C - E) \quad \text{for } 0 < x < x_0 \quad (3.5)$$

Here, the subscript x for the wavevector (k_e) has been dropped for convenience and henceforth, any k used will refer to the x directed momentum. $x=0$ and $x=x_0$ are defined as the turning points at which $E_C=E$ and $E_V=E$, respectively, as shown in **Figure 3.11(a)**. Thus E_C-E increases from 0 to E_G as x increases from 0 to x_0 . However, an interesting situation occurs for $E_C-E > E_G/2$ for which we observe that the square root term on the left hand side of equation (3.5) becomes negative, which is unphysical. The reason is the following. Let us define the point at which $E_C-E = E_G/2$ as $x=x_t$. From 0 to x_t , the barrier for electrons is less than that for holes and hence, the electron properties should dominate. However, for $x > x_t$ the situation reverses and the use of the equation for electron tunneling in this region gives rise to the unphysical situation. The correct equations considering electron-hole duality are:

$$\sqrt{t_0^2 + t_n^2 - 2t_0t_n \cos\left(\frac{3k_e a}{2}\right)} - \frac{E_G}{2} = -(E_C - E) \quad \text{for } 0 < x \leq x_t \quad (3.6a)$$

$$-\sqrt{t_0^2 + t_n^2 - 2t_0t_n \cos\left(\frac{3k_h a}{2}\right)} + \frac{E_G}{2} = E - E_V \quad \text{for } x_t \leq x < x_0 \quad (3.6b)$$

Using the WKB approximation, the effective tunneling probability (T_{EHD}) can then be written as:

$$T_{EHD} = \exp\left\{-2\left(\int_0^{x_t} \kappa_e dx + \int_{x_t}^{x_0} \kappa_h dx\right)\right\}; \quad k_e = i\kappa_e, k_h = i\kappa_h \quad (3.7)$$

In **Figure 3.11(b)**, the EHD within the forbidden gap is illustrated.

An analytical formula for the tunneling probability in case of a constant force can be derived by assuming a simplified conical dispersion relation near the Dirac points [144]. Employing the EHD concept we can write:

$$\sqrt{(\hbar v_f k_e)^2 + \left(\frac{E_G}{2}\right)^2} - \frac{E_G}{2} = -qFx \quad \text{for } 0 < x \leq x_t \quad (3.8a)$$

$$-\sqrt{(\hbar v_f k_h)^2 + \left(\frac{E_G}{2}\right)^2} + \frac{E_G}{2} = E_G - qFx \quad \text{for } x_t \leq x < x_0 \quad (3.8b)$$

For a constant force, the transition point occurs in the middle i.e., $x_t = x_0/2$. Using equations (3.7) and (3.8) we obtain, $T_{EHD} = \exp(-\pi E_G^2 / 4v_f q\hbar F)$.

Figure 3.12 shows the tunneling probability for the case of a constant force (e.g. $F_1 = F_2 = F$ in **Figure 3.11(a)**) applied to the GNR. The EHD model shows close match with the rigorous quantum mechanical simulation using NEGF. Use of the barrier of the form given by *Flietner* in equation (3.5) or consideration of either electron or hole tunneling can give rise to significant errors.

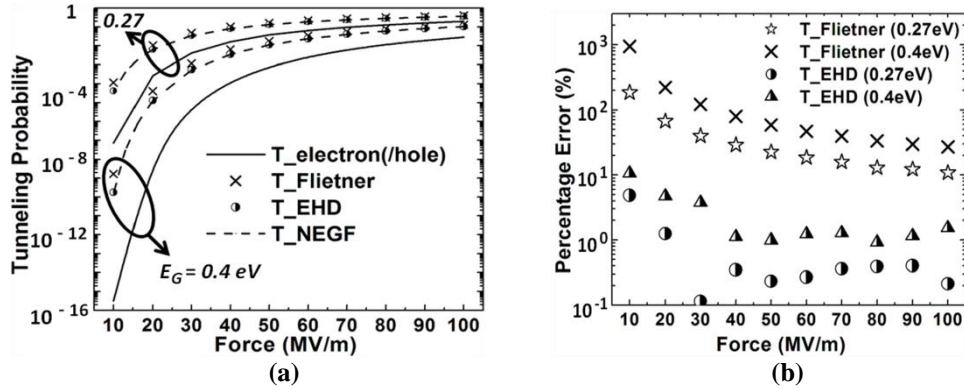


Figure 3.12(a) Tunneling probability as a function of the applied force. $T_{electron(/hole)}$ is calculated using the effective mass approximation (as the use of $E-k$ relation for either electron (hole) tunneling gives rise to the unphysical situation), taking E_C-E ($E-E_V$) as the barrier. It is clear that using only the electron or the hole barrier leads to considerable deviations from NEGF calculations. **(b)** The percentage errors for the EHD model and Flietner's model compared to NEGF simulations are plotted separately for clarity for two different values of E_G (0.27 eV and 0.4 eV). It is seen that the EHD model, expressed as equations (3.6) and (3.7), shows very good agreement with simulations based on the NEGF while use of Flietner's form of barrier can lead to significant errors. All models have been numerically solved to provide meaningful comparison.

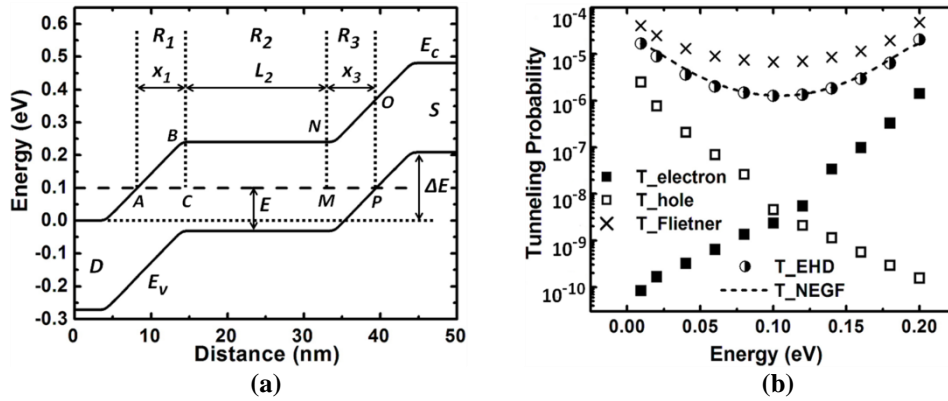


Figure 3.13(a) Band structure during direct tunneling between source and drain in a GNR TFET. E_G is taken to be 0.27 eV and $F_1=F_2=24$ MV/m. **(b)** Tunneling probability as a function of the energy level E shown in **Figure 3.13(a)**. The EHD model, expressed as (3.9), shows close match with the NEGF simulations. Consideration of either electron or hole tunneling underestimates the tunneling probability by several orders of magnitude while use of Flietner's formula leads to considerable overestimation of the same. All models have been numerically solved to provide meaningful comparison.

To take into account the tunneling between source (or drain) and channel in a TFET, the band bending can be approximately taken to be that due to a constant

force. However, this approximation is not valid for the case of direct tunneling between source and drain (**Figure 3.13(a)**). **Figure 3.13(b)** shows the accuracy of the EHD model in calculating the direct source-to-drain tunneling probability. Here, we also derive an analytical expression for it. For that we divide the area between the drain and source into three distinct regions (R_1 , R_2 and R_3 in **Figure 3.13(a)**). We assume constant force F_1 and F_3 in the drain-channel (R_1) and source-channel (R_3) junction, respectively. We assume the bands in the region (R_2) between R_1 and R_3 to be flat. Now using the EHD model, we can find the wave-vector in the three regions and the tunneling probability (T_{SD}) can be written as:

$$T_{SD} = \exp \left\{ -2 \left(\int_0^{x_1(E)} \kappa_1 dx + \int_0^{L_2} \kappa_2 dx + \int_0^{x_3(E)} \kappa_3 dx \right) \right\} \quad (3.9)$$

It is to be noted that the length of integration in R_1 (x_1) and R_3 (x_3) are energy dependent. To find x_1 , we note from **Figure 3.13(a)** that traversing from A-B-C brings us to the same energy. To find x_3 , we move along M-N-O-P. Hence we can write:

$$qF_1 x_1(E) - E_G + E = 0 \quad (3.10a)$$

$$E_G - E + qF_3 x_3(E) - E_G = 0 \quad (3.10b)$$

Let I_1 , I_2 and I_3 represent the first, second and third integration in equation (3.9), respectively. Using (3.6), (3.9) and (3.10) we derive the expressions for I_1 , I_2 and I_3 and finally for the tunneling probability as:

$$\begin{aligned}
I_1 &= \frac{1}{\hbar v_f} \frac{1}{qF_1} \left\{ \frac{\pi E_G^2}{16} + \frac{\sqrt{(E_G - E)E}(E_G - 2E)}{4} + \frac{E_G^2}{8} \sin^{-1} \left(\frac{E_G - 2E}{E_G} \right) \right\} \\
I_2 &= \frac{L_2}{\hbar v_f} \sqrt{(E_G - E)E} \\
I_3 &= \frac{1}{\hbar v_f} \frac{1}{qF_3} \left\{ \frac{\pi E_G^2}{16} - \frac{\sqrt{(E_G - E)E}(E_G - 2E)}{4} - \frac{E_G^2}{8} \sin^{-1} \left(\frac{E_G - 2E}{E_G} \right) \right\} \\
T_{SD} &= \exp \left\{ -2(I_1 + I_2 + I_3) \right\} \tag{3.11}
\end{aligned}$$

While the above analytical formulas can provide better physical insight, more accurate results can be obtained by using direct numerical solutions to equation (3.7) or (3.9) as employed in **Figure 3.12** and **Figure 3.13(b)**.

Finally, it is important to note that the large error in the tunneling probability attributed to the use of WKB method, is mainly due to its improper use. It is shown here, that with proper understanding of the EHD concept and use of accurate E - k relation, WKB can actually yield results in very good agreement with rigorous NEGF calculations. However, since the effective barrier for tunneling is reduced due to the interplay of both electrons and holes compared to that due to consideration of only one of them, it is important to know the regime of validity of the WKB method in light of the EHD concept. The WKB equation is derived under the condition that $k^{-2} dk/dx \ll 1$. It can be observed from **Fig 3.14(a)** that the required condition for WKB is not satisfied in the regions near the turning points and that, this region expands with increasing force. However, it has been argued that the errors introduced

by the use of WKB will not be significant for any arbitrary barrier given that the condition $x_0 \bar{\phi}^{1/2} \geq 4$ holds [145] where x_0 is the barrier width in Å and $\bar{\phi}$ is the mean barrier height in eV. Since consideration of either electron or hole tunneling overestimates the tunneling barrier, it will also overestimate the regime of applicability of WKB while the actual case considering EHD is shown in **Fig 3.14(b)**, as a function of bandgap and applied force.

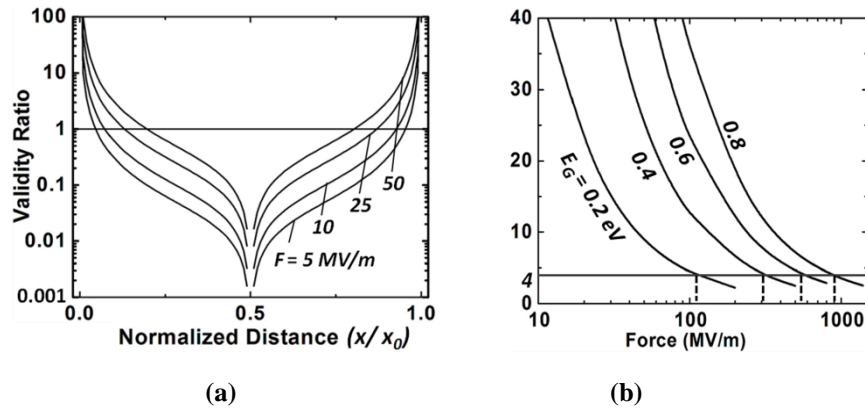


Figure 3.14(a) The factor $k^{-2} dk/dx$, which we define as WKB validity ratio for different forces applied to a GNR ($E_G = 0.4$ eV) as a function of the normalized distance between the two turning points. As force increases, the region where the validity condition is not satisfied increases. **(b)** Regime in which WKB can be used, as a function of E_G . The projection of the points at which the curve for a particular bandgap intersects the line $y=4$, on the x -axis define the maximum force up to which WKB would be applicable for that bandgap.

3.3.3. Analytical Modeling of TFETs

Though rigorous quantum mechanical treatment of tunneling can be achieved through the *Non-Equilibrium Green's Function* (NEGF) formalism, computationally efficient analytical models are required for fast calculations. Hence, here we develop analytical modeling for BTBT probability and current.[146] First, we develop an analytical model for the potential profile in the device and thereby, the band-to-band

tunneling current (I_{BTBT}) in response to a particular gate-dielectric surface potential (ϕ). This surface potential equals to the gate voltage (V_{GS}) in the case of a digital FET, while in the case of a FET based biosensor, it is the potential developed on the surface of the dielectric due to attachment of biomolecules. The modified 1D Poisson equation can be written as

$$\frac{d^2\psi_f(x)}{dx^2} - \frac{\psi_f(x) + \phi}{\lambda^2} = 0 \quad (3.12)$$

where ψ_f is the potential at the semiconductor-oxide interface, x is the direction along the channel as shown in **Figure 3.8(b)** and λ is defined as the natural length scale [1]. The right hand side of the above equation is set to zero since for TFETs the channel is intrinsic or very lightly doped. For the boundary condition at the left side, the potential at the source-channel junction is set to the potential of the source and hence, $\psi_f(0)$ is set to 0. This assumption is valid when the depletion region and the potential drop in the source are negligible, which is usually valid due to high doping of the source. Note that $\psi_f(x)$ is defined as the potential energy profile of the valence band. The potential at channel-drain junction is taken as U_d so that $\psi_f(L_{ch}) = U_d$ where L_{ch} is the length of channel region of TFET. Using the above boundary conditions, ψ_f can be derived as:

$$\psi_f = \frac{e^{\frac{x}{\lambda}}(-U_d - \phi + \phi e^{-\frac{L_{ch}}{\lambda}})}{e^{-\frac{L_{ch}}{\lambda}} - e^{\frac{L_{ch}}{\lambda}}} - \frac{e^{-\frac{x}{\lambda}}(-U_d - \phi + \phi e^{\frac{L_{ch}}{\lambda}})}{e^{\frac{L_{ch}}{\lambda}} - e^{-\frac{L_{ch}}{\lambda}}} - \phi \quad (3.13)$$

For $L_{ch} \gg \lambda$ and considering only the potential profile near the source-channel junction (ψ_{fj}), we can simplify the above equation as

$$\psi_{fj} = \phi(e^{-x/\lambda} - 1) \quad (3.14)$$

This formula is valid when the effect of drain voltage on the potential profile at source-channel junction is negligible. The electric field/force can be obtained by taking the derivative of the potential profile with respect to distance x and is given by

$$F = \phi e^{-x/\lambda} / \lambda \quad (3.15)$$

For obtaining analytical expression for BTBT probability, the maximum value of electric field ($F_{mid-max}$) in the middle of the bandgap (since the region near the middle of the bandgap has maximum contribution to the tunneling probability [147]) is required to be derived. The effective $F_{mid-max}$ occurs at energy $E=0$ as shown in **Figure 3.8(b)** since above $E=0$, the current is cut off by the bandgap of the semiconductor and as we go below $E=0$ the electric field decreases. For deriving $F_{mid-max}$ at $E=0$, we first find the value of x_{mid} , which is the point at which the intrinsic potential i.e., the midgap potential falls to $E=0$. x_{mid} can be found by solving the equation

$$\phi e^{-x_{mid}/\lambda} - \phi + E_G/2 = 0 \quad (3.16)$$

Hence, we derive the x_{mid} as

$$- \lambda \ln((\phi - E_G/2)/\phi) \quad (3.17)$$

Substituting this value of x_{mid} in the equation for electric field given by equation (3.15), $F_{mid-max}$ can be derived as

$$F_{mid-max} = (2\phi - E_G)/(2\lambda) \quad (3.18)$$

where E_G is the bandgap of the semiconductor material. Now, that the effective force is determined, next, we derive the tunneling probability as a function of force (F) using the WKB approximation and the two-band approximation as follows.

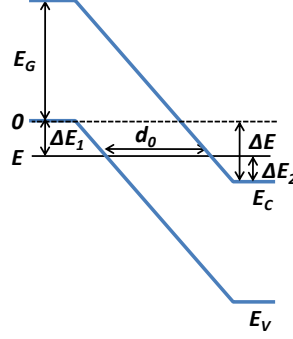


Figure 3.15. Schematic diagram of band bending under a constant electric field.

From the two-band approximation, the relation between energy and wave-vector is given by

$$\frac{\hbar^2 k^2}{2m_c} = \frac{(E - E_V)(E - E_V - E_G)}{E_G} \left(1 - \alpha \frac{(E - E_V)}{E_G} \right) \quad \text{where } \alpha = 1 - \sqrt{\frac{m_c}{m_v}} \quad (3.19)$$

where, m_c and m_v are the effective masses of the conduction and valence band respectively, in the transport direction and $\hbar = h/2\pi$ where h is the Planck's constant.

Note that, while EHD theory is general and can be used for any semiconductor, the two-band approximation is useful for easily deriving the tunneling probability in case of conventional semiconductors with parabolic bandstructure.

From WKB equation, the tunneling probability can be written as

$$T = \exp \left\{ -2 \left(\int_0^{d_0} \kappa dx \right) \right\}; \quad (3.20)$$

$$k = i\kappa$$

Consider the band bending shown in **Figure 3.15**. Let F is the electric field and represents the slope of the bands. Let us consider an energy level E which cuts the valence band at $x=0$ and the conduction band at $x=d_0$ where $d_0=E_G/qF$. We can write $E-E_V = q F x$. Using this relation, the tunneling probability can be derived as

$$T = \exp \left(- \frac{\sqrt{2}\pi m_{low}^{1/2} E_G^{3/2} (2 - 2r^{1/4} - (1 - \sqrt{r}))}{q\hbar F (1 - \sqrt{r})^2} \right) \quad (3.21)$$

where $r = \frac{m_{low}}{m_{high}}$

where, m_{low} ($/m_{high}$) are the lower and higher of m_c and m_v . The tunneling probability can be written in a simplified form as follows

$$T = \exp \left(- \frac{\sqrt{2}\pi m_{low}^{1/2} E_G^{3/2}}{4q\hbar F} \times retard \right) \quad (3.22)$$

$$retard = \frac{4(2 - 2r^{1/4} - (1 - \sqrt{r}))}{(1 - \sqrt{r})^2}$$

For, similar effective masses (m^*) of valence and conduction bands in the tunneling direction the above equation reduces to the well known Kane's formula given by

$$T = \exp \left(- \pi m^{*1/2} E_G^{3/2} / 2\sqrt{2}q\hbar F \right) \quad (3.23a)$$

Putting $F=F_{mid-max}$ in the above equation, the tunneling probability can be written as

$$T = \exp \left(- \pi \sqrt{q} m^{*1/2} E_G^{3/2} \lambda / (\sqrt{2}\hbar(2\phi - E_G)) \right) \quad (3.23b)$$

The above tunneling probabilities are valid for 1D systems. In 3D systems, the effect due to the presence of momentum in directions (y and z) transverse to the transport direction (x). needs to be considered. The effect of transverse momentum (k_t) can be taken into account by effectively increasing the bandgap in the tunneling probability as given by

$$T = \exp\left(-\frac{\sqrt{2}\pi m_{low}^{1/2} \text{retard}}{4q\hbar F} \left(E_G + \frac{\hbar^2 k_t^2}{2m_{ct}} + \frac{\hbar^2 k_t^2}{2m_{vt}}\right)^{3/2}\right) \quad (3.24)$$

$$k_t^2 = k_y^2 + k_z^2$$

where, m_{ct} and m_{vt} are the effective masses of the conduction and valence band respectively, in the transverse direction. If the effective masses in the y and z direction are different, then their average values should be considered. Putting reduced transverse effective mass as $1/m_{rt} = 1/m_{ct} + 1/m_{vt}$ and assuming the bandgap, is much higher than the transverse energy, we can write

$$E_G^{3/2} \left(1 + \frac{\hbar^2 k_t^2}{2m_{rt} E_G}\right)^{3/2} = E_G^{3/2} \left(1 + \frac{3\hbar^2 k_t^2}{4m_{rt} E_G}\right) \quad (3.25)$$

Thus, the tunneling probability can be written as:

$$T = \exp\left(-\frac{\sqrt{2}\pi m^{*1/2} E_G^{3/2} \text{retard}}{4q\hbar F}\right) \exp\left(-\frac{k_t^2}{cnst}\right) \quad (3.26)$$

$$cnst = \frac{16qFm_{rt}}{3\sqrt{2}\pi\hbar\sqrt{E_G m_{low}} \text{retard}}$$

Next we derive the energy window ΔE through which the effective tunneling occurs. As is clear from **Figure 3.8(b)**, ΔE is defined from the valence band of the source to the point at which the conduction band in the channel becomes flat. By putting the double derivative of the conduction band potential profile with respect to x to zero and assuming $L_{ch} \gg \lambda$, ΔE can be derived as

$$\Delta E = (\phi - E_G) \quad (3.27)$$

Note that here ΔE is derived for relatively small gate voltages such that $\Delta E < U_d$, in which we are interested. For larger gate voltages, ΔE will be given by the difference in energy between the valence band of the source and conduction band of the drain. Finally, using the Landauer's formula, the tunneling current for 1D systems can be written as:

$$I_{BTBT}(\phi) = \frac{2q^2 \exp\left(-\pi \sqrt{q} m^{*1/2} E_G^{3/2} \lambda / (\sqrt{2} \hbar (2\phi - E_G))\right)}{h} \times Fnc(\phi - E_G) \quad (3.28)$$

where the function $Fnc(\phi - E_G)$ is given by

$$Fnc(\phi - E_G) = \int_0^{\phi - E_G} (f_S(E - E_{f_S}) - f_D(E - E_{f_D})) dE \quad (3.29)$$

Here f_S, f_D are the Fermi functions and E_{f_S}, E_{f_D} are the Fermi levels at source and drain respectively. In the energy window ΔE , the source has plenty of available electrons and hence f_S can be set to 1 while, the drain is devoid of electrons and hence f_D can be set to 0. Thus, further simplification can be achieved and $Fnc(\phi - E_G)$ reduces to $(\phi - E_G)$.

In case of 3D systems, the current needs to be integrated over the transverse momentum states, and hence, the limits on the transverse momentum needs to be determined. We consider the case where no inelastic scattering is involved during tunneling and the transverse momentum is conserved. From **Figure 3.15**, we can write

$$\frac{\hbar^2 k_{vx}^2}{2m_v} + \frac{\hbar^2 k_{vt}^2}{2m_{vt}} = \Delta E_1 \quad (3.30a)$$

$$\frac{\hbar^2 k_{cx}^2}{2m_c} + \frac{\hbar^2 k_{ct}^2}{2m_{ct}} = \Delta E_2 \quad (3.30b)$$

$$\Delta E_1 + \Delta E_2 = \Delta E \quad (3.30c)$$

As the transverse momentum is conserved $k_{ct} = k_{vt}$, and we get the following limiting conditions on transverse momentum given by

$$k_t^2 \leq \frac{2m_{vt} \Delta E_1}{\hbar^2} \quad (3.31a)$$

$$k_t^2 \leq \frac{2m_{ct} \Delta E_2}{\hbar^2} \quad (3.31b)$$

Thus, considering an energy level nearer to the valence band (ΔE_1 is small), k_t will be limited by the equation (3.31a) while considering that near to the conduction band (ΔE_2 is small), it will be limited by the equation (3.31b). At the energy level where the crossover between the two limiting conditions occur, we get

$$\frac{2m_{vt} \Delta E_{1cross}}{\hbar^2} = \frac{2m_{ct} \Delta E_{2cross}}{\hbar^2} \quad (3.32)$$

Using equation (3.30c), we get

$$\Delta E_{1cross} = \frac{m_{ct} \Delta E}{m_{ct} + m_{vt}} \quad (3.33)$$

Now, considering the energy at the valence band edge at the p-type semiconductor to be zero, and writing ΔE_{1cross} as E_{cross} , the current (I_t) can be written using Landauer's formula as

$$I_t = \frac{q}{h\pi} T_{eff} \left[\int_0^{E_{cross}} dE \int_0^{\sqrt{2m_{vt}E}/\hbar^2} k_t e^{-\frac{k_t^2}{cnst}} + \int_{E_{cross}}^{\Delta E} dE \int_0^{\sqrt{2m_{ct}(\Delta E-E)}/\hbar^2} k_t e^{-\frac{k_t^2}{cnst}} \right] \quad (3.34)$$

where, $E_{cross} = m_{ct} \Delta E / (m_{ct} + m_{vt})$.

Solving the integrals in equation (3.34), we get

$$I_t = \frac{q}{h\pi} T_{eff} cnst \left[\Delta E + \frac{C_1 + C_2}{C_1 C_2} (e^{-A\Delta E} - 1) \right] \quad (3.35)$$

where, $C_1 = \frac{2m_{vt}}{\hbar^2 cnst}$, $C_2 = \frac{2m_{ct}}{\hbar^2 cnst}$ and $A = \frac{2\Delta E}{\hbar^2 cnst} \frac{m_{ct} m_{vt}}{m_{ct} + m_{vt}}$.

3.3.4. Development of Numerical Quantum Mechanical Simulator

While analytical formulae can provide insights, numerical simulations can provide accurate results. Device simulations require self-consistent Poisson and Schrodinger equations. Non Equilibrium Green's Function Formalism (NEGF) [148] is an efficient method of solving Schrodinger equation within the channel which takes into account the effect of source and drain contacts through the self energy terms Σ_S and

Σ_D , respectively and the effect of electron injection through the source term S . Thus the modified Schrodinger equation for the wave-function (ψ) can be written as

$$\left[H - E - U - \Sigma_s - \Sigma_D \right] \psi = S \quad (3.36)$$

The details for solving the above equation for a Hamiltonian (H) considering one energy band is well known. However, as discussed above, BTBT involves transition between two bands. Hence, here we develop the models for NEGF using two-band Hamiltonian and derive the respective self-energy and source terms.

The two band Hamiltonian interacting through k.p perturbation, is given by [149]

$$H = \begin{bmatrix} E_G + \frac{\hbar^2 k^2}{2m} & \frac{\hbar p k}{m} \\ \frac{\hbar p k}{m} & \frac{\hbar^2 k^2}{2m} \end{bmatrix} \quad (3.37)$$

where p is the momentum matrix element and k is the momentum operator and can be written as $k = -i d/dx$. Hence, considering a 1D wire and the wavefunctions for the two bands as ψ_A and ψ_B , we can write

$$\begin{bmatrix} E_G - \frac{\hbar^2}{2m} \frac{d^2}{dx^2} & -i \frac{\hbar p}{m} \frac{d}{dx} \\ -i \frac{\hbar p}{m} \frac{d}{dx} & -\frac{\hbar^2}{2m} \frac{d^2}{dx^2} \end{bmatrix} \begin{bmatrix} \psi_A \\ \psi_B \end{bmatrix} = E \begin{bmatrix} \psi_A \\ \psi_B \end{bmatrix} \quad (3.38)$$

Now, writing in the matrix format

$$H = \begin{bmatrix} E_G I + H_1 & H_2 \\ H_2 & H_1 \end{bmatrix} \quad (3.39a)$$

$$H_1 = \begin{bmatrix} 2t & -t & & & & \\ -t & 2t & -t & & & \\ & -t & 2t & -t & & \\ & & & & & \\ & & & & & \\ & & & & -t & 2t \end{bmatrix}_{NP \times NP} \quad (3.39b)$$

$$H_2 = \begin{bmatrix} 0 & -t_p & & & & \\ t_p & 0 & -t_p & & & \\ & t_p & 0 & -t_p & & \\ & & & & & \\ & & & & & \\ & & & & & 0 \end{bmatrix}_{NP \times NP} \quad (3.39c)$$

where NP is the number of grid points into which the 1D wire is divided, $t = \hbar^2/2ma^2$, $t_p = i\hbar p/2ma$ and a is the distance between two adjacent points.

The Self Energy Function Due To Contacts

From equation (3.38) and (3.39), we can write for the n th point

$$(E_G + 2t - E)\psi_A(n) - t\psi_A(n+1) - t\psi_A(n-1) - t_p\psi_B(n+1) + t_p\psi_B(n-1) = 0 \quad (3.40a)$$

$$-t_p\psi_A(n+1) + t_p\psi_A(n-1) + (2t - E)\psi_B(n) - t\psi_B(n+1) - t\psi_B(n-1) = 0 \quad (3.40b)$$

For right contact, using plane waves for wave functions, we can write

$$\psi_A(n) = e^{inka} \quad (3.41a)$$

$$\psi_B(n) = e^{inka} \quad (3.41b)$$

And putting $n=NP$ in equation (3.40), we get

$$(E_G + 2t - E)\psi_A(NP) - te^{ika}\psi_A(NP) - t\psi_A(NP-1) - t_p e^{ika}\psi_B(NP) + t_p\psi_B(NP-1) = 0 \quad (3.42a)$$

$$-t_p e^{ika}\psi_A(NP) + t_p\psi_A(NP-1) + (E_G + 2t - E)\psi_B(NP) - te^{ika}\psi_B(NP) - t\psi_B(NP-1) = 0 \quad (3.42b)$$

For left contact, using plane waves for wave functions

$$\psi_A(n) = C e^{ink a} + D e^{-ink a} \quad (3.43a)$$

$$\psi_A(0) = e^{ik a} \psi_A(1) + C(1 - e^{i2ka}) \quad (3.43b)$$

$$\psi_B(0) = e^{ik a} \psi_B(1) + C(1 - e^{i2ka}) \quad (3.43c)$$

And putting $n=1$, in equation (3.40), we get

$$(E_G + 2t - E)\psi_A(1) - t\psi_A(2) - t\psi_A(0) - t_p \psi_B(2) + t_p \psi_B(0) = 0 \quad (3.44a)$$

$$-t_p \psi_A(2) + t_p \psi_A(0) + (2t - E)\psi_B(1) - t\psi_B(2) - t\psi_B(0) = 0 \quad (3.44b)$$

using equation (3.43c), we get

$$(E_G + 2t - E)\psi_A(1) - t\psi_A(2) - [t e^{ik a} \psi_A(1) + tC(1 - e^{i2ka})] - t_p \psi_B(2) + [t_p e^{ik a} \psi_B(1) + t_p C(1 - e^{i2ka})] = 0 \quad (3.44c)$$

$$-t_p \psi_A(2) + [t_p e^{ik a} \psi_A(1) + t_p C(1 - e^{i2ka})] + (2t - E)\psi_B(1) - t\psi_B(2) - [t e^{ik a} \psi_B(1) + tC(1 - e^{i2ka})] = 0 \quad (3.44d)$$

From equations (3.42) and (3.44), the self energy function can be written as

$$\Sigma = \Sigma_R + \Sigma_L = \begin{bmatrix} \Sigma_1 & \Sigma_2 \\ \Sigma_2 & \Sigma_1 \end{bmatrix} \quad (3.45 a)$$

$$\Sigma_1 = \begin{bmatrix} t e^{ik a} \\ \\ \\ t e^{ik a} \end{bmatrix}_{NP \times 1} \quad (3.45 b)$$

$$\Sigma_2 = \begin{bmatrix} -t_p e^{i k a} \\ \\ \\ t_p e^{i k a} \end{bmatrix}_{NP \times 1} \quad (3.45 c)$$

The Source Term

From equation (3.44), we can write the source term as

$$S = \begin{bmatrix} S_1 & S_2 \\ S_2 & S_1 \end{bmatrix} \quad (3.46 a)$$

$$S_1 = \begin{bmatrix} t C (1 - e^{i 2 k a}) \\ \\ \\ \end{bmatrix}_{NP \times 1} \quad (3.46 b)$$

$$S_2 = \begin{bmatrix} -t_p C (1 - e^{i 2 k a}) \\ \\ \\ \end{bmatrix}_{NP \times 1} \quad (3.46 c)$$

From equation (3.46), we can write

$$\begin{aligned} S S^* (1) = S S^* (NP) &= |t C (1 - e^{i 2 k a})|^2 + |t_p C (1 - e^{i 2 k a})|^2 \\ &= |C|^2 |2t \sin(ka)|^2 + |C|^2 |2t_p \sin(ka)|^2 \end{aligned} \quad (3.47)$$

We can write C as

$$\begin{aligned} |C|^2 &= \frac{D(E)}{2} f_L(E) \\ &= \frac{1}{\frac{2\pi}{a} \frac{dE}{dk}} f_L(E) \end{aligned} \quad (3.48)$$

We use the following plane waves in equation (3.40 a)

$$\psi_A(n) = e^{i n k a} \quad (3.49 \text{ a})$$

$$\psi_B(n) = e^{i n k a} \quad (3.49 \text{ b})$$

Thus, we get

$$\begin{aligned} E &= (E_G + 2t) - t e^{ika} - t e^{-ika} - t_p e^{ika} + t_p e^{-ika} \\ &= (E_G + 2t) - 2t \cos(ka) - 2it_p \sin(ka) \end{aligned} \quad (3.50)$$

We can find the derivative of energy with respect to k as

$$\begin{aligned} \frac{dE}{dk} &= 2at \sin(ka) - 2iat_p \cos(ka) \\ &= 2at \sin(ka) + 2a|t_p| \cos(ka) \end{aligned} \quad (3.51)$$

From equations (3.48) and (3.51) we can write

$$|C|^2 = \frac{1}{4\pi [t \sin(ka) + |t_p| \cos(ka)]} f_L(E) \quad (3.52)$$

Using equations (3.47) and (3.52), we get

$$S S^*(1) = S S^*(NP) = \frac{|\sin(ka)|^2 (|t|^2 + |t_p|^2)}{\pi [t \sin(ka) + |t_p| \cos(ka)]} f_L(E) \quad (3.53)$$

Here, the SS^* is not proportional to $\Sigma - \Sigma^*$

3.3.5. Performance Improvement : Nanoparticle Assisted Tunneling

The TFETs face a major challenge because of their low ON-current. Here, we propose and show that the incorporation of metallic nanoparticles at the tunnel-junction can lead to increased tunneling probability and hence increased current. The current in TFETs is essentially limited by the barrier through which the tunneling occurs. For BTBT process, the tunneling barrier is determined by the bandgap of the semiconductor. A barrier is faced within the forbidden gap because of the absence of available states there to accommodate the electrons while the barrier reduces to zero at the conduction and valence band edges. If somehow states could be created within the forbidden gap of the semiconductor, it would lead to reduction in the effective tunneling barrier.[150][151] This is precisely what can be achieved by incorporation of metallic nanoparticles at the tunnel junction. When these nanoparticles are inserted, the barrier reduces to zero at the nanoparticles since metals have overlapping valence and conduction bands. Thus, essentially the tunnel-mechanism takes place in two steps: first step involves tunneling between the valence band of the semiconductor in segment-1 and metal while the second step involves that between the metal and the conduction band of the semiconductor in segment-2 as shown in **Figure 3.16(a)**. [150][151] Growth of metallic islands within a semiconductor is possible as has been demonstrated experimentally [152]–[154].

Theoretical Analysis

To enable direct comparison of the metallic nanoparticle (MN) assisted tunneling probability with the well known Kane's formula [149], we consider here the case of constant force (F) and similar effective masses for electrons and holes (m^*). Moreover, for such a case, an analytical formula for tunneling probability can be derived, which provides better physical insights. The insights developed here can be easily extended to non-uniform forces and non-symmetric effective masses.

For the standard case, i.e., without the presence of any states in the forbidden gap, the tunneling probability (T) is given by equation (3.23a).

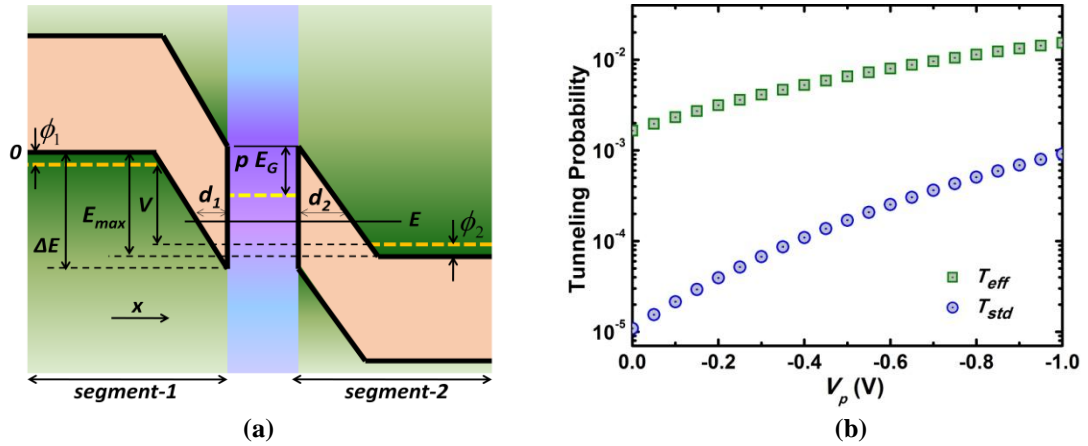


Figure 3.16(a) Schematic band diagram of a tunnel junction where metallic nanoparticles have been incorporated leading to zero bandgap between segment-1 and segment-2. Due to the presence of the nanoparticles, tunneling process can now be divided into two parts: through segment-1 and segment-2 (denoted by blue arrows). V is the voltage applied across the junction. ϕ_1 (ϕ_2) denote the energy differences between the valence (/conduction) band in segment-1 (/segment-2) and the Fermi level. The Fermi level pinning position at the metal-semiconductor interface is denoted by p which is defined from the conduction band as a fraction of the bandgap (E_G). d_1 and d_2 represent the tunneling distances in segment-1 and 2 respectively for a particular energy level E . **(b)** Comparison of theoretically calculated tunneling probability without (T_{std}) and with (T_{eff}) metallic NPs at an energy level E where $d_1 = d_2$.

For MN-tunneling, we can write the tunneling probability through each segment from **Figure 3.16(a)**, using the WKB approximation and the two-band approximation [149] as

$$T = \exp\left(-2\int_0^d \sqrt{\frac{2m^*}{\hbar^2 E_G} (E_G qFx - (qFx)^2)} dx\right) \quad (3.54)$$

E_G and m^* are the bandgap and carrier effective mass of the semiconductor material, respectively. It is to be noted, that the tunneling probability here depends on the energy level at which tunneling occurs. This is because the region of integration determined by d , which we define as the tunneling length, is energy dependent. At a particular energy level E , the tunneling distance for step 1 and 2 are shown as d_1 and d_2 in **Figure 3.16(a)**. d_1 and d_2 add up to E_G/qF , where E_G is the bandgap, q is the electronic charge and F is the electric field in the intrinsic region. The tunneling probability for each step can be derived as [150]

$$T = \exp\left(\begin{array}{l} \sqrt{\frac{m^*}{2E_G} \frac{(qFE_G - 2q^2F^2d)\sqrt{qFE_Gd - q^2F^2d^2}}{\hbar q^2F^2}} \\ -\frac{1}{2\sqrt{2}} \frac{\sqrt{m^*} E_G^{3/2}}{q\hbar F} \tan^{-1}\left(\frac{qF(d - E_G/2qF)}{\sqrt{qFE_Gd - q^2F^2d^2}}\right) \\ \frac{1}{8} \frac{\pi\sqrt{2} m^{*1/2} E_G^{3/2}}{q\hbar F} \end{array}\right) \quad (3.55)$$

where m^* is the carrier effective mass of the semiconductor material, \hbar is the reduced Plank's constant and d should be replaced by d_1 or d_2 for obtaining the tunneling probability for the 1st (T_1) or 2nd (T_2) step respectively. The effective tunneling probability (T_{eff}) combining both the steps i.e., the tunneling probability from the valence band of the P-region to the conduction band of the N-region is given by [148]

$$\frac{1}{T_{eff}} = \frac{1}{T_1} + \frac{1}{T_2} - 1 \quad (3.56)$$

Note, T_{eff} is not simply given by $T_1 T_2$ or the multiplication of tunneling probabilities for the 1st and 2nd step. This is because of the multiple quantum mechanical reflections [148] that take place at the region of zero bandgap at the metallic NPs between the two barriers formed by the bandgap of the semiconductor material.

It is noteworthy, that putting d as E_G/qF in equation (3.55) or simple multiplication of T_1 and T_2 (and putting $d_1 + d_2 = E_G/qF$) will lead to the tunneling probability which is exactly same as that for the standard case (T_{std}), i.e., without any metallic NPs, which can be given by equation (3.23a).

However, the tunneling probability in the case with metallic NPs, given by T_{eff} in equation (3.56), is much higher than T_{std} (**Figure 3.16(b)**).[151]

Now, with the expression for tunneling probability being derived, we want to explore the characteristics of the MN-tunneling in greater details.[150] On application of a voltage V across the junction, the applied voltage gets divided among the left and right segments (**Figure 3.16(a)**).The fraction of the voltage dropped in each segment depends on the Fermi-level pinning position and the doping in the segments and can be calculated using the condition of continuity of current flowing through segment-1 and segment-2 where the equation of current through each segment can be written as

$$I = \frac{2q}{h} \int_0^{\Delta E} T(E)(f_i(E) - f_f(E))dE \quad (3.57)$$

Here f_i and f_f denote the Fermi functions of the initial and final states from and to which the tunneling occurs, respectively. Here ΔE denotes the energy window over which the current flows as shown in **Figure 3.16(a)**.

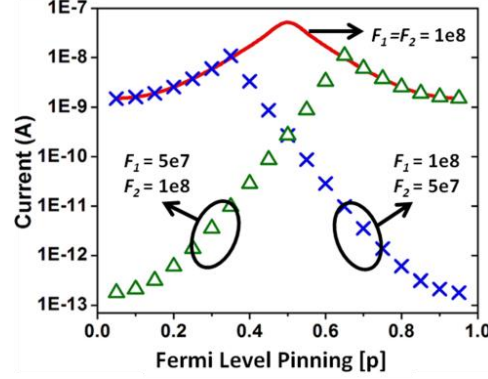


Figure 3.17. Current as a function of Fermi level pinning position p (defined in Figure 3.16(a)) for similar ($F_1 = F_2$) as well as dissimilar ($F_1 \neq F_2$) forces in the two segments. For $F_1 = F_2$, the peak current occurs at $p=0.5$ while for $F_1 \neq F_2$ the peak position shifts depending on the forces.

In **Figure 3.17**, the current is plotted as a function of the Fermi level pinning position (p), which is defined from the conduction band as a fraction of the bandgap (**Figure 3.16 (a)**). It is observed that depending on the forces applied in the two segments there is always an optimum value of p , which leads to the highest current. When the force in the two segments are equal, the peak current is obtained when the Fermi-level is pinned at the midgap ($p=0.5$) while it decreases at either ends. This is because when $p=0.5$, the band bending is symmetrical in both segments, voltage being equally divided between segment-1 and segment-2. Hence, the maximum value of tunneling length is given by

$$d_{\max_mid} = \frac{E_{\max_mid}}{qF} = \frac{E_G / 2 + V / 2 + \phi}{qF} \quad (3.58)$$

Here, the subscript *mid* denotes that the Fermi level pinning occurs at the midgap and we consider $\phi_1 = \phi_2 = \phi$. The symbol E_{max} is defined in **Figure 3.16(a)**. Now, when p is either smaller or greater than 0.5, then on one segment, the maximum value of tunneling length will be greater than d_{max_mid} while on the other it would be less than d_{max_mid} . Since the current is dominated by the most resistive region, the increased d in one of the segments will lead to decrease in the current. When the forces in the two segments are considered to be different, then the current peak will occur away from $p=0.5$ due to the asymmetry caused by the different forces.

Figure 3.18 shows the current as a function of force, which is taken to be same in both the segments. Fermi-level pinning is considered to be at $p=0.5$. It is clear that the current is increased significantly due to MN-tunneling compared to that without the incorporation of nanoparticles. Improvement in current of about 3 orders of magnitude at lower values of force and around 2 orders at higher forces is obtained.

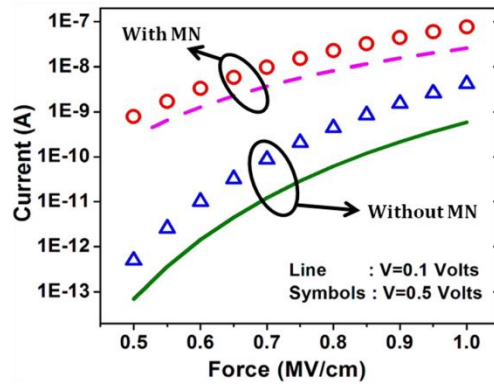


Figure 3.18. Current as a function of the force ($F_1 = F_2$) for two different values of V and $p=0.5$. It is observed that MN-tunneling leads to substantial increase in current compared to those without MN.

Till now we have considered the pinning level to be same for both the segments and found that $p=0.5$ leads to the maximum current value for similar force in both regions. On plotting the current density as a function of E (**Figure 3.19(a)**), we observe that the current initially increases with increase in E . However, with further increase in E the current decreases again. This is because with increase in E the number of vacant states, into which the particle can tunnel to, reduces (or in other words $f_f(E)$ in equation (3.55) increases) and becomes particularly small as E goes down from the Fermi-level of the metal. Thus, though the $T(E)$ term in the expression for current in equation (3.55) increases with E , the current decreases due to the decrease in the term $(f_i(E) - f_f(E))$. Thus, we are not able to harness the full advantage of the very high tunneling probability at larger E . Now let us explore whether further improvement can be achieved through use of dissimilar pinning levels in the two segments, which we will now refer to as p_1 and p_2 . It is to be noted that the tuning of pinning level at the metallic nanoparticles has been demonstrated experimentally [154]. We observe that if we use dissimilar Fermi level pinning at the two segments such that at segment-1, pinning is more towards the valence band i.e., $p_1 > 0.5$ while at segment-2 pinning is more towards the conduction band i.e., $p_2 < 0.5$, as shown in **Figure 3.19(b)**, then we could effectively use the regions with higher E or smaller d with higher tunneling probability. It is seen clearly from **Figure 3.19(c)** that as p_1 increases and p_2 decreases, the region over which the tunneling occurs shifts towards smaller values of d . In **Figure 3.19(d)**, the current is plotted as a function of force for dissimilar p_1 and p_2 with p_2 set to $1 - p_1$. We observe that with increase in p_1 , the

current increases substantially and we get much higher current than what we achieved using identical pinning level for the two segments.

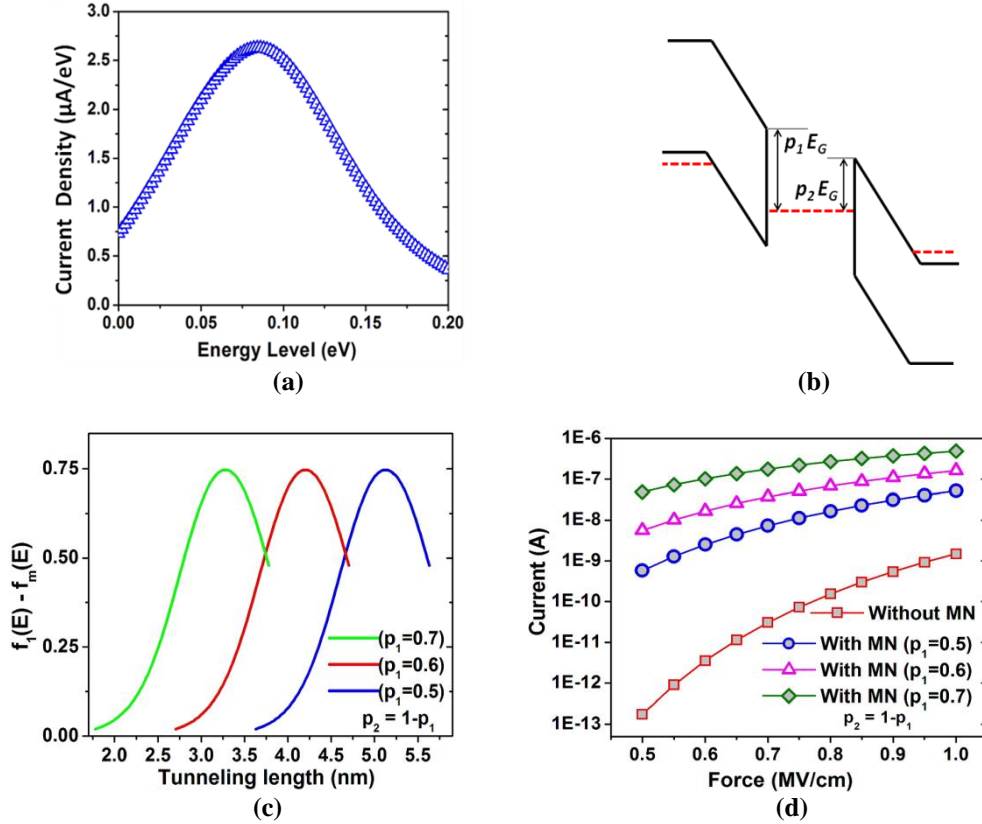


Figure 3.19(a) Current density as a function of the energy level E plotted from 0 to ΔE . It is seen that the current initially increases with increase in E due to increase in the tunneling probability but then decreases due to decrease in $(f_1(E) - f_m(E))$. (b) Schematic band diagram showing different pinning positions defined by p_1 and p_2 at the two segments where $p_1 > 0.5$ while $p_2 < 0.5$. (c) The difference in Fermi function between the left segment and the metal given by $(f_1(E) - f_m(E))$ as a function of the tunneling length for different p_1 with $p_2 = 1 - p_1$. We observe that as p_1 increases, the window of tunneling length over which current flows (which also corresponds to the energy window ΔE) shifts towards lower values of tunneling lengths. (d) Effective increase in the tunneling current with increase in p_1 .

It is to be noted that depending on the interface roughness at the nanoparticle-semiconductor junction and temperature, the degree of coherence for MN-assisted tunneling will vary. Simulations capturing varying degree of coherence will require a full-fledged quantum-mechanical treatment. In this dissertation, we have treated the

MN-assisted tunneling in the *non-coherent* limit (since during the 2nd tunneling step, phase information of the 1st tunneling step is lost). Such treatment allows the development of analytical models with better physical insights and captures the advantages of nanoparticle-assisted tunneling compared to that without the nanoparticles, without involving severe computational complexity.

Experimental Demonstration

In this section, we experimentally demonstrate the improvement in BTBT current due to insertion of metallic NPs,[151] which is a proof of concept of the idea proposed in the previous section. To this end we fabricated P-I-N diodes with a short I-region and incorporated metallic NPs at the middle of this I-region (**Figure 3.20(a)**). P-I-N diodes with exactly the same structure and doping but without the NPs were also fabricated to act as a standard for comparison.

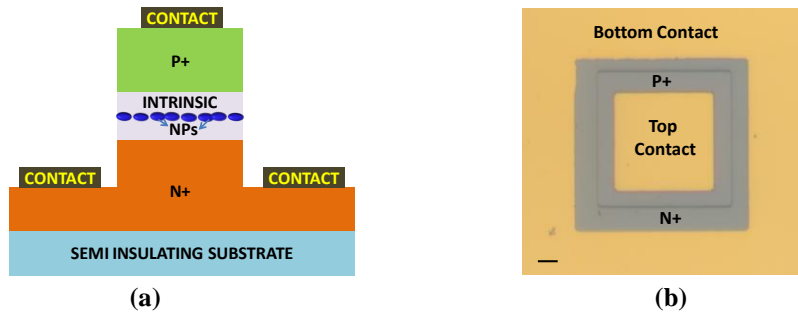


Figure 3.20(a) Schematic diagram of a P-I-N diode with metallic NPs at the middle of the I-region. **(b)** The optical image of a fabricated P-I-N junction. Scale bar : 10 μm .

The optical image of the fabricated P-I-N junction is shown in **Figure 3.20(b)**. The P-I-N diode was formed by growing doped GaAs or $\text{In}_{0.53}\text{Ga}_{0.47}\text{As}$ using a modified VG V80H solid source MBE system on InP (001) substrates. P and N doping was

obtained by using Be and Si respectively, while ErAs or ScAs formed the nanoparticles. Conventional effusion cells were used for Ga, In, Al, Si and Be, a valved cracker for As and a high temperature effusion cell for Er or Sc. For each sample, the wafer's native oxide was desorbed at 490-520°C under an As overpressure. The oxide desorption process was also used to calibrate a pyrometer from which subsequent temperatures during growth were adjusted. For InP, during oxide desorption, a thin layer of InAs may form from an As-P exchange reactions that can act as a parallel conduction path [155], [156]. A 200 nm thick InAlAs buffer layer was grown at 490°C over this interfacial layer with the intent of minimizing parallel conduction in the InAs during electrical transport measurements by acting as a back barrier and also for obtaining a smooth, atomically clean surface for InGaAs growth. Next, InGaAs active layers were grown at 490°C at a rate of 1 $\mu\text{m/h}$. The growth rate and composition of InGaAs was calibrated with RHEED oscillations during GaAs, and InGaAs growth and confirmed with x-ray diffraction. Si and Be were incorporated in the InGaAs layer by codeposition. The Si/Be doping flux was calibrated by Hall measurements of Si/Be doped GaAs. First, N-region was formed followed by I- and then P-regions. For, incorporating the nanoparticles which constitutes of rare earth elements Er or Sc, in the I-region, the rare earth fluxes were calibrated by Rutherford backscattering measurements on Si substrates. The nanoparticles were grown on InGaAs by an embedding mechanism achieved by depositing less than 3 monolayers of ErAs or ScAs [157]. After the growth, mesas of different areas were etched into the samples, up to about 300 nm deep into the N

region followed by formation of metallic contacts to the P and N region for electrical characterization.

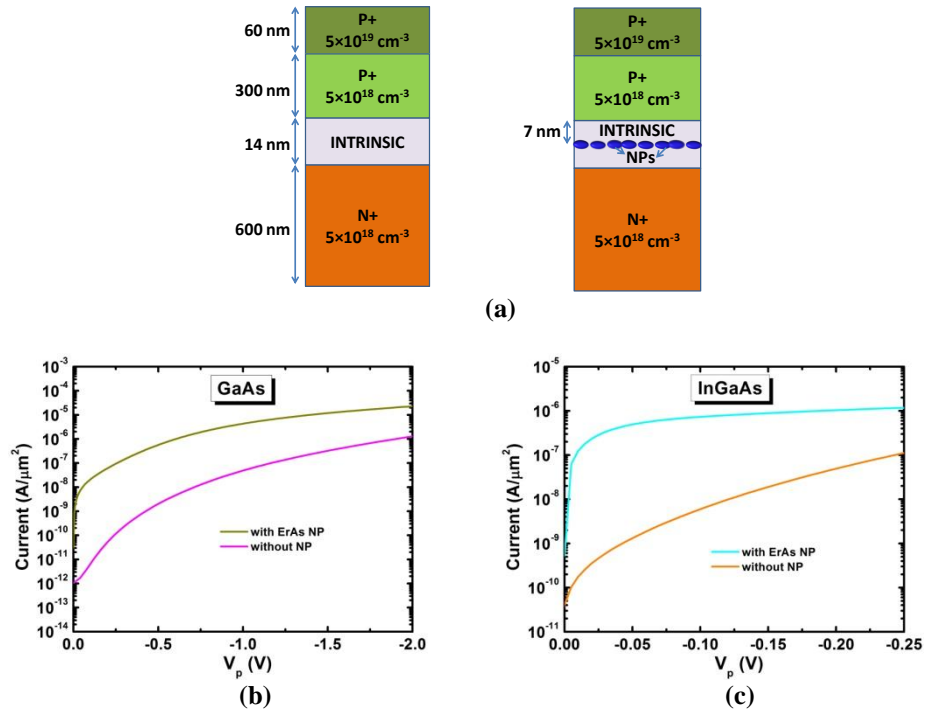


Figure 3.21(a) Schematic diagram of fabricated P-I-N diodes without any NPs (left) as well as with semi-metallic ErAs NPs at the middle of the I-region (right), showing the dimensions and doping concentration of the respective regions. **(b)** Comparison of measured current in GaAs P-I-N diodes without and with ErAs NPs at room temperature. **(c)** Comparison of measured current in InGaAs P-I-N diodes without and with ErAs NPs at room temperature.

Figure 3.21(a) shows the dimensions and doping of the epitaxial layers grown on the substrate for both GaAs and InGaAs with and without the ErAs NPs. The reverse bias characteristics of the GaAs diode with and without the ErAs NPs is shown in **Figure 3.21(b)**. In this dissertation, we will focus on the reverse bias region as the TFETs operate under reverse bias where the current is dominated by BTBT. It is observed that incorporation of BTBT can lead to substantial increase in current compared to the standard case without the NPs. Though diode characteristics of GaAs

with and without NPs have been investigated in literature for photonic applications [153], the high bandgap of GaAs is not suitable for TFET applications due to lower current levels. Hence, low bandgap InGaAs is explored and the improvement in current due to insertion of ErAs NPs is studied. **Figure 3.21(c)** illustrates that ErAs NPs can lead to significant increase in current for InGaAs diodes as well, which is promising for TFET applications.

The temperature dependence of the reverse biased current is explored in **Figure 3.22**. It is observed from **Figure 3.22(a)** that the current increases with temperature for InGaAs diode having ErAs, indicating thermally assisted tunneling. In **Figure 3.22(b)**, the reverse bias current of InGaAs diode with ErAs NPs is compared to that without the NPs at a low temperature of 3K, where thermally assisted tunneling is negligible. Substantial increase in current is observed even at a low temperature of 3K, due to ErAs NPs compared to that without the NPs. This proves that the current improvement does not come mainly from the thermally assisted tunneling but the two step tunneling process plays a significant role in increasing the tunneling probability. However, thermally assisted tunneling can degrade the subthreshold swing of TFET. Hence, it is necessary to reduce the surface scatterings at the interface of NPs with the semiconductor to suppress carrier thermalization so that the non-equilibrium carrier distribution at the NPs remain below the thermal limit.

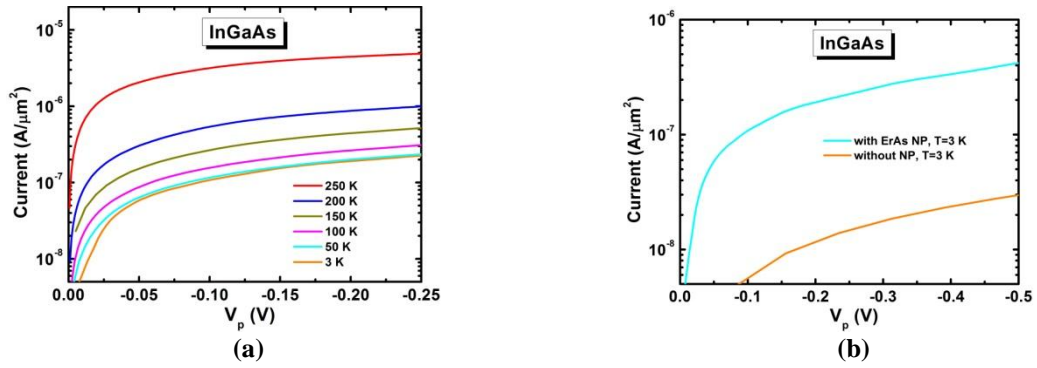


Figure 3.22(a) Measured current in a InGaAs P-I-N diode with ErAs NPs for different temperatures. **(b)** Comparison of measured current in InGaAs P-I-N diodes without and with ErAs NPs at a temperature of 3 K.

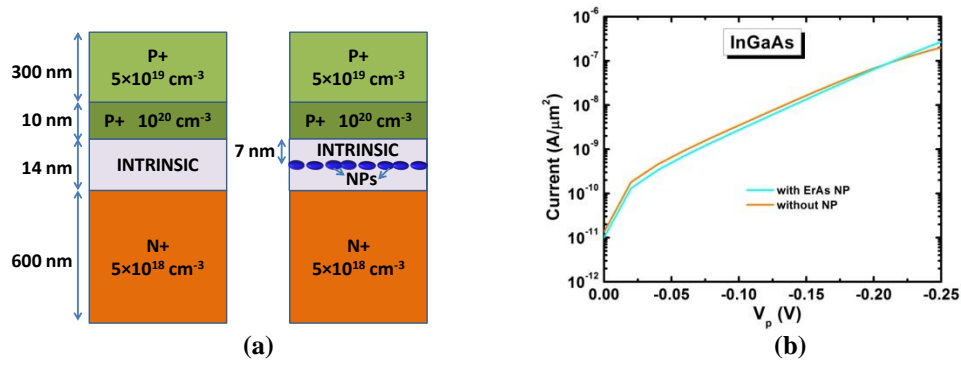


Figure 3.23(a) Schematic diagram of fabricated P-I-N diodes without any NPs (left) as well as with semi-metallic ErAs NPs at the middle of the I-region (right), showing the dimensions and doping concentration of the respective regions. The doping concentration of P region near the intrinsic region is increased compared to that in Figure 3.21(a). **(b)** Comparison of measured current in InGaAs P-I-N diodes without and with ErAs NPs at room temperature for structures shown in (a).

The effect of increasing the doping concentration is investigated in **Figure 3.23**. To mimic source of N-type TFET with very high doping, the P region is highly doped to about 10^{20} cm^{-3} near the interface with I-region as shown in **Figure 3.23(a)**. Strangely, no change in current is observed with and without ErAs NPs for this doping scheme (**Figure 3.23(b)**). This is because, with the increase in doping concentration there is significant diffusion of dopants in the I-region which goes below the region where NPs are inserted. So, due to the diffusion of atoms, the NPs

are effectively located at the P region and not at the I-region between P and N regions where band bending occurs. Thus, the NPs do not influence the tunneling probability or the current.

Apart from ErAs, the effect of ScAs NPs incorporated into the InGaAs diodes was also studied. **Figure 3.24** shows the comparison of reverse bias current for InGaAs diode without any NPs, with ErAs NPs and with ScAs NPs. The diode dimensions and doping are similar to that shown in **Figure 3.21(a)**. It is observed that incorporation of ScAs NPs can lead to even higher increase in current (compared to the current in diode without the NPs) than that obtained in case of ErAs NPs. Probable reasons could be pinning of fermi level more towards the mid-gap which can lead to higher current as explained above in the theoretical section [150] or lower interfacial scattering for ScAs NPs.

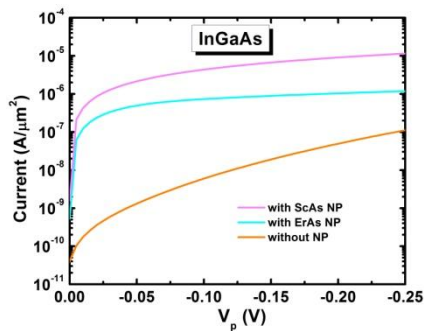


Figure 3.24. Comparison of measured current in InGaAs P-I-N diodes without any NPs, with ErAs NPs and with ScAs NPs at room temperature for structures shown in Figure 3.21(a).

3.4. Summary

In this chapter, we discussed the two fundamentally different carrier transport mechanisms which can lead to sub-thermionic subthreshold swing as well as require less disruptive technologies, namely the impact ionization and band-to-band tunneling. A novel impact ionization MOS (I-MOS) is proposed which can lead to significant reduction in the breakdown voltage. However, the I-MOS suffers from reliability issues. Hence, as an alternative, Tunnel-FETs are studied and in-depth understanding of band-to-band tunneling is provided. Analytical formula for potential profile in the Tunnel-FETs, tunneling probability and tunneling current are derived which can provide physical insights. At the same time, a novel methodology based on Non-Equilibrium Green's Function Formalism, for efficient numerical simulation is also developed. Finally, for improving the performance of Tunnel-FETs a novel strategy of incorporation of metallic/semi-metallic nanoparticles in the tunnel junction is theoretically explored and experimentally demonstrated.

Chapter 4: Beyond Low Power Computation

4.1. Introduction

In previous chapters, we discussed that the use of 2D materials can lead to excellent device electrostatics while implementation of novel carrier transport technology can provide steep sub-thermionic turn-ON characteristics, both of these attributes being highly advantageous for ultra-dense low-power electronic computational elements. In this chapter, we will show that, beyond low power computation, these attributes can revolutionize a diverse arena of gas/bio-sensing technology. Sensors, specially, biosensors are indispensable for modern society due to their wide applications (**Figure 4.1**) in public healthcare, national and homeland security, forensic industries as well as environmental protection. There is a great demand for ultra sensitive biosensors which can detect biomolecules with high reliability and specificity in complex environment such as whole blood. Moreover, detection ability at low biomolecule concentration is necessary for screening many cancers [158], neurological disorders [159], [160] and early stage infections [161] such as HIV.

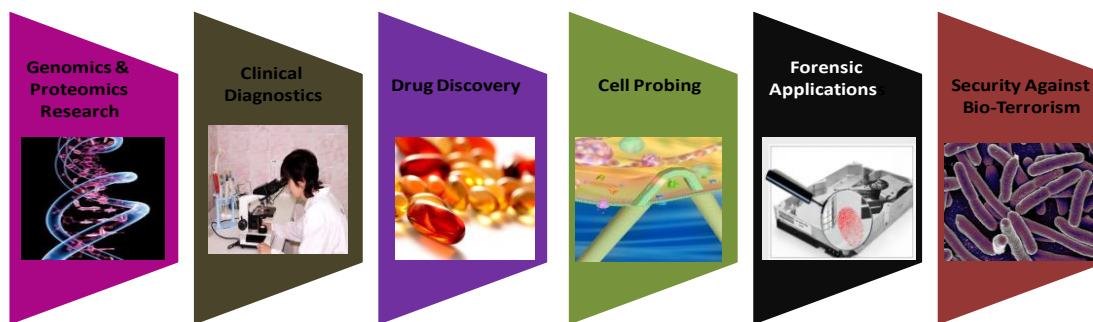


Figure 4.1. The various applications of a biosensor emphasizing its significance to modern society

Currently, Enzyme-linked immunosorbent assay (ELISA) based on optical sensing technology is widely used as a medical diagnostic tool as well as a quality-control check in various industries. For ELISA the labeling of biomolecules is needed, which might alter the target-receptor interaction by conformation change. Moreover, ELISA requires the use of bulky, expensive optical instruments and hence, is not suitable for fast point-of-care clinical applications. On the other hand, the biosensors based on field-effect-transistors (FETs) [4], [162]–[165] are highly attractive as they promise real-time label-free electrical detection, scalability, inexpensive mass production, and possibility of on-chip integration of both sensor and measurement systems (**Figure 4.2**). In a conventional FET used for digital computational applications, two electrodes (source and drain) are used to connect a semiconductor material (channel). Current flowing through the channel between the source and drain is modulated by a third electrode called the gate, which is capacitively coupled through a dielectric layer covering the channel region. In the case of an FET biosensor, the physical gate present in a logic transistor is removed and the dielectric layer is functionalized with specific receptors for selectively

capturing the desired target biomolecules. The charged biomolecules when captured produce a *gating effect*, which is transduced into a readable signal in the form of change in electrical characteristics of the FET such as drain-to-source current or channel conductance. In this chapter, we first demonstrate the huge potential of 2D semiconducting materials for sensing[4] and then we show that use of steep turn-on characteristics can make possible the realization of ultra-sensitive and fast sensors.[146]

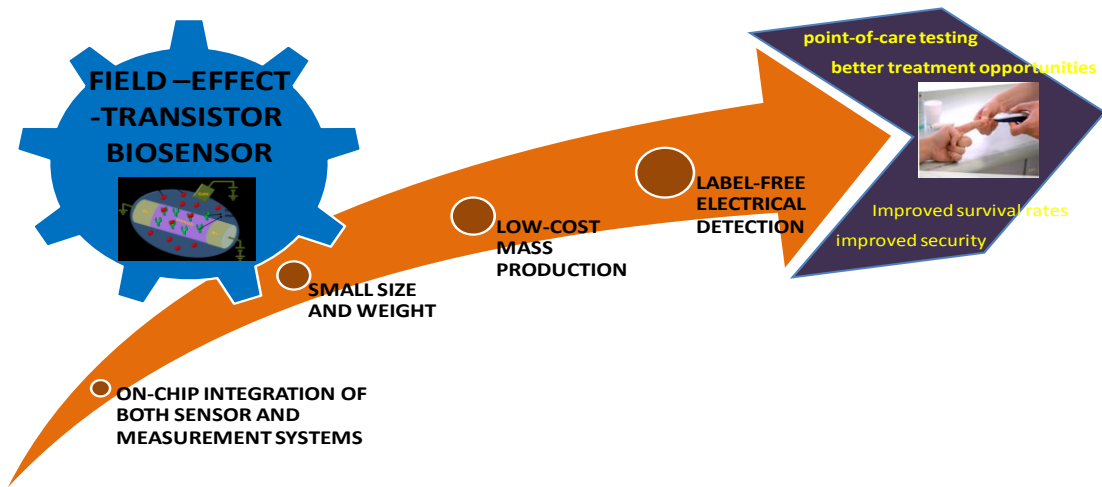


Figure 4.2 Schematic showing the potential of biosensors based on Field-Effect-Transistors.

4.2. 2D Material for Sensing

4.2.1. FET based Biosensor

Given the importance of FET biosensors, there has been a lot of work on identifying an appropriate channel material for the same. Among the various materials reported, nanostructured materials Carbon Nano-Tubes (CNTs) and Si-

Nanowires (NWs) have been found to be most attractive due to their size compatibility and ability to provide high sensitivity [165]–[167]. However, the same 1D nature that leads to efficient electrostatics and hence higher sensitivity, also leads to difficulty in fabrication thereby creating a major challenge for the success of 1D technologies. While the top down fabrication technique for 1D structures suffers from high cost and slow production rate [168], the bottom-up method faces severe integrability issue [166], [168], thus hampering the practical usability of such structures. The 2D materials, on the other hand, are highly promising as they can not only provide excellent electrostatics due to their atomically thin structures but also possess planar nature, which is amenable to large-scale integrated device processing and fabrication. It is worth noting that, thinning down of 3D materials such as Si, into 2D structures is not only fabrication-wise expensive but would also suffer severely due to interface defects and uncontrollable bandgap variation when scaled down. Hence, naturally 2D layered materials are desirable leading to interest in graphene based FET biosensors [166], [169]–[172]. However, we show here that the lack of a bandgap in graphene fundamentally limits its sensitivity. In this work, we bring forward the tremendous potential of MoS₂, which is a biocompatible material [173], as the channel material in label-free FET biosensors (**Figure 4.3(a)**). [4] As discussed in Chapter 2, MoS₂ belongs to the class of Transition-Metal-Dichalcogenides (TMDs), which consist of 2D stacked layers of covalently bonded transition metal and dichalcogenide atoms arranged in a hexagonal lattice where adjacent layers are held together by relatively weak Van der Waal's forces. Due to this weak inter-layer

bonding in TMDs, it is possible to obtain atomically thin films with pristine interfaces, a monolayer of MoS₂ being only around 0.65 nm thick. While MoS₂ based photodetectors[174], fluorogenic nanoprobe [175], gas detectors [176], chemical sensors[177] and electrodes for electrochemical sensing[178] have been reported in literature, this work represents the first demonstration of MoS₂ (for that matter any TMD) based FET biosensors working in aqueous environment and in subthreshold region, which is capable of ultra-sensitive and specific detection of biomolecules.[4] We demonstrate that the proposed biosensor achieves excellent sensitivity for pH sensing as well as biomolecule detection. Also, MoS₂ has pristine surfaces (without out-of-plane dangling bonds), which reduces surface roughness scattering and interface traps. This results in low density of interface states on the semiconductor-dielectric interface, which can not only lead to better electrostatic control but also reduction in low frequency (flicker) noise, which is one of the main sources of noise in FET biosensors [179]. In addition, we show through rigorous theoretical calculations that MoS₂ based biosensors can achieve ultimate scaling limits while retaining high sensitivity, which is useful for detection at low biomolecular concentrations as well as reduction in power and space requirements, crucial for achieving dense integrated structures. Furthermore, ultra-thin MoS₂ possesses transparency [180] as well as high flexibility and mechanical strength [181]. MoS₂ devices fabricated on transparent and flexible substrates can adapt to the curvilinear surfaces of human body and thereby hold great promise for wearable and implantable biosensor devices.

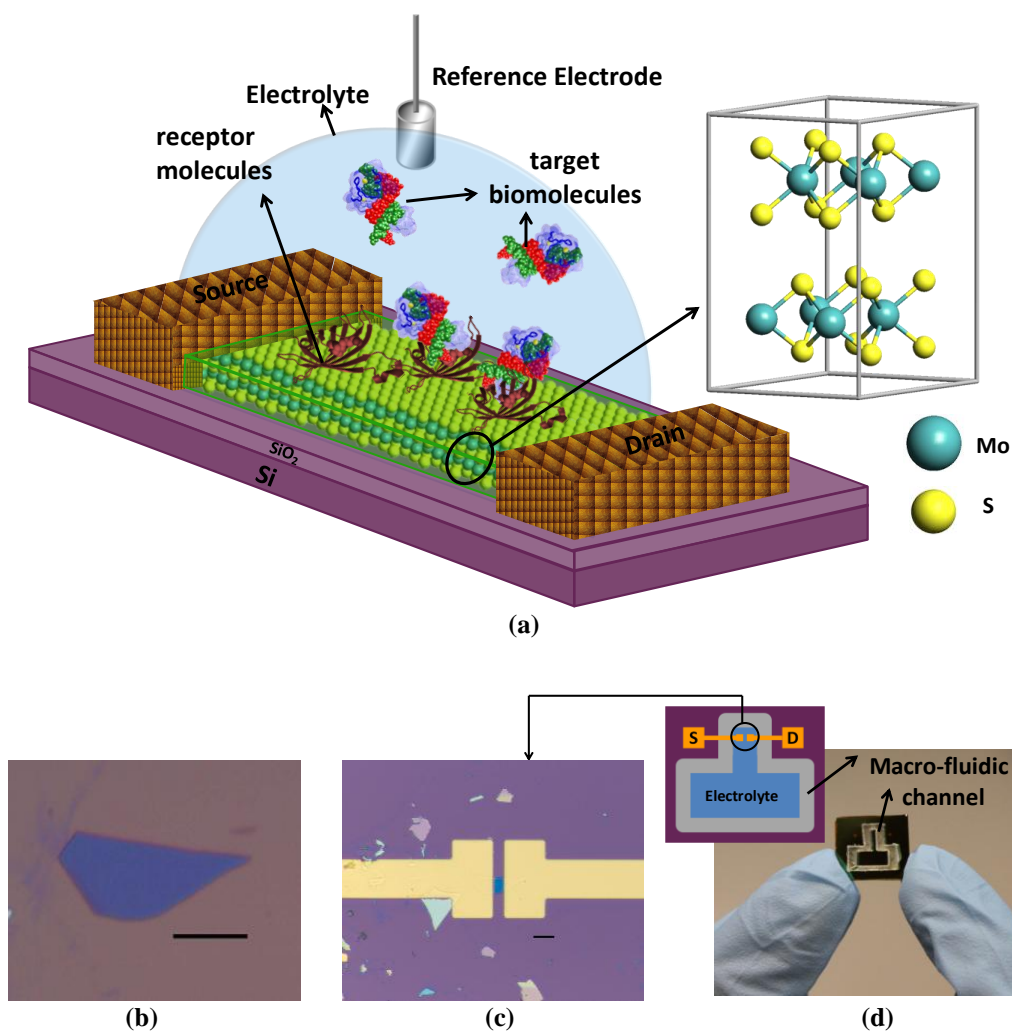


Figure 4.3(a) Schematic diagram of MoS₂ based FET biosensor. For biosensing, the dielectric layer covering the MoS₂ channel is functionalized with receptors for specifically capturing the target biomolecules. The charged biomolecules after being captured, induce gating effect, modulating the device current. An electrolyte gate in the form of Ag/AgCl reference electrode is used for applying bias to the electrolyte. The source and drain contacts are also covered with a dielectric layer to protect them from the electrolyte (not shown in this figure). (b) Optical image of MoS₂ flake on 270 nm SiO₂ grown on degenerately doped Si substrates. Scale bar, 10 μm. (c) Optical image of the MoS₂ FET biosensor device showing the extended electrodes made of Ti/Au. Scale bar, 10 μm. (d) Image and schematic diagram (inset figure) of the chip with the biosensor device and macrofluidic channel for containing the electrolyte. Inlet and outlet pipe for transferring the fluid and the reference electrode is not shown in the figure.

Note on Transduction Mechanism And Sensor Performance

It is well known that if the bare FET channel is in contact with the electrolyte, direct absorption of biomolecules can lead to non-specificity [168], [182]. To achieve specificity, so that the non-specific biomolecules cannot directly get absorbed on the channel, the channel should have an *effective layer i.e.*, it should either be directly functionalized with specific groups/linker/receptors [183]–[186] or covered with dielectric/ lipid/polymer [165], [187], [188] *etc.*, which enable functionalization. This is necessary even for pH sensing in case of graphene, CNTs or TMDs as pH sensing on bare sensor surface, is dependent on defects and this will lead to large variation in response depending on the presence/absence or density of defect sites [189]. Moreover, a defect less surface is desirable to avoid unwanted effects such as scattering.

Furthermore, transduction mechanism is complicated in case of bare channel surface and can be a combination of different effects including 1) electrostatic gating, 2) direct charge transfer, and 3) mobility modulation [182], [190]. It is worthwhile to mention here, that the source/drain metal electrodes should be passivated to avoid the issue of the biomolecules getting adsorbed directly on the electrodes changing the local work function of the metal and hence the contact resistance [190], [191].

Now, an unambiguous transduction mechanism is desirable for advancement of FET biosensor technology. The essence of biosensors based on field effect transistors, as the name suggests, is that transduction occurs through field effect, *i.e.*, through electrostatic control of the channel through the charge induced either by biomolecules

or pH change. As long as an unambiguous transduction mechanism of field-effect is achieved, (now the effect can take place through any effective layer be it oxide, lipids, polymer, linker/receptor layers or any other groups), the parameters that will dictate the sensitivity of the FET biosensor are the shift of potential on the effective layer (which mainly depends on the properties of effective layer like density of sites, type and concentration of biomolecules, ionic concentration and pH of solution etc) and how the shift of potential can change the current (which depends on the effective layer as well as the channel material).

Thus, while the biosensing will be affected by various factors (properties of effective layer, biomolecules and solution), this work focuses on the way channel material will affect the biosensor performance. In this work, we tried to bring forward the potential of MoS₂ as channel material and used one of the possible effective layers *i.e.*, covering the MoS₂ using HfO₂ and demonstrated excellent sensitivity. HfO₂ layer also helps to provide near-ideal change in surface potential with change in pH for a wide pH range as demonstrated in the dissertation. Moreover, using HfO₂ as effective layer allows taking leverage of the vast body of literature that exists on the functionalization of oxides. Nevertheless, other effective layers and functionalization methods (such as direct functionalization on MoS₂ surface using chelating agents [192], different dielectric layers, or functionalization using polymers etc) can also be tried in future. While, using different effective layers can lead to different numerical values of sensitivity but as long as the transduction mechanism occurs unambiguously through field effect (which is desirable, and the essence of field effect transistors),

this does not affect the fundamental conclusions of the chapter with regards to evaluation of the channel material.

Biosensor Characterization

The micromechanical exfoliation technique which has been widely employed for prototyping experiments on various 2D materials [3][63], has been used to obtain the MoS₂ flakes (**Figure 4.3(b)**). The devices (**Figure 4.3(c)**) were fabricated on 270 nm SiO₂/Si substrates with 60nm/100nm Ti/Au as source and drain metal contacts and 30-35 nm of high-k dielectric Hafnium oxide (HfO₂) as gate dielectric. The source and drain contacts are passivated with dielectric layer to protect them from the electrolyte. A fluidic channel (**Figure 4.3(d)**) for containing the electrolyte is fabricated using acrylic sheet. An Ag/AgCl reference electrode, referred to as the electrolyte gate, is used to apply bias to the electrolyte, which is necessary for the stable operation as well as for controlling the operation regime of the biosensor [146].

First the electrical characterization of the devices are carried out in dry environment by measuring the transfer characteristics as a function of drain and back gate voltages (the highly doped Si and the 270 nm SiO₂ act as the back gate and the gate dielectric respectively) illustrating n-type FET characteristics (**Figure 4.4(a)** and **(b)**). High back gate voltage is required to turn on the device due to the presence of very thick back gate oxide. For biosensing applications, it is necessary that the devices are able to operate in wet environment. Hence, the devices were measured in wet environment by transferring electrolyte solution to the fluidic channel. **Figure 4.4(c)** and **(d)** illustrates that efficient control of the proposed biosensor device is

possible in the wet environment with the successful demonstration of electrolytic top gating on MoS₂ channel.

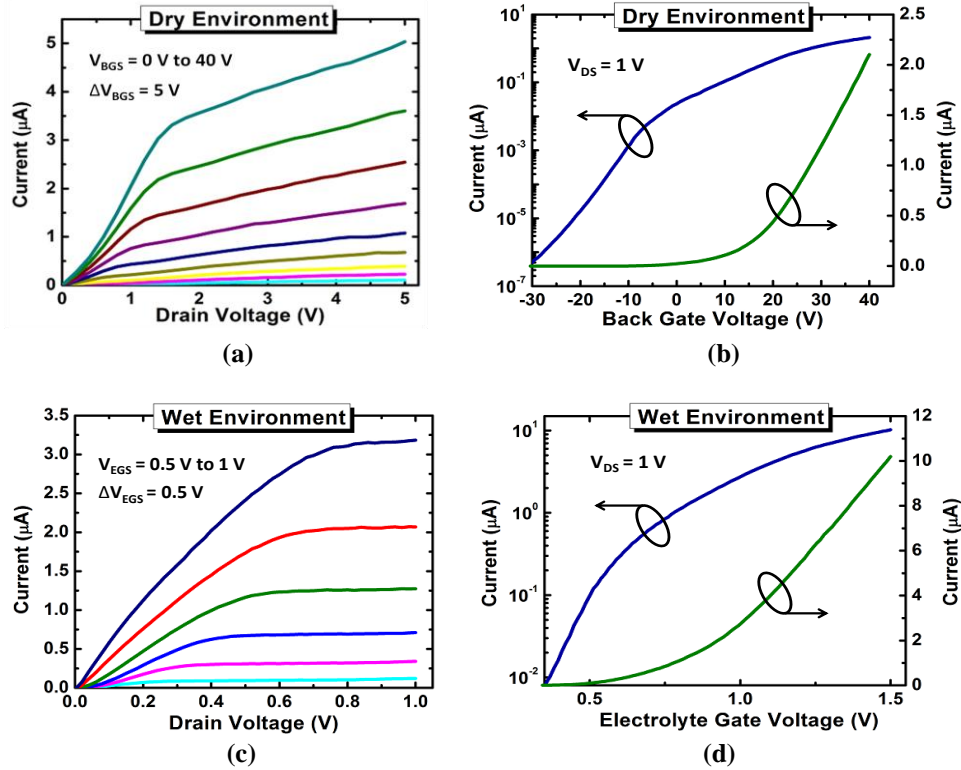


Figure 4.4(a) Drain current as a function of drain voltage with the back gate voltage (V_{BGS}) varying from 0 V to 40 V in steps of 5 V. The thickness of the MoS₂ used is 5 nm. (b) Drain current *versus* back gate voltage with drain voltage fixed at 1V. Left axis shows current in logarithmic scale while right axis shows that in linear scale. (c) Drain current as a function of drain voltage with the back gate voltage floating and electrolyte gate voltage (V_{EGS}) varying from 0.5 V to 1 V in steps of 0.5 V with observation of robust current saturation. The electrolyte used is 0.01X PBS solution. (d) Drain current *versus* electrolyte gate voltage with drain voltage fixed at 1V.

pH Sensing

The operation of MoS₂ biosensor is first demonstrated for the case of detection of pH changes of the electrolytic solution. The pH sensing is based on the protonation/deprotonation of the OH groups on the gate dielectric (**Figure 4.5(a)**) depending on the pH value of the electrolyte, thereby changing the dielectric surface

charge. This pH dependent surface charge together with the electrolyte gate voltage applied through the reference electrode determines the effective surface potential of the dielectric. The drain current as a function of the electrolyte gate voltage for different pH values of the electrolyte is shown in **Figure 4.5(b)**. A significant increase in current is obtained at a particular applied bias with decrease in pH value (or higher positive charge on the dielectric surface that causes lowering of the threshold voltage of the FET) leading to the successful demonstration of MoS₂ pH sensor.

The shift in threshold voltage (which has been calculated using the extrapolation in the saturation region (ESR) method [193]) is found be 59mV/pH. This threshold voltage shift can be understood from the following discussion. The change in surface potential on dielectric with change in pH of the electrolyte can be written as [194]

$$\frac{d\phi_s}{dpH} = -2.3\alpha \frac{k_B T}{q} \quad (4.1a)$$

$$\alpha = \left(2.3 \frac{k_B T}{q^2} \frac{C_S}{\beta_S} + 1 \right)^{-1} \quad (4.1b)$$

where ϕ_s : surface potential on the gate dielectric, k_B : Boltzmann constant, T : temperature, q : electronic charge, C_S : electrical surface capacitance and β_S : intrinsic buffer capacity which depends on the number of sites on the dielectric per unit area (which can be either protonated, de-protonated or neutral) as well as the dissociation constants. The ideal change in surface potential that can be obtained is 59.6 mV/pH at

300K when α approaches 1. When the intrinsic buffer capacity of the dielectric surface is high, α can reduce to 1 leading to almost ideal response, which has been shown to be the case for HfO_2 [195]. This has also been confirmed by our investigations.

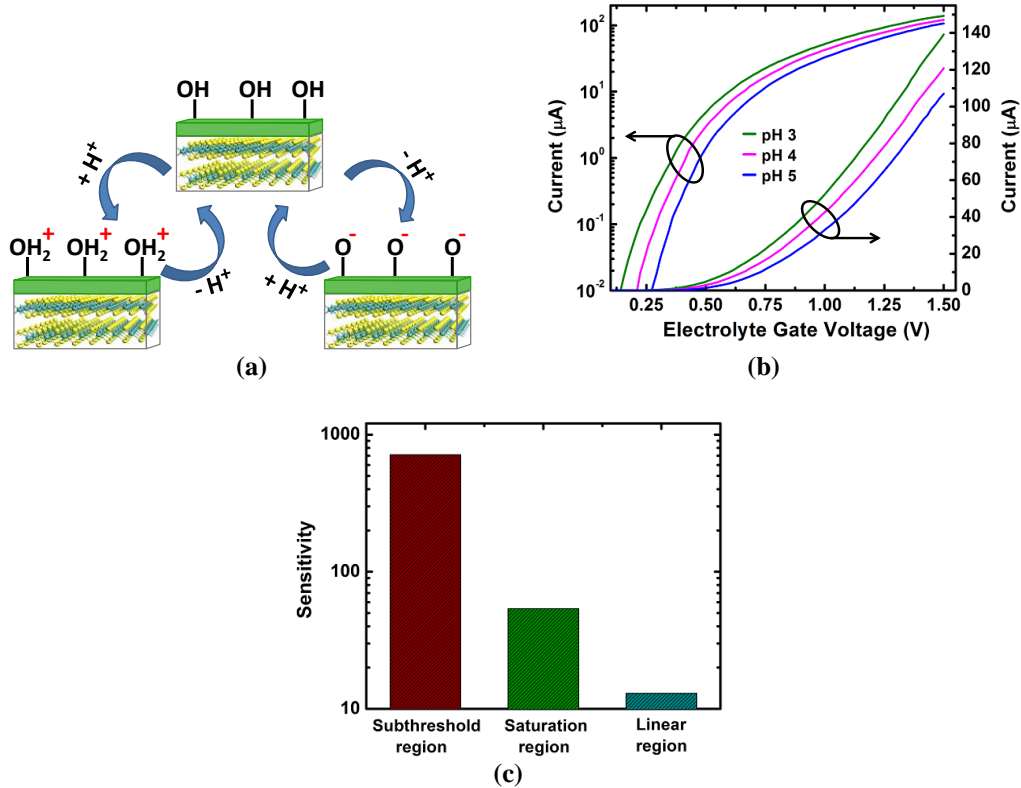


Figure 4.5(a) Illustration of the principle of pH sensing. At lower pH (higher concentration of H^+ ions), the OH group on the dielectric surface gets protonated to form OH_2^+ leading to a positive surface charge on the dielectric while at higher pH, the OH group gets deprotonated to form O^- leading to a negative surface charge on the dielectric. **(b)** Drain current for an n-type MoS_2 FET based pH sensor is plotted as a function of electrolyte gate voltage for three different pH values of the solution. The thickness of the MoS_2 used is around 2 nm and the SS obtained is around 78mV/decade. Decrease in pH values lead to increase in device current consistent with higher positive charge at lower pH and n-type behavior of the FET biosensor. **(c)** Comparison of sensitivity in subthreshold, saturation and linear region for a pH change of 4 to 5 of the electrolyte solution derived from the I_d - V_g curves shown in (b). Subthreshold region shows substantially higher sensitivity of 713 while the saturation and linear regions exhibit much lower sensitivities of 53.69 and 12.96 respectively.

Sensitivity for pH sensing (defined as $S_{n_pH} = (I_{pH2} - I_{pH1}) / I_{pH1} * 100$, where I_{pH1} and I_{pH2} are the values of current at two different pH of the electrolyte, $pH1$ and $pH2$ respectively, where $pH1 > pH2$) is deduced from the curves in subthreshold, saturation and linear regions. **Figure 4.5(c)** shows the comparison of pH sensitivity in these three different regions. In the subthreshold region the drain current has exponential dependence on the gate dielectric surface potential, while in saturation and linear region the relationship is quadratic and linear, respectively. Hence the sensitivity in the subthreshold region is much higher compared to those in the saturation and linear region [146], [196]. Sensitivity values as high as 697 and 713 are obtained for pH change from 3 to 4 and 4 to 5, respectively. The critical parameter of an FET, which gives indication of the efficiency of gating effect and hence, the sensitivity of the biosensor is the subthreshold swing (SS) [146]. SS , as discussed in Chapter 1, is given by the inverse of the slope of their $\log_{10}(I_D)$ - V_{GS} curve where I_D and V_{GS} are the drain-to-source current and gate-to-source voltage, respectively. Therefore, the SS of a device essentially indicates the change in gate voltage required to change the subthreshold current by one decade ($SS = dV_{GS} / d(\log_{10}(I_D))$). Thus, smaller the SS , higher will be the change in current for a particular change in the dielectric surface potential due to gating effect produced by the pH change or attachment of biomolecules and hence, higher the sensitivity. The dependence of sensitivity (S_n) on SS is given by [146]

$$S_n = 10 \left[\int_{\phi_i}^{\phi_f} \frac{1}{SS} d\phi \right] - 1 \quad (4.2)$$

which depicts the exponential dependence of sensitivity on SS where ϕ_i and ϕ_f denote the initial and final surface potential on the gate dielectric before and after attachment of the target biomolecules. In **Figure 4.6** we have plotted the sensitivity as a function of SS , which clearly illustrates that by lowering the SS of a device, sensitivity can be increased substantially.

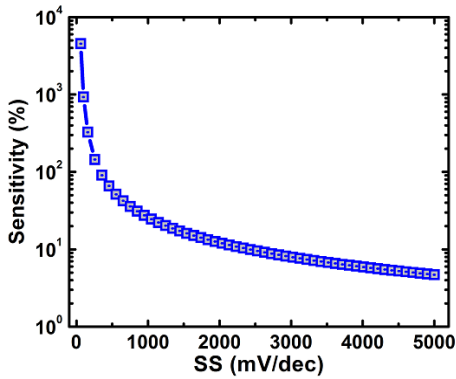


Figure 4.6. Sensitivity as a function of the subthreshold swing (SS) showing that sensitivity increases exponentially with the reduction of SS .

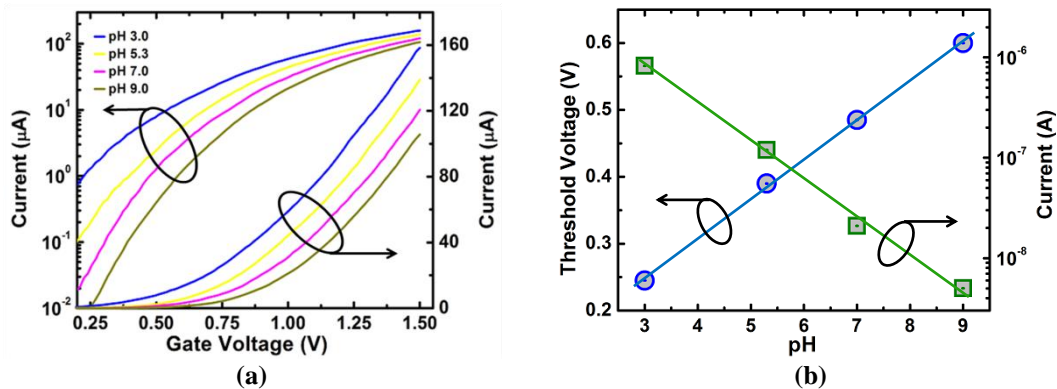


Figure 4.7(a) Drain current for an n-type MoS_2 FET based pH sensor as a function of electrolyte gate voltage for different pH values of the solution. Left axis shows current in logarithmic scale while the right axis shows that in linear scale. **(b)** Change in threshold voltage and current of the MoS_2 FET for a wide range of pH (3-9). Left axis shows the threshold voltages while right axis corresponds to the current in the subthreshold region. The thickness of the MoS_2 used is around 15 nm. The subthreshold swing of the device was found to be around 208 mV/decade.

The ultra-thin nature of MoS₂ and its pristine interfaces lead to excellent *SS* and hence high sensitivity of the proposed device in spite of presence of very thick gate dielectric (30 nm). In **Figure 4.7(a)** and **(b)** we show the current as well as threshold voltages for a large pH range (3-9). From our measurements, the shift in threshold voltage (59 mV/pH) is linear over the wide pH range (3-9) as is clear from **Figure 4.7(b)**.

Specific Detection of Biomolecules

Next, the specific sensing of biomolecules using the MoS₂ biosensor is investigated through the well-known biotin-streptavidin interaction where the biotin and streptavidin act as models for receptor and target molecules, respectively. **Figure 4.8(a)** shows that a device functionalized with biotin exhibited substantial decrease in current on addition of streptavidin solution compared to that measured in pure buffer without streptavidin. This is in agreement with the negative charge of the streptavidin, as the pH of the solution (0.01X PBS) used is greater than the *isoelectric point* (abbreviated as pI and defined for a particular molecule as the pH at which that molecule is neutral) of streptavidin. Addition of pure buffer again caused negligible

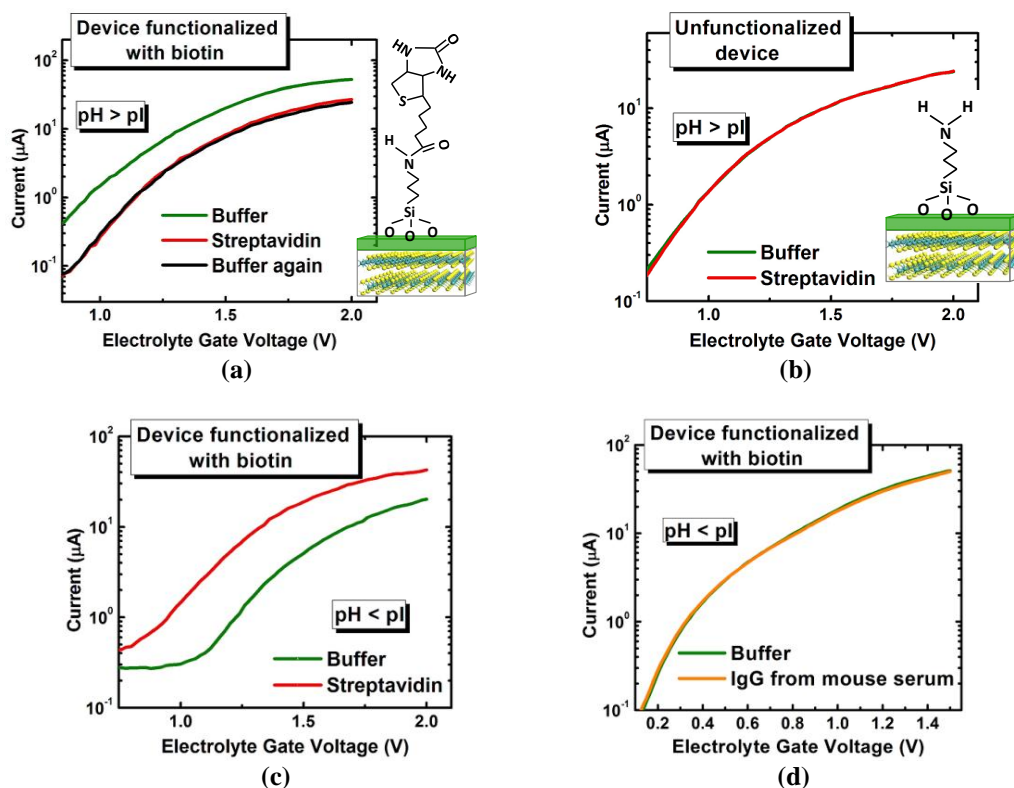


Figure 4.8(a) Device functionalized with biotin (as shown by schematic diagram) was first measured in pure buffer (0.01X PBS) as shown by the green curve. Addition of streptavidin solution (10 μM in 0.01X PBS) leads to decrease in current (red curve) due to the negative charge of the protein as pH of solution is more than the pI of streptavidin. The device is then measured again in pure buffer leading to no significant change (black curve). **(b)** An unfunctionalized device (device with only 3-Aminopropyl triethoxysilane (APTES) attached to it but not functionalized with biotin), as shown by the schematic diagram exhibit similar current in pure buffer and streptavidin solution (solutions used are same as in (a)) confirming that there are no false signals. **(c)** Addition of streptavidin solution (10 μM) at a pH of 4.75, which is less than the pI of streptavidin, leads to increase in current consistent with the positive charge of the protein. **(d)** Addition of IgG (56 $\mu\text{g/ml}$) at pH of 4.75 (which is smaller than the pI of IgG), leads to negligible change in device current as IgG is not specific for biotin.

change in current consistent with the strong binding between biotin and streptavidin.

To rule out the possibility of non-specific interactions and false signals, a number of control experiments are carried out. First, an unfunctionalized device exhibited similar current levels in pure buffer and streptavidin solution (**Figure 4.8(b)**) indicating absence of false signals. Second, a lower value of pH ($< \text{pI}$ of streptavidin and thereby attributing positive charge to it) was used, and it is observed that the

addition of streptavidin solution to a device functionalized with biotin leads to an increase in current compared to that in pure buffer (**Figure 4.8(c)**). In yet another experiment, a device functionalized with biotin did not result in current change (**Figure 4.8(c)**) on addition of immuno-globulin G (IgG) which is not specific for biotin, confirming the absence of non-specific bindings.

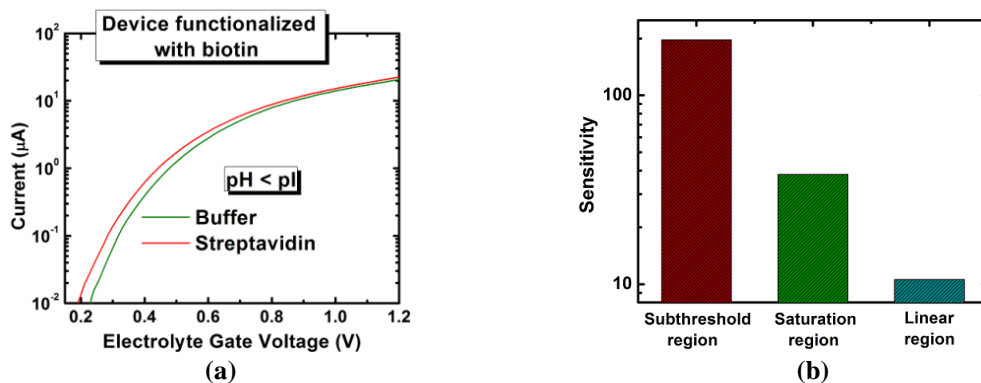


Figure 4.9(a) High sensitivity of the MoS₂ biosensor device is illustrated for quad-layer MoS₂ (around 2.7 nm thick) as significant increase in current is obtained on addition of streptavidin solution (100 fM) at pH 3. **(b)** Comparison of sensitivities in the subthreshold, saturation and linear region showing that subthreshold region has substantially higher sensitivity.

All the above experiments were done with comparatively thicker MoS₂ flakes, which are relatively easier to locate optically on the substrate. In order to obtain improved *SS* and hence, sensitivity, ultra-thin layer MoS₂ consisting of only 4 atomic layers was explored (**Figure 4.9(a)** and **(b)**). An excellent *SS* of 90 mV/dec was obtained even with very thick dielectric layer (35 nm). Sensitivity (defined as the ratio of difference in current before and after biomolecule binding to the lower of the two currents) as high as 196 was achieved in the subthreshold region for streptavidin solution of 100 fM. Similar to case for pH sensing, sensitivity in the subthreshold

region is significantly higher compared to those in the saturation and linear regions (**Figure 4.9(b)**).

Note that, while in this work, we demonstrated the specific detection of biomolecules using streptavidin and biotin as examples of target and receptor molecules, respectively, the proposed biosensor can be used for selective sensing of other biomolecules as well. For this purpose, functionalization of the gate dielectric surface with respective specific receptors can be realized taking leverage of the vast body of literature that exists on the functionalization of oxides as well as semiconducting surfaces [197], [198]. Also, in our experiments we have used biomolecules in PBS solution which is a standard procedure used for demonstrating the operation of FET based biosensors [196], [199]. It is to be noted that detection of biomolecules from whole blood using FET biosensors has already been demonstrated using a microfluidic purification chip [200]. This technique is independent of channel material and can also be extended to the MoS₂ based FET biosensor for detection of biomolecules in the complex environment of whole blood.

Scalability and Single Molecule Detection Analysis

It is of particular interest in biosensing to detect biomolecules at very low concentrations, specially a biosensor which can detect down to a single molecule is highly desirable. Low concentration detection (LCD) is dependent on various factors including the site density on effective layer, type of biomolecule, sensor area, analyte mass transport in the solution *etc.* Since in this section, we are focusing on the channel material, we discuss the way in which the channel material will impact the

LCD. The channel material will be evaluated in terms of LCD through the criteria whether a few or in the most desired case a single biomolecule attached to the effective layer, can cause measurable change in the current. In case of graphene it has been shown that single gas molecules can be detected [201]. However, in this case the gas molecules dope the graphene by getting directly absorbed into it which as discussed earlier leads to non-specificity and is not desirable for biosensors. To achieve specificity, an effective layer is necessary (as discussed above) and the fundamental limitations of graphene for electrostatic modulation of current through effective layer is discussed in the next section. Single biomolecule detection has been reported using CNTs where the transduction mechanisms involve bridging gap in the channel [202] or modulation of scattering [203] and not electrostatic field effect. The limitations of CNTs for practical usability has been discussed earlier and in addition creating gaps in CNTs requires complex processing and leads to low yield [202], which upset the advantages of using FET platform. Detection of single virus with a Si NW FET [204] and single bacterium using graphene [205] have been demonstrated. Viruses (around 100 nm) and bacteria (several micrometers) are typically of larger size. For detection of a single entity of smaller biomolecules such as DNA or small proteins (< 10 nm) with high sensitivity using a FET biosensor, aggressive downscaling of device dimensions is required as shown through theoretical analysis presented below. A simple yet effective theoretical model is developed to understand the effect of dimensionality on sensitivity. In the model we consider a small biomolecule with impact dimension of 5 nm, placed at the centre of the channel on

top of the gate dielectric of an SOI FET (without the physical gate). For the simulations, this biomolecule is represented by a uniform surface charge distribution over the impact dimension. This representation has been validated through numerical solution of Poisson–Boltzmann [206].

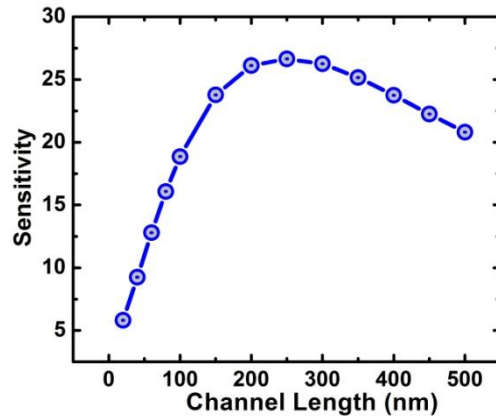


Figure 4.10. Sensitivity as a function of channel length for a biomolecule with impact dimension of 5 nm placed in the middle of the channel. The Si channel thickness is taken to be 20 nm. The dielectric used is 5 nm thick HfO_2 .

As observed from **Figure 4.10**, with the decrease in channel length, the sensitivity first increases. This is because the ratio of region that is influenced by the biomolecule to the total channel length increases. However, with further decrease in the channel length (beyond ~ 250 nm), the sensitivity begins to decrease. This is because the electric field from the source/drain region begins to influence the channel potential at shorter channel lengths decreasing the effective influence of the biomolecule and hence the sensitivity. In order to maximize the sensitivity, it is desirable to make the channel length similar to that in which charge due to a biomolecule affects (we call it the *impact-dimension*) and at the same time it is

required that the influence of the source/drain electric fields on the channel is minimal and that the channel is mainly controlled through the *gating effect*. A parameter that indicates the efficiency of gate control is the natural length scale (λ) [1], which is a function of the permittivity and thickness of the gate dielectric as well as those of the semiconducting channel. In general, to ensure that the channel is controlled mainly by the gate it is necessary that λ is 5-10 times smaller than the channel length (L_g) [2]. Expressions for λ for SOI structure and nanowire are given by equation (4.3a) and (4.3b) respectively.

$$\lambda_{SOI} = \sqrt{\frac{\epsilon_s}{\epsilon_d} t_d t_s} \quad (4.3a)$$

$$\lambda_{NW} = \sqrt{\frac{\epsilon_s r_{NW}^2 \ln(1+t_d/r_{NW})}{2\epsilon_d}} \quad (4.3b)$$

where ϵ_d and ϵ_s are the permittivity of the gate dielectric and the semiconducting channel respectively, t_d and t_s are the thickness of the gate dielectric and the semiconducting channel (for the SOI structure) respectively. r_{NW} is the radius of the nanowire. Now, for example, taking the parameters of Silicon as the semiconducting channel and 3 nm HfO₂ as the gate dielectric, and considering $\lambda = L_g/5$, in order to maximize sensitivity for a single biomolecule with 5 nm impact dimension, an SOI structure with silicon channel thickness of 0.69 nm or alternatively a nanowire structure with radius of about 2.2 nm is required. To achieve such small dimensions with Si, highly complex processing techniques will be required. Moreover, the interface roughness at such ultra-thin dimensions will pose to be a major issue. Now,

taking the parameters of MoS₂ and the same dielectric, the thickness of MoS₂ required is 1.225 nm, which is close to that of bilayer MoS₂. In fact, with MoS₂, even smaller thickness can be achieved easily since the thickness of a monolayer flake is ~0.65 nm. Due to the layered structure of MoS₂, ultra-thin layers can be easily obtained. In addition, the layered structure also leads to pristine interfaces. Thus, MoS₂ can achieve the ultimate scaling limits, which can not only maximize the sensitivity for detection of single biomolecules but also lead to reduction in power and space requirements.

Currently the TMD technology is at an early phase and still undergoing development. Scaling down of the gate dielectric thickness remains to be achieved and the dielectric thickness used in this work is around 35 nm. In order to realistically determine the true potential of MoS₂ for single molecule detection, such that its performance is not screened by the thick dielectric layer, rigorous quantum mechanical simulations based on Non-Equilibrium Green's Function Formalism [148] are performed to obtain the Local Density of States as a function of applied biases (**Figure 4.11(a)**) and hence, the current (**Figure 4.11(b)**). Thereby, it is shown that even at 5 nm channel length, MoS₂ can maintain excellent gate control over the channel leading to near ideal SS (**Figure 4.11(c)**), which is critical for obtaining high sensitivity. Thus, MoS₂ is highly advantageous for scaling down of FET biosensor devices, which can not only lead to higher sensitivity for detection of single quanta of biomolecular element especially when the entity is of smaller size but can also highly facilitate low-power (due to lower OFF-currents at low FET supply voltages) and

high density biosensor device architectures. The increase in response time associated with the analyte transport at low concentration (not associated with the channel material) could be addressed by methods for increasing total flux towards the sensor, for example, through application of electrostatic or magnetic fields[207], [208].

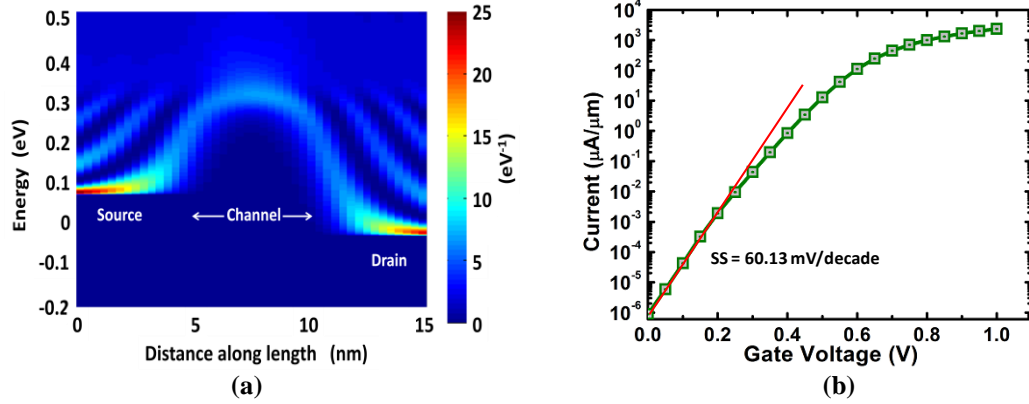


Figure 4.11. Numerical results of rigorous quantum mechanical simulations based on Non-Equilibrium Green's Function Formalism. **(a)** Local density of states (LDOS) diagram as a function of energy (y-axis) and distance along device length (x-axis) of a 4-layer MoS₂ device with 5 nm channel length, 3 nm HfO₂ as gate dielectric, at a drain voltage of 0.1V and gate voltage of 0.4V. The density-of-states (in eV⁻¹) are local in the sense that they vary with position. The structure of LDOS varies with applied biases and illustrates the band bending in the channel. **(b)** Drain-to-source current as a function of gate-to-source voltage. Almost perfect subthreshold swing of 60.13 mV/decade is obtained indicating highly efficient gate control even for an ultra-scaled device length.

Comparison with Graphene

In previous sections, we discussed the superiority of MoS₂ with 2D layered structure for FET based biosensing compared to other conventional materials or 1D structures. It might be expected that graphene, which is also a 2D layered material will share the same virtues as MoS₂. However, as discussed below, graphene suffers from fundamental constraints in sensitivity as well as detection limits. As discussed in Chapter 2, the zero bandgap of graphene leads to very high SS even though excellent electrostatics can be achieved due to its ultra-thin nature. As is evident from equation

(4.2), the high SS leads to low sensitivity. (It is to be noted that in case of low band gap materials, the term SS is used to denote the mathematical factor $dV_{GS}/d(\log_{10}(I_D))$ and not the swing in subthreshold region since the threshold voltage is not well defined due to high leakage).

Table-4.1

Graphene FET Biosensors	pH / Molecule Detected	Concentration	Sensitivity
Jnl. American Chem. Soc. 130, 14392-14393 (2008)	pH	2-4	≈ 3.77
Nano Letters 9, 3318-3322 (2009)	pH	4-5.1	≈ 12
Nano Letters 10, 1864-1868 (2010)	pH	6-7	≈ 14
Nano Letters 9, 3318-3322 (2009)	BSA	300 nM	≈ 0.363
Jnl. American Chem. Soc. 132, 18012-18013 (2010)	IgE	290 pM	≈ 0.436
Adv. Mater. 22, 1649-1653 (2010)	DNA	10 pM	≈ 15
Nanoscale, 4, 293 (2012)	DNA	100 nM	≈ 2
Nano Letters 12, 5082, 2012	amyl butyrate	400 fM	≈ 10
ACS Nano 4(6), 3201-3208 (2010)	dopamine	2 mM	≈ 0.75
ACS Nano 5(3), 1990-1994 (2011)	Ca ²⁺	10 μ M	≈ 11
ACS Nano 6(2), 1486-1493 (2012)	VEGF	100 fM	≈ 0.3

Sensitivity of graphene based FET biosensors measured in wet environment from previous literature. For sensing similar and even higher concentration of molecules or pH change, sensitivity of graphene based FET biosensors are much lower than that based on MoS₂.

A rough comparison of the sensitivity of FET biosensor based on graphene and MoS₂ can also be drawn by taking example of previous papers published in literature. While the sensitivity in case of MoS₂ for a pH change of 3 to 4 is 193 and that for 100fM streptavidin solution is 196, the sensitivity in case of graphene for similar or

even higher pH-change/concentration of biomolecules is always much lower than that of MoS₂ as shown in the **Table 4.1**.

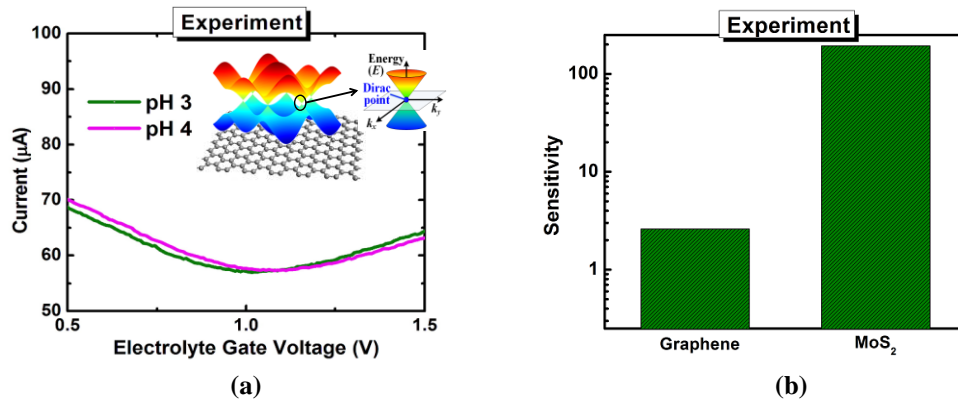


Figure 4.12(a) Graphene exhibits very little modulation of current and very high *SS* with the variation of electrolyte gate voltage. This is due to the lack of bandgap in graphene as illustrated through the bandstructure of graphene in the inset figure. Change in pH of the solution from 3 to 4 leads to significantly lower change in current compared to that in MoS₂ based pH sensor. The thickness of the graphene used in this experiment is around 7 nm. **(b)** Comparison of sensitivity of graphene and MoS₂ based FET biosensors for the same change in pH from 3 to 4. Sensitivity of MoS₂ based FET biosensor is 74-fold higher compared to that based on graphene.

For proper comparison, it is necessary to compare graphene and MoS₂ for the same type of biomolecules or same pH change. Hence, we have performed experiments with FET biosensors based on graphene and MoS₂ having similar channel thickness, length and top dielectric thickness and measured under similar conditions in the model case of pH sensing for the same pH change. The experimental findings are in-line with the theoretical predictions as graphene biosensor exhibits an *SS* of more than 5000 mV/dec even though it has ultra-thin body (**Figure 4.12(a)**). MoS₂ on the other hand due to its ultra-thin nature and pristine interfaces can not only achieve excellent electrostatics but at the same time due to its sizeable bandgap (the bandgap of MoS₂ varies in the range of 1.8 eV (for monolayer) to 1.2 eV (for bulk))

can also suppress tunneling leakage currents, which degrades SS at bandgaps below around 0.4 eV (**Figure 2.3(d)**). Combination of both these factors leads to excellent SS in case of MoS_2 . Even with a very thick (35 nm) dielectric, MoS_2 with similar thickness as graphene provides an excellent SS of 150 mV/dec. Hence, graphene provides much lower sensitivity of 2.6 compared to that (193) achieved by MoS_2 (**Figure 4.12(b)**) for the same change in pH of the electrolyte (from pH of 3 to pH of 4). Graphene based pH sensor reported in literature [170] has shown a sensitivity of about 12 for a pH change of 1.1. In ref [170], the electrolyte is directly in contact with the graphene channel (without any dielectric layer) in which case the sensing mechanism is complicated and in addition, for detection of biomolecules there is possibility of non-specific interactions. Moreover, since we measured the MoS_2 and graphene devices with same dielectric thickness and under similar conditions, our values provide a more appropriate comparison. It is to be noted that opening a bandgap in graphene remains extremely challenging [16]–[19]. On the other hand, while the other popular form of carbon: CNTs possess bandgap, their application as biosensors is severely limited due to the challenges in integrability as well as the chirality issue [166].

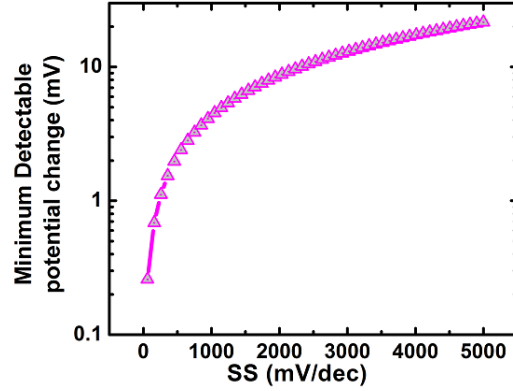


Figure 4.13. Minimum detectable change in the surface potential of the dielectric for a FET biosensor as a function of its subthreshold swing (SS). Minimum detection limit degrades substantially with increase in SS .

The minimum detection limit of graphene is also fundamentally constrained due to its limitation of SS as explained below. Considering the minimum change in current (with respect to the initial current) required for detection ability as Ξ , it can be derived that the change in surface potential ($\Delta\phi_{min}$) that is required to produce this required current change is given by:

$$\Delta\phi_{min} = SS \log_{10}(\Xi + 1) \quad (4.4)$$

This is the minimum change in surface potential needed for the detectable signal and as is clear from equation (4.4), is directly proportional to the SS . Hence, an FET biosensor with lower SS , requires a lower $\Delta\phi_{min}$ (**Figure 4.13**) and hence lower change in pH (or lower number of biomolecule conjugations) for detectable signal and hence a lower detection limit. With MoS_2 based FET biosensor, it is possible to obtain the ideal SS of 60 mV/dec, while for graphene, due its lack of bandgap, SS will be around 1000 or higher. Thus, as per the discussion above on the relation of SS and

detection limit, the minimum detection limit of graphene is also much worse than that of MoS₂ (Figure 4.14).

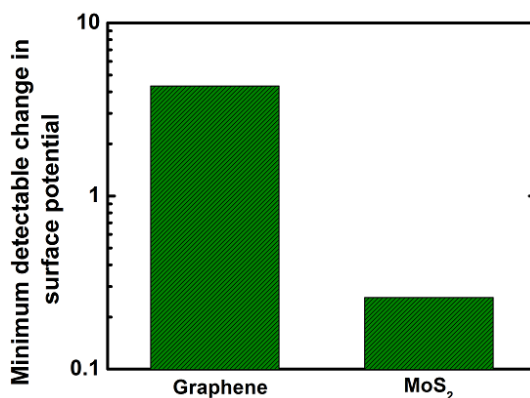


Figure 4.14. Minimum change in surface potential that is detectable by MoS₂ FET biosensor and graphene FET biosensor.

Table 4.2

Reduced Graphene Oxide (rGO) based FET Biosensors	Molecule Detected	Molar Concentration	Sensitivity
Adv. Mater. 22 , 3521–3526 (2010)	IgG	12	≈ 11
ACS Nano 4 (6), 3201–3208 (2010)	dopamine	2 mM	≈ 0.75
ACS Nano 5 (3), 1990–1994 (2011)	Ca ²⁺	10 μM	≈ 11
ACS Nano 6 (2), 1486–1493 (2012)	vascular endothelial growth factor (VEGF)	100 fM	≈ 0.3
Nanoscale, 4 , 293 (2012)	DNA	100 nM	≈ 2

Sensitivity of rGO based FET biosensors from previous literature. For sensing similar and even higher concentration of molecules or pH change, sensitivity of graphene (rGO) based FET biosensors are much lower than that of MoS₂.

In the case of reduced-Graphene-Oxide (rGO), variability, lack of precise control of bandgap and presence of defects are major issues [209], which severely limit the performance. In-depth understanding of the surface modification reactions for bandgap modulation of rGO is still lacking. The uncontrollable bandgap together with the low purity of rGO leads to very low sensitivity of rGO based biosensors as is evident from the following **Table 4.2**. It is to be noted that MoS₂ not only possesses ultra-thin nature and considerable bandgap, but also has pristine interfaces free of dangling bonds, which in combination, leads to its ultra-high sensitivity.

4.2.2. Work-Function Modulated Gas-sensor

TMDs are not only highly promising for biosensing, their large surface to volume ratio make them a potential candidate as gas-sensor material. Moreover, functionalization using noble metallic nanoparticles (NPs) can also open up new avenues for gas sensing[53]–[55] applications, as has been demonstrated in case of nanotubes/nanowires or graphene oxide. It is clear from the discussion in Chapter 2, that metallic NPs can be used to adjust the threshold voltage of TMD based FETs which can be useful for digital applications. Apart from digital applications, the modulation of work-function of metallic NPs can also be employed as the transduction mechanism for building effective gas-sensors. As an example, we configured an MoS₂ based FET functionalized with Pd NPs as a gas sensor for sensing Hydrogen gas. Pd can adsorb hydrogen which leads to a change in its work function.[57] As shown in theChapter 2, the doping effect and hence the electrical characteristics of the

MoS₂ FETs are dependent on the WF of the metallic NPs. Hence, change in the WF of Pd NPs due to adsorption of Hydrogen can be detected in real time through the change in current in a Pd NP functionalized MoS₂ FET. **Figure 4.15(a)** shows the current in a MoS₂ FET before the incorporation of any NPs. Negligible change in device current is observed upon exposure to hydrogen (3 ppm). The same device was then incorporated with Pd NPs and measured again in real time (**Figure 4.15(b)**). In both the cases, the gate voltage was chosen to make the FET operate in the subthreshold region for obtaining maximum sensitivity[4], [146], [210]–[212]. The current level was seen to increase substantially upon exposure to the same hydrogen level as before. This is because adsorption of hydrogen led to decrease in the Pd WF[211], thus decrease in the p-type doping and hence increase in the current level of the n-type MoS₂ transistor. Previously, sensitivity (defined as the ratio of change in conductivity/current to the initial conductivity/current) of much less than 1 was obtained at room temperature for 3 ppm of hydrogen gas exposure by using bulk MoS₂. [213] In this work, for the same hydrogen concentration, sensitivity of about 5 is obtained at room temperature. This improvement is due to the use of few layer MoS₂ (8 nm thick) and biasing the device in subthreshold region.

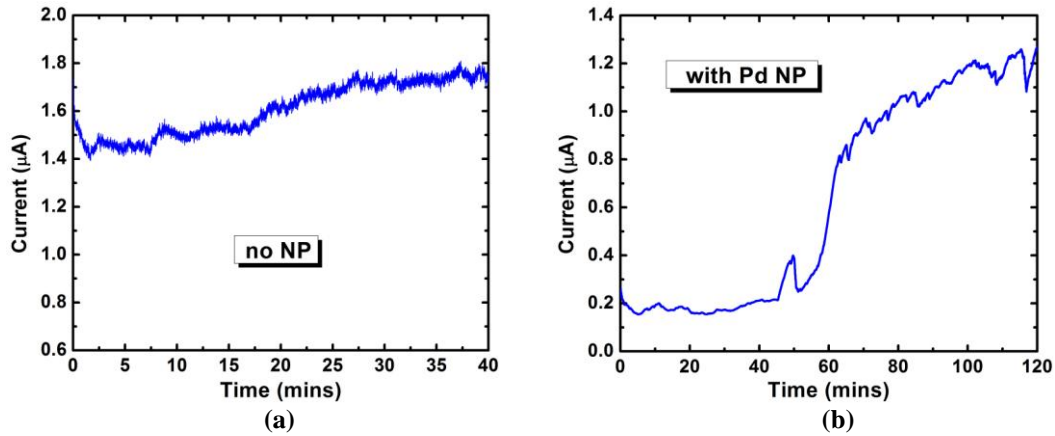


Figure 4.15 (a) Real-time measurement of current of MoS₂ FET without any NPs. Negligible change in current was observed when the device was exposed to hydrogen (at time=20 mins). (b) Real-time measurement of current of the same MoS₂ FET after incorporation of Pd NPs. Current increases substantially upon exposure to hydrogen (3ppm at time=45 mins) from 0.2 μA to about 1 μA.

4.3. Fundamental Limitation of Electrical Sensors and the Solutions

In the previous sections the advantages of 2D TMDs as a channel material, in sensing applications are discussed. The dependence of sensitivity on subthreshold swing (SS) is also derived (equation 4.2). From this equation, it is clear that the fundamental limitation on the minimum achievable SS , also poses fundamental limitation on the sensitivity of conventional FET (CFET) based biosensors, irrespective of the channel material.[144] While the relation between sensitivity and SS can be understood easily from intuition, it is not quite intuitive that the thermionic SS also limits the response time of the biosensors and this effect will be discussed below. In the following sections, we propose and theoretically demonstrate that these limitations can be overcome by employing steep transistors with sub-thermionic SS , focusing on comparatively less disruptive technologies namely, Tunnel FET

(TFET) and Impact-Ionization MOS (IMOS).

4.3.1. TFET based Biosensor

The working mechanism of TFET based biosensor (**Figure 4.16**),[144] is similar to that of TFETs (**Figure 3.8**) used for digital applications which are discussed in Chapter 3. Before the attachment of biomolecules to the sensor surface, the tunneling barrier between source and channel is high (width of the barrier is depicted by the length of the blue arrow) and hence the current in TFET is low. After biomolecule-receptor conjugation, due to the charges present in the biomolecules (positive charge is assumed here), the bands in the channel bend down, leading to a decrease in the tunneling barrier (width of the barrier is depicted by the length of the brown arrow) and hence, increase in the tunneling current. Thus, the biomolecules can be detected by monitoring the change in current through the TFET biosensor device.

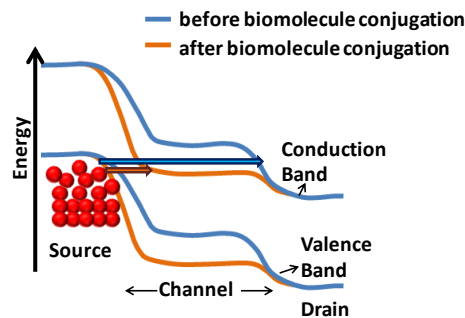


Figure 4.16. Schematic diagram depicting the working mechanism of TFET based biosensor.

Here, we establish the supremacy of TFET biosensor compared to that based on CFETs. We present extensive numerical simulations based on Non-Equilibrium

Green's function formalism for accurate results as well as analytical solutions with the aim of providing easy physical insights. The modeling scheme can be divided into two major parts. First part deals with the kinetics of biomolecules within the electrolyte, their capture by the receptors and thereby the development of surface potential (ϕ_{bio}) on the oxide in the presence of electrostatic screening by the ions present in the electrolyte. Second part deals with the electrical response of the TFET or the change in tunneling current with the change in the surface potential developed due to attachment of the biomolecules. Here, we will focus on 1D structures for computational efficiency. However, the conclusions derived are general and can also be applied to 2D or 3D structures.

First, we deal with the first part of the modeling scheme i.e., derivation of surface potential (ϕ_{bio}) due to the binding of charged biomolecules by receptors. The biomolecule-receptor conjugation occurs through two processes [215]. First process involves the diffusion of the biomolecules to the oxide surface, which has been functionalized with specific receptors and is described by the equation

$$\frac{d\rho}{dt} = D\nabla^2\rho \quad (4.5)$$

where ρ is the concentration and D is the diffusion coefficient of the biomolecules in the solution. Second process involves the capture of the biomolecules by the receptors and is described by the equation

$$\frac{dN_{bio}}{dt} = k_F(N_0 - N_{bio})\rho_s - k_R N_{bio} \quad (4.6)$$

where N_{bio} is the surface density of conjugated receptors or in other words, surface density of the captured biomolecules, N_0 is the surface density of receptors used to functionalize the surface of the oxide, ρ_s is the concentration of the biomolecules on the surface of the oxide, k_F is the capture constant and k_R is the dissociation constant. Using the above two equations, the surface density of charge due to attached biomolecules on the sensor surface can be calculated [215].

Now, the surface charge formed on the sensor surface attracts the ions within the electrolyte, which forms a second layer of charge (of opposite polarity). This second layer electrostatically screens the first layer and hence decreases the effective potential developed on the oxide surface. This double layer charge density can be calculated using the nonlinear Poisson–Boltzmann equation, which for a 1-1 electrolyte is given by [216]

$$-\nabla^2\phi(r)+\frac{K_B T}{\lambda_{DH}^2 q} \sinh\left(\frac{q\phi}{K_B T}\right)=\frac{q}{\epsilon_w} \sum_i z_i \delta(r-r_i) \quad (4.6)$$

Here λ_{DH} denotes the Debye–Huckel screening length and is given by

$$\sqrt{\epsilon_w K_B T / 2q^2 I_0 N_{avo}} \quad (4.7)$$

where, ϵ_w is the dielectric constant, I_0 is the ion concentration of the electrolyte, N_{avo} denotes the Avagadro’s number, z_i is the partial charge and r_i is the location of the atoms within the biomolecule. Finally, ϕ_{bio} can be found by equating the surface charge on the oxide due to the conjugated receptors to the sum of the charge in the

electrolyte double layer and the charge developed within the semiconductor 1D structure [196], [215]

Next, we discuss the second part of modeling scheme and it is this part that dictates the critical differences between the CFET and TFET based biosensors. The analytical formula for band-to-band tunneling (BTBT) current (I_{BTBT}) has been derived in Chapter 2, and can be used to obtain the sensitivity of the biosensor which is defined as

$$S_n = \{I_{BTBT}(\phi_0 + \phi_{bio}) - I_{BTBT}(\phi_0)\} / I_{BTBT}(\phi_0) \quad (4.8)$$

where ϕ_0 denotes the initial surface potential on the oxide before the attachment of biomolecules. In above equation, it is implicit that ϕ_0 is tuned such that the current is dominated by the source-channel BTBT and the energy window $\Delta E \geq 0$. The TFETs exhibit ambipolarity and for $\Delta E < 0$ the current is mainly dominated by channel-drain tunneling (**Figure 3.8 (a)**). Hence, to avoid undesirable ambipolar effects, it is required to tune ϕ_0 such that the operational mode of the biosensor always remains in the regime where source-channel current dominates. Using equations (3.28) and (4.8), the analytical formula for sensitivity can be derived as

$$S_n = \exp\left(\frac{\pi\sqrt{2q} m^{*1/2} E_G^{3/2} \lambda \phi_{bio}}{\hbar(2\phi_0 - E_G)(2\phi_0 + 2\phi_{bio} - E_G)}\right) \left(1 + \frac{\phi_{bio}}{\phi_0 - E_G}\right) - 1 \quad (4.9)$$

The above analytical formula provides important insights regarding the dependence of sensitivity on the initial surface potential ϕ_0 . It can be observed that the sensitivity increases as ϕ_0 is decreased (keeping $\Delta E \geq 0$). This is because, for

TFETs, the rate of increase in current with gate voltage is higher for smaller values of ΔE (and thus for smaller values of ϕ_0) giving rise to increased sensitivity at lower values of ϕ_0 . Note that small value of ΔE indicates TFET operation in the subthreshold region. Thus, equation (4.9) indicates that in order to achieve high sensitivity, the TFET biosensor should be operated in the subthreshold regime. Equation (4.9) also provides direct physical insights regarding the dependence of the sensitivity on the bandgap of the material. As is evident from the equation, sensitivity increases with increase in bandgap. This is because of the decrease in the current before the capture of biomolecules i.e., $I_{BTBT}(\phi_0)$ with increase in bandgap.

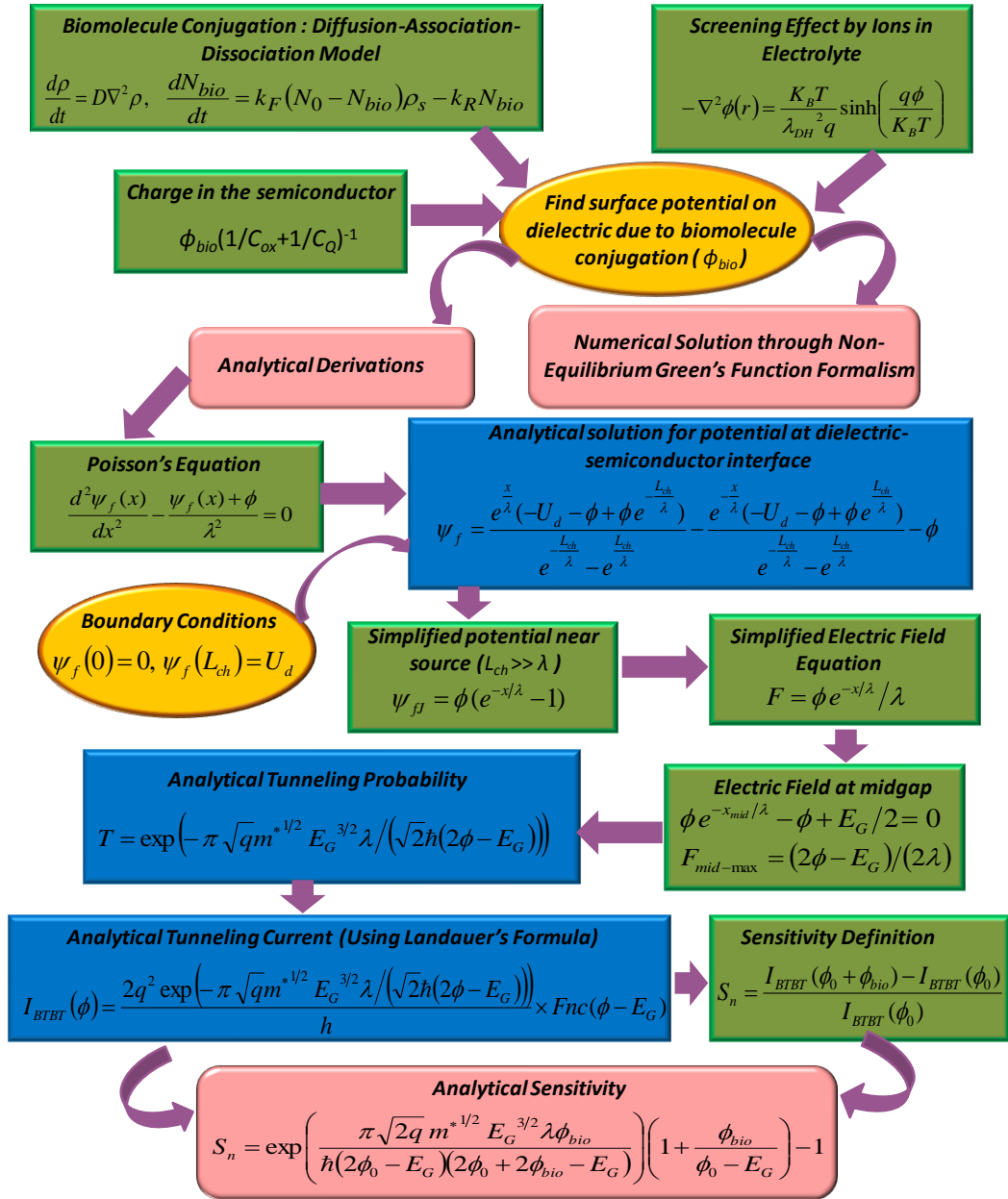


Figure 4.17. Diagram representing the modeling scheme for TFET based biosensors.

For TFETs with relatively large bandgap materials or employing asymmetric design techniques at source and drain to reduce ambipolarity, ϕ_0 may be tuned so that

the current is mainly dominated by the relatively smaller reverse biased P-I-N junction current (I_{rev}) and the sensitivity will be given by

$$S_n = (I_{BTBT}(\phi_0 + \phi_{bio}) - I_{rev}(\phi_0)) / I_{rev}(\phi_0) \quad (4.10)$$

In this case, the sensitivity will increase with decreasing bandgap at the source-channel junction due to the exponential increase in $I_{BTBT}(\phi_0 + \phi_{bio})$. The whole modeling scheme is represented through a diagram in **Figure 4.17**.

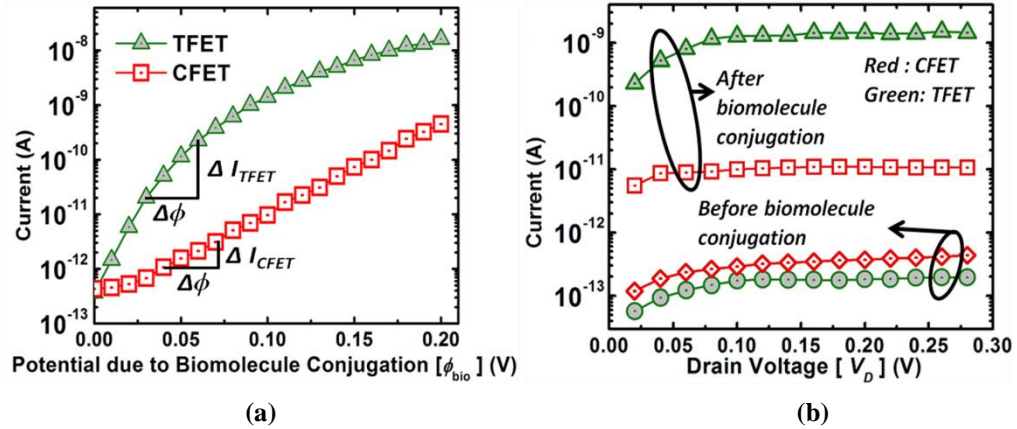


Figure 4.18 (a) Current as a function of surface potential developed due to biomolecule conjugation (ϕ_{bio}) at a drain voltage (V_D) of 0.3V. Due to the smaller subthreshold swing in TFETs, they can lead to higher change in current compared to CFETs for the same change in surface potential. (b) Current as a function of drain voltage before and after biomolecule conjugation for $\phi_{bio}=0.1\text{eV}$.

The subthreshold regime forms the optimal sensing domain not only for TFET biosensors as discussed above but also for the conventional FET biosensors [196]. CFETs suffer from a fundamental limitation on the minimum achievable SS of $[K_B T/q \ln(10)]$ due to the *Boltzmann tyranny* effect where K_B is the Boltzmann constant and T is the temperature. However, the TFETs overcome this limitation due to the *Fermi-tail cutting* by the bandgap of the semiconductor. The charged biomolecules

essentially produce gating effect on the semiconductor channel. Hence, the change in current in TFET biosensors, because of their smaller SS , is substantially higher than that for CFET biosensors in the subthreshold region for the same surface potential developed due to attachment of biomolecules (ϕ_{bio}) as illustrated in **Figure 4.18(a)**.

Figure 4.18(b) shows the current as a function of the drain voltage for both CFET and TFET biosensors before and after the biomolecule conjugation. It is observed that for similar currents in both biosensors before biomolecule conjugation, the current in TFET biosensors can be more than 2 orders of magnitude higher than that in CFETs after the attachment of the biomolecules, which obviously indicates significant increase in the sensitivity.

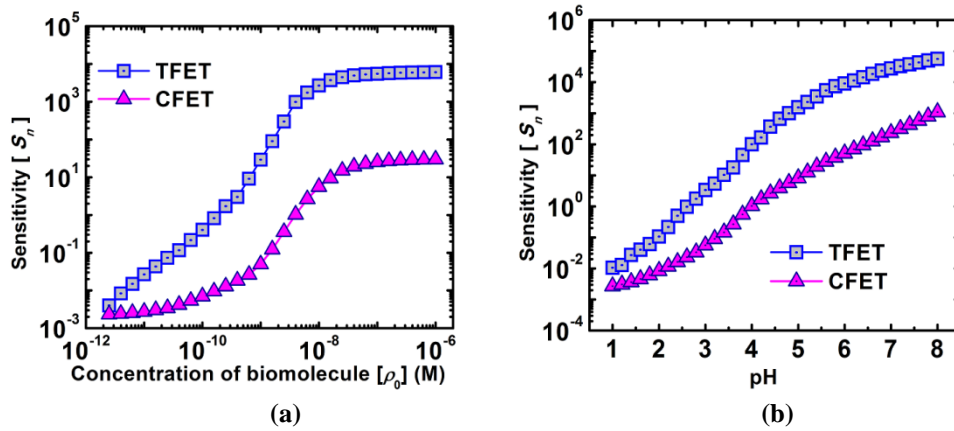


Figure 4.19(a) Sensitivity for sensing of biomolecules as a function of biomolecule concentration. **(b)** Sensitivity for pH sensing for different pH values. ϕ_0 is tuned for TFET and CFET so that they operate in the subthreshold regime. The bandgap and the effective masses used in the simulations are 0.4 eV and $0.15m_0$ respectively (where m_0 denotes the mass of a free electron) and the diameter of nanowire is taken as 5 nm.

Comparison of the performance of CFET and TFET biosensors, for biomolecule as well as pH sensing, clearly shows that the sensitivity of TFET biosensors can surpass that of CFET biosensors by several orders of magnitude (**Figure 4.19(a)**) and

(b)). The dependence of S_n on SS is depicted by equation (4.2), which depicts the strong relation between the two. Thus, TFETs can harness the benefits of the substantial increase in sensitivity (up to more than four orders of magnitude) with decreasing subthreshold swing and lead to ultra-sensitive biosensors while CFET biosensors are strictly restricted to a higher limit on the maximum achievable sensitivity as highlighted in **Figure 4.20**.

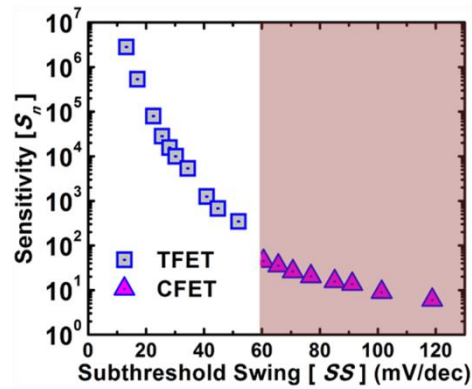


Figure 4.20. Sensitivity as a function of subthreshold swing averaged over 4 orders of magnitude of current for both CFET and TFET based biosensors. Surface potential change due to attachment of biomolecules (ϕ_{bio}) is taken to be 0.1V. Sensitivity increases substantially with the decrease in subthreshold swing. The shaded region shows the sensitivity values for CFET biosensors indicating that there is a restriction on the maximum achievable sensitivity since the subthreshold swing in CFETs cannot be minimized below 60 mV/dec at room temperature. All simulations in this figure are performed through self-consistent solutions of Poisson's and Schrodinger's equations within the framework of Non-Equilibrium Green's function formalism.

In the following discussions, we show that TFET biosensors not only lead to substantial increase in sensitivity, but also provide significant improvement in terms of the response time, which is defined as the time required to obtain a desired sensitivity (more specifically the time needed to capture a certain number of biomolecules in order to achieve a desired change in electrical signal). First, we derive an analytical formula for the surface density of biomolecules (N_{bio}) that is

required to be captured in order to obtain a particular sensitivity. N_{bio} can be related to ϕ_{bio} as $((1/C_{ox}+1/C_{NW})^{-1} + C_{DL})\phi_{bio}$ [196] where C_{ox} , C_{NW} and C_{DL} represent the oxide, quantum and electrolyte double layer capacitance respectively. From equation (4.2), we can write ϕ_{bio} as $SS_{avg} \times \log_{10}(S_n+1)$ where SS_{avg} denotes the average value of subthreshold swing over the range ϕ_0 to $(\phi_0 + \phi_{bio})$. In the subthreshold region $(1/C_{ox}+1/C_{NW})^{-1} + C_{DL} \approx C_{DL}$ and hence, N_{bio} can be written as

$$N_{bio} = \frac{\pi\epsilon_w R_{NW} K_1(R_{NW}/\lambda_{DH}) SS_{avg} \log_{10}(S_n + 1)}{\lambda_{DH} K_0(R_{NW}/\lambda_{DH})} \quad (4.11)$$

In the above equation we have used the expression for C_{DL} as $\pi\epsilon_w R_{NW}/\lambda_{DH} \times K_1(R_{NW}/\lambda_{DH})/K_0(R_{NW}/\lambda_{DH})$ [196]. Here, λ_{DH} denotes the Debye–Huckel screening length, ϵ_w is the dielectric constant of the electrolyte, R_{NW} is the radius of the 1D structure, and K_0 and K_1 are the zero- and first-order modified Bessel functions of the second kind. It is clear that N_{bio} decreases with decreasing values of the swing (**Figure 4.21(a)**). This can be easily explained by the fact that, better the response of the sensor to the gating effect, lower would be the required change in oxide surface potential (ϕ_{bio}) and hence in the required N_{bio} for achieving the same sensitivity. The response time (t_r) can be related to N_{bio} [217]. Now, using equation (4.11), the dependence of response time to the subthreshold swing is derived as

$$t_r = \frac{\pi\epsilon_w R_{NW}^2 K_1(R_{NW}/\lambda_{DH}) \log_{10}(S_n + 1)}{\lambda_{DH} K_0(R_{NW}/\lambda_{DH}) D N_{avo}} \times \frac{SS_{avg}}{\rho_0} \quad (4.12)$$

where ρ_0 is the concentration of biomolecules, N_{avo} denotes the Avagadro's number and D is the diffusion coefficient of the biomolecules in the solution. Since the

CFETs are plagued by the Boltzmann tyranny effect, there exists fundamental limitations to the minimum response time that can be obtained from biosensors based on them. This lower limit in CFETs can be derived using (4.12) as

$$t_{r-\min} = \frac{\pi \varepsilon_w R_{NW}^2 K_1 (R_{NW} / \lambda_{DH}) \ln(S_n + 1) K_B T}{\lambda_{DH} K_0 (R_{NW} / \lambda_{DH}) D N_{avo} \rho_0} \quad (4.13)$$

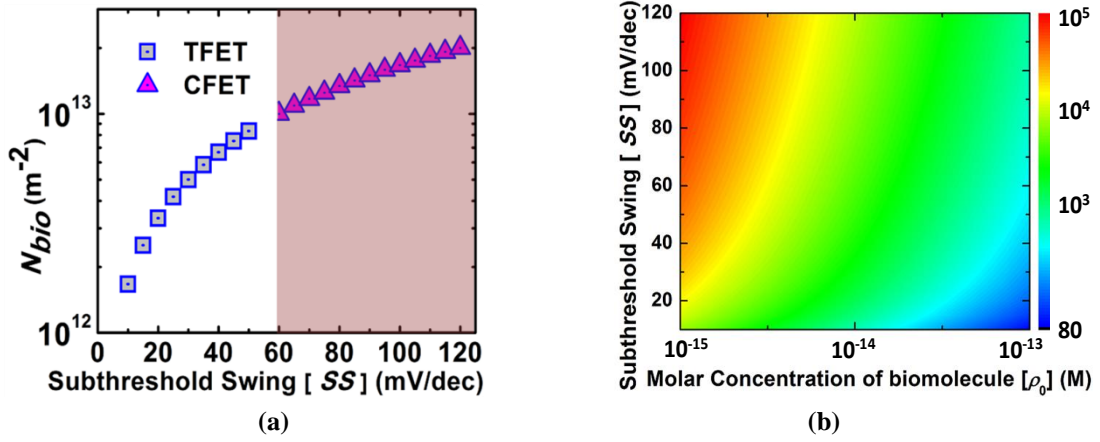


Figure 4.21(a) Surface density of biomolecules (N_{bio}) required to be attached to the sensor surface for both CFET and TFET biosensors in order to achieve the same sensitivity value in both, as a function of subthreshold swing. It is observed that N_{bio} decreases significantly with decrease in the subthreshold swing. **(b)** 2D colormap showing the response time (in seconds) of the biosensor as a function of the subthreshold swing and the molar concentration of the biomolecules in the solution.

In **Figure 4.21(b)**, the response time is plotted as a function of both the subthreshold swing and the biomolecule concentration in the electrolyte. Since, TFET biosensors are not bound by a lower limit on the subthreshold swing, they can be highly advantageous for reduction of response time (up to more than an order of magnitude) and detection of biomolecules at low concentrations.

It is to be noted that in this work we have presented the results for n-TFET assuming a positive charge of the biomolecules. In general the biomolecules such as DNA possess negative charge. However, this sign change does not affect the general discussion and results presented here.

4.3.2. I-MOS based Biosensor

Here, we show that the phenomenon of impact ionization can be leveraged to beat the limits of conventional FET biosensors, thereby leading to an ultra-sensitive and fast electrical biosensor [212].

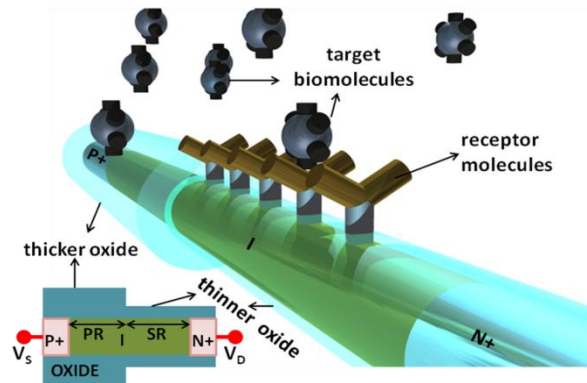


Figure 4.22. Schematic diagram of a nanowire based IFET biosensor for detection of positively charged biomolecules. A nanowire structure is chosen to provide high electrostatic control and large surface-to-volume ratio. The inset figure shows the source/drain and channel doping scheme, the protected region (PR) and sensing region (SR) in the channel. For detection of negatively charged biomolecules, the position of PR and SR should be interchanged.

The structure of the proposed nanowire based impact-ionization MOSFET biosensor for detecting positively charged biomolecules is shown in **Figure 4.22**. While the most commonly used acronym for impact-ionization MOSFET is I-MOS, we will use IFET as the acronym here, in conjunction with CFET and TFET. The ends of the nanowire are doped to form a P^+-I-N^+ diode, which is to be operated in the

reversed bias mode. Portion of the I-region towards P^+ source is covered with thick oxide to prevent the influence of biomolecules in that region and we call it the protected region (PR). This region is needed due to the requirement of a threshold length for impact ionization to occur as well as to prevent band-to-band tunneling from valence band of source to conduction band of I-region. The rest of the I-region is covered with a thin oxide for effective *gating effect* through charged biomolecules and we call it the sensing region (SR).

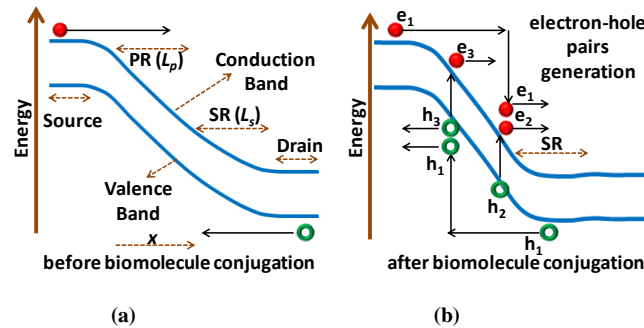


Figure 4.23. Band diagram (a) before and (b) after biomolecule conjugation in IFET biosensor. The source is biased at a negative voltage, slightly below the breakdown voltage. Hence, no impact ionization occurs before biomolecule conjugation. Attachment of the biomolecules in the SR leads to increase in electric field in PR (b). Now an electron e_1 can gain enough energy from the electric field to knock out an electron from the valence band creating an electron (e_2) and hole (h_2). Similarly, a hole h_1 can lead to generation of an electron (e_3) and hole (h_3). Thus carriers get multiplied leading to impact ionization.

If the source is biased at a negative voltage such that the reverse bias is below the avalanche breakdown voltage, no impact ionization occurs before biomolecule conjugation (Figure 4.23(a)). The attachment of charged biomolecules in SR increases the effective electric field in PR activating impact ionization (Figure 4.23(b)).

Occurrence of impact ionization leads to a sharp increase in current or in other words, to ultra-low Subthreshold Swing (SS) as shown in **Figure 4.24**. By altering the source voltage this sharp increase in current can be made to occur at very small values of surface potential in SR developed due to biomolecule conjugation (**Figure 4.24**).

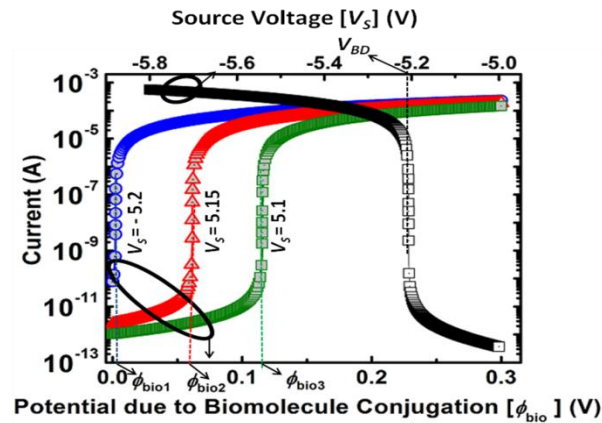


Figure 4.24. The black curve (involving left and top axis) shows the current as a function of source voltage (V_s) before biomolecule conjugation. Breakdown occurs when absolute value of V_s is little higher than 5.2 V (marked as V_{BD} in the top axis) leading to sharp increase in current. If the V_s is kept ≤ 5.2 V, the breakdown can be made to occur through the surface potential on the oxide developed due to biomolecule conjugation (ϕ_{bio}) as shown by the blue, red and green curves (involving left and bottom axis). The value of ϕ_{bio} at which the breakdown occurs depends on the applied V_s and are shown in the figure as ϕ_{bio1} , ϕ_{bio2} and ϕ_{bio3} for V_s equal to 5.2V, 5.15V and 5.1V respectively. It is clear that ϕ_{bio} required for breakdown decreases as source is biased closer to the breakdown point.

While accurate results can be obtained through numerical simulations using TCAD tools, analytical formalism is necessary for gaining easy physical insight. Hence, in the following discussion we focus on deriving analytical formula for sensitivity using a simplified 1D model. The modified 1D Poisson equation for the PR and SR can be written as equations (4.14a) and (4.14b) respectively.

$$\frac{d^2\psi_p(x)}{dx^2} = 0 \quad (4.14a)$$

$$\frac{d^2\psi_s(x)}{dx^2} - \frac{\psi_s(x) + \phi}{\lambda^2} = 0 \quad (4.14b)$$

Here, ψ_p and ψ_s are the potential at the semiconductor-oxide interface in PR and SR respectively, ϕ is the potential at the oxide-electrolyte interface in the SR, x is the direction from source to drain as shown in **Figure 4.23(a)** and is taken to be 0 at the source-PR junction. λ is defined as the natural length scale [1]. The band-bending in the source/drain regions are neglected, which is a valid assumption for highly doped regions. The semiconductor-oxide interface potential at the drain-SR junction is taken as the reference point and hence set to 0 and that at source-PR junction is defined as U_{src} . Thus, $\psi_s(L_p + L_s) = 0$ and $\psi_p(0) = U_{src}$ where L_p and L_s are the lengths of the PR and SR respectively as shown in **Figure 4.23(a)**. The other two boundary conditions for solving the Poisson equations given by equation (4.14) are obtained from the continuity equations between ψ_p and ψ_s and their derivatives as $\psi_p(L_p) = \psi_s(L_p)$ and $d\psi_p(x)/dx|_{x=L_p} = d\psi_s(x)/dx|_{x=L_p}$. The solution of the potentials are given by

$$\psi_p(x) = -\frac{\{(U_{src} + \phi) \cosh(L_s/\lambda) - \phi\}x}{\lambda \sinh(L_s/\lambda) + L_p \cosh(L_s/\lambda)} + U_{src} \quad (4.15a)$$

$$\begin{aligned} \psi_s(x) = & \frac{\lambda(U_{src} - \phi) \sinh((L_p + L_s - x)/\lambda) + L_p \phi \cosh((x - L_p)/\lambda)}{\lambda \sinh(L_s/\lambda) + L_p \cosh(L_s/\lambda)} \\ & + \frac{\lambda \phi L_p \phi \sinh((x - L_p)/\lambda)}{\lambda \sinh(L_s/\lambda) + L_p \cosh(L_s/\lambda)} - \phi \end{aligned} \quad (4.15b)$$

Since, impact ionization occurs in the PR, it is necessary to simplify the equation of semiconductor-oxide interface potential in that region given by equation (4.15a) in order to obtain simplified equation for the impact ionization current. It is to be noted that the impact of SR has been intrinsically incorporated in equation (4.15a) through the factors ϕ , λ and L_s . Using the condition $L_s \gg \lambda$, which is the case in an electrostatically well controlled device, equation (4.15a) can be simplified as

$$\psi_p(x) = -\frac{(U_{src} + \phi)x}{\lambda + L_p} + U_{src} \quad (4.16)$$

Using equation (4.16), the electric field in the PR can be derived as

$$F_p = \frac{(U_{src} + \phi)}{\lambda + L_p} \quad (4.17)$$

This electric field can be used to calculate the impact ionization coefficient α , which is defined as the number of electron-hole pairs generated by a carrier per unit distance travelled and is given by $\alpha = \alpha_\infty e^{-F_{crit}/|F_p|}$ where α_∞ is an empirical parameter and F_{crit} is the critical electric field. For deriving a simplified analytical solution, α_∞ and F_{crit} for electron and holes is assumed to be similar and thus the ionization integral M can be written as $M = \int_0^{L_p} \alpha dx$. Using equation (4.17) M can be derived as

$$M = L_p \alpha_\infty e^{-F_{crit} \left/ \left| \frac{(U_{src} + \phi)}{\lambda + L_p} \right| \right.} \quad (4.18)$$

The avalanche breakdown occurs when M reaches the value of 1. Now, the potential ϕ can be divided into two parts: the initial potential ϕ_0 which can be adjusted using the electrolyte reference electrode and the potential developed due to biomolecule conjugation ϕ_{bio} . The threshold value of the potential due to biomolecule attachment that is required for avalanche breakdown (ϕ_{bio_th}) can be derived by equating M to 1 and thus we obtain

$$\phi_{bio_th} = \frac{F_{crit}(\lambda + L_p)}{\ln(\alpha L_p)} - U_{src} - \phi_0 \quad (4.19)$$

For $\phi_{bio} < \phi_{bio_th}$, the current (I_i) is given by $I_{rev}/(1-M)$ where I_{rev} is the reverse biased P-I-N junction current. Thus we can write

$$I_i = I_{rev} \left/ \left\{ 1 - L_p \alpha_{\infty} e^{-F_{crit} \left/ \left(\frac{U_{src} + \phi_0 + \phi_{bio}}{\lambda + L_p} \right) \right.} \right\} \right. \quad \text{for } \phi_{bio} < \phi_{bio_th} \quad (4.20)$$

After avalanche breakdown the current in the IFET biosensor will behave like the conventional FET with an effective drain-to-source voltage (V_{ds_eff}) equal to the potential at $x=L_p$ at $\phi_{bio} = \phi_{bio_th}$. Using equation (4.16) and (4.19), V_{ds_eff} can be derived as

$$V_{ds_eff} = -\frac{F_{crit} L_p}{\ln(\alpha L_p)} + U_{src} \quad (4.21)$$

Now, the current (I_c) for $\phi_{bio} > \phi_{bio_th}$ can be written as

$$I_c = \mu W / (2L) C \left\{ \phi - (\phi_0 + \phi_{bio_th}) \right\}^2 \quad \text{for } \phi_{bio} - \phi_{bio_th} < V_{ds_eff} \quad (4.22a)$$

$$I_c = \mu W / L_s C \left\{ \phi - (\phi_0 + \phi_{bio_th}) \right\} V_{ds_eff} - V_{ds_eff}^2 / 2 \quad \text{for } \phi_{bio} - \phi_{bio_th} > V_{ds_eff} \quad (4.22b)$$

Using the equations of current given by equation (4.20) and (4.22), analytical formulae for sensitivity can be derived where sensitivity is defined as the ratio of the change in current due to biomolecule conjugation to the initial current before conjugation. For $\phi_{bio} < \phi_{bio_th}$, S_n is derived as

$$S_n = \left\{ 1 - L_p \alpha_\infty e^{-F_{crit} / \left| \frac{(U_{src} + \phi_0)}{\lambda + L_p} \right|} \right\} / \left\{ 1 - L_p \alpha_\infty e^{-F_{crit} / \left| \frac{(U_{src} + \phi_0 + \phi_{bio})}{\lambda + L_p} \right|} \right\} - 1 \quad (4.23a)$$

For $\phi_{bio} > \phi_{bio_th}$, S_n can be written as

$$S_n = \frac{I_c - I_i}{I_i} \quad (4.23b)$$

From the analytical derivations it can be observed that the sensitivity is dependent on the initial condition of the IFET, which can be tuned by source and reference gate bias, thus modulating U_{src} and ϕ_0 , respectively. These two knobs should be adjusted in such a way that the IFET biosensor is always below the breakdown potential before biomolecule conjugation. Also, it is clear from (4.19), that by proper tuning of U_{src} and ϕ_0 , the threshold value of potential due to biomolecule conjugation can be reduced and thus a fewer number of biomolecules attaching to the biosensor surface will be able to cause a substantial increase in the current.

Figure 4.25(a) shows the results of source bias sweep calculated through TCAD simulations in IFET biosensor before and after the biomolecule conjugation for different values of biomolecule concentration (ρ_0) in the electrolyte. The results of

drain voltage sweep for a CFET biosensor is shown in **Figure 4.25(b)**. Because of the sharp increase in current due to impact ionization in IFET, the current curves after biomolecule conjugation are distinctly distinguishable from the one before the conjugation even at very small values of ρ_0 . For CFET biosensors, on the other hand, there is very small change in current after conjugation as ρ_0 is decreased.

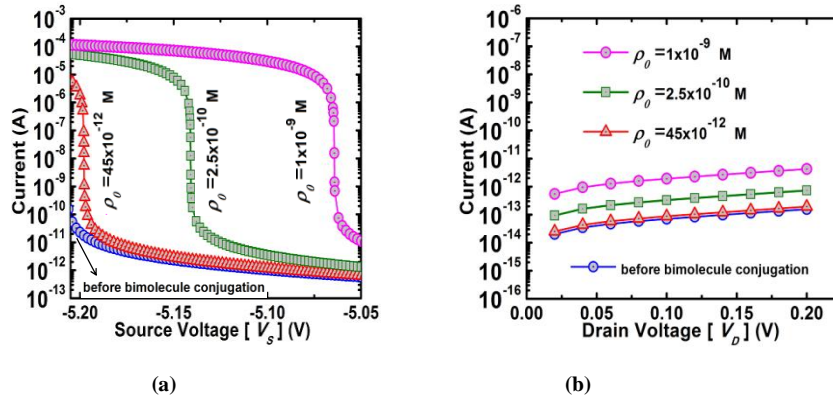


Figure 4.25. The current as a function of source bias in **a)** IFET and **b)** CFET biosensor before and after biomolecule conjugation for different values of biomolecule concentration (ρ_0) in the electrolyte. Unless mentioned otherwise, all simulations for IFET biosensor are done for a silicon nanowire with diameter of 30 nm with enclosing oxide thickness of 3 nm, and the ionic concentration I_0 is taken as 10^{-5} M.

In **Figure 4.26(a)**, the sensitivity is plotted as a function of ρ_0 for CFET and two different bias points of IFET. When V_s and ϕ_0 in IFET are adjusted to obtain the minimum SS (bias pt1), even low ρ_0 can lead to sharp increase in current and hence very high sensitivity (around 4 orders of magnitude higher compared to CFET). However, if IFET is biased at lower V_s (bias pt2) high ρ_0 is required in order for breakdown to occur. Once sufficient ρ_0 is reached, current and hence sensitivity increases sharply. For higher values of ρ_0 , sensitivity at bias pt2 is higher (around 6 orders of magnitude higher compared to CFET) than that at bias pt1 (around 2.5

orders of magnitude higher compared to CFET) because of the lower initial current before biomolecule conjugation at bias pt1. Since high sensitivity at low biomolecule concentration is desirable, bias pt1 is preferable for IFET biosensor operation. As is clear from **Figure 4.26(b)**, advantage of IFET biosensor over CFET is retained even when the ionic concentration of the electrolyte is increased (which increases the electrostatic screening by the ions).

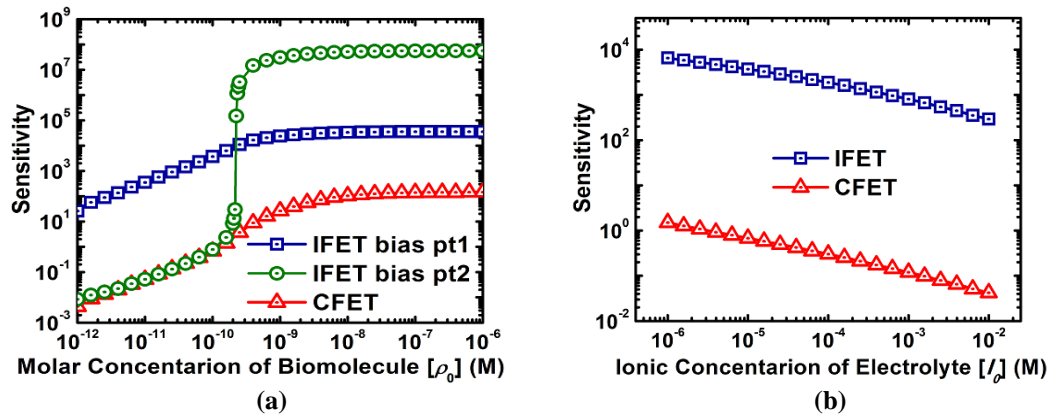


Figure 4.26 (a) Sensitivity of both IFET and CFET biosensors as a function of biomolecule concentration (ρ_0). Bias pt1 refers to the condition of IFET where V_s and ϕ_0 are adjusted to obtain the minimum SS while bias pt2 refers to the condition when V_s is 0.05V below that in bias pt1. The average SS of the IFET over 3 orders of magnitude of drain current is around 1.7 mV/dec. (b) Sensitivity as a function of ionic concentration (I_0). While sensitivity decreases for both IFET and CFET biosensors with the increase in I_0 due to electrostatic screening, the IFET biosensor still exhibits substantially higher sensitivity. In this case, IFET is at bias pt 1.

Figure 4.27 shows the sensitivity comparison between IFET and CFET biosensors for pH sensing. The pH sensing is based on the change in surface charge due to protonation/deprotonation of the OH groups on the enclosing oxide surface, which depends on the concentration of H^+ ions and hence on the pH value. It is observed that IFET biosensor can lead to around 4 orders of magnitude increase in sensitivity compared to that in CFET for pH detection.

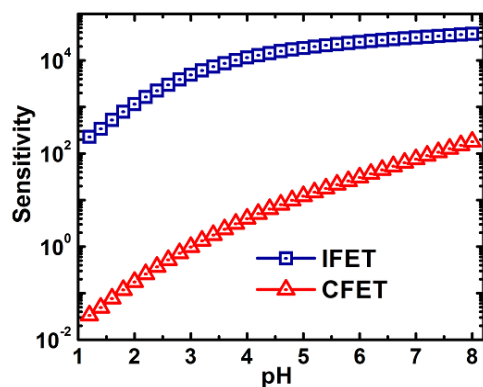


Figure 4.27. Sensitivity comparison between IFET and CFET biosensors for pH sensing as a function of pH values. Here, IFET is at bias pt 1.

Apart from sensitivity, another critical parameter for gauging the performance of the biosensors is the response time. Response time (t_r) is defined as the time required to obtain a desired sensitivity. Before a target analyte molecule can bind at the sensor surface and electrostatically modulate the channel conductance, the molecule must diffuse from the bulk solution to the sensor surface. This diffusion process takes time and sets lower limits on achievable detection times at a given analyte concentration [218]. Hence, a more specific definition of response time is the time needed to capture a certain surface density of biomolecules (N_{bio}) [217] in order to achieve a desired change in electrical signal. **Figure 4.28(a)** illustrates that t_r is directly proportional to the required N_{bio} and inversely proportional to ρ_0 . **Figure 4.28(b)** shows that the IFET can lead to significant reduction in response time compared to CFET. This effect can be understood in the following way. Extremely Low SS of IFET implies that for obtaining the same change in current and hence same sensitivity, the required change in surface potential (ϕ_{bio}) is much lower in IFET compared to that

in CFET. Since t_r is directly proportional to N_{bio} , which is again directly proportional to ϕ_{bio} , decrease in ϕ_{bio} leads to decrease in N_{bio} and consequently to reduction in t_r . From **Figure 4.28(b)** we can also conclude that within a same desired response time, IFET can detect biomolecules at substantially lower biomolecule concentration.

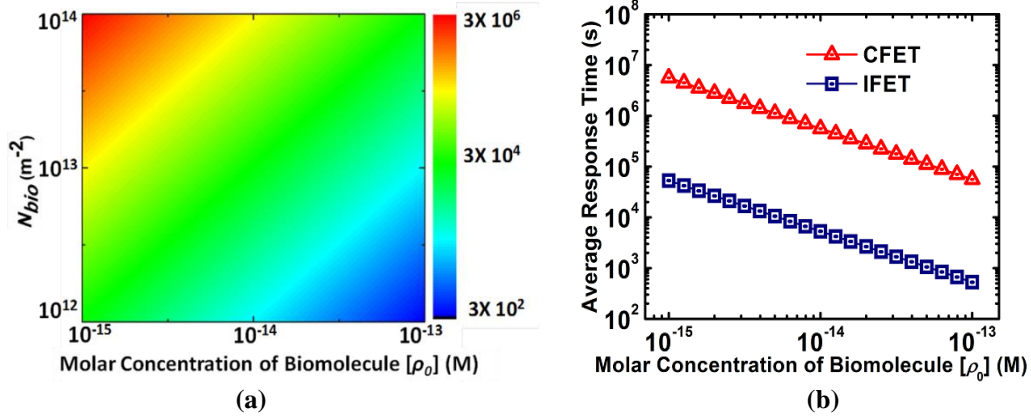


Figure 4.28(a) The colormap showing the average response time (t_r) in seconds of the biosensor as a function of the required surface density of biomolecules (N_{bio}) on the oxide surface to achieve the desired sensitivity, and the concentration (ρ_0) of the biomolecules in the solution. t_r increases as ρ_0 is decreased as it takes more time to capture the biomolecules when its concentration in the solution is low. t_r increases with increase in N_{bio} . This is because if the required surface density of biomolecules is more, it will take more time to reach that value. **(b)** Average response time as a function of the biomolecule concentration (ρ_0). For the same value of ρ_0 , IFET can lead to significant reduction in t_r . If the response time is kept constant, then within the same desired t_r , IFET can lead to detection at much lower biomolecule concentrations.

It is to be noted that tunnel-FETs (TFETs) employing interband tunneling can also lead to sharper increase in current or lower SS compared to CFETs as discussed in previous section, and hence, is attractive as a sensor for biomolecules [146], [210] as well as gaseous species [211]. The best reported average SS value over 4 decades of current at a low voltage of 0.1 V for TFETs is 36.5 mV/dec [81] and further improvement is expected. The phenomenon of impact ionization has been shown to lead to SS as low as 72 μ V/decade [219]. The IFETs based on Silicon, however have

very high breakdown voltage and application of novel technology is required for lowering the operating bias [122]. From an ultra-low power perspective, the TFET biosensors remain attractive. Since, IFETs suffer from reliability issues, they may be more promising as dispensable sensors. Though, here the results are presented for Silicon nanowire based IFETs the general discussion is valid for other materials and structures as well.

4.3.3. TFET based Gas-sensor

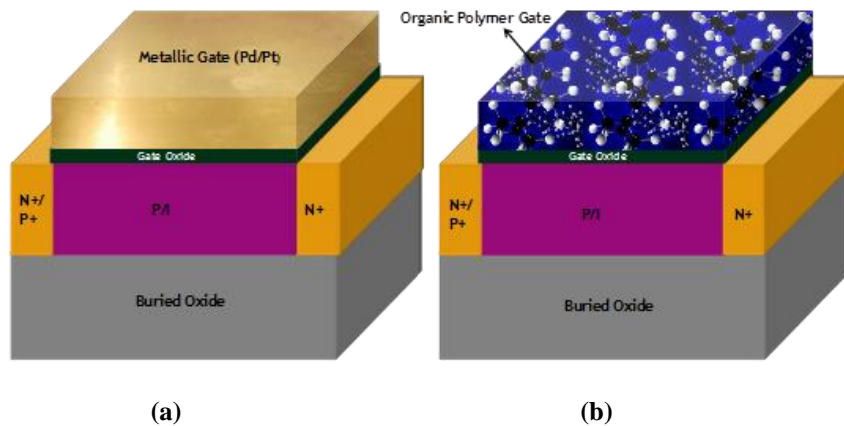


Figure 4.29. The schematic diagram of a Field-Effect-Transistor gas-sensor based on SOI structure with metallic gate **(a)** and organic conducting polymer gate **(b)** as the sensing element. For conventional n-type MOSFET based sensor, the doping in source, channel and drain are N+, P and N+, respectively while for that based on n-type TFET, the sequence is P+, I and N+. Continuous Pd and Pt film is explored for metallic gates, while polyaniline and polypyrrole are discussed for polymer gates. Semiconductor material is taken to be Silicon. Note that we use the term MOSFETs generically to specify conventional FETs even in case of a polymer gate.

In this section, we propose a gas sensor that leverages the band-to-band-tunneling current-injection mechanism of TFET to achieve much superior performance under ambient conditions compared to conventional FETs.[211] The results are discussed in

terms of two important sensing elements: metal (Pd/Pt) and conducting polymers as the gate material (**Figure 4.29**).

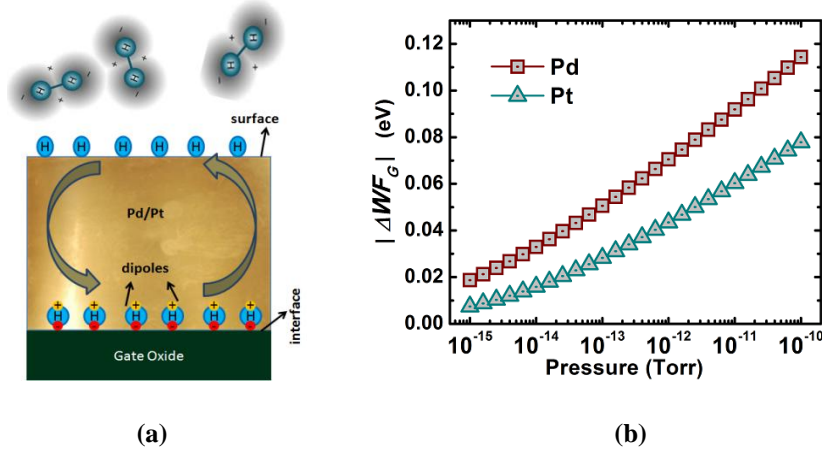


Figure 4.30(a) The schematic diagram of dipoles at the interface of metal and oxide layer. **(b)** Change in work-function of Pd and Pt metal gate as a function of hydrogen gas pressure. Interface concentration of hydrogen sites and sticking coefficient is lower for Pt [220] compared to Pd leading to lower values of ΔWF_G for same hydrogen pressure. Note that ΔWF_G is negative and absolute values have been plotted here.

First, we will discuss the gas-sensors with metallic gate as sensing element. Thick, continuous metallic gate can be used to sense hydrogen [221], [222]. The transduction mechanism involves dissociation and adsorption of hydrogen molecules at the metal surface and thereby diffusion of some atomic hydrogen into metal which form dipoles at the interface changing the gate work function (WF_G) (**Figure 4.30(a)**). This process depends on the flux of gas Ψ given by $\Psi = P/\sqrt{2\pi m_g K_B T}$, heat of adsorption at surface ΔH_s and interface ΔH_i , which follows the Tempkin Isotherm as $\Delta H_i = \Delta H_{i0}(1 - \alpha \xi_i)$ where $\alpha = q\mu N_i / (\varepsilon \Delta H_{i0})$, P : gas pressure, m_g : gas molecular mass, K_B : Boltzmann constant, T : temperature, ΔH_{i0} : initial heat of adsorption, ξ_i : interface coverage of hydrogen, N_i : concentration of interface hydrogen sites, q : elementary

charge of an electron, μ : effective dipole constant, ε : permittivity. The change in work function is given by [222]

$$\Delta WF_G = -(\xi_i N_i \mu) / \varepsilon \quad (4.24)$$

Figure 4.30(b) shows the ΔWF_G of metal gate as a function of hydrogen gas pressure.

The ΔWF_G can be employed to bend the bands in a TFET and hence modulate its current. A non-local 2D model based on self-consistent solutions of Poisson's and Schrodinger's equations including the effect of phonons, is used for detailed device simulations. At the same time, in order to provide better physical insights, an analytical expression for sensitivity (S_n) is derived using simplified 1D model. The 1D Poisson's equation (4.25) is solved to obtain the potential in the channel assuming high source doping and hence neglecting band bending in source.

$$\frac{d^2 \phi_i(x)}{dx^2} - \frac{\phi_i(x) + V_G - WF_G + WF_S}{\lambda^2} = 0 \quad (4.25)$$

Here, ϕ_i : potential at semiconductor-oxide interface, WF_S : semiconductor work function, V_G : gate voltage, λ : natural length scale [1]. Then, calculating tunneling probability using the WKB approximation and the two-band approximation, the band-to-band-tunneling current (I_{BTBT}) is derived using Landauer's formula [148] following the procedure described Chapter 3 [146] as

$$I_{BTBT}(WF_G) = 2q^2/h \exp\left(-\pi \sqrt{q} m^{*1/2} E_G^{3/2} \lambda / (\sqrt{2\hbar} (2(V_G - WF_G + WF_S) - E_G))\right) \times \int_0^{V_G - WF_G + WF_S - E_G} (f_S - f_D) dE \quad (4.26)$$

Here, h : Plank's constant, m^* :carrier effective mass, E_G : bandgap of semiconductor, f_s : Fermi function at source, f_d : Fermi function at drain.

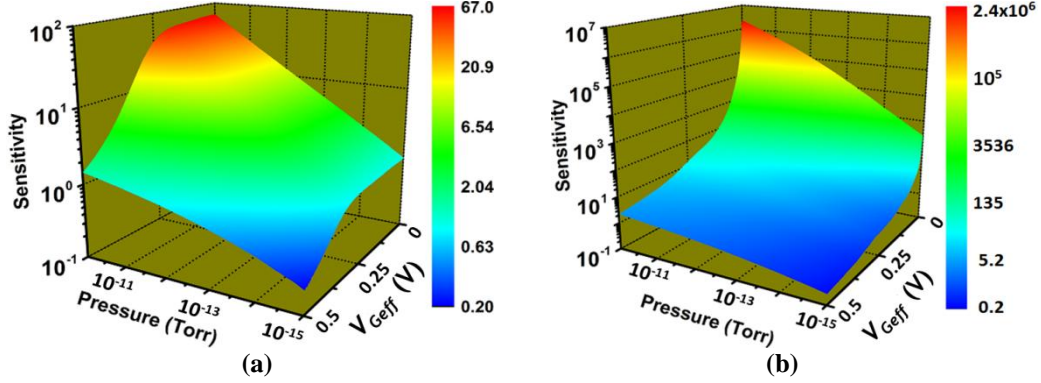


Figure 4.31(a) Color-map showing the importance of gate bias and operation regime of FET on performance of MOSFET (a) and TFET (b) gas-sensor. Pd is used as a gate material. For convenience of plotting and understanding, the effective gate voltage is offset from the actual gate voltage such that for MOSFET, V_{Geff} is taken to be 0 at 0.35eV lower than the threshold voltage. For TFET $V_{Geff}=0$ where the subthreshold swing (SS) is minimum. At any value of gas pressure, sensitivity of MOSFET gas-sensor remains almost constant for lower values of V_{Geff} due to the almost constant SS of MOSFET. However, with increase in V_{Geff} , effect of gate decreases as MOS crosses the subthreshold region and hence the sensitivity degrades. For TFET gas-sensor, sensitivity keeps on increasing as V_{Geff} is decreased due to the improvement in SS . By effective tuning of gate bias, sufficient improvement in sensitivity can be achieved through TFET gas-sensor compared to that of MOSFET gas-sensors.

Sensitivity (S_n) is defined as the ratio of change in current after gas adsorption to the initial current before gas adsorption and is given by

$$S_n = \{I_{BTBT}((V_G - WF_{G0}) - \Delta WF_G) - I_{BTBT}(V_G - WF_{G0})\} / I_{BTBT}(V_G - WF_{G0}) \quad (4.27)$$

Using equation (4.24), (4.26) and (4.27), S_n of TFET gas sensor is derived as

$$S_n = \exp \left(\frac{\pi \sqrt{2q} m^{*1/2} E_G^{3/2} \lambda (\xi_i N_i \mu) / \varepsilon}{\hbar (2(V_G - WF_{G0} + WF_s) - E_G) (2(V_G - WF_{G0} + WF_s) + 2(\xi_i N_i \mu) / \varepsilon - E_G)} \right) \times \left(1 + \frac{(\xi_i N_i \mu) / \varepsilon}{V_G - WF_{G0} + WF_s - E_G} \right) - 1 \quad (4.28)$$

In **Figure 4.31 (a)** and **(b)**, S_n is plotted as a function of the gate bias and the gas pressure for MOSFET and TFET respectively. It is observed that for both, maximum S_n is obtained in the subthreshold region. This can be understood since the highest effect of gate occurs in the subthreshold region. In MOSFETs the Subthreshold Swing (SS) is limited by the Boltzmann Tyranny effect to $[k_B T/q \ln(10)]$, which also puts severe limitations on the achievable sensitivity. TFETs overcome this limitation due to Fermi-tail cutting by the bandgap and hence can lead to significantly higher S_n for gas sensing as shown in **Figure 4.32**.

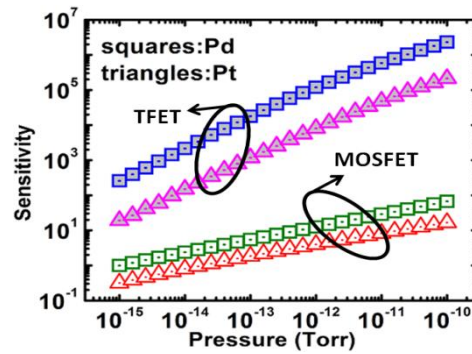


Figure 4.32. Comparison of sensitivity of MOSFET and TFET gas-sensor both biased at $V_{Geff}=0$.

Now, we will focus on organic conducting polymer gate as sensing element. Organic conducting polymers can be used to obtain selective detection of specific target gas molecules. The gas molecules form a charge transfer complex with the polymer matrix through the exchange of a fractional charge δ [223], [224]. Depending on the sign(positive/negative) of δ , the gas molecules behave as a secondary dopant (acceptor/ donor) and change the Fermi level and hence the bulk component of work function of the polymer(WF_P). ΔWF_P is given by [224]

$$\Delta WF_P = K_B T / 2 \delta \ln \left(P / \sum_i k_i P_i + 1 \right) \quad (4.29)$$

where $\delta = \gamma(E_F - \chi_g)$, E_F : Fermi level of polymer, χ_g : Mulliken electro-negativity coefficient of gas, P_i : pressure of background non-specific gases, k_i : selectivity coefficients, WF_{P0} : work function before gas absorption, γ : proportionality constant [223]. Using equations (4.26), (4.27) and (4.29) analytical formula for sensitivity of TFET gas-sensor is derived as

$$S_n = \exp \left(\frac{\pi \sqrt{2q} m^{*1/2} E_G^{3/2} \lambda |\Delta WF_P|}{\hbar (2(V_G - WF_{PS0}) - E_G) (2(V_G - WF_{PS0}) + 2|\Delta WF_P| - E_G)} \right) \times \left(1 + \frac{|\Delta WF_P|}{V_G - WF_{PS0} - E_G} \right) - 1 \quad (4.30)$$

where ΔWF_{PS0} is initial work function difference between polymer and semiconductor. From **Figure 4.33(a)** and **(b)**, it is clear that TFETs provide substantial increase in S_n compared to conventional FETs as shown for detection of NH_3 and CH_3OH with Polyaniline (PANI) and poly-pyrrole-tetrafluoroborate (PPTFB), respectively. The change in WF of polymers depends on its initial WF (WF_{P0}), which varies with varying growth conditions [223]. If E_F equals χ_g , no charge transfer takes place and $\Delta WF_P = 0$. We call this point the neutrality point (NP). $|\Delta WF_P|$ increases as WF_{P0} moves away from NP. For MOSFETs reasonable S_n is obtained only further away from NP (**Figure 4.33(c)**) and thus requires high control of polymer growth conditions to achieve specific WF_{P0} . In TFETs high S_n can be achieved even in regions near NP (**Figure 4.33(c)**) and thus providing flexibility and facilitating ease of polymer growth process.

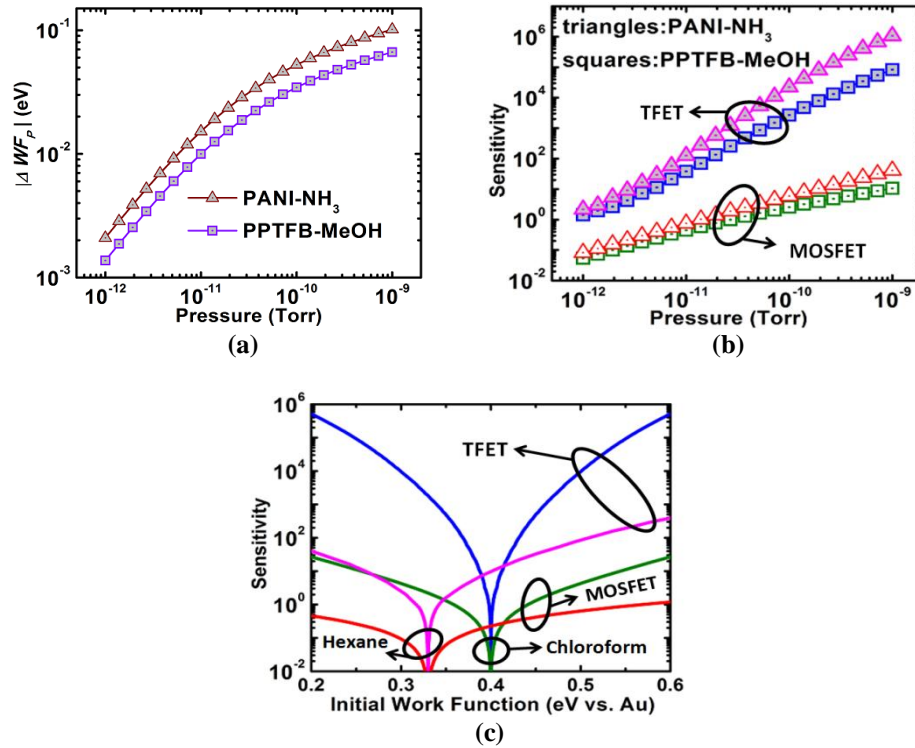


Figure 4.33(a) Change in work-function of polymer gate (a) and sensitivity comparison of TFET and MOSFET sensors (b), as a function of gas pressure. Results are shown for sensing of ammonia with polyaniline (PANI) and Methanol with poly-pyrrole-tetrafluoroborate (PPTFB). The effect of non-specific background gases is captured through the term $\sum k_i P_i$ and is taken to be 10^{-11} in both cases. Sensitivity of MOSFET and TFET gas-sensor with polymer gate based on polypyrrole and p-polypyrrole for sensing Hexane and Chloroform as a function of initial work function of the polymer (versus the work function of the Au reference grid). TFET gas-sensors lead to much higher sensitivity compared to those based on MOSFETs even in the region near the neutrality point.

In **Figure 4.34**, S_n is plotted as a function of SS taking an example each from metallic gate as well as polymer gate as sensing element. It is observed that in both cases S_n increases substantially with the decrease in SS . This figure has important technological implications and shows that extremely high S_n can be achieved through implementation of low SS devices like TFETs in gas-sensor technology.

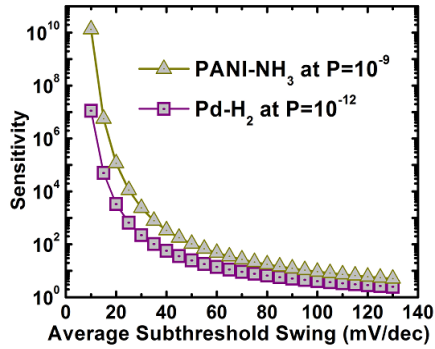


Figure 4.34. Sensitivity as a function of average subthreshold swing for both metallic gate (Pd for sensing hydrogen at pressure of 10^{-9} Torr) as well as polymer gate (PANI for sensing ammonia at pressure of 10^{-12} Torr) as the sensing element.

To be applicable for practical applications, a sensor should possess high efficiency under ambient conditions in the presence of non-specific background gases. In the case of polymer film, it is clear from equation (4.29) that increase in $\sum k_i P_i$ term (which represents the effect of background gases) decreases ΔWF_P . In the case of metallic gate, the presence of oxygen in air sufficiently reduces the surface and interface coverage of hydrogen (**Figure 4.35(a)**) and hence the $|\Delta WF_G|$ (**Figure 4.35(b)**) due to water formation and subsequent desorption reactions [225]. From **Figure 4.35(c)** it is observed that if the SS is reduced, the $|\Delta WF_G|$ required to achieve a desired sensitivity can be more than an order lower. Hence, TFETs with low SS can be highly beneficial in detection of target gas molecules under atmospheric conditions where presence of non-specific gases screen the change in gate work function.

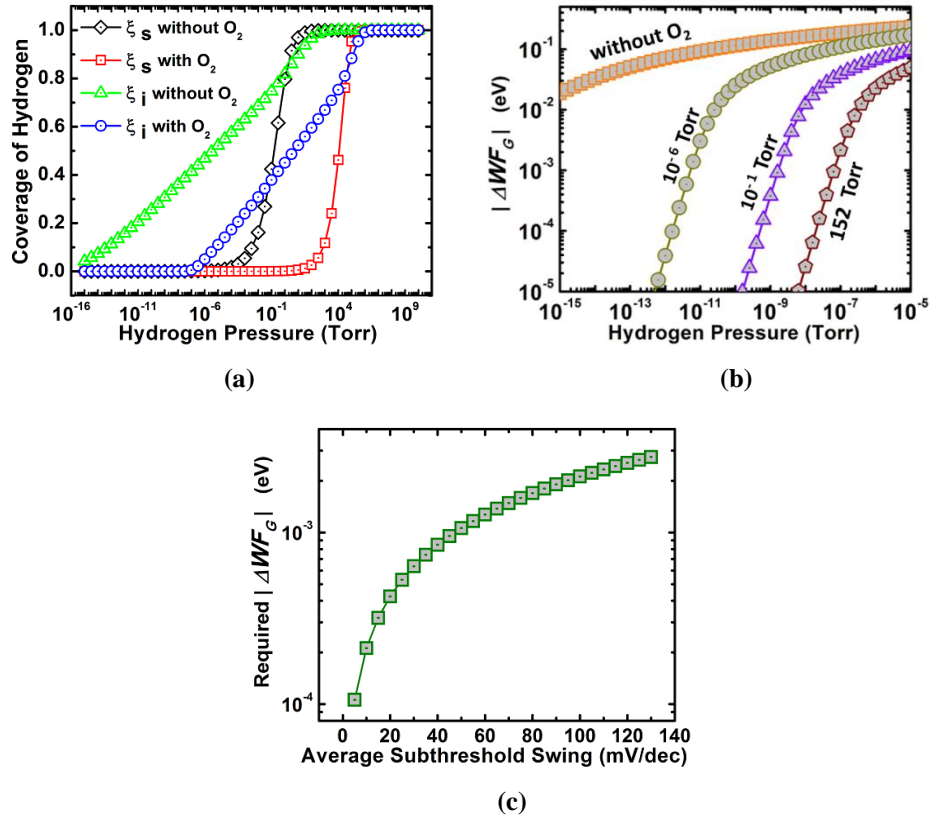


Figure 4.35(a) The surface (ξ_s) and interface (ξ_i) coverage of hydrogen in Pd without and in the presence of oxygen (152 Torr) as a function of hydrogen pressure. **(b)** Effect of varying oxygen pressures (10^{-6} - 152 Torr) on $|\Delta WF_G|$. ξ_s , ξ_i and $|\Delta WF_G|$ decrease in the presence of oxygen **(c)** The change in gate work function that is required to obtain a desired sensitivity (here the desired value is taken to be 0.05) is plotted as a function of the average Subthreshold Swing. The required $|\Delta WF_G|$ decreases strongly with decrease in SS. Hence, the same sensitivity can be achieved at much lower values of $|\Delta WF_G|$ for low SS devices like TFET.

For stable operation, the influence of temperature (T) variations on the sensor performance should be minimal. T affects the sensor performance by influencing i) interaction between gas and sensing element and ii) properties of semiconductor. Here, the effect of T is discussed taking the metallic gate as an example and it is seen that the increase in T leads to the reduction in hydrogen coverage and hence the $|\Delta WF_G|$ (**Figure 4.36(a)**).

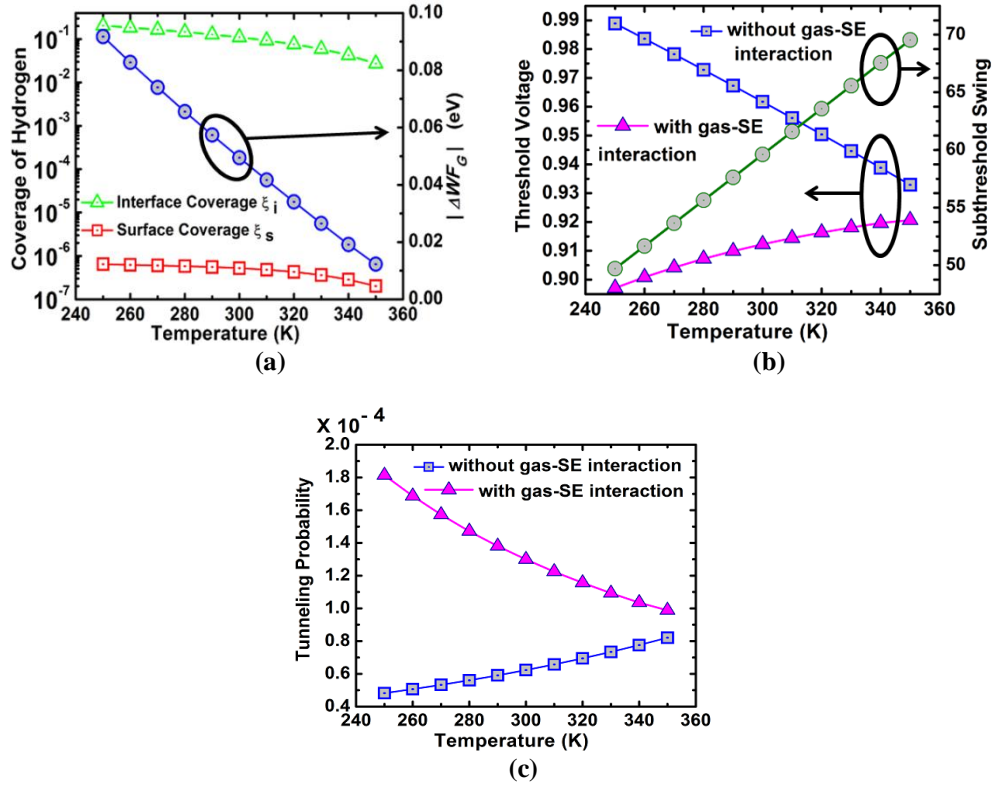


Figure 4.36. Effect of temperature (T) variations on gas-sensor performance. $|\Delta WF_G|$ decreases with T due to decrease in the surface (ξ_s) and interface (ξ_i) coverage of hydrogen (a). A_{T-MOS} is dominated by change in threshold voltage (V_{th}) through modification in interaction term between gas and sensing element (SE) ($\mu N_i \xi_i / \epsilon$) and semiconductor properties (ϕ_b , E_G and EA) and the change in SS (b). A_{T-TFET} is dominated by change in tunneling probability through modification of WF_G (due to gas-SE interaction) and semiconductor bandgap (c).

We define the T affectability (A_T) as

$$A_T = \{I(T + \Delta T) - I(T)\} / I(T) \quad (4.31)$$

Analytical equations of T affectability are derived for both MOSFET (A_{T-MOS}) and TFET (A_{T-TFET}) based gas-sensors and are given by

$$A_{T-MOS} = \exp\left(-\frac{(N_i \mu \Delta \xi_i) / \varepsilon + \Delta \varphi_b - \Delta E_G / 2 - \Delta EA}{K_B (T + \Delta T) / q}\right) \times \exp\left(-\frac{\Delta T / T (V_G - WF_G - \varphi_b + E_G / 2 + EA - qNa t_{Si} / C_{ox})}{K_B (T + \Delta T) / q}\right) - 1 \quad (4.32)$$

$$A_{T-TFET} (WF_G) = \exp\left(-\pi \sqrt{qm}^{*1/2} \lambda / \sqrt{2\hbar} \times \Delta Fnc (T)\right) - 1 \quad (4.33a)$$

$$Fnc (T) = E_G (T)^{3/2} / (2(V_G - WF_G (T) + WF_S (T)) - E_G (T)) \quad (4.33b)$$

Here, φ_b : energy difference between Fermi level of semiconductor and its intrinsic Fermi level, EA : electron affinity of semiconductor, Na : channel doping concentration, t_{Si} : silicon thickness, C_{ox} : gate capacitance. T influence MOSFET subthreshold current mainly through change in the threshold voltage (V_{th}) and SS . It is well known that in MOSFETs, V_{th} decreases as T increases. However, the MOSFET gas-sensor exhibits a counter-intuitive opposite trend (**Figure 4.36(b)**). This behavior can be explained by the increase in $WF_G (=WF_{G0} - |\Delta WF_G|)$ with T due to decrease in gas adsorption and hence $|\Delta WF_G|$. The SS of MOSFET increases linearly with T . For a silicon TFET for digital applications, it has been experimentally demonstrated [226] that dominant factor through which T influences the current is through increase in the tunneling probability (P_{BTBT}) due to the decrease in bandgap (E_G) (phonon emission is nearly independent of T). For TFET gas-sensor, the situation is different and the factor through which T dominantly affects the current is given by $Fnc(T)$ (equation (4.33b)). It is observed that the increase in P_{BTBT} due to decrease in E_G is offset by the increase in WF_G term that occurs in the denominator of $Fnc(T)$. Hence, P_{BTBT} of TFET gas sensor decreases with T (**Figure 4.36(c)**). From **Figure 4.37(a)**

and (b), it is clear that the TFET has substantially lower A_T than that of MOSFETs and hence it is much less vulnerable to T variations.

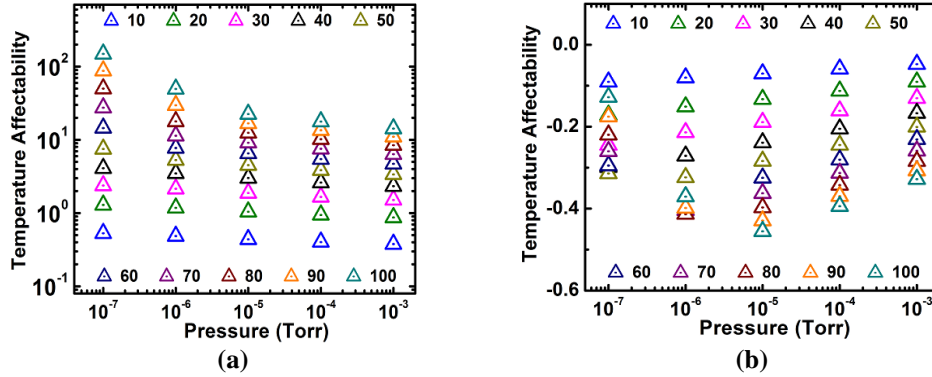


Figure 4.37. A_T is plotted for MOSFET (d) and TFET (e) with $T=250$ K and ΔT varying from 10K to 100K. A_T is positive in MOSFET (current increases with T) due to the increase in SS compensated to some extent due to increase in V_{th} . A_T is negative in TFET due to the decrease in tunneling probability with T . Overall A_{T-TFET} is much smaller than $A_{T-MOSFET}$. Note, that the isothermal point (IP) of MOSFET occurs in the linear region, which will lead to degraded sensitivity and IP will vary with gas adsorption. Hence, a TFET based gas-sensor can offer much more stable operation under T variations compared to that based on MOSFETs.

4.4. Summary

In this chapter, we show that, while 2D semiconductors and steep transistors have mainly evolved with an aim of obtaining ultra-scalability and reduction of power consumption in digital electronics, they also hold great promise in a completely diverse arena of bio/gas-sensor technology. Here, we demonstrated FET biosensors based on molybdenum disulphide (MoS_2) which provides extremely high sensitivity and at the same time offer easy patternability and device fabrication, thanks to its 2D atomically layered structure. While graphene is also a 2D material, we show here that it cannot compete with MoS_2 based FET biosensor, which surpasses the sensitivity of that based on graphene by more than 74-fold. Moreover, we establish through

theoretical analysis that MoS₂ is greatly advantageous for biosensor device scaling without compromising its sensitivity. Furthermore, MoS₂ with its highly flexible and transparent nature can offer new opportunities in advanced diagnostics and medical prosthesis. This unique fusion of desirable properties makes MoS₂ a highly potential candidate for next-generation low-cost biosensors. Apart from biosensing, it is also shown that MoS₂ can also be used for gas sensing applications through functionalization of its surface by noble metallic nanoparticles. While MoS₂ has these excellent properties as a channel material, we elucidate that conventional FET based sensors suffer from fundamental limitations on the maximum sensitivity and minimum detection time achievable due to their fundamental limitations in subthreshold swing. We proposed and theoretically demonstrated that sensors based on steep transistors can overcome such limitations and lead to substantially higher sensitivity (over four orders of magnitude) and over an order of magnitude lower response time and hence, are highly desirable for sensing applications.

Subthermionic Transistor

5.1. Introduction

The unprecedented growth of Information Technology has historically been sustained by scaling the Metal-Oxide-Field-Effect-Transistors (MOSFETs), following the rules, prescribing the reduction of the critical dimensions of the FET and the operating voltage by the same factor, so that transistor density is increased without the corresponding rise in the power density. However, as discussed in Chapter 1, the current MOSFET technology faces two major issues, which pose serious challenges for further scaling. The first issue is the degradation of device electrostatics (or ability of the transistor's gate electrode to control its channel potential), with decrease in the transistor channel length, when conventional 3D (or bulk) materials are used as channel. In Chapter 2, we studied 2D layered semiconducting materials such as Transition Metal Dichalcogenides (TMDs) and black Phosphorous, which are highly promising as channel material in FETs, for mitigating this effect and hence, have attracted a lot of attention, recently [3], [5], [39], [60], [61], [63], [227]. Their ultra-thin structure and pristine interfaces can lead to excellent electrostatics and at the same time their planar nature facilitates easy fabrication compared to 1D structures

(such as nanowires and nanotubes) that can also provide excellent electrostatics but are far less fabrication-friendly.

Even in presence of excellent electrostatics, the inability to scale down the supply voltage leads to the increase in power density, compromising the benefits of scaling. This arises from the fundamental thermionic limitation of the subthreshold swing (inverse of the subthreshold slope given by $SS = (d \log_{10} I_{DS} / dV_{GS})^{-1}$ where I_{DS} : drain-to-source current, V_{GS} : gate-to-source voltage) of $2.3K_B T/q$ (or 60 mV/dec at room temperature) in conventional FETs. Thus, using just 2D semiconducting-channel materials only partially addresses the scaling issue, and use of novel device technology based on 2D materials is necessary for simultaneous achievement of efficient electrostatics as well as novel carrier transport mechanism (as explored in Chapter 3), in order to achieve sub 60 mV/dec SS and thereby, combat power density increase and enable scaling to continue in future. Apart from digital electronics, achievement of a 2D semiconducting-channel material based device with sub-thermionic SS will be highly desirable for next-generation ultra-sensitive, low-power and fast bio/gas sensors as elucidated in Chapter 4. Toward these ends, an important milestone is achieved in this dissertation, with the first demonstration of planar transistors based on 2D semiconducting material, which overcomes the fundamental limitation in SS of conventional FETs and offers a minimum SS of 3.9 mV/dec and an average SS of 31.1 mV/dec for over 4 decades of drain current at room temperature.[81] This is achieved by using a fundamentally different transport

mechanism in the form of quantum mechanical band-to-band tunneling (BTBT)[126], [135].

5.2. Challenges and Novel Solution through 3D-2D Hetero-TFET

Tunnel-FET (TFET) utilizing BTBT,[103], [127]–[132] is a promising candidate for achievement of sub-thermionic *SS*. In spite of high interest in TFETs with 2D materials as channel due to the advantages mentioned above, and experimental works[228], [229] towards this direction using electrostatic doping technique, there has not been any successful experimental demonstration of a TFET and for that matter any transistor based on 2D material with sub-thermionic *SS*, to date. This is due to the challenges in doping the 2D layered materials and in obtaining high electric field at the tunnel junctions. Moreover, use of electrostatic doping requires an extra gate electrode for functioning and hence, is not energy-efficient. Here, we built an unique vertical TFET with sub-thermionic *SS*, by engineering the substrate, portions of which are configured as a highly doped semiconductor source and other portions are etched and filled with a dielectric for hosting the drain and gate metal contacts, while ultrathin 2D TMD forms the channel (**Figure 5.1(a)**, in the diagram Ge and MoS₂ are used as the example of 3D and 2D materials, respectively).[81] This TFET structure offers several unique advantages as explained below. First, the use of 2D TMD material as channel attributes not only excellent electrostatics but also, small tunneling distance (which is determined by the channel thickness), needed for increasing the BTBT current. Note that using 3D material as the source does not

hamper device electrostatics, as the channel region is the one that needs to get modulated by the gate and it is atomically-thin in our case. Second, combining 3D and 2D materials opens up unprecedented opportunities for designing custom-built heterostructures. Third, the heterojunction is formed with van der Waal's bond and thus has strain free interfaces. Fourth, while methodologies for obtaining stable as well as high doping in 2D layered materials is very challenging and still under investigation, 3D materials already enjoy well developed doping technologies that has been leveraged in this work, for forming highly doped source. This enables the creation of ultra-sharp doping profile and hence, high electric field at the source-channel interface as there is negligible chance of diffusion of dopant atoms across the heterojunction due to the presence of van der Waal's gap. Last but not the least, since 2D channel material is placed on top of 3D source forming a vertical source-channel junction, BTBT can take place across the entire area of channel-source overlap, which leads to higher ON-current than that in case of line overlap obtained in lateral junctions.

It is important to emphasize here, that though we are using the term Tunnel-FET in a general way, our device specifically is a Band-to-Band Tunnel-FET, involving transition of carriers from the valence band (of 3D source) to the conduction band (of 2D channel). Though "tunneling-transistors" using heterostructures of 2D materials have been reported in literature,[230], [231] they did not involve BTBT and hence,

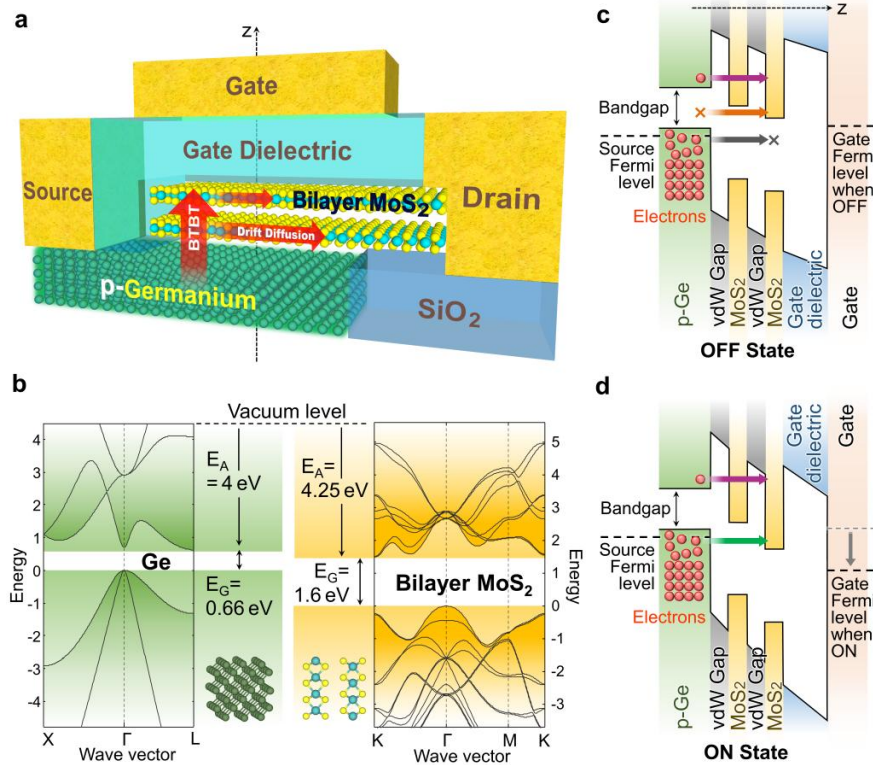


Figure 5.1 (a) Schematic diagram illustrating the cross-sectional view of the ATLAS-TFET with ultra-thin bilayer MoS₂ (1.3 nm) as channel and degenerately doped p-type Ge as the source. Path for electron transport is shown by the red arrows which run vertically from the Ge source to the MoS₂ and then laterally through the MoS₂ layers to the drain. As the Ge is highly doped, the tunneling barrier height is mainly determined by the effective bandgap of MoS₂ (including van der Waals gap) while the tunneling width is determined by the MoS₂ thickness. (b) Band alignment of Ge and bilayer MoS₂ showing their electron affinities (E_A) and bandgaps (E_G) and thus, illustrating the formation of a staggered vertical heterojunction. The crystal structure of both the materials are shown below while the bandstructures are shown on both sides. Band diagrams along vertical dashed line in (a), in both OFF (c) and ON (d) states. The white regions represent the forbidden gaps (zero density of states). While the effective bandgap of bilayer MoS₂ has been illustrated in (b), here the bands for the two layers are shown separately with the van der Waal's (vdW) gap between them for better visual interpretation of current flow. Note that the drain contact is located perpendicular to the plane of the figure and is not shown in it. In the OFF state, electrons from the valence band of Ge, cannot transport to MoS₂ due to the non availability of density of states (*DOS*) in MoS₂ (black arrow and cross sign). At higher energies, empty *DOS* is available in MoS₂, but no *DOS* is available in Ge, again forbidding electron flow (orange arrow and cross mark). With further increase in energy reaching above the conduction band of Ge, *DOS* is available in both Ge and MoS₂. However, the number of electrons available in the conduction band of Ge source is negligible due to the exponential decrease in electron concentration with increase in energy above the Fermi level according to Boltzmann distribution. Thus, very few electrons can flow to the MoS₂ (purple arrow), leading to very low OFF-state current. With the increase in gate voltage (d), when the conduction band of MoS₂ at the dielectric interface, is lowered below the valence band of the Ge source, electrons start to flow (green arrow), resulting in an abrupt (sub-thermionic) increase in BTBT current.

cannot lead to sub 60 mV/dec SS , because of the fundamental inability of single carrier tunneling barrier to provide the same (as explained in Chapter 3).

The band alignment is shown in **Figure 5.1(b)**. **Figure 5.1(c)** and **(d)** demonstrates the operation of our Atomically-thin and Layered Semiconducting-Channel Tunnel-FET or ATLAS-TFET through the band diagrams along vertical dashed line in **Figure 5.1(a)**, in OFF (**Figure 5.1(c)**) and ON (**Figure 5.1(d)**) states. Here, n-type transistor is achieved where positive voltage is applied to the drain electrode contacting the MoS_2 layers with respect to the highly p-doped Ge source. Hence, electrons tend to move from the Ge to the MoS_2 and this electron transport can be modulated by the gate to turn the device ON or OFF. In the OFF state, only electrons above the conduction band of Ge can transport to MoS_2 (purple arrow), leading to ultra-low current due to the scarcity of available electrons at high energies above the Fermi level. At lower energies, no electrons can flow either due to the non-availability of Density of States (DOS) in Ge source (orange arrow) or in MoS_2 channel (black arrow). Hence, the OFF current is very low. As the gate voltage is increased, the conduction band of MoS_2 , is lowered below the valence band of the Ge source (ON state), and hence filled DOS in the source gets aligned with empty DOS in the channel, leading to an abrupt increase in electron flow (green arrow) and hence, current, which can lead to sub-thermionic SS . Electrons after tunneling from the Ge source to the MoS_2 , are sucked in laterally by the drain contact as shown by the red arrows in **Figure 5.1(a)**.

5.3. Exploration of 3D-2D Tunnel Junctions

As discussed in the previous section, heterostructures formed by combining 3D and 2D materials can be highly promising for building TFETs. In order to achieve the optimum heterojunction with high BTBT, a detailed exploration of different 3D and 2D materials is carried out here.[232] For forming the tunnel junctions, the layered semiconductor material was obtained by micromechanical exfoliation from bulk sample and was transferred to the desired highly doped conventional material. The thicknesses of the layered materials were characterized using Atomic Force Microscopy (AFM). An AFM image along with height profile of a MoS₂ flake on Si is shown in **Figure 5.2**. While for building the TFETs atomically thin films as channel are required, for characterizing the channel junctions, relatively thick films are used here, as they are comparatively easy to obtain.

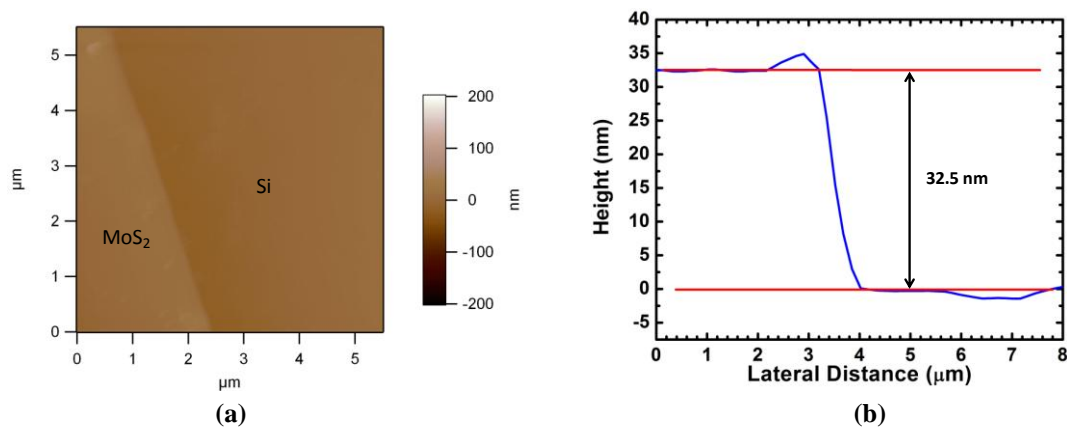


Figure 5.2 (a) Atomic force microscope (AFM) image of a MoS₂ flake on Si. (b) Height profile of MoS₂ showing that the MoS₂ has a thickness of about 32.5nm.

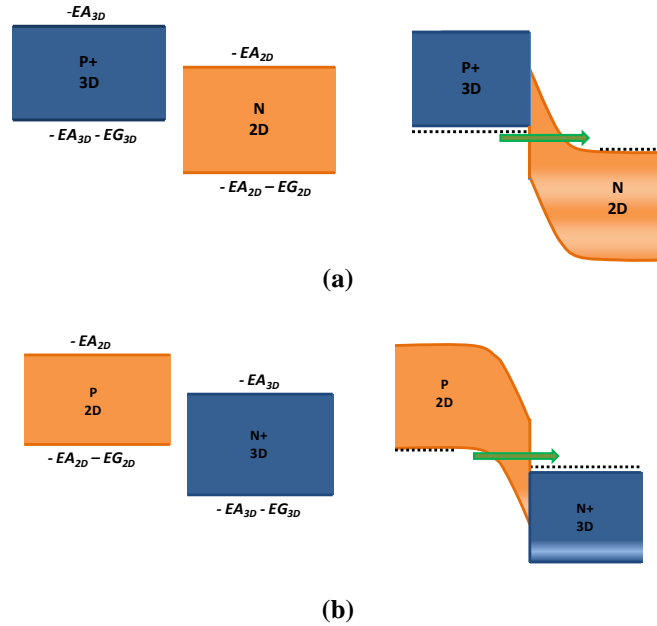


Figure 5.3(a) Schematic diagram illustrating the cross-sectional view of the p-n heterojunction formed by the combination of 3D and 2D materials. There are two main types of junctions possible from the doping point of view. Either, the 3D material is highly p-doped with the 2D material forming the n-region, or the 3D material is highly n-doped and the 2D material forms the p region. Band alignment and band bending required to obtain efficient BTBT for 1st (a) and 2nd case (b). The band overlap between p and n regions should be minimized for lowering the tunneling barrier and increasing the BTBT. Hence, the electron affinities and bandgaps of both the materials should be chosen appropriately for minimizing the band overlap. The green arrows indicate the flow of electrons due to BTBT.

Since, stable and efficient doping of 2D materials still remains a challenge, the 2D materials used in this work are without any external doping. To increase the junction electric field, the 3D material has been highly doped taking advantage of the well-developed doping technologies for conventional semiconductors. The heterojunction explored in this work can be divided into two main categories. In the first category, the 3D material is highly P-doped with high workfunction (WF) metal contact while, a low WF metal contacts the 2D material. In this case, to obtain low band overlap at the interface, the sum of electron affinity (EA) and bandgap (EG) of the 3D material should be low while the EA of 2D material should be high (**Figure 5.3(a)**). For the

second category, the favorable heterojunction is that between a degenerately N-doped 3D material with high EA and a 2D material with low $EA+EG$ (**Figure 5.3(b)**).

Figure 5.4 shows the optical image of a prototype device.

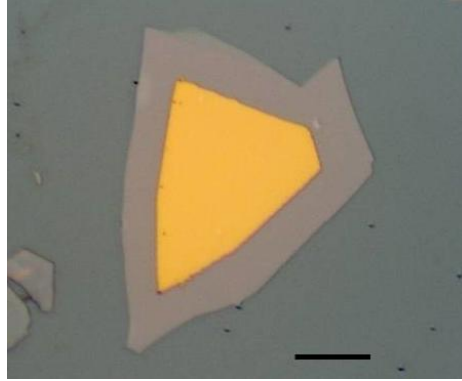


Figure 5.4. Optical micrograph of a prototype fabricated device showing the metal contact on the 2D material. Metal contact for the 3D material is not shown. The materials in this case are highly n-doped InGaAs and 30 nm WSe₂ without any external doping. Scale bar: 10 μm .

5.3.1. Junction with Highly P-doped 3D Material

In this section, we present the electrical characterization of the 1st category of hetero-junctions. The P-N junction characteristics of Si-MoS₂ junction is shown in **Figure 5.5(a)**. Si is chosen as the 3D material as it has relatively low EA among the common 3D semiconductors, while MoS₂ is used as the 2D material as it is naturally N-doped and has relatively high EA among most commonly characterized 2D semiconductors. The main region of interest in this work is the reversed biased characteristics ($V_p < 0$) of the hetero-junctions, where the current is dominated by the BTBT. It is observed that the BTBT current is almost independent of the thickness of the MoS₂ which is varied from 30 nm to 130 nm. This is because, at thicknesses higher than that of the depletion region, the bands remain almost flat (**Figure 5.5(b)**).

Hence, increasing the thickness of MoS₂ above that of the depletion region, does not lead to any change in band bending at the interface and hence, negligible change in BTBT is observed. Also, it is noteworthy that Negative Differential Resistance (NDR) characteristics which are obtained in highly doped P-N junctions at low forward bias ($V_p > 0$), are not observed here due to the low doping level in MoS₂ and hence, small energy window (ΔE) for tunneling at low forward bias (**Figure 5.5(b)**).

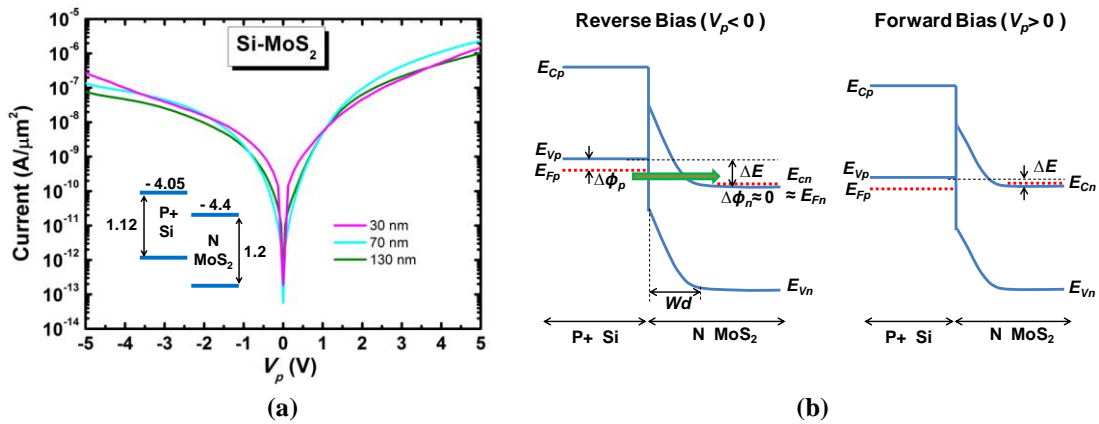


Figure 5.5(a) P-N junction characteristics of heterojunction formed between P+ Si and naturally N doped MoS₂ for different thicknesses of the MoS₂ varying from 30 nm to 130 nm. Bias is applied on the P-region (V_p) while the contact to N-region is grounded. The characteristics is shown in both forward ($V_p > 0$) as well as reverse ($V_p < 0$) bias conditions. Inset figure shows the band alignment of Si-MoS₂ junction along with the values for EA and EG for both materials. **(b)** Band diagram of the Si-MoS₂ junction in forward and small reverse bias conditions. Here, E_{vp} , E_{cp} and E_{fp} are the valence band, conduction band and Fermi level respectively, in the P region, while E_{vn} , E_{cn} and E_{fn} represent those in the N region. $\Delta\phi_p$ is the energy gap between the valence band and Fermi level of P region while $\Delta\phi_n$ is the energy gap between the conduction band and Fermi level of N region. ΔE is the energy window between the valence band of P region and conduction band of N region. Wd is the depletion region in the layered material.

When MoS₂ with higher N-doping is used a trend towards NDR is observed as shown in **Figure 5.6**. The difference of this device from the junctions with MoS₂ presented above (**Figure 5.5**) is that the MoS₂ flake used to fabricate this heterostructure is exfoliated from a bulk sample having higher natural n-doping.

Higher n-doping is confirmed by shift of threshold voltage to more negative gate biases when FETs were fabricated with MoS₂ from this bulk sample compared to that used for the structures shown in **Figure 5.5**. This higher n-doping in MoS₂, leads to higher energy window for tunneling at forward bias. The crossover of current from tunneling to thermionic emission is seen as a trend towards NDR in the forward bias characteristics. If MoS₂ could be externally n-doped to very high levels, then observation of prominent NDR could have been possible.

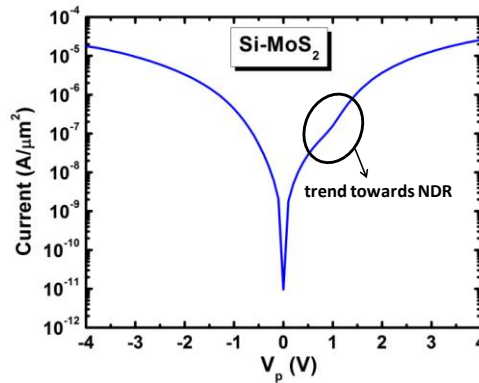


Figure 5.6. Current as a function of V_p in both forward and reverse bias of a Si-MoS₂ junction showing trend towards NDR at forward bias. Thickness of MoS₂ used here is 70 nm.

Overall, the BTBT current obtained from Si-MoS₂ junction is low and not very promising for building electronic switches. For improving the BTBT current, Ge can be the potential 3D material as it not only possesses low EA like Si, but also has lower EG which reduces $EA+EG$ and hence, the band overlap at the Ge-MoS₂ interface (inset **Figure 5.7**). This leads to extremely high BTBT current at the reverse bias condition as show in **Figure 5.7**.

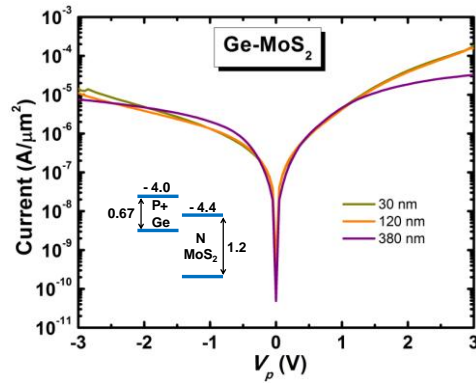


Figure 5.7. P-N junction characteristics of heterojunction formed between P+ Ge and naturally N doped MoS₂ for different thicknesses of the MoS₂ varying from 30 nm to 380 nm. Inset figure shows the band alignment of Ge-MoS₂ junction along with the values for EA and EG for both materials.

The BTBT current can be further boosted by using Black Phosphorous as the 2D material which has even higher EA than MoS₂ leading to a negative band overlap or broken junction with Ge (inset **Figure 5.8**). For clear comparison, the BTBT current for the Si-MoS₂, Ge-MoS₂ and Ge-BP hetero-junctions, with the same film thickness of the 2D material in all the three cases, has been plotted in **Figure 5.8**, demonstrating the importance of interface band-engineering and the versatility of 3D-2D hetero-junctions.

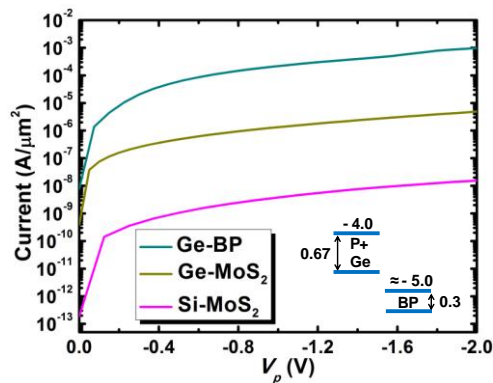


Figure 5.8. Comparison of BTBT current between Si-MoS₂, Ge-MoS₂ and Ge-BP heterojunctions. Inset figure shows the band alignment of Ge-BP junction along with the values for EA and EG for both materials. Thickness of the 2D material in all cases is 30 nm.

5.3.2. Junction with Highly N-doped 3D Material

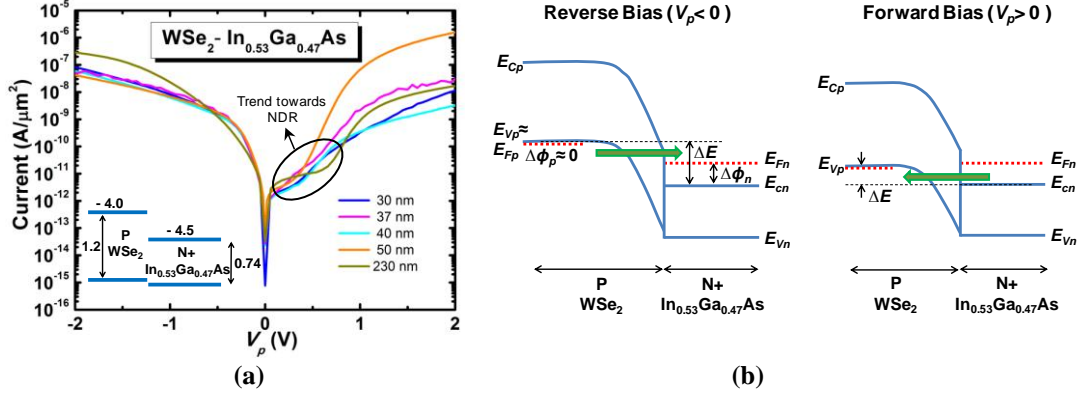


Figure 5.9. (a) P-N junction characteristics of heterojunction formed between WSe₂ and highly P doped In_{0.53}Ga_{0.47}As for different thicknesses of the MoS₂ varying from 30 nm to 230 nm. Inset figure shows the band alignment of WSe₂- In_{0.53}Ga_{0.47}As junction along with the values for EA and EG for both materials. (b) Band diagram of the WSe₂- In_{0.53}Ga_{0.47}As junction in forward and reverse bias conditions.

The electrical characterization of the 2nd category of hetero-junctions is presented here. The current as a function of V_p for a heterojunction formed between WSe₂ with relatively low EA and In_{0.53}Ga_{0.47}As with relatively high EA is illustrated in **Figure 5.9(a)**. High BTBT is obtained in the reverse bias which is also relatively independent of the thickness similar to the case of 1st category of hetero-junctions. Contrary to the previous observations, the WSe₂ - In_{0.53}Ga_{0.47}As heterojunction exhibits a trend towards NDR in the forward bias characteristics as is clear from **Figure 5.9(a)**. This is because of the low electron effective mass of In_{0.53}Ga_{0.47}As which raises the Fermi level much higher with respect to the conduction band edge or in other words, $\Delta\phi_n$ (energy separation between Fermi level and N region) is large, as shown in **Figure 5.9(b)**. This increases the energy window (ΔE) for BTBT for small forward bias (**Figure 5.9(b)**), leading to significant BTBT current at low forward bias. With

further increase in forward bias, the BTBT decreases and the current is mainly contributed by the thermionic emission. This switch over from BTBT to thermionic emission leads to observation of trend towards NDR.

The BTBT current in reverse bias, which is the one important for building TFETs, can be increased by lowering the *EA* of the N+ 3D semiconductor which will lead to lower band overlap with WSe₂. This can be achieved by increasing the In concentration from 53% to 100% as shown in **Figure 5.10(a)**. It is observed from **Figure 5.10(b)**, that the BTBT current increases significantly with the increase in the In concentration.

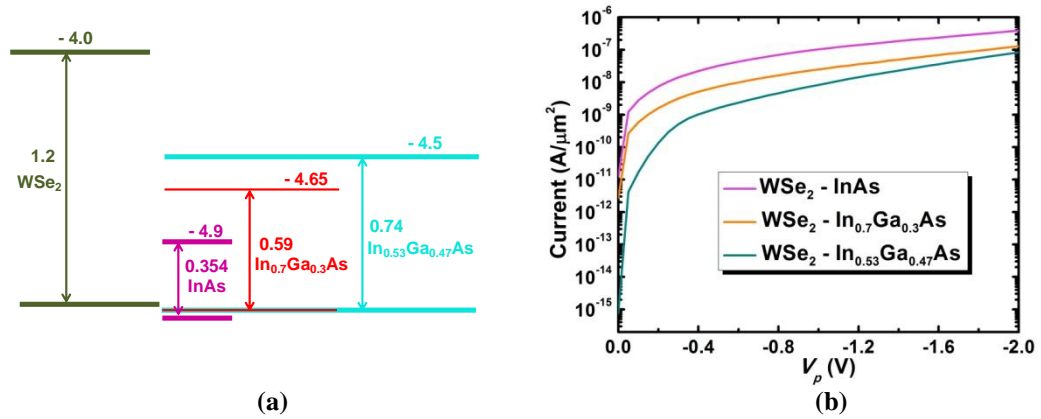


Figure 5.10(a) Band alignment of WSe₂ with respect to In_{0.53}Ga_{0.47}As , In_{0.7}Ga_{0.3}As and InAs. **(b)** Comparison of BTBT current between WSe₂-In_{0.53}Ga_{0.47}As , WSe₂-In_{0.7}Ga_{0.3}As and WSe₂-InAs heterojunctions. Thickness of the 2D material in all cases is 30 nm

5.3.3. Comparison With Experimental 2D Tunnel-Junctions

Table-5.1

References	Materials	Specifics	Lateral (L)/ Vertical (V)	Thickness of Layered Material	Normalized current at reverse bias of 1V (A/um ⁻²)
This Work	BP-Ge	Broken gap	V	30 nm	2.36×10^{-4}
Roy et. al.[229]	MoS ₂ -WSe ₂	High gate voltage : 3.5 V, -4 V	V	Bilayer - Bilayer	2.22×10^{-10}
Xu et. al.[233]	MoTe ₂	PEO-CsClO ₄ , doping by quenching	L	6 nm	4.38×10^{-10}
Li et al. [234]	MoS ₂	n-type by benzyl viologen (BV), p-type by AuCl ₃ , V _{BG} =60V	L	11 nm	6.5×10^{-14}
Baughner et. al.[235]	WSe ₂	gate voltage : +10 V	L	Monolayer	2.6×10^{-13}
Yu et. al.[236]	MoS ₂ -WSe ₂		V	40 nm - 100 nm	10^{-16}
Yan et. al.[237]	BP-SnSe ₂	Broken gap	V	50 nm to 100 nm	10^{-7}
Feng et. al.[238]	InSe-CuInSe ₂		L	20 nm to 50 nm	5.04×10^{-14}
Deng et. al.[239]	BP-MoS ₂		V	11 nm - Monolayer	2.01×10^{-11}

The above Table 5.1 compares the tunnel junction (Ge-BP) with best BTBT current presented in this work with previously reported experimental 2D tunnel junctions. As is clear from the above table, the BTBT current obtained surpass previously reported

current values by more than 3 orders of magnitude even without any external complicated doping procedures for layered material or application of high gate voltages.

5.3.4. Analytical Modeling

Here, we present the analytical modeling of the novel 3D-layered material heterojunction. First the band bending of the device is determined along the direction from the 3D conventional semiconductor to the layered material. Since the conventional semiconductor is highly doped, its band bending can be assumed to be negligible and the applied voltage mainly drops in the layered semiconductor and the interfacial oxide. The potential profile (ψ_l) in the layered material can be obtained by solving the Poisson's equation as follows

$$\frac{d^2\psi_l(x)}{dx^2} = \frac{q \times dop_l}{\epsilon_l} \quad (5.1)$$

where, ϵ_l and dop_l are the dielectric constant and doping concentrations, respectively, in the layered material. We have defined $x=0$ at the interface of the oxide (with a thickness of t_{ox}) and layered material (with a thickness of t_l), q is the electronic charge.

The boundary conditions for solving equation (5.1), are given by

(i) $\psi_l(0) = Ev_{offset} - V_{ox}$ where Ev_{offset} is the valence band offset of the layered material with respect to conventional semiconductor and V_{ox} is the voltage drop in the interfacial oxide. Note that Ev_{offset} is negative in the case considered.

(ii) $\psi_l(Wd) = U_l$ where U_l is the valence band position of layered material at $x=Wd$. Since, most voltage drops in the depletion region, the band can be assumed to be flat at thickness higher than the depletion width (Wd).

Now, using the above boundary conditions, equation (5.1) can be solved as

$$\psi_l(x) = \frac{1}{2} \frac{q \text{dop}_l x^2}{\epsilon_l} + \frac{1}{2} \frac{\{2U_l \epsilon_l - q \text{dop}_l Wd^2 - 2\epsilon_l (Ev_{\text{offset}} - V_{ox})\} x}{Wd \epsilon_l} + Ev_{\text{offset}} - V_{ox} \quad (5.2)$$

In the above equation, Wd and V_{ox} are unknowns. V_{ox} can be written as $E_{ox} t_{ox}$ where E_{ox} can be obtained from

$$E_{ox} = -\frac{d\psi_l(0)}{dx} \times \frac{\epsilon_l}{\epsilon_{ox}} \quad (5.3)$$

Thus, by solving $V_{ox} = -\frac{d\psi_l(0)}{dx} \times \frac{\epsilon_l}{\epsilon_{ox}} \times t_{ox}$ and putting the equation for ψ_l from equation

(5.2), V_{ox} can be derived as a function of Wd as

$$V_{ox} = \frac{1}{2} \frac{\{-2U_l \epsilon_l + q \text{dop}_l Wd^2 + 2\epsilon_l Ev_{\text{offset}}\} t_{ox}}{Wd \epsilon_{ox} + t_{ox} \epsilon_l} \quad (5.4)$$

Now, only one unknown is remaining i.e., Wd . As discussed earlier, the bands can be assumed to be flat (or $\frac{d\psi_l}{dx} = 0$) at x equal to and higher than the depletion width.

Hence, by solving $\frac{d\psi_l(Wd)}{dx} = 0$, Wd can be obtained as

$$Wd = -\frac{-t_{ox} q \text{dop}_l \epsilon_l + [(t_{ox} q \text{dop}_l \epsilon_l)^2 - 2\epsilon_{ox}^2 q \text{dop}_l \epsilon_l (U_l - Ev_{\text{offset}})]^{1/2}}{q \epsilon_{ox} \text{dop}_l} \quad (5.5)$$

Now, that all the unknowns have been obtained, the tunneling probability can be derived. It has been shown that if maximum electric field instead of average value, is used in the analytical equation for tunneling probability, it leads to excellent matching

with experimental results for both homo- as well as hetero-junctions. The maximum electric field in the layered material (F_l) occurs at its interface with the oxide i.e., $x=0$.

From equation (5.2), F_l can be derived as

$$F_l = -\frac{1}{2} \frac{2U_l \epsilon_l - q dop_l W d^2 - 2 \epsilon_l (E_{v_{offset}} - V_{ox})}{W d \epsilon_l} \quad (5.6)$$

Now, the tunneling probability through the layered material can be derived as a function of F_l using WKB equation and the two band approximation, as shown below

$$P_l = e^{-2qF_l \sqrt{\frac{2m_r}{\hbar^2 EG_l}} \int_{a_1}^{a_2} \sqrt{x(a_2-x)} dx} \quad (5.7)$$

where, m_r is the reduced effective mass and EG_l is the bandgap of the layered semiconductor, $\hbar = h/2\pi$ with h being the Planck's constant, $a_1 = E_{v_{offset}} / q F_l$ and $a_2 = EG_l / q F_l$. Carrying out the integration, the exponent (t_{fact_1}) can be derived as

$$t_{fact_1} = \frac{1}{8qF_l \hbar} \sqrt{\frac{2m_r}{EG_l}} \left\{ 4\sqrt{-(E_{v_{offset}} - V_{ox})(EG_l + E_{v_{offset}} - V_{ox})(EG_l + 2(E_{v_{offset}} - V_{ox}))} \right. \\ \left. + 2EG_l^2 \arcsin\left(\frac{EG_l + 2(E_{v_{offset}} - V_{ox})}{EG_l}\right) + EG_l^2 \pi \right\} \quad (5.8)$$

Writing equation (5.8), in terms of the band overlap (E_{ov}) between the conventional and layered material, we get

$$t_{fact_1} = \frac{1}{8qF_l \hbar} \sqrt{\frac{2m_r}{EG_l}} \left\{ 4\sqrt{(E_{ov} - V_{ox})(EG_l - (E_{ov} - V_{ox}))(-EG_l + 2(E_{ov} - V_{ox}))} \right. \\ \left. + 2EG_l^2 \arcsin\left(\frac{-EG_l + 2(E_{ov} - V_{ox})}{EG_l}\right) + EG_l^2 \pi \right\} \quad (5.9)$$

Note that, $E_{ov} = EG_l + Ev_{offset}$ and it represents the energy overlap in absence of any interfacial oxide. Due to the voltage drop in the oxide, the effective overlap is given by $E_{ov} - V_{ox}$. The, tunneling probability is given by $P_l = \exp(-t_{fact_l})$.

The analytical formula for current considering momentum conservation has been derived in Chapter 3. In heterostructures, it is difficult to obtain a single wave-vector connecting the valence and conduction bands, which makes involvement of phonons necessary for tunneling. Along with phonon scattering, surface scattering will result in loss of momentum conservation. In such case, the current is proportional to the integral within the tunneling window, of the product of density of states of the conventional 3D material, that of the layered material, tunneling probability and the Fermi function difference between the P and N regions.. Since, the layered material used for forming the P-N junction is very thick, its density of states behave like that of a 3D material. For deriving analytical formula for current, we do the following simplifications. We use the tunneling probability corresponding to maximum force and assume a Fermi function difference of 1. Thus, we can the BTBT current as

$$I_{BTBT} \propto P_l (\Delta E)^2 \quad (5.10)$$

As shown in **Figure 5.11**, The current obtained using the above analytical formula can lead to excellent matching with experimental result with only one matching parameter.

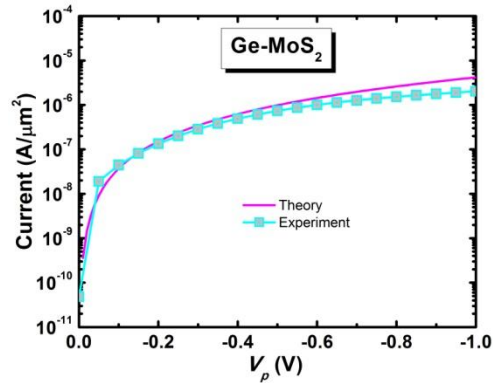


Figure 5.11. Comparison of experimental result with theoretical calculation. The 3D conventional and layered materials are taken as Ge and MoS₂ respectively.

5.4. Steep TFET with 2D Channel

5.4.1. Device Design and Fabrication

From the discussion of different hetero-junctions presented above, it is clear that the Ge-BP junction (broken gap) leads to the highest BTBT current. However, phonon assisted vertical tunneling can degrade the *SS* in case of broken-gap junctions [240]. Among the staggered heterojunctions, Ge-MoS₂ leads to the highest BTBT current and hence, we use this material combination for building our Atomically-thin and Layered Semiconducting-Channel Tunnel-FET or ATLAS-TFET. While the P-N junctions were studied using exfoliated thick layered materials, atomically thin bilayer MoS₂ is used for as the channel for ATLAS-TFET in order to obtain excellent device electrostatics as well as low tunneling barrier width. Note that bilayer MoS₂ is used instead of a monolayer. Though the thickness of bilayer MoS₂ is higher by 0.65 nm compared to that of monolayer, bilayer MoS₂ still offers excellent electrostatics and

ultra-low tunneling barrier width and at the same time, has smaller bandgap[61] and is more robust to surface scattering[32].

We used Chemical vapor deposition method (CVD) to synthesize the MoS₂ layers instead of using mechanical exfoliation, in order to enable a scalable technology. Sulfur (S) and Molybdenum Oxide (MoO₃) powder were used as the S and Mo precursor, respectively.[241] MoO₃ powder contained in a boat was inserted in a fused quartz tube and placed at the center of the CVD furnace. S powder was placed at the upstream region of the furnace, which had lower temperature. A clean Si wafer with thermally grown SiO₂ (275 nm) on top was used as the substrate for MoS₂ growth and it was put above the MoO₃ powder with the SiO₂ layer facing down. The furnace temperature was increased to 850 °C in 20 min, and was held at that temperature for 10 min, leading to the formation of bilayer MoS₂. The temperature of sulfur was kept at about 200 °C. Throughout the process, 50 sccm of argon was used as the carrier gas and the growth was carried out under atmospheric pressure. The high resolution Scanning Transmission Electron Microscopy (STEM) images were recorded at 300 KV to investigate the MoS₂ samples.

The fabrication process flow for ATLAS-TFET is shown in **Figure 5.12(a)**. We started with a commercially available Ge wafer, highly doped (p-type) with Ga and having a resistivity of 0.0011 ohm.cm. The wafer was patterned using photolithography and 300 nm trenches were etched using deep reactive ion etching. Subsequently, without removing the photoresist, about 350 nm of SiO₂ was grown using ebeam deposition. Next, the photoresist was removed using acetone upon which

oxide only remained in the trenches and was washed away (with the resist) from the other regions. After that, very dilute HF was used to slowly etch out the SiO₂ in the trenches, to planarize it with respect to the surrounding Ge. This made the substrate ready for device fabrication. MoS₂ synthesized using CVD was then transferred to the engineered substrate using PMMA transfer process and then the PMMA was removed using acetone. MoS₂ was etched from the regions where devices were not intended to be built using Inductively Coupled Plasma (ICP) etching based on BCl₃ (15 sccm) and Ar (60 sccm) at pressure of 0.6 Pa, RF source power of 100 W and RF bias power of 50 W[242] for 1 min. Drain contacts were formed using ebeam lithography and subsequent metallization using Yttrium/Gold (Yttrium was chosen due to its low workfunction of 3.1 eV and presence of d-orbitals which can lead to efficient contacts[75], [76], [243]). In our work, we have used solid polymer electrolyte (PE) gating. The drain electrode is covered with SiO₂ to prevent the drain voltage from influencing the electric double layer[78] formed in the polymer. The gate electrode is formed using ebeam lithography and metallization of 20 nm/ 50 nm Yttrium/Gold using ebeam deposition. For polymer electrolyte gating, the gate electrode does not need to be directly above the channel and is formed on the side as shown in **Figure 5.12**. The PE is formed by mixing poly(ethylene oxide) (PEO) and lithium perchlorate (LiClO₄) in 8:1 ratio in methanol and it can be drop casted or even lithographically patterned[79]. The dielectric constant for the PEO matrix has been reported in literature as 5.[80] A fabricated prototype device is shown in **Figure 5.13**.

Note that a p-type ATLAS-TFET can also be achieved on the same substrate using highly n-doped Ge source and WSe_2 with low electron affinity as the channel. Moreover, it is possible to build large scale circuits with complimentary ATLAS-TFETs in a planar platform. By starting with a undoped Ge wafer and selectively doping certain portions of it as p-type and other portions as n-type and then transferring in-plane heterostructures of MoS_2 and WSe_2 to it, it is possible to build both p and n-type ATLAS-TFETs for integrated circuits. The recent experimental demonstration[244] of CVD synthesis of in-plane heterostructures of MoS_2 and WSe_2 , indicate the feasibility of the growth of such structures. It is possible to build the complimentary circuits even without the use of the in-plane heterostructures by employing a 2-step procedure in which large scale MoS_2 can be first transferred to the substrate and patterned followed by the transfer and patterning of large scale WSe_2 .

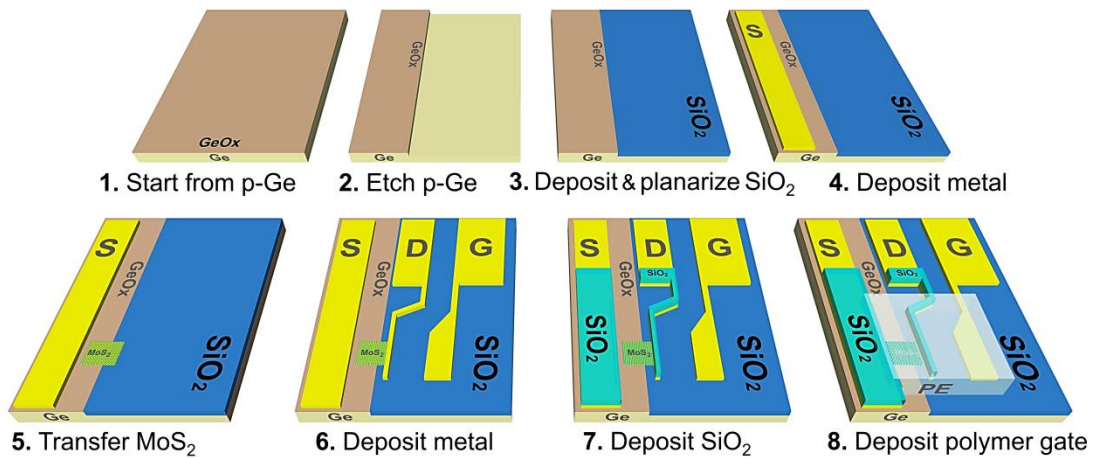


Figure 5.12. Schematic diagram showing fabrication process flow of ATLAS-TFET.

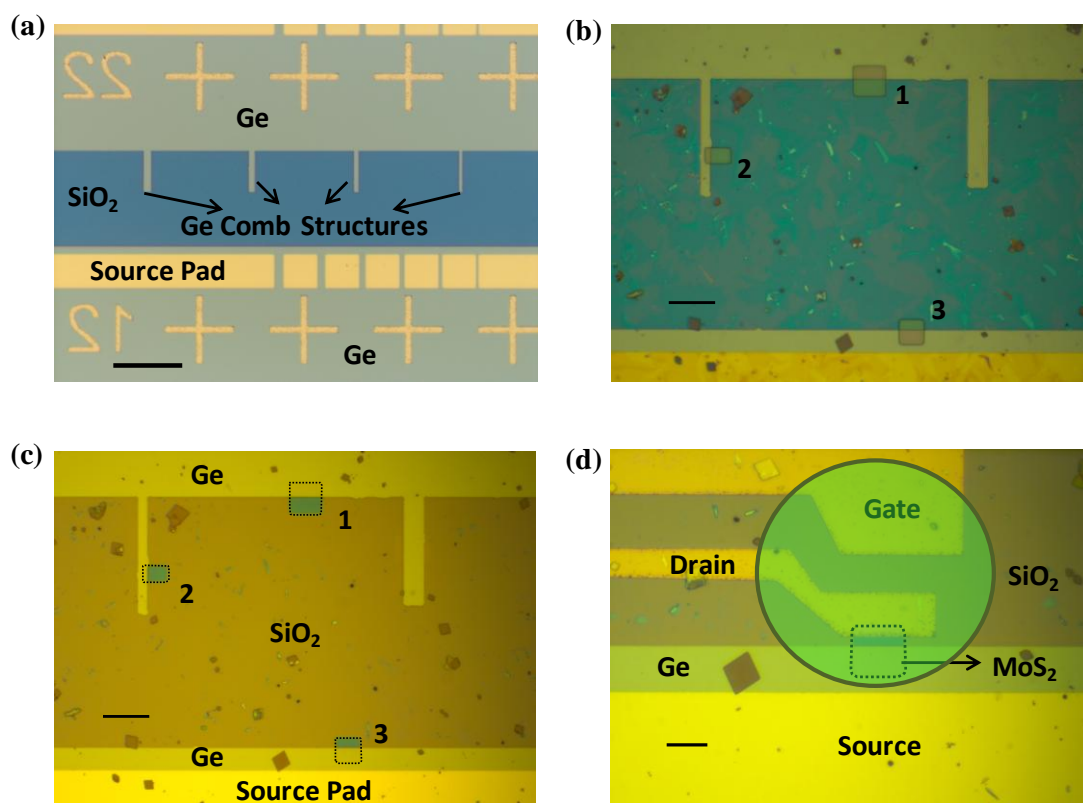


Figure 5.13(a) Engineered substrate consisting of alternate layers of Ge and SiO₂ along with Ge comb structures. The Ge comb structures increase the probability of achieving "necessary overlap regions", which means that part of the MoS₂ flake overlaps the Ge while the other part overlaps the SiO₂ and thus combs are important, especially if the flakes are small. Metal source pads as well as markings required to assist ebeam lithography are also shown. Scale bar: 100 μm . **(b)** Engineered substrate with the CVD synthesized MoS₂ transferred on it. Regions marked 1, 2 and 3 in the image show three different ways in which "necessary overlap regions" can be obtained. Scale bar: 25 μm . **(c)** After etching the MoS₂ from other regions except for the regions marked 1, 2 and 3. Scale bar: 25 μm . **(d)** The ATLAS-TFET device showing the source, drain and gate contacts. The circled region represents the solid polymer electrolyte. The covering of drain electrode with oxide has not been shown in this figure for clarity. The flake used is that marked 3 in (b) and (c). Scale bar: 10 μm .

5.4.2. Material Characterization

The MoS₂ sample is characterized using Atomic Force Microscopy as well as Raman Spectroscopy as shown in **Figure 5.14(a)** and **Figure 5.14(b)**, respectively. The transmission electron microscope (TEM) image of the cross-section of bilayer MoS₂ on Ge is presented in **Figure 5.14(c)**, which clearly reveals the 2 MoS₂ layers, the Ge crystal and the presence of a thin layer of native Germanium oxide.

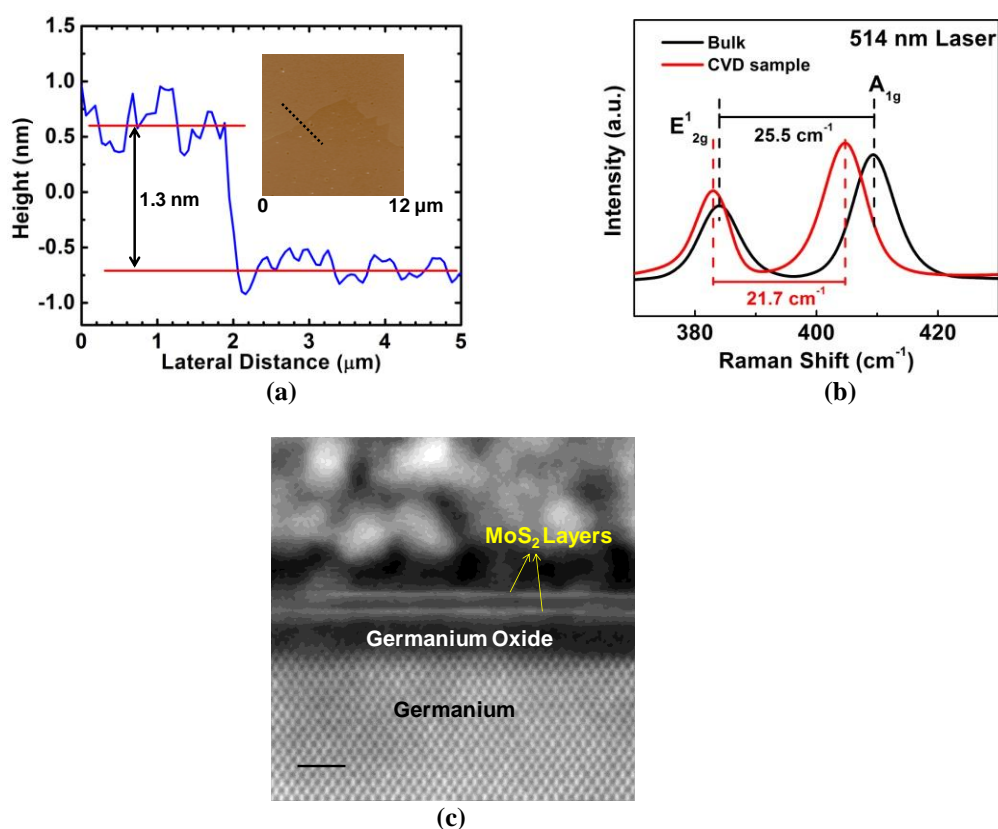


Figure 5.14(a) Atomic Force Microscopy performed on bilayer MoS₂ confirming that the thickness is 1.3 nm. The height profile is plotted along the dotted line in the inset figure. **(b)** Raman Spectroscopy (using 514 nm laser) of the CVD bilayer sample (red curve), showing E_{2g}^1 peak at 383.0 cm^{-1} and A_{1g} peak at 404.7 cm^{-1} , which confirms that the sample is indeed bilayer MoS₂. Comparison is also shown with bulk MoS₂ (black curve) for reference. **(c)** Cross-sectional TEM image of bilayer MoS₂ on Ge. Scale bar: 2 nm

X-ray Photoelectron Spectroscopy (XPS) can be used to investigate the electronic structure of the materials. It involves knocking out electrons from the surface of a material using X-rays and measuring the kinetic energy of the emitted electrons. Then the binding energy (BE) of the electrons can be calculated as

$$BE = E_{X\text{-ray}} - (E_{kinetic} + \phi) \quad (5.12)$$

where ϕ is the work function. In case of a junction formed of two different materials, XPS can indicate the presence of band bending through the shift of the BE . Moreover, the direction of the shift of BE can tell whether the band bending is due to positive (shift towards higher BE) or negative (shift towards lower BE) charge.

In case the sample for XPS is conducting, the photoelectrons emitted from the material are compensated by the electrons from the sample holder. However, if the sample is insulating, charge compensation cannot occur and there can be build-up of positive charges due to knocking out of electrons, which can shift the binding energies to higher values than actual. This is called charging effect. In the XPS setting, a charge neutralizer, which provides extra electrons to the sample, can be used. In the case of insulating substrate, use of charge neutralizer (CN), shifts the binding energies to lower values than actual, due to the presence of negative charges due to extra electrons. By doing the XPS measurements with and without the CN, it can be found out whether there is any charging effect in the sample. If the BE does not change, with and without the CN, then it can be confirmed that charging is absent while if the BE changes, then charging effect is present. In our case, the MoS_2 on Ge did not show any charging effect as both Ge and MoS_2 are conducting as confirmed

by measurements with and without CN. However, the MoS₂ on SiO₂/Si substrate suffers from charging effect due to the presence of 280 nm thick insulating SiO₂. To mitigate this effect, and find the actual *BE*, we used the procedure shown by Alay et al.[245] First, XPS measurements were performed with and without the CN and the shift in *BE* for both Oxygen (O) and Molybdenum core levels were derived and found to be similar. This implies that charging effect leads to similar shift in MoS₂ and SiO₂ core levels. Next, Si with ultra-thin 1 nm SiO₂ was measured with and without CN, and no charging effect was found. The actual *BE* of O core level can be found from this experiment as charging is absent. The error in *BE* due to charging was calculated by subtracting this actual *BE* of O from the *BE* of O obtained from XPS of 280 nm SiO₂ on Si without CN. The core levels of MoS₂ measured in the case of MoS₂ on SiO₂/Si substrate without CN, were corrected for this error to obtain the actual *BE*.

XPS was performed for investigating the electronic structure of the Ge-MoS₂ heterostructure. XPS data were measured using a Kratos Axis Ultra DLD system (monochromated Al k-alpha radiation 1486 eV). While survey scans were measured using a pass energy of 80 eV, high-resolution scans were run using 20 eV.

As evident from **Figure 5.15(a)**, Mo 3d core level in the heterostructure shifts toward higher binding energies by about 480 meV compared to that of pristine MoS₂. The Sulfur 2s levels also shift by the same amount. This shift is due to the band bending in MoS₂ in the heterostructure due to the presence of positive charges in it. No shift in the Ge core levels is observed, which is consistent with the fact that the band bending

in Ge is almost negligible due to its high doping (**Figure 5.15(b)**). The deconvolution of the Ge 3d core level is shown in **Figure 5.15(c)**.

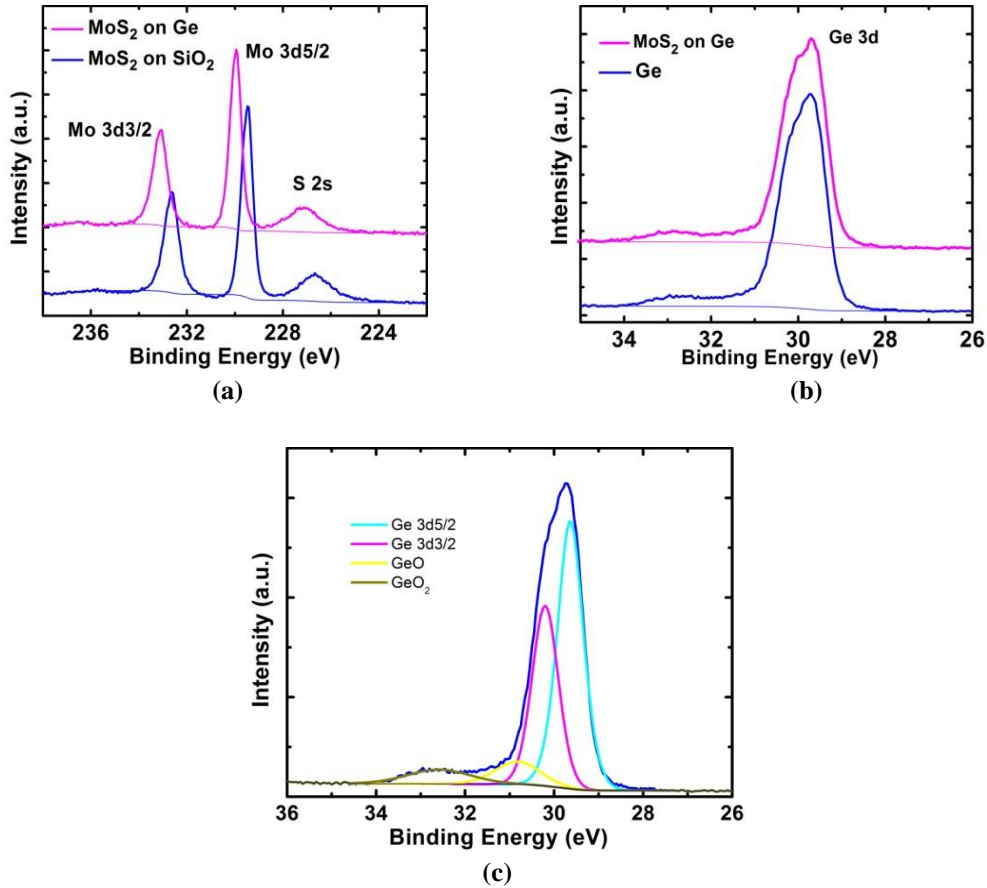


Figure 5.15(a) Comparison of Mo 3d core level doublet (3d_{3/2} and 3d_{5/2}) of MoS₂ on SiO₂ with that of MoS₂ on Ge showing a 480 meV shift toward higher binding energy in the latter case. This is due to band bending in MoS₂ because of the presence of positive charges in it when placed on Ge. Sulfur 2s core level also show similar shift in binding energy. **(b)** Comparison of Ge 3d core level for Ge alone and for Ge with MoS₂ on it, showing negligible difference between the two indicating absence of band bending in Ge due to its high doping level. **(c)** The Ge core level (blue) deconvoluted to show Ge 3d_{5/2} (cyan), Ge3d_{3/2} (magenta), GeO (yellow) and GeO₂ (dark yellow).

5.4.3. Proof of Band-to-Band Tunneling

The electrical characterization of the device is first performed in a two terminal configuration, just using the source and drain contacts, without any gate (**Figure 5.16(a)**). Then the device essentially behaves like a p-n junction (**Figure 5.16(b)**).

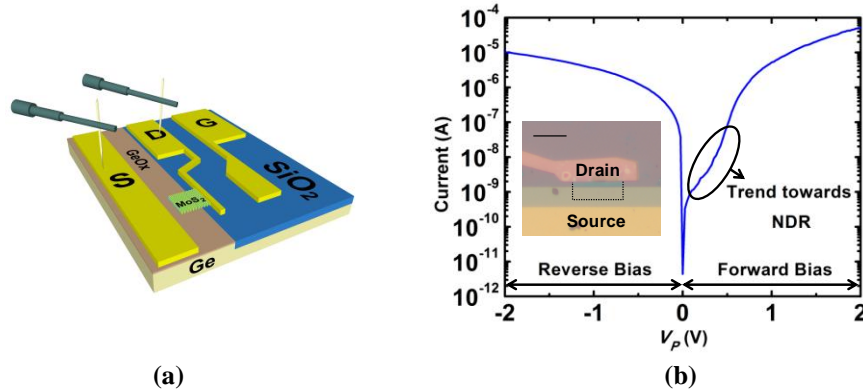


Figure 5.16(a) Schematic diagram showing the probing configuration for measurement of the characteristics of p-n junction diode formed by highly p-doped Ge and naturally n-doped MoS₂. The presence of a thin layer of Germanium Oxide is also shown in the schematic. Note that, though there is a layer of Germanium Oxide layer between source contact and the Ge, we have still achieved ohmic contact to Ge, due to the ultrathin nature of the oxide. **(b)** Current as a function of applied bias on Ge while the contact to MoS₂ is grounded. The p-n junction characteristics are shown in both forward as well as reverse bias conditions. The circled region in the forward biased characteristics shows a trend toward Negative Differential Resistance (NDR) confirming Band-to-Band-Tunneling (BTBT) current (as explained below). The measured device is shown in the inset figure (scale bar: 10 μm). The length and width of the device are 5.1 μm and 15 μm respectively and the area of overlap of MoS₂ and Ge is 54.6 μm^2 .

Note that no rectification is observed and large current is obtained even under the reverse bias condition because of the high BTBT current due to the ultra-thin tunneling barrier. The trend toward Negative Differential Resistance as shown by the circled region in the forward bias characteristics confirms the existence of BTBT as explained below.

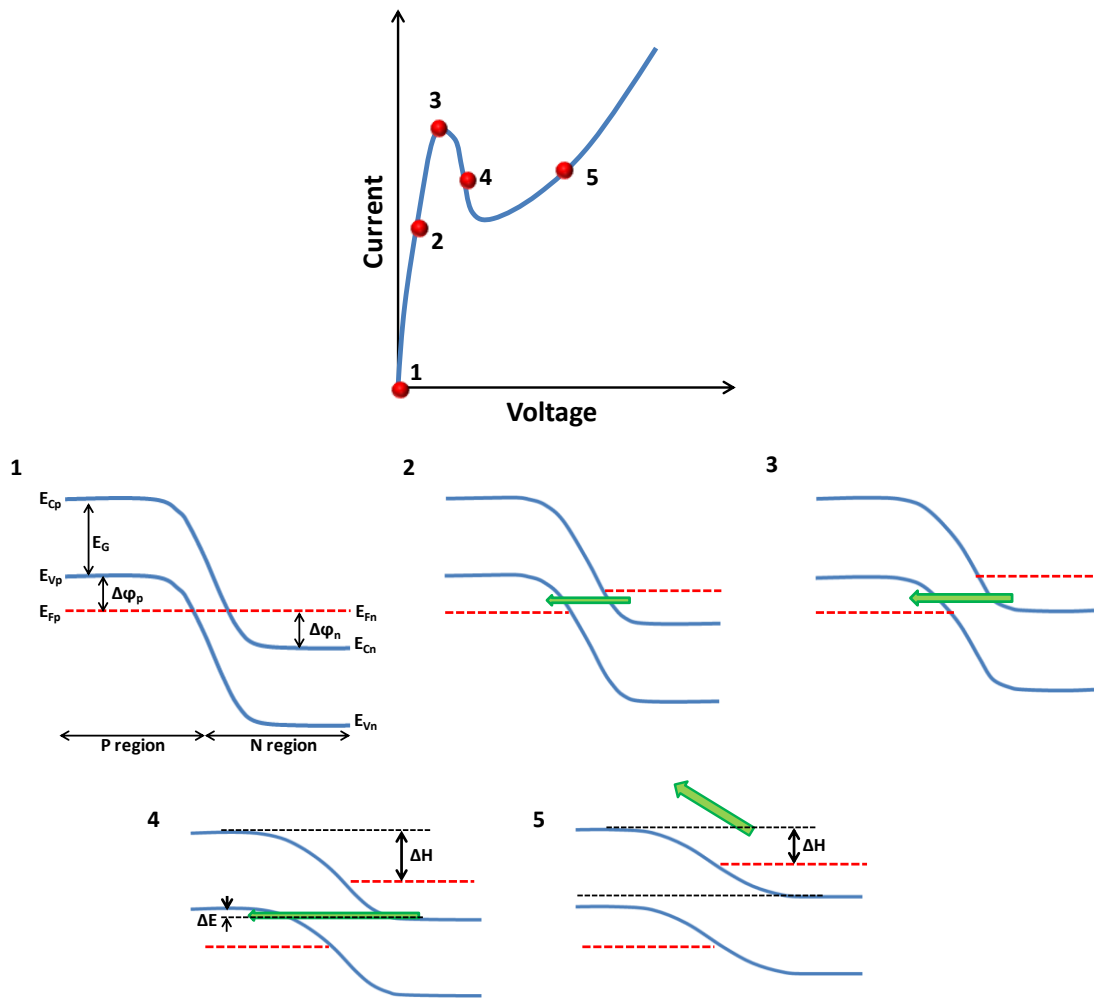


Figure 5.17. The forward bias characteristics of a highly doped p-n junction along with band diagrams representing different points in the current-voltage curve.

Here, we explain why we see a trend towards Negative Differential Resistance (NDR) in the forward bias characteristics of the p-n junction measurements. For that, we first explain the case where we can observe prominent NDR[246]. Prominent NDR can be observed in a p-n junction when both the p and n regions are highly doped. The current in forward bias condition of such a p-n junction as a function of voltage applied to the p-region with respect to the n-region is shown in **Figure 5.17**. The band diagrams corresponding to different points in the curve marked with numbers from 1

to 5 are also shown. When the applied voltage is zero, the Fermi levels in p and n regions align and there is no current flow (point 1, **Figure 5.17**). When a positive bias is applied to the p region, the electrons from the filled states of n region can tunnel into the empty states of p-region leading to current flow (point 2, **Figure 5.17**). When the bias is increased and the energy of most of the electrons in n-region gets aligned with that of the free states in p-region, maximum current is achieved (point 3, **Figure 5.17**). With further increase in bias, the number of electrons in n-region with energy aligned to the empty states in p-region decreases, resulting in decrease in current and hence, NDR (point 4, **Figure 5.17**). As the bias is increased yet further, the barrier height (shown by ΔH) for electrons in the n-region to be thermionically emitted to the p-region decreases, and hence current begins to increase again due to thermionic emission (point 5, **Figure 5.17**). As is clear from the current-voltage curve, prominent NDR effect can be observed here as the tunneling current at point 3 is much higher than the thermionic emission at that bias. However, in case either p or n-region is lightly doped, prominent NDR is not observed (**Figure 5.18**). Supposing the n region is lightly doped and the Fermi level is very near or below the conduction band in that region, then there are very few electrons available that can tunnel to p region, leading to lower tunneling current (point 2, **Figure 5.18**). Thus, the tunneling current in forward bias is not substantially higher than the thermionic current leading to a more smoother transition from tunneling (point 2, **Figure 5.18**) to thermionic emission (point 3, **Figure 5.18**) showing a trend towards NDR.

In our case, the p-region (Ge) is highly doped while n-region (MoS₂) is lightly doped. Hence, we also observe a trend toward NDR.

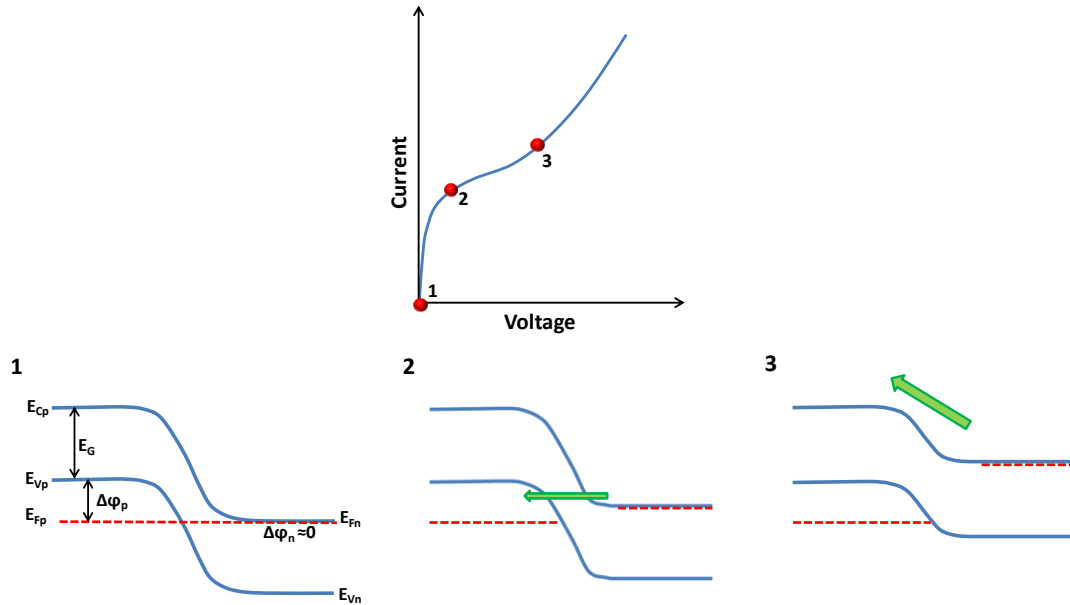


Figure 5.18. The forward bias characteristics of a p-n junction with highly doped p region and lightly doped n region, along with band diagrams representing different points in the current-voltage curve.

In **Fig 5.19**, the p-n junction current of our device measured in a two terminal configuration (where source pad contacts the p-type Ge and drain pad contacts the naturally n-type MoS₂) at different temperatures is shown. We observe negligible temperature dependence in the reverse bias characteristics. Negligible temperature dependence of the current is a typical signature that the current is dominated by BTBT and not thermionic emission, since BTBT is relatively temperature independent.

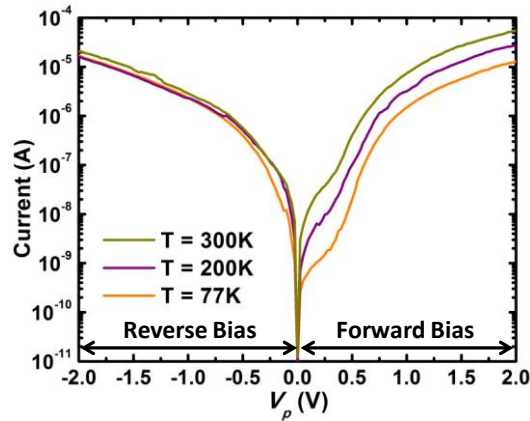


Figure 5.19. The forward and reverse bias p-n junction characteristics shown for 3 different temperatures of 77K, 200K and 300K. The reverse bias current is dominated by band-to-band tunneling and shows negligible temperature dependence. The forward bias current involves thermionic emission as well as recombination and hence, is temperature dependent.

5.4.4. Beating the Fundamental Thermionic Limitation

Here, the transistor analyzed is measured in a 3-terminal configuration using the source, drain and gate (**Figure 5.20a**). **Figure 5.20b** shows the transfer (I_{DS} - V_{GS}) characteristics of the device for different V_{DS} starting from drain voltage as low as 0.1 V to 1 V. It is observed that for all the drain voltages, the ATLAS-TFET can beat the fundamental limitations of SS (60 mV/dec at room temperature) in MOSFETs, and sub-60 mV/dec SS is obtained over about 4 decades of current. It is to be noted that though the low SS occurs at a negative gate voltage, it can be adjusted by changing the work function of the gate metal.

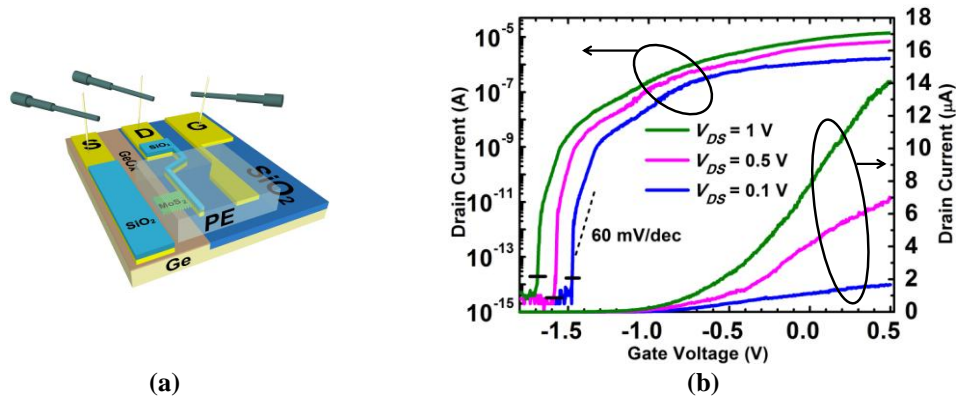


Figure 5.20(a) Schematic diagram showing the probing configuration for measurement of the characteristics of ATLAS-TFET. Note that the source and drain electrodes are covered with SiO₂ to prevent these electrodes from influencing the polymer electrolyte as well as to reduce leakage between these electrode and gate. **(b)** Drain current as a function of gate voltage for 3 different drain voltages of 0.1 V, 0.5 V and 1 V. The point (let us call it cross point), where drain current become similar to the gate leakage current level, is shown by a short black dash on each curve in logarithmic scale for particular V_{DS} . Below these cross points, current from gate flows into the source and drain terminals and contaminates the source-drain current. In our case, current from the gate mainly goes to the source due to the higher overlap between Ge and the polymer complex gate. The cross points occur at or below 3×10^{-14} A for all the V_{DS} values plotted. We have derived SS over the current range above 10^{-13} A (specifically 10^{-13} A - 10^{-9} A), which is well above the cross points and hence the SS is not contaminated by the gate leakage. The dashed black line indicates a slope of 60 mV/dec. Though in **(b)**, from an eye estimation, the SS may appear steeper than 60 mV/dec only for $V_{DS} = 0.5$ V, in the current range between 2 pA and 1 nA, in actuality, the SS is below 60 mV/dec in that current range for V_{DS} of 0.1 V and 1 V, as well. The average SS in the current range between 2 pA and 1 nA for V_{DS} of 0.1 V and 1 V are 52.6 mV/dec and 46.4 mV/dec, respectively. The device measured is the same as in **Figure 5.19(b)**. The shift in the curves to the left with increasing V_{DS} is due to the higher drain capacitance, which is a general feature of all TFETs (as discussed below).

The SS of the ATLAS-TFET is plotted in **Figure 5.21**. In the case of ATLAS-TFET, not only minimum SS as low as 3.9 mV/dec is obtained, but excellent average SS of 5.5 mV/decade, 12.8 mV/decade, 22 mV/decade and 31.1 mV/decade are obtained over 1, 2, 3 and 4 decades of current, respectively. These average values of SS have been derived using equation (3.1) and the data points corresponding to drain current of around 10^{-13} A and $10^{-12}/(10^{-11}/10^{-10}/10^{-9})$ A are used for obtaining the average over 1(2/3/4) decades of current. In **Figure 5.21**, the noisy data points have

been eliminated and thus, the average of the point SS values of ATLAS-TFET, plotted in that figure leads to similar average SS over 4 decades, as obtained above.

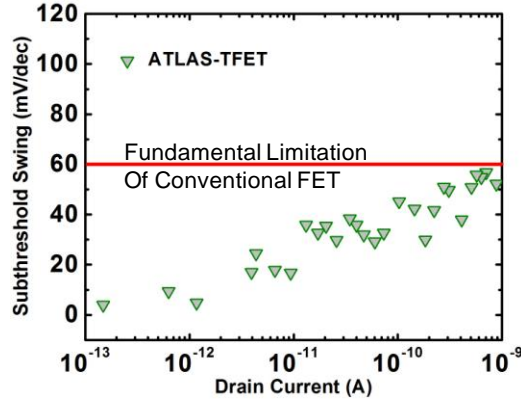


Figure 5.21. Subthreshold Swing as a function of drain current for ATLAS-TFET (green triangles) at $V_{DS}=0.5$ V. The red line demarcates the fundamental lower limit of subthreshold swing of conventional FETs.

The gate leakage (I_G - V_{GS}) characteristics of the ATLAS-FET is illustrated in **Figure 5.22(a)**. As observed from this figure, absolute values of I_G first decreases with increase in gate voltage, reaches a minimum point (around or below -1.5 V) and then increases again. This is because I_G is positive when electrons flow into the gate and is negative when electrons flow out of it and the zero crossing point between the positive and negative values leads to the minimum point. The effect of V_{DS} on zero crossing point can be explained as follows. For a particular V_{DS} say 0.1 V, let us consider any V_{GS} (let us call it V_{GS1}) just to the right of the zero crossing where I_G is positive, meaning electrons are flowing into the gate. Now, if V_{DS} is increased, making the potential at the source-channel junction more positive, electrons will have a tendency to flow out of the gate making the I_G negative at $V_{GS} = V_{GS1}$. This will lead

to the shift in the zero crossing point to the right with increasing V_{DS} as observed in **Figure 5.22(a)**.

This effect is not unique to the polymer gate. We had also fabricated devices having conventional gating with HfO_2 as gate dielectric and similar effect can be observed there as well as shown in **Figure 5.22(b)**.

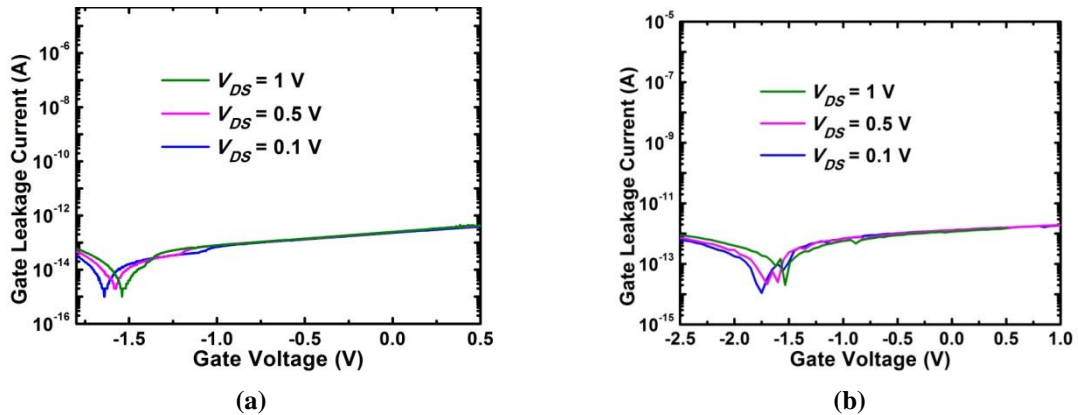


Figure 5.22 (a) Gate leakage current as a function of gate voltage for 3 different drain voltages of 0.1V, 0.5V and 1 V for ATLAS-TFET with polymer gating. (b) Gate leakage current as a function of gate voltage for 3 different drain voltages of 0.1V, 0.5V and 1 V in the case of conventional gating with HfO_2 as gate dielectric. HfO_2 is deposited using Atomic Layer Deposition and its thickness is around 50 nm.

The output (I_{DS} - V_{DS}) characteristics of the device is illustrated in **Figure 5.23**. TFETs generally have high saturation voltage for drain current [247], [248] and we also do not observe saturation till V_{DS} of 1V in our ATLAS-TFET. This is because of the high value of drain to channel capacitance.[249] This arises from the fact that while there is a tunneling barrier between the source and channel, no such barrier exists between channel drain and hence, electrons from drain can easily transport to the channel compared to that from source, leading to higher drain to channel capacitance compared to source to channel capacitance. Thus, it is difficult to bring

the conduction band of channel below that of the drain, as electrons from drain can easily populate the channel and bring the conduction band up. Due to this effect, at very small V_{DS} , it becomes difficult to bring the conduction band of channel below the valence band of source for turning the device ON. This effect occurs in all TFETs, in general. In ATLAS-TFET, this effect is reduced to some extent due to the low tunneling barrier, high junction electric field and higher tunneling area, which increases the source to channel coupling and hence, the source to channel capacitance. This effect can be further reduced by incorporation of proper drain engineering techniques such as drain underlap or heterogeneous dielectrics.[250], [251] The curves in **Figure 5.20(b)** shift to the left with increasing V_{DS} , due to this higher drain capacitance effect. Drain voltage can also influence the SS. At very small drain voltages, the SS degrades due to the drain capacitance effect. SS first improves with increase in drain voltage but, at higher drain biases, degrades again due to drain induced barrier thinning.

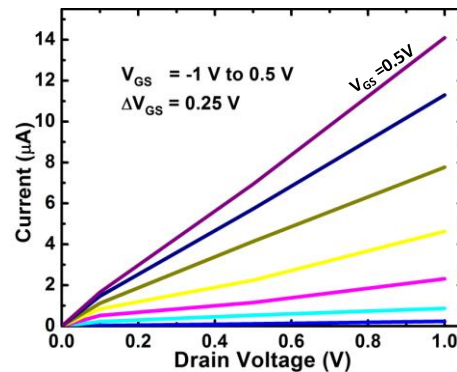


Figure 5.23. Drain current as a function of drain voltage for different gate voltages starting from -1V to 0.5 V. The data is obtained from measured I_{DS} - V_{GS} characteristics at different drain voltages.

5.4.5. Control Experiments

As a control experiment, conventional FET (CFET) is fabricated using bilayer MoS₂, the same polymer gating and measured under similar conditions and with same tools as that of ATLAS-TFET. The schematic diagram of a conventional FET is shown in **Figure 5.24**. Here, the source and drain metallic contacts are both on MoS₂ and current flows from the source to the drain laterally. The substrate consists of 280 nm thermally grown SiO₂ on Si and is used to host the ultra-thin MoS₂ conventional FET. Note, that the same polymer gating technique has been used for this CFET, as has been used for ATLAS-TFET. The *SS* obtained for CFET (**Figure 5.25**), is above 60 mV/dec for all the drain voltages. This control experiment, proves that the sub-60 mV/dec *SS* in case of ATLAS-TFET is not the outcome of polymer gating or instrumentation used in measurements.

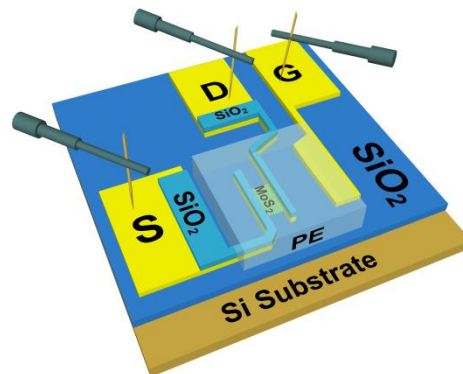


Figure 5.24. Schematic diagram of a conventional FET with bilayer MoS₂ as the channel material.

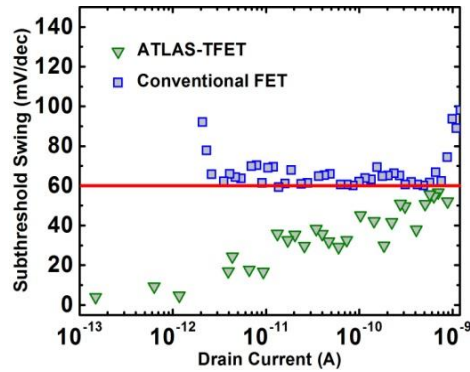


Figure 5.25. Subthreshold Swing as a function of drain current for a conventional-FET (blue squares) as well as ATLAS-TFET (green triangles), both at $V_{DS}=0.5$ V. The red line demarcates the fundamental lower limit of subthreshold swing of conventional FETs.

To confirm that the sub-thermionic SS in case of ATLAS-TFET is not due to the substrate effect, we have fabricated a MoS_2 FET with p-Ge as part of the substrate. The FET device, is similar in structure to that shown in **Figure 5.13(d)** and with source metal contacting the MoS_2 . The polymer complex gate overlapped the source region as shown in **Figure 5.26(a)**. In this case, since the source metal is directly contacting the MoS_2 , electrons from the source metal can directly transport to the MoS_2 channel and hence, the current is mainly dominated by the thermionic emission. Thus, the SS of this device is above the fundamental limitation of 60mV/dec (**Figure 5.26(b)**).

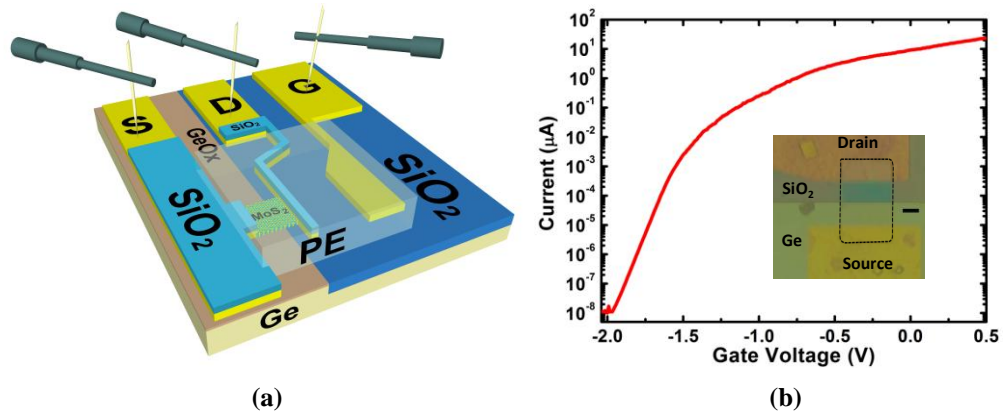


Figure 5.26 (a) Schematic diagram of a FET based on bilayer MoS₂ with p-Ge as part of the substrate. The structure is similar to that of ATLAS-TFET and the source metal is connected directly to the MoS₂. (b) Drain current as a function of gate voltage at $V_{DS}=0.5V$. The SS obtained is around 78 mV/dec. The inset figure shows the optical image of the device. Scale bar: 5 μm . Length and width of the device are 11.8 μm and 14.7 μm , respectively. MoS₂ is shown by the dotted rectangular region.

5.4.6. Repeatability and Hysteresis

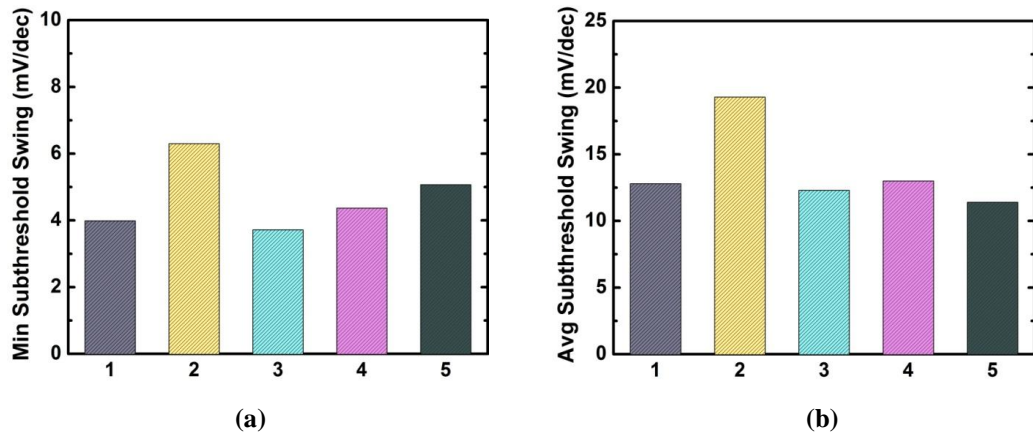


Figure 5.27 (a) Minimum and (b) average subthreshold swing (over two decades of current) of 5 devices.

The minimum as well as average subthreshold swings (over two decades of current) of 5 devices are shown in **Figure 5.27(a)** and **(b)**, respectively. Devices 1-3 were fabricated on the same substrate and were processed and measured together. Devices 4 and 5 were on a different substrate and were processed and measured a month later.

This shows that the achievement of sub-60 mV/dec SS in ATLAS-TFETs can be repeated.

The transfer characteristics of the device show negligible hysteresis as evident from **Figure 5.28** where it is shown that the I_{DS} - V_{GS} curve measured from negative to positive gate voltages (blue) coincides with that measured from positive to negative voltages (red).

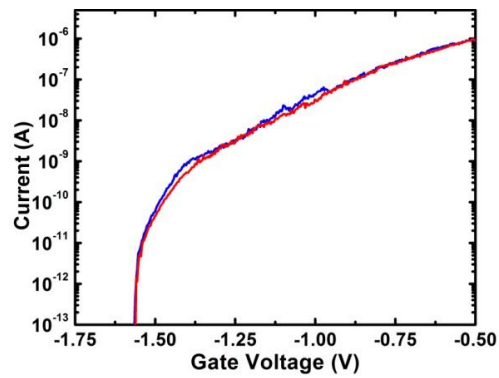


Figure 5.28. The I_{DS} - V_{GS} characteristics of ATLAS-TFET showing negligible hysteresis.

5.4.7. Comparison with Previous Experimental TFETs

Table-5.2 U: unknown, N: Did not achieve Sub-thermal SS_{avg} over 4 decades

References	Channel Material	Structure [Channel Dimension] (nm)	$ V_{DS} $ (V)	SS_{min} (mV/dec)	SS_{avg} over 3 decades (mV/dec)	Sub-thermal SS_{ave} over 4 decades (mV/dec)	I_{on} ($\mu A/\mu m$)	I_{on}/I_{off} Ratio
<i>This work</i>	MoS_2	Planar [1.3]	1	4.3	31	34.3	1	1.6×10^8
			0.5	3.9	22	31	0.5	8.3×10^7
			0.1	3.8	33	36.5	0.11	1.8×10^7
Tomioka et. al. [252] (Hokkaido Univ./JST)	Si/III-V Hetero-J	NW [30]	1	12	21	21	1	2×10^6
			0.1	U	21	N	0.001	1×10^6
Gandhi et. al. [253], [254] (NUS/IME/UCSB)	Si	NW [30-40]	0.1	30	50	N	0.003	1×10^4
		NW [18]	0.1	30	50	N	0.44	1.6×10^5
Jeon et. al. [255] (SEMATECH/Berkeley/Texas State Univ.)	Si	SOI [40]	1	32	~55	N	1.2	6×10^6
Kim et. al. [256] (UC. Berkeley)	Si	SOI [70]	0.5	38	~50	N	0.42	3.5×10^6
Mayer et. al. [257] (CEA-LETI)	Si	SOI [20]	0.8	42	>60	N	0.02	4×10^4
			0.1	42	>60	N	4×10^{-4}	4×10^4
Choi et. al. [258] (UC. Berkeley)	Si	SOI [70]	1	52.8	>60	N	12.1	2×10^3
			0.1	~52.8	>60	N	1	1×10^4
Appenzeller et. al. [259] (IBM)	CNT	SOI [U]	0.5	40	>60	N	0.01	1×10^3
Knoll et. al. [260] (Peter Grunberg Inst.)	Si	NW [7×45]	0.1	30	>60	N	2	2×10^7
			0.5	>30	>60	N	10	2×10^6
Krishnamohan et. al. [261] (Stanford Univ.)	Ge	DG [10]	0.5	50	>60	N	1	2×10^6
Huang et. al. [262] (Peking Univ.)	Si	SOI [100]	0.6	29	70	N	20	1×10^8
			0.05	~29	~70	N	1.5	7.5×10^6
Villalon et. al. [263] (CEA-LETI)	Ge_xSi_{1-x}	SOI [7-11]	0.1	33	>60	N	1	1×10^7
Ganjipour et. al. [264] (Lund Univ.)	InP/GaAs Hetero-J	NW [85-100]	0.75	50	150	N	2.2	1.1×10^7
Kim et. al. [265] (U. Tokyo/JST-CREST)	Si	SOI [10-13]	0.05	28	70	N	0.1	1×10^7
Dewey et. al. [266] (Intel)	III-V Hetero-J	bulk	0.05	~58	>60	N	0.3	3×10^4

The above Table 5.2 summarizes the key features of all the experimental TFETs in literature, to date, reporting minimum SS of sub 60 mV/dec at room temperature. It is evident from the table that out of all such previously reported TFETs, only those reported by the four groups (as highlighted in the 2nd to 5th rows in bold) achieved an average SS below 60 mV/dec (at least over 3 decades). ITRS has prescribed attainment of average sub-thermionic SS over 4 decades and the TFETs achieving the same are highlighted in blue in the table. It can be observed that, except, Tomioka et. al., no other previous groups have been able to achieve this. Tomioka et. al., have reported average sub-thermionic SS over 4 decades at $V_{DS}=1V$. The ATLAS-TFET is the first TFET in a planar platform to satisfy this ITRS prescription. Also, it is the only TFET to be able to do so up to a low V_{DS} of 0.1V. Our ON currents are comparable to those of previously reported TFETs with average sub-thermal SS (at least over 3 decades). Moreover, an excellent ON-OFF ratio spanning over 7-8 decades of current has been achieved in our ATLAS-TFET.

5.4.8. Potential for High Performance

The presence of intrinsic germanium oxide leads to additional tunneling resistance in ATLAS-TFET. Drain current of the ATLAS-TFET can be improved by removing the intrinsic oxide. Intrinsically, ATLAS-TFET is advantageous for obtaining high ON current. Not only it leads to larger area for tunneling, but it is also easier to scale down the tunneling barrier width (W_t), which basically depends on the thickness of the channel. Note that in case of a point-TFET where the gate is perpendicular to the source-channel junction (**Figure 5.29(a)**), it is very difficult to scale down the W_t .

This is because in case of point-TFET, W_t is primarily determined by the device electrostatics. Thus, a point-TFET would lead to much higher W_t compared to that of line-TFET, even if bilayer MoS₂ and similar gate capacitance are used. For elucidating the above argument, we derive the analytical expression for band profile in case of point-TFET. Assuming the source to be highly doped and band bending in it to be negligible, the Poisson's equation for conduction band profile in the channel ($\phi_p(x)$) for point-TFET can be written as[1]

$$\frac{d^2\phi_p(x)}{dx^2} = \eta(\phi_p(x) - EG_{ov} + V_{GSeff}) \quad (5.13)$$

EG_{ov} is the band overlap between source and channel, V_{GSeff} is the effective gate to source voltage and given by $V_{GSeff} = V_{GS} - V_{FB}$ where V_{GS} is the applied gate to source voltage and V_{FB} is the flat-band voltage and η is the inverse of the square of natural length scale, which for the single gated SOI structure can be given by

$$\eta = \frac{\epsilon_{Di}}{\epsilon_{Ch} t_{Ch} t_{Di}}$$

where, t_{Di} and ϵ_{Di} are the thickness and dielectric constant of the gate dielectric respectively, and t_{Ch} and ϵ_{Ch} represent those of the channel.

Setting $x=0$ at the source-channel junction and $E=0$ at the valence band of the source, the boundary conditions can be written as

$$\phi_p(0) = EG_{ov}$$

$$\phi_p(L) = Ec_D$$

where, L is the channel length and Ec_D is the channel conduction band potential at the drain end.

Solving equation (5.13) using the above boundary conditions, we can derive the channel potential profile as

$$\varphi_p(x) = e^{(x-L)/\sqrt{\eta}} (EC_D + V_{GS\text{eff}} - EG_{ov}) + e^{-x/\sqrt{\eta}} V_{GS\text{eff}} - V_{GS\text{eff}} + EG_{ov} \quad (5.14)$$

Using equation (5.14), the channel conduction band profile for point-TFET near the source-channel junction is plotted in **Figure 5.29(b)**, assuming all material properties remaining same as ATLAS-TFET (such as bandoverlap at source-channel junction, solid polymer electrolyte gating and bilayer MoS₂ as channel). It is observed that the W_t where the conduction band of the channel lowers down to the valence band of the source ($E=0$), is around 5 nm which is much higher than W_t of 1.3 nm in case of line-TFET. Thus, for the same length and width, ATLAS-TFET can lead to higher current due to the lower W_t as well as higher area of tunneling. Note that, while with the scaling down of channel length the benefit due to larger area of tunneling decreases, advantage arising from ultra-small W_t and hence, higher electric field can still lead to high current.

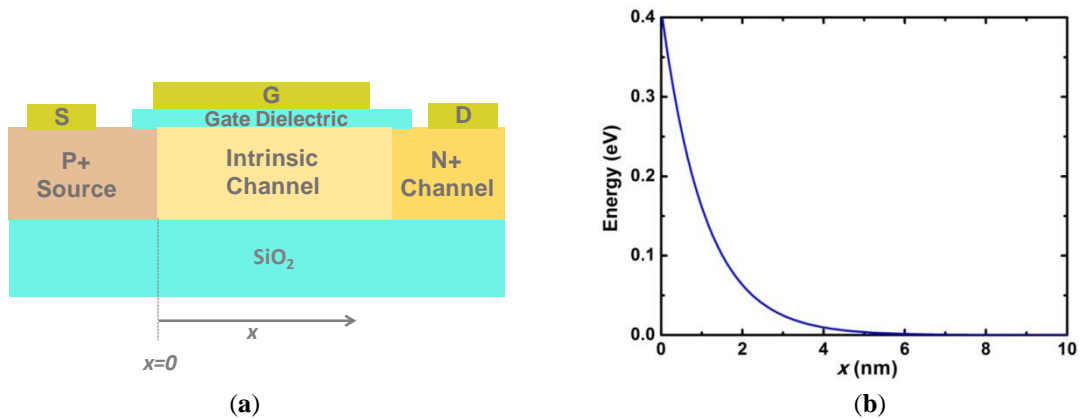


Figure 5.29(a) Schematic diagram of a point-TFET. $x=0$ represents the source-channel junction. (b) Channel conduction band profile for point-TFET near the source-channel junction as a function of distance (x) along the channel.

It is also noteworthy that, till date, there has not been any successful experimental demonstration of line-TFET with sub-thermionic SS. This undermines the importance of atomically thin MoS₂ with dangling-bond free interfaces, which has helped in the first successful realization of a line-TFET with sub-thermionic SS.

The vertical band-to-band tunneling (BTBT) is the major factor determining the drain current in ATLAS-TFET as the tunneling resistance is higher than the lateral drift-diffusion resistance due to presence of a tunnel barrier. The region where BTBT takes place is the area of overlap between the MoS₂ and the Ge. There are two ways of normalizing the current. One is to normalize with respect to the width, which is the conventional method for MOSFETs and can allow comparison with MOSFETs as well as point TFETs. Another way is to normalize with respect to the overlap area as the current scales with the area. Both methods have been used in the literature. To avoid any ambiguity, we have plotted the current in absolute sense but have

mentioned both the width and area of overlap in the caption of **Figure 5.19**, so that comparison can be done as per requirement.

5.4.9. Note on 1D TFETs and 2D-2D Tunnel Junctions

The ATLAS-TFET will be advantageous compared to 1D TFETs. When compared to 1D point-TFET (**Figure 5.30(a)**), the current of ATLAS-TFET can be much higher due to 2 reasons. First, the ATLAS-TFET presents larger area for tunneling. Second, it will be difficult to achieve tunneling width as small as in the ATLAS-TFET with a 1D point-TFET.

The channel conduction band profile for 1D point-tunnel FET can be given by equation (5.14), except that the equation for η will be different and can be written as

$$\eta_{1D} = \frac{\epsilon_{ch} r^2 \ln(1+t_{Di}/r)}{2\epsilon_{Di}}$$

where r is the radius of the 1D channel. The channel conduction band profile for point-TFET is plotted in **Figure 5.31 (b)** for different radii of 1D structure. It is observed that, all other material properties remaining same (such as bandoverlap at source-channel junction, solid polymer electrolyte gating as well as channel dielectric constant), a 1D point-TFET will require a radius smaller than 1 nm to match the $W_t = 1.3$ nm of 2D line-TFET based on bilayer MoS₂. It will be extremely challenging to achieve such small radius with nanowires. Though nanotubes can have small radius, they suffer from chirality issues. Overall, processing of 1D structures is much more difficult compared to planar architectures.

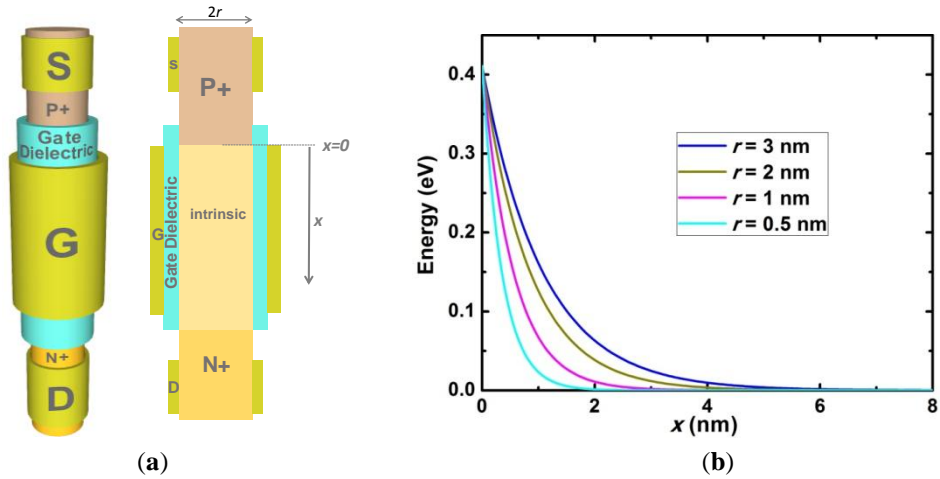


Figure 5.30(a) Schematic diagram of a 1D point-TFET showing both the 3D view (left) and cross-sectional view (right). $x=0$ represents the source-channel junction. **(b)** Channel conduction band profile for 1D point-TFET as a function of distance (x) along the channel for different radii of the 1D structure.

Moreover, fabrication of a 1D line-TFET, will be even more challenging. A schematic of a 1D line-TFET is shown in **Figure 5.31**. Realization of such a structure will require fabrication of concentric cylinders of P+ source and N/intrinsic channel. To make the structure work like an 1D architecture, the radii of the cylinders should be very small. Fabrication of such a structure is extremely daunting.

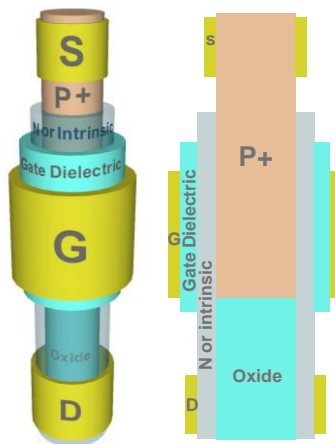


Figure 5.31. Schematic diagram of a 1D line-TFET showing both the 3D view (left) and cross-sectional view (right).

It is noteworthy, that 2D-2D tunnel junctions have been theorized to lead to steep SS , due to the unique transverse momentum conservation effect[267]. In practical TFETs, it is necessary to form tunnel junctions between two different materials leading to heterostructures. In such heterostructures, it is difficult to obtain a single wave-vector connecting the valence and conduction bands, which makes involvement of phonons necessary for tunneling. Along with phonon scattering, surface scattering will result in loss of momentum conservation, and thereby, loss of the advantage due to momentum conservation in 2D-2D junctions.

5.5. Summary

In this chapter, first, novel heterojunctions formed between on 3D (conventional) and layered materials, with record band-to-band tunneling current is demonstrated. Then, selecting the optimal heterojunction, ATLAS-TFET, the thinnest channel band-to-band tunnel transistor to overcome the fundamental limitation of SS suffered by conventional MOSFETs is achieved, which is highly promising for simultaneous scaling of device channel length as well as supply voltage. Leveraging the mature doping technique in 3D semiconducting materials and the ultra-thin and layered nature of 2D materials, a vertical strain-free hetero-interface is developed, which can not only lead to high junction electric field but also to small tunneling distance as well as large tunneling area. Using this unique device architecture, it has been possible to satisfy the ITRS recommended prescription of attainment of sub-thermionic SS over 4 decades of current for the first time at room temperature in a

planar platform as well as at ultra-low voltages. This device can potentially address both the scalability and energy-efficiency requirements of nanoscale FETs, and like its geographical namesake, the ATLAS-TFET can guide pathways toward next-generation ultra-low power integrated electronics and sensors.

Chapter 6: Conclusions and Future Work

Aggressive technology scaling as per Moore's law has resulted in exponential increase in power dissipation levels due to the degradation of device electrostatics as well as the fundamental thermionic limitation in the steepness of turn-on characteristics or subthreshold swing of conventional Field-Effect Transistors (FETs). This dissertation, explores novel two-dimensional (2D) materials (MoS₂, WSe₂ etc) for obtaining improved electrostatic control and Tunneling-Field-Effect-Transistors (TFETs), employing a fundamentally different carrier transport mechanism in the form band-to-band tunneling (BTBT) for overcoming the fundamental limitations of conventional FETs. This tailoring of both material and device technology can lead to transistors with super steep turn-ON characteristics, crucial for obtaining high energy-efficiency and ultra-scalability which can lead to the development of low power switches as well as ultra-sensitive sensors as discussed below.

6.1. Ultra-Scalable Low Power Switches

To achieve dimensional scalability, the present dissertation explores two-dimensional (2D) layered semiconductors such as Transition Metal Dichalcogenides (TMDs). Tuning the electrical properties of TMDs through charge transfer or doping is necessary for various optoelectronic applications. Hence, experimental investigation of the doping effect on TMDs, mainly focusing on molybdenum disulphide (MoS₂),

by metallic nanoparticles (NPs), exploring noble metals such as Silver (Ag), Palladium (Pd) and Platinum (Pt) as well as the low workfunction metals such as Scandium and Yttrium, is carried out for the first time. It is observed that Au, Ag, Pd, Pt and Sc lead to p-type doping, which shows an increasing trend with increasing WF of the metals. Pt with the highest WF resulted in the highest doping, which is about 2-folds higher than that of most commonly used Au NPs. Pt NPs can lead to a shift in threshold voltage as high as 137V in the case of monolayer MoS₂. While n-type doping can be obtained using Y, the doping effect is found not to be stable. It is also shown in this dissertation, that by stepwise increasing the dose of NPs, the doping intensity can be changed accordingly. It is also shown that doping effect increases with decreasing TMD thickness. In addition to doping, achievement of near ideal subthreshold swing using polymer complex gating as well as reduction of contact resistance using Yttrium/Gold contacts have been demonstrated in this dissertation.

Aiming towards "all 2D" integrated circuits, apart from transistor applications, this dissertation presents the first detailed methodology for the accurate evaluation of high-frequency impedance of graphene based structures relevant to on-chip interconnect and inductor applications. Going beyond the simplifying assumptions of Ohm's law, the effects of electric-field variation within a mean free path and current dependency on the non-local electric-field are taken into account in order to accurately capture the high-frequency behavior of graphene ribbons (GRs). At the same time, a simplified approach that may be adopted at lower frequencies is also explained. Starting from the basic Boltzmann equation and combining with the

unique dispersion relation for graphene in its hexagonal Brillouin zone, the current density across the GR structure is derived. First, a semi-infinite slab of GR is analyzed using the theory of Fourier integrals, which is followed by the development of a rigorous methodology for practical finite structures based on a self-consistent numerical calculation of the derived current density using the Green's function approach. Based on the developed methodology, this dissertation for the first time, embarks on the rigorous investigation of the intricate processes occurring at high frequencies in GRs such as Anomalous Skin Effect (ASE), high-frequency resistance and inductance saturation, intercoupled relation between the edge specularity and ASE and the influence of the linear dimensions on impedance. A comparative study of the high-frequency response of GRs with that of carbon nanotubes (CNT) and Cu is made to highlight the potential of GR interconnects for high-frequency applications. Subsequently the high-frequency performance of GR inductors is analyzed and it is shown that they can achieve 32% and 50% improvements in maximum Q-factor compared to Cu and single-walled CNT (SWCNT) inductors with 1/3 metallic fraction, respectively.

While 2D materials can provide dimensional scalability, in order to achieve power supply scalability, novel carrier transport mechanisms for lowering the subthreshold swing below the thermionic limit, specially, band-to-band tunneling (BTBT) is investigated. This dissertation provides clear insight into the interplay between electron and hole characteristics of carriers within the forbidden gap during the BTBT process, taking graphene-nanoribbons as an example. Accurate numerical models are

presented and analytical formulas for tunneling probabilities are derived for both source/drain to channel and direct source-drain tunneling based on the Wentzel–Kramers–Brillouin (WKB) method. It is shown that not considering the electron-hole duality can lead to significant errors in numerical calculations and more importantly, lack of proper understanding of the phenomenon gives rise to seriously misleading conclusions. Furthermore, the regime of validity of the WKB approximation for graphene-nanoribbon Tunnel-Field-Effect-Transistors (TFETs) is discussed in light of the electron-hole duality concept.

For improving the BTBT current, metallic nanoparticle assisted band-to-band tunneling is proposed and the impact of such nanoparticle induced states on the tunneling probability and current is modeled and analyzed. An analytical formula for tunneling probability is derived for the case of constant force and it is shown that the incorporation of these particles in the forbidden gap can lead to substantial increase in the tunneling probability. The effect of the Fermi-level pinning position on the tunneling current is studied and the pinning value for obtaining maximum improvement in current is discussed depending on the force conditions. It is also shown that an asymmetric pinning is required to leverage maximum benefits from the insertion of metallic nanoparticles.

The effect of insertion of semi-metallic nanoparticles in a semiconducting P-I-N junction is experimentally investigated and in line with theoretical predictions, substantial increase in BTBT current upon incorporation of the nanoparticles, is demonstrated. While it is shown that both GaAs and InGaAs diodes with

nanoparticles exhibit significant current improvement compared to the respective diodes without the nanoparticles, this study mainly focuses on InGaAs as the semiconductor material, since it leads to overall higher current due to its lower bandgap than that of GaAs. Temperature dependent measurements are carried out in order to shed light on the mechanism of current enhancement. The effect of increasing the doping concentration is also discussed. Different semi-metallic nanoparticles such as ErAs and ScAs are explored to maximize the tunneling current improvement.

In order to enable scaling to continue without power penalty, it is necessary to develop transistors with 2D materials as channels and employing novel carrier transport mechanism for obtaining sub-thermionic subthreshold swing (SS), such as BTBT, which had remained an unmet goal for long. With the knowledge gained from the investigation of 2D materials as well as BTBT process, this dissertation, achieves a critical milestone and furnishes the demonstration of TFETs based on 2D semiconducting-channel material exhibiting steep turn-on, with a minimum SS of 3.9 mV/dec as well as an excellent average SS of 31.1 mV/dec for 4 decades of drain-current at room temperature. By engineering the substrate to employ a highly doped Germanium as source and using atomically-thin molybdenum disulphide (MoS_2) as the layered semiconducting-channel, an unique vertical heterostructure device is built, not only retaining the advantages of 2D materials but adding extra functionality, to achieve excellent electrostatics, strain-free heterointerface, low tunneling barrier, and large tunneling area in a manufacturing-friendly planar-platform. These attributes are

difficult to achieve with conventional 3D materials or 1D structures. Our Atomically-thin and Layered Semiconducting-Channel Tunnel-FET or ATLAS-TFET provides several beneficial attributes compared to other sub-thermionic transistors. With the use of bilayer MoS₂, which is only 1.3 nm thick, we have achieved the world's thinnest channel transistor with sub-thermionic *SS*, which can lead to unprecedented opportunities for ultra-dense and low-power electronic applications. We have achieved this on a planar platform, which is easily manufacturable compared to 1D structures such as nanowires and nanotubes. It is noteworthy that, ITRS has prescribed the attainment of average *SS* lower than 60 mV/decade over 4 decades of current. To date, the only experimental TFET reported in literature to obtain this metric is the one by Tomioka et al.[252] who have used a 1D (nanowire) based structure. ATLAS-TFET is the first TFET demonstrated in planar architecture to satisfy this ITRS prescription and in fact, the only one to achieve so in any architecture, at an ultra-low drain-source voltage of 0.1 V, which is highly desirable for lowering of supply voltage and hence, power dissipation.

6.2. Extremely Sensitive and Fast Sensors

This dissertation, establishes for the first time that the tailoring of material and device technology, that is advantageous for low-power scalable digital electronics, can also be leveraged to obtain ultra-high sensitivity and fast response time in sensors.

Sensors, specially, biosensors based on Field-Effect-Transistor (FET) have attracted a lot of attention as they offer rapid, inexpensive and label-free detection technique. While the low sensitivity of FET biosensors based on bulk 3D structures has been overcome by using 1D structures (nanotubes/nanowires), the latter face severe fabrication challenges impairing their practical applications. In this dissertation, we demonstrate FET biosensors based on molybdenum disulphide (MoS_2) which provides extremely high sensitivity and at the same time offer easy patternability and device fabrication, thanks to its 2D atomically layered structure. A MoS_2 based pH sensor achieving sensitivity as high as 713 for a pH change by 1 unit along with efficient operation over a wide pH range (3-9) is demonstrated. Ultra-sensitive and specific protein sensing is also achieved with a sensitivity of 196 even at 100 femto-Molar concentration. While graphene is also a 2D material, we show here that it cannot compete with MoS_2 based FET biosensor, which surpasses the sensitivity of that based on graphene by more than 74-fold. Moreover, we establish through theoretical analysis that MoS_2 is greatly advantageous for biosensor device scaling without compromising its sensitivity. Furthermore, MoS_2 with its highly flexible and transparent nature can offer new opportunities in advanced diagnostics and medical

prosthesis. This unique fusion of desirable properties makes MoS₂ a highly potential candidate for next-generation low-cost biosensors.

While 2D semiconductors can help to achieve good electrostatics and lead to flexibility and ease of fabrication, the thermionic emission current injection mechanism in CFET based biosensors puts fundamental limitations (minimum subthreshold swing of 60mV/decade) on their maximum sensitivity and minimum detection time.

In this dissertation, we propose a novel biosensor that exploits the phenomenon of band-to-band tunneling, to overcome the fundamental limitations in CFET based biosensors by employing a tunnel-FET (TFET) sensor. The TFET biosensor is shown to be both time-efficient and 10,000 times more sensitive than sensors based on conventional FETs. The key concept behind the TFET biosensor device is to leverage biomolecule conjugation to bend the energy bands in the channel region leading to the quantum-mechanical phenomenon of band-to-band tunneling that is a fundamentally different current injection mechanism. This results in an abrupt increase in current, which is instrumental in increasing the sensitivity and reducing the response time of the proposed sensor. The sharp (<60mV/decade) turn-on feature of the TFETs also allow ultra-low voltage and low off-state-leakage (and hence low power) operation that is desirable for hand-held, battery operated point-of-care biosensors as well as for deployment of such sensor arrays in remote locations.

A novel gas-sensor based on Tunnel-Field-Effect-Transistor (TFET) is also proposed in this dissertation, that leverages the unique current injection mechanism in the form of quantum-mechanical band-to-band tunneling to achieve substantially improved performance compared to conventional MOSFETs for detection of gas species under ambient conditions. While nonlocal phonon-assisted tunneling model is used for detailed device simulations, in order to provide better physical insights analytical formula for sensitivity is derived for both metal as well as organic conducting polymer based sensing elements. Analytical derivations are also presented for capturing the effects of temperature on sensor performance. Combining the developed analytical and numerical models, intricate properties of the sensor such as gate bias dependence of sensitivity, relation between required work-function (WF) modulation and subthreshold swing, counter-intuitive increase in threshold voltage and reduction in tunneling probability with temperature are explained. It is shown that TFET gas-sensors can not only lead to more than 10000x increase in sensitivity, but also provide design flexibility and immunity against screening of WF modulation through non-specific gases as well as ensure stable operation under temperature variations.

6.3. Future Work

6.3.1. Drain Current Improvement

Though the current in ATLAS-TFET is at par with other experimental TFETs with steep SS , further improvement in current is required specially for digital electronic applications. The current can be improved by removing the interfacial germanium oxide layer, which adds extra tunneling resistance in series in the tunneling path from the Ge to the MoS₂. To gauge the impact of this resistance, the tunneling probability through this oxide as a function of the voltage applied to the MoS₂ with respect to the Ge is derived, since inverse of this tunneling probability gives indication of the tunneling resistance. For the above derivation, first the band bending in the device needs to be determined, for which, Poisson equations are solved in the device. The Poisson equations in the 3 different regions namely the Ge, interfacial oxide and MoS₂ (TMD) is given below

$$\frac{d^2\psi_{Ge}(x)}{dx^2} = \frac{q \times dop_{Ge}}{\epsilon_{Ge}} \quad (6.1a)$$

$$\frac{d^2\psi_{ox}(x)}{dx^2} = 0 \quad (6.1b)$$

$$\frac{d^2\psi_{MoS_2}(x)}{dx^2} = \frac{q \times dop_{MoS_2}}{\epsilon_{MoS_2}} \quad (6.1c)$$

where ψ_{Ge} , ψ_{ox} and ψ_{MoS_2} are the potential profile of valence band of Ge, interfacial oxide and MoS₂ respectively, ϵ_{Ge} , and ϵ_{MoS_2} are the dielectric constants of Ge and MoS₂ respectively while, dop_{Ge} , and dop_{MoS_2} are the doping concentrations in Ge and

MoS₂, respectively. x is in the direction from Ge to MoS₂ and we have defined $x=0$ at the interface of the oxide (with a thickness of t_{ox}) and MoS₂ (with a thickness of t_{MoS_2}), q is the electronic charge.

Equations (6.1a) and (6.1c) are first solved with the following four boundary conditions given by

(i) $\frac{d\psi_{Ge}(-Wd-t_{ox})}{dx} = 0$ as electric field is zero in Ge beyond the depletion region (Wd) in it.

(ii) $-\frac{d\psi_{Ge}(-t_{ox})}{dx} \times \epsilon_{Ge} = F_{ox} \times \epsilon_{ox} = -\frac{d\psi_{MoS_2}(0)}{dx} \times \epsilon_{MoS_2}$ due to the continuity of electric displacement field where ϵ_{Ge} , ϵ_{ox} and ϵ_{MoS_2} are the dielectric constants of Ge, interfacial oxide and MoS₂ respectively and F_{ox} is the electric field in the oxide.

(iii) $\psi_{MoS_2}(0) = \psi_{Ge}(-t_{ox}) + E_{v_{offset}} - V_{ox}$ where $E_{v_{offset}}$ is the valence band offset of MoS₂ with respect to Ge and V_{ox} is the voltage drop in the interfacial oxide and can be

written as $-\frac{d\psi_{MoS_2}(0)}{dx} \times \frac{\epsilon_{MoS_2}}{\epsilon_{ox}} \times t_{ox}$

(iv) $\psi_{MoS_2}(t_{MoS_2}) = U_{MoS_2}$ where U_{MoS_2} is the valence band position of MoS₂ at $x=t_{MoS_2}$.

By solving equations (6.1a) and (6.1c) with the above boundary conditions we obtain the potential profile in the Ge and the MoS₂ with the depletion region in Ge (Wd) being the unknown factor in them as given below:

$$\begin{aligned} \psi_{Ge}(x) = & \frac{1}{2} \frac{q \text{dop}_{Ge} x^2}{\epsilon_{Ge}} + \frac{q \text{dop}_{Ge} (Wd + t_{ox}) x}{\epsilon_{Ge}} + \frac{1}{2} \frac{1}{\epsilon_{MoS_2} \epsilon_{ox} \epsilon_{Ge}} \left\{ -2\epsilon_{MoS_2} \epsilon_{Ge} t_{ox} q \text{dop}_{Ge} Wd \right. \\ & - 2\epsilon_{ox} \epsilon_{Ge} t_{MoS_2} q \text{dop}_{Ge} Wd + 2\epsilon_{MoS_2} \epsilon_{ox} t_{ox} q \text{dop}_{Ge} Wd - 2\epsilon_{MoS_2} \epsilon_{Ge} \epsilon_{ox} E_{v_{offset}} \\ & \left. + \epsilon_{MoS_2} \epsilon_{ox} q \text{dop}_{Ge} t_{ox}^2 - \epsilon_{Ge} \epsilon_{ox} q \text{dop}_{MoS_2} t_{MoS_2}^2 + 2\epsilon_{MoS_2} \epsilon_{Ge} \epsilon_{ox} U_{MoS_2} \right\} \end{aligned} \quad (6.2a)$$

$$\psi_{MoS_2}(x) = \frac{1}{2} \frac{q \text{dop}_{MoS_2} x^2}{\epsilon_{MoS_2}} + \frac{q \text{dop}_{Ge} Wd x}{\epsilon_{MoS_2}} - \frac{1}{2} \frac{q \text{dop}_{MoS_2} t_{MoS_2}^2 - 2U_{MoS_2} \epsilon_{MoS_2} + 2t_{MoS_2} q \text{dop}_{Ge} Wd}{\epsilon_{MoS_2}} \quad (6.2b)$$

Now, without any loss of generality, $\psi_{Ge}(-Wd - t_{ox})$ is set to zero such that all other potentials are calculated with respect to it. Hence, by solving $\psi_{Ge}(-Wd - t_{ox}) = 0$ using equation (6.2a), we can derive Wd as:

$$\begin{aligned} Wd = & -\frac{1}{q \epsilon_{MoS_2} \epsilon_{ox} \text{dop}_{Ge}} \left\{ \epsilon_{Ge} \epsilon_{MoS_2} t_{ox} q \text{dop}_{Ge} + \epsilon_{Ge} \epsilon_{ox} t_{MoS_2} q \text{dop}_{Ge} + \left[(\epsilon_{Ge} \epsilon_{MoS_2} t_{ox} q \text{dop}_{Ge})^2 \right. \right. \\ & + 2\epsilon_{Ge}^2 \epsilon_{MoS_2} t_{ox} q^2 \text{dop}_{Ge}^2 \epsilon_{ox} t_{MoS_2} + (\epsilon_{Ge} \epsilon_{ox} t_{MoS_2} q \text{dop}_{Ge})^2 \\ & \left. \left. + 2\epsilon_{MoS_2}^2 \epsilon_{ox}^2 q \text{dop}_{Ge} \epsilon_{Ge} (U_{MoS_2} - E_{v_{offset}}) - \epsilon_{MoS_2} \epsilon_{ox}^2 q^2 \text{dop}_{Ge} \epsilon_{Ge} \text{dop}_{MoS_2} t_{MoS_2}^2 \right]^{1/2} \right\} \end{aligned} \quad (6.3)$$

The voltage drop in Ge, V_{Ge} can be derived by subtracting the potential of Ge at the interface of Ge and interfacial oxide ($\psi_{Ge}(-t_{ox})$) from the potential at the end of the depletion region ($\psi_{Ge}(-Wd - t_{ox})$ which has been set to zero). Therefore, $V_{Ge} = 0 - \psi_{Ge}(-t_{ox})$ and from equation (6.2a), we can derive,

$$\begin{aligned} V_{Ge} = & \frac{1}{2} \frac{1}{\epsilon_{MoS_2} \epsilon_{ox} \epsilon_{Ge}} \left(-2\epsilon_{MoS_2} \epsilon_{Ge} t_{ox} q \text{dop}_{Ge} Wd - 2\epsilon_{Ge} \epsilon_{ox} t_{MoS_2} q \text{dop}_{Ge} Wd \right. \\ & - 2\epsilon_{MoS_2} \epsilon_{Ge} \epsilon_{ox} E_{v_{offset}} - \epsilon_{Ge} \epsilon_{ox} q \text{dop}_{MoS_2} t_{MoS_2}^2 \\ & \left. + 2\epsilon_{MoS_2} \epsilon_{Ge} \epsilon_{ox} U_{MoS_2} \right) \end{aligned} \quad (6.4)$$

Now, F_{ox} can be derived from equation (6.2b) using $-\frac{d\psi_{MoS_2}(0)}{dx} \times \frac{\epsilon_{MoS_2}}{\epsilon_{ox}}$ as:

$$F_{ox} = \frac{q \text{dop}_{Ge} Wd}{\epsilon_{ox}} \quad (6.5)$$

With the electric field in the interfacial oxide being derived, we can now derive the tunneling probability (P_{ox}) through it. Using the WKB approximation, the tunneling probability at the energy of the valence band edge of Ge at $x=-t_{ox}$ can be written as:

$$P_{ox} = e^{-2\sqrt{\frac{2mq}{\hbar^2}} \int_0^{t_{ox}} \sqrt{Offset_{ox} - F_{ox}x} dx} \quad (6.6)$$

where $Offset_{ox}$ is the height of the oxide conduction band with respect to the valence band of Ge, $\hbar = h/2\pi$ with h being the Planck's constant, m is the mass of the carrier.

Solving the integral in equation (6.6), the tunneling probability can be derived as:

$$P_{ox} = e^{-\frac{4}{3}\sqrt{\frac{2mq}{\hbar^2}} \frac{(Offset_{ox})^{3/2} - (Offset_{ox} - V_{ox})^{3/2}}{F_{ox}}} \quad (6.7)$$

In **Figure 6.1**, the tunneling probability through the oxide is plotted as a function of the voltage on MoS_2 with respect to Ge and it is observed that the probability is extremely low and is relatively independent of the applied bias. This implies that even by increasing the bias, it is not possible to increase the tunneling probability (and hence, decrease the resistance posed by the interfacial oxide) significantly.

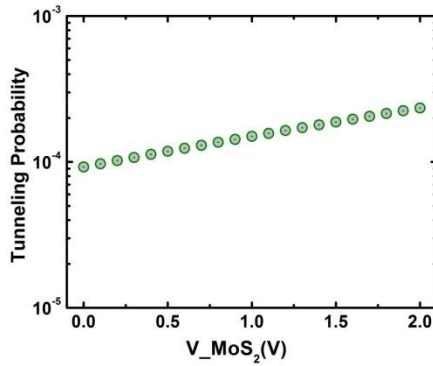


Figure 6.1. Tunneling probability through the interfacial oxide as a function of the voltage applied to MoS_2 .

6.3.2. Experimental Demonstration of 2D-TFET based Sensors

In Chapter 4, we demonstrated the unique advantages of employing 2D semiconducting materials as channel in electrical biosensors. 2D semiconductors can not only lead to high sensitivity due to improved electrostatic control arising from their ultra-thin nature and pristine interfaces, but also offer easy processability due to their planar structure. In addition 2D material based biosensors can maintain high sensitivity even at ultra-scaled dimensions and hence, are highly promising for single-molecule detection. Apart from proper material selection, it is demonstrated theoretically in Chapter 4, that employment of novel device technology such as TFETs can lead to further improvement in biosensor performance because of their low subthreshold swing (SS). It has been shown that the sensitivity of a biosensor increases exponentially with the decrease in SS . Moreover, lowering the SS can also lead to reduced average response time. Thus, TFETs with 2D material as channel (or in short 2D-TFET) can be highly promising for biosensing applications. This dissertation presented the first experimental demonstration of a 2D-TFET as discussed in Chapter 5. However, configuration of this device as a biosensor has not been achieved yet and would require future work. The employment of the demonstrated 2D-TFET as a biosensor would require the development of good quality ultra-thin gate dielectrics with high dielectric constant, which can provide high capacitance gating effect on biomolecule conjugation.

Such a ultra-sensitive biosensor based on 2D-TFETs can potentially revolutionize the growing field of personalized medicine which is an extension of

traditional treatment methodologies, based on the probing of molecular makeup of each patient and tailoring of medical care to individual patient's genetic and proteomic profile, thus making the treatment more effective and reducing undesirable negative side-effects. This will lead to better treatment opportunities for many complex diseases such as cancer, diabetes, heart disease and Alzheimer which are related to genetic origin. The ability of 2D-TFET biosensors to detect biomolecules at low concentration will enable the health care professionals to know the onset of a disease before symptoms even appear. This will lead to earlier disease intervention and focus on prevention and prediction of a disease which will not only increase by manifold the success rate in combating the disease but will also result in a massive reduction in the healthcare costs. The 2D-TFET biosensors can also provide real-time, lab-quality results within seconds enabling the physician to take fast medical decisions and thus highly facilitating the point-of-care applications. The proposed sensor works in the subthreshold region and consumes very little power and thus is very advantageous for battery operated applications in mobile systems. Moreover, these miniaturized biosensors are highly suitable for hand held diagnostic tools. Thus the proposed highly efficient biosensors can extend the medical care to developing countries and remote areas and largely improve the survival rates in those regions. In short, the 2D-TFET biosensor can lead to a paradigm shift in health care and clinical diagnostics. Beyond medical applications, the proposed sensor can also revolutionize security and forensic industries and provide better protection of our environment, food and water supplies.

References

- [1] R. Yan, A. Ourmazd, and K. F. Lee, “Scaling the Si MOSFET : from bulk to SOI to bulk,” *IEEE Trans. Electron Devices*, vol. 39, no. 7, pp. 704–710, 1992.
- [2] J. Colinge, “Multiple-gate SOI MOSFETs,” *Solid State Electron.*, vol. 48, pp. 897–905, 2004.
- [3] B. Radisavljevic, A. Radenovic, J. Brivio, V. Giacometti, and A. Kis, “Single-layer MoS₂ transistors,” *Nat. Nanotechnol.*, vol. 6, no. 3, pp. 147–50, Mar. 2011.
- [4] D. Sarkar, W. Liu, X. Xie, A. C. Anselmo, S. Mitragotri, and K. Banerjee, “MoS₂ field-effect transistor for next-generation label- free biosensors,” *ACS Nano*, vol. 8, no. 4, pp. 3992–4003, 2014. Reprinted with permission from American Chemical Society © 2014.
- [5] Q. H. Wang, K. Kalantar-Zadeh, A. Kis, J. N. Coleman, and M. S. Strano, “Electronics and optoelectronics of two-dimensional transition metal dichalcogenides,” *Nat. Nanotechnol.*, vol. 7, no. 11, pp. 699–712, Nov. 2012.

- [6] H. Zeng, J. Dai, W. Yao, D. Xiao, and X. Cui, “Valley polarization in MoS₂ monolayers by optical pumping,” *Nat. Nanotechnol.*, vol. 7, no. 8, pp. 490–3, Aug. 2012.
- [7] H. Pan and Y.-W. Zhang, “Edge-dependent structural, electronic and magnetic properties of MoS₂ nanoribbons,” *J. Mater. Chem.*, vol. 22, no. 15, p. 7280, 2012.
- [8] A. T. Neal, H. Liu, J. Gu, and P. D. Ye, “Magneto-transport in MoS₂: phase coherence, spin-orbit scattering, and the hall factor.,” *ACS Nano*, vol. 7, no. 8, pp. 7077–82, Aug. 2013.
- [9] J. Kang, W. Cao, X. Xie, D. Sarkar, W. Liu, and K. Banerjee, “Graphene and beyond-graphene 2D crystals for next-generation green electronics,” *Proc. SPIE 9083, Micro- Nanotechnol. Sensors, Syst. Appl. VI*, p. 908305, Jun. 2014.
- [10] J. Kang, D. Sarkar, Y. Khatami, and K. Banerjee, “Proposal for all-graphene monolithic logic circuits,” *Appl. Phys. Lett.*, vol. 103, no. 8, p. 083113, 2013.
- [11] A. K. Geim and K. S. Novoselov, “The rise of graphene,” *Nat. Mater.*, vol. 6, pp. 183–192, 2007.
- [12] H. Li, Y. Khatami, D. Sarkar, J. Kang, C. Xu, W. Liu, and K. Banerjee, “Carbon Integrated Electronics,” in *Intelligent Integrated Systems:*

Technologies, Devices and Architectures, no. August, S. Deleonibus, Ed. WSPC-Pan Stanford (Singapore), 2014.

- [13] R. Saito, G. Dresselhaus, and M. S. Dresselhaus, *Physical Properties of Carbon Nanotubes*. London, U. K.: Imperial College Press, 1998.
- [14] Y.-W. Son, M. L. Cohen, and S. G. Louie, “Energy Gaps in Graphene Nanoribbons,” *Phys. Rev. Lett.*, vol. 97, no. 21, p. 216803, Nov. 2006.
- [15] P. Avouris, Z. Chen, and V. Perebeinos, “Carbon-based electronics.,” *Nat. Nanotechnol.*, vol. 2, no. 10, pp. 605–15, Oct. 2007.
- [16] Y. Zhang, T.-T. Tang, C. Girit, Z. Hao, M. C. Martin, A. Zettl, M. F. Crommie, Y. R. Shen, and F. Wang, “Direct observation of a widely tunable bandgap in bilayer graphene.,” *Nature*, vol. 459, no. 7248, pp. 820–3, Jun. 2009.
- [17] M. Han, B. Özyilmaz, Y. Zhang, and P. Kim, “Energy Band-Gap Engineering of Graphene Nanoribbons,” *Phys. Rev. Lett.*, vol. 98, no. 20, p. 206805, May 2007.
- [18] X. Li, X. Wang, L. Zhang, S. Lee, G. Incorporated, and N. Incorporated, “Chemically Derived, Ultrasooth Graphene Nanoribbon Semiconductors,” *Science (80-.)*, vol. 319, pp. 1229–1232, 2008.

- [19] L. Jiao, L. Zhang, X. Wang, G. Diankov, and H. Dai, “Narrow graphene nanoribbons from carbon nanotubes.” *Nature*, vol. 458, no. 7240, pp. 877–80, Apr. 2009.
- [20] W. Liu, S. Kraemer, D. Sarkar, H. Li, P. M. Ajayan, and K. Banerjee, “Controllable and Rapid Synthesis of High-Quality and Large-Area Bernal Stacked Bilayer Graphene Using Chemical Vapor Deposition,” *Chem. Mater.*, vol. 26, no. 2, pp. 907–915, Jan. 2014.
- [21] C. Xu, H. Li, and K. Banerjee, “Modeling , Analysis , and Design of Graphene Nano-Ribbon Interconnects,” *IEEE Trans. Electron Devices*, vol. 56, no. 8, pp. 1567–1578, 2009.
- [22] D. Sarkar, C. Xu, H. Li, and K. Banerjee, “High-Frequency Behavior of Graphene-Based Interconnects — Part I : Impedance Modeling,” *IEEE Trans. Electron Devices*, vol. 58, no. 3, pp. 843–852, 2011. Reprinted with permission from IEEE © 2011.
- [23] D. Sarkar, C. Xu, H. Li, and K. Banerjee, “High-Frequency Behavior of Graphene-Based Interconnects — Part II : Impedance Analysis and Implications for Inductor Design,” *IEEE Trans. Electron Devices*, vol. 58, no. 3, pp. 853–859, 2011. Reprinted with permission from IEEE © 2011.

- [24] D. Sarkar, C. Xu, H. Li, and K. Banerjee, "AC conductance modeling and analysis of graphene nanoribbon interconnects," in *2010 IEEE International Interconnect Technology Conference*, 2010, pp. 1–3. Reprinted with permission from IEEE © 2010.
- [25] Q. Shao, G. Liu, D. Teweldebrhan, and a. a. Balandin, "High-Temperature Quenching of Electrical Resistance in Graphene Interconnects," *Appl. Phys. Lett.*, vol. 92, no. 20, p. 202108, 2008.
- [26] A. Naeemi and J. D. Meindl, "Conductance Modeling for Graphene NanoRibbon (GNR) Interconnects," *IEEE Trans. Electron Devices*, vol. 28, no. 5, pp. 428–431, 2007.
- [27] A. a Balandin, S. Ghosh, W. Bao, I. Calizo, D. Teweldebrhan, F. Miao, and C. N. Lau, "Superior Thermal Conductivity of Single-Layer Graphene," *Nano Lett.*, vol. 8, no. 3, pp. 902–7, Mar. 2008.
- [28] K. I. Bolotin, K. J. Sikes, J. Hone, H. L. Stormer, and P. Kim, "Temperature-Dependent Transport in Suspended Graphene," *Phys. Rev. Lett.*, vol. 101, no. 9, p. 096802, Aug. 2008.
- [29] W. Cao, J. Kang, D. Sarkar, W. Liu, and K. Banerjee, "Performance evaluation and design considerations of 2D semiconductor based FETs for sub-10 nm VLSI," in *IEEE International Electron Devices Meeting*, 2014, pp. 30.5.1–30.5.4.

- [30] W. Cao, J. Kang, D. Sarkar, W. Liu, and K. Banerjee, "2D Semiconductor FETs- Projections and Design for Sub-10 nm VLSI," *IEEE Trans. Electron Devices*, 2015.
- [31] M. Schmidt, M. C. Lemme, H. D. B. Gottlob, F. Driussi, L. Selmi, and H. Kurz, "Mobility extraction in SOI MOSFETs with sub 1nm body thickness," *Solid. State. Electron.*, vol. 53, no. 12, pp. 1246–1251, Dec. 2009.
- [32] W. Liu, J. Kang, W. Cao, D. Sarkar, Y. Khatami, D. Jena, and K. Banerjee, "High-performance few-layer-MoS₂ field-effect-transistor with record low contact-resistance," in *IEEE International Electron Devices Meeting*, 2013, pp. 499–502.
- [33] W. Liu, D. Sarkar, J. Kang, W. Cao, and K. Banerjee, "Impact of Contact on the Operation and Performance of Back-Gated Monolayer MoS₂ Field-Effect-Transistors," *ACS nano (Article ASAP DOI 10.1021/nn506512j)*, 2015.
- [34] H. T. Yuan, M. Toh, K. Morimoto, W. Tan, F. Wei, H. Shimotani, C. Kloc, and Y. Iwasa, "Liquid-gated electric-double-layer transistor on layered metal dichalcogenide, SnS₂," *Appl. Phys. Lett.*, vol. 98, no. 1, p. 012102, 2011.
- [35] J. Pu, Y. Yomogida, K.-K. Liu, L.-J. Li, Y. Iwasa, and T. Takenobu, "Highly flexible MoS₂ thin-film transistors with ion gel dielectrics.," *Nano Lett.*, vol. 12, no. 8, pp. 4013–7, Aug. 2012.

- [36] V. E. Fedorov, N. G. Naumov, A. N. Lavrov, M. S. Tarasenko, S. B. Artemkina, and A. I. Romanenko, "Tuning Electronic Properties of Molybdenum Disulfide by a Substitution in Metal Sublattice," in *36th International Convention on Information & Communication Technology Electronics & Microelectronics (MIPRO)*, 2013, vol. 2, pp. 17–20.
- [37] M. R. Laskar, D. N. Nath, L. Ma, E. W. Lee, C. H. Lee, T. Kent, Z. Yang, R. Mishra, M. a. Roldan, J.-C. Idrobo, S. T. Pantelides, S. J. Pennycook, R. C. Myers, Y. Wu, and S. Rajan, "p-type doping of MoS₂ thin films using Nb," *Appl. Phys. Lett.*, vol. 104, no. 9, p. 092104, Mar. 2014.
- [38] Q.-Q. Sun, Y.-J. Li, J.-L. He, W. Yang, P. Zhou, H.-L. Lu, S.-J. Ding, and D. Wei Zhang, "The physics and backward diode behavior of heavily doped single layer MoS₂ based p-n junctions," *Appl. Phys. Lett.*, vol. 102, no. 9, p. 093104, 2013.
- [39] H. Fang, S. Chuang, T. C. Chang, K. Takei, T. Takahashi, and A. Javey, "High performance single layered WSe p-FETs with chemically doped contacts," *Nano Lett.*, vol. 12, p. 3788, 2012.
- [40] S. Tongay, J. Zhou, C. Ataca, J. Liu, J. S. Kang, T. S. Matthews, L. You, J. Li, J. C. Grossman, and J. Wu, "Broad-range modulation of light emission in two-dimensional semiconductors by molecular physisorption gating.," *Nano Lett.*, vol. 13, no. 6, pp. 2831–6, Jun. 2013.

- [41] Y. Li, C. Xu, P. Hu, and L. Zhen, "Carrier Control of MoS₂ Nanoflakes by Functional Self-Assembled Monolayers," *ACS Nano*, vol. 7, no. 9, pp. 7795–7804, 2013.
- [42] Y. Du, H. Liu, A. T. Neal, M. Si, and P. D. Ye, "Molecular Doping of Multilayer MoS₂ Field-Effect Transistors : Reduction in Sheet and Contact Resistances," *IEEE Electron Device Lett.*, vol. 34, no. 10, pp. 1328–1330, 2013.
- [43] S. Mouri, Y. Miyauchi, and K. Matsuda, "Tunable photoluminescence of monolayer MoS₂ via chemical doping.," *Nano Lett.*, vol. 13, no. 12, pp. 5944–8, Dec. 2013.
- [44] M. Chen, H. Nam, S. Wi, L. Ji, X. Ren, L. Bian, S. Lu, and X. Liang, "Stable few-layer MoS₂ rectifying diodes formed by plasma-assisted doping," *Appl. Phys. Lett.*, vol. 103, no. 14, p. 142110, 2013.
- [45] S. Wi, H. Kim, M. Chen, H. Nam, L. J. Guo, E. Meyhofer, and X. Liang, "Enhancement of Photovoltaic Response in Multilayer MoS₂ Induced by Plasma Doping.," *ACS Nano*, vol. 8, no. 5, pp. 5270–5281, May 2014.
- [46] H. Fang, M. Tosun, G. Seol, T. C. Chang, K. Takei, J. Guo, and A. Javey, "Degenerate n-doping of few-layer transition metal dichalcogenides by potassium.," *Nano Lett.*, vol. 13, no. 5, pp. 1991–5, May 2013.

- [47] K. Chen, D. Kiriya, M. Hettick, M. Tosun, T.-J. Ha, S. R. Madhvapathy, S. Desai, A. Sachid, and A. Javey, "Air stable n-doping of WSe₂ by silicon nitride thin films with tunable fixed charge density," *APL Mater.*, vol. 2, no. 9, p. 092504, Sep. 2014.
- [48] J. D. Lin, C. Han, F. Wang, R. Wang, D. Xiang, S. Qin, X.-A. Zhang, L. Wang, H. Zhang, A. T. S. Wee, and W. Chen, "Electron-Doping-Enhanced Trion Formation in Monolayer Molybdenum Disulfide Functionalized with Cesium Carbonate.," *ACS Nano*, no. Xx, May 2014.
- [49] L. Yang, K. Majumdar, Y. Du, H. Liu, H. Wu, M. Hatzistergos, P. Y. Hung, R. Tieckelmann, W. Tsai, C. Hobbs, and P. D. Ye, "High-Performance MoS₂ Field-Effect Transistors Enabled by Chloride Doping : Record Low Contact Resistance ($0.5 \text{ k}\Omega \cdot \mu\text{m}$) and Record High Drain Current ($460 \mu\text{A} / \mu\text{m}$)," *Symp. VLSI Technol.*, pp. 1–2, 2014.
- [50] C. Functionalization, P. Zhao, D. Kiriya, A. Azcatl, C. Zhang, M. Tosun, Y. Liu, M. Hettick, J. S. Kang, S. McDonnell, S. Kc, J. Guo, K. Cho, R. M. Wallace, and A. Javey, "Air Stable p - Doping of WSe₂ by," *ACS Nano*, 2014.
- [51] J. Lin, J. Zhong, S. Zhong, H. Li, H. Zhang, and W. Chen, "Modulating electronic transport properties of MoS₂ field effect transistor by surface overlayers," *Appl. Phys. Lett.*, vol. 103, no. 6, p. 063109, 2013.

- [52] L. Cattin, M. Morsli, and J. Bernède, “Improvement in the Lifetime of Planar Organic Photovoltaic Cells through the Introduction of MoO₃ into Their Cathode Buffer Layers,” *Electronics*, vol. 3, no. 1, pp. 122–131, Mar. 2014.
- [53] S. Mubeen, T. Zhang, B. Yoo, M. a. Deshusses, and N. V. Myung, “Palladium Nanoparticles Decorated Single-Walled Carbon Nanotube Hydrogen Sensor,” *J. Phys. Chem. C*, vol. 111, no. 17, pp. 6321–6327, May 2007.
- [54] J. L. Johnson, A. Behnam, S. J. Pearton, and A. Ural, “Hydrogen sensing using pd-functionalized multi-layer graphene nanoribbon networks.,” *Adv. Mater.*, vol. 22, no. 43, pp. 4877–80, Nov. 2010.
- [55] Y. Zhang, J. Xu, P. Xu, Y. Zhu, X. Chen, and W. Yu, “Decoration of ZnO nanowires with Pt nanoparticles and their improved gas sensing and photocatalytic performance.,” *Nanotechnology*, vol. 21, no. 28, p. 285501, Jul. 2010.
- [56] S. Mao, G. Lu, K. Yu, Z. Bo, and J. Chen, “Specific protein detection using thermally reduced graphene oxide sheet decorated with gold nanoparticle-antibody conjugates.,” *Adv. Mater.*, vol. 22, no. 32, pp. 3521–6, Aug. 2010.
- [57] D. Sarkar, X. Xie, J. Kang, H. Zhang, W. Liu, J. Navarrete, M. Moskovits, and K. Banerjee, “Functionalization of transition metal dichalcogenides with metallic nanoparticles: implications for doping and gas-sensing,” *Nano Lett.*,

vol. 15, no. 5, pp. 2852–62, May 2015. Reprinted with permission from American Chemical Society © 2015.

- [58] T. S. Sreeprasad, P. Nguyen, N. Kim, and V. Berry, “Controlled, Defect-Guided, Metal-Nanoparticle Incorporation onto MoS₂ via Chemical and Microwave Routes: Electrical, Thermal, and Structural Properties,” *Nano Lett.*, vol. 13, no. 9, pp. 4434–4441, 2013.
- [59] Y. Shi, J.-K. Huang, L. Jin, Y.-T. Hsu, S. F. Yu, L.-J. Li, and H. Y. Yang, “Selective decoration of Au nanoparticles on monolayer MoS₂ single crystals,” *Sci. Rep.*, vol. 3, p. 1839, Jan. 2013.
- [60] K. S. Novoselov, D. Jiang, F. Schedin, T. J. Booth, V. V Khotkevich, S. V Morozov, and A. K. Geim, “Two-dimensional atomic crystals,” *Proc. Natl. Acad. Sci. U. S. A.*, vol. 102, no. 30, pp. 10451–3, Jul. 2005.
- [61] K. F. Mak, C. Lee, J. Hone, J. Shan, and T. F. Heinz, “Atomically thin MoS₂: a new direct-gap semiconductor,” *Phys. Rev. Lett.*, vol. 105, no. 13, p. 136805, Sep. 2010.
- [62] S. Kim, A. Konar, W.-S. Hwang, J. H. Lee, J. Lee, J. Yang, C. Jung, H. Kim, J.-B. Yoo, J.-Y. Choi, Y. W. Jin, S. Y. Lee, D. Jena, W. Choi, and K. Kim, “High-mobility and low-power thin-film transistors based on multilayer MoS₂ crystals,” *Nat. Commun.*, vol. 3, p. 1011, Jan. 2012.

- [63] W. Liu, J. Kang, D. Sarkar, Y. Khatami, D. Jena, and K. Banerjee, "Role of Metal Contacts in Designing High-Performance Monolayer n-Type WSe₂ Field Effect Transistors," *Nano Lett.*, vol. 13, no. 5, pp. 1983–1990, 2013.
- [64] X. Xie, D. Sarkar, W. Liu, J. Kang, O. Marinov, J. Deen, K. Banerjee, C. Engineering, S. Barbara, and U. States, "Low-Frequency Noise in Bilayer MoS₂," *ACS Nano*, vol. 8, no. 6, pp. 5633–5640, 2014.
- [65] J. N. Coleman, M. Lotya, A. O'Neill, S. D. Bergin, P. J. King, U. Khan, K. Young, A. Gaucher, S. De, R. J. Smith, I. V Shvets, S. K. Arora, G. Stanton, H.-Y. Kim, K. Lee, G. T. Kim, G. S. Duesberg, T. Hallam, J. J. Boland, J. J. Wang, J. F. Donegan, J. C. Grunlan, G. Moriarty, A. Shmeliov, R. J. Nicholls, J. M. Perkins, E. M. Grieveson, K. Theuwissen, D. W. McComb, P. D. Nellist, and V. Nicolosi, "Two-dimensional nanosheets produced by liquid exfoliation of layered materials.," *Science*, vol. 331, no. 6017, pp. 568–71, Feb. 2011.
- [66] R. J. Smith, P. J. King, M. Lotya, C. Wirtz, U. Khan, S. De, A. O'Neill, G. S. Duesberg, J. C. Grunlan, G. Moriarty, J. Chen, J. Wang, A. I. Minett, V. Nicolosi, and J. N. Coleman, "Large-scale exfoliation of inorganic layered compounds in aqueous surfactant solutions.," *Adv. Mater.*, vol. 23, no. 34, pp. 3944–8, Sep. 2011.
- [67] K.-K. Liu, W. Zhang, Y.-H. Lee, Y.-C. Lin, M.-T. Chang, C.-Y. Su, C.-S. Chang, H. Li, Y. Shi, H. Zhang, C.-S. Lai, and L.-J. Li, "Growth of large-area

and highly crystalline MoS₂ thin layers on insulating substrates.,” *Nano Lett.*, vol. 12, no. 3, pp. 1538–44, Mar. 2012.

- [68] Y. Zhan, Z. Liu, S. Najmaei, P. M. Ajayan, and J. Lou, “Large-area vapor-phase growth and characterization of MoS₂ atomic layers on a SiO₂ substrate.,” *Small*, vol. 8, no. 7, pp. 966–71, Apr. 2012.
- [69] H. Li, Q. Zhang, C. C. R. Yap, B. K. Tay, T. H. T. Edwin, A. Olivier, and D. Baillargeat, “From Bulk to Monolayer MoS₂: Evolution of Raman Scattering,” *Adv. Funct. Mater.*, vol. 22, no. 7, pp. 1385–1390, Apr. 2012.
- [70] B. Chakraborty, A. Bera, D. V. S. Muthu, S. Bhowmick, U. V. Waghmare, and a. K. Sood, “Symmetry-dependent phonon renormalization in monolayer MoS₂ transistor,” *Phys. Rev. B*, vol. 85, no. 16, p. 161403, Apr. 2012.
- [71] S. Grimme, J. Antony, S. Ehrlich, and H. Krieg, “A consistent and accurate ab initio parametrization of density functional dispersion correction (DFT-D) for the 94 elements H-Pu.,” *J. Chem. Phys.*, vol. 132, no. 15, p. 154104, Apr. 2010.
- [72] J. P. Perdew and A. Zunger, “Self-Interaction Correction to Density-Functional Approximations for Many-Electron Systems,” *Phys. Rev. B*, vol. 23, no. 10, p. 5048, 1981.

- [73] “Atomistix ToolKit v.13.8.0, QuantumWise A/S,”
<http://www.quantumwise.com/>.
- [74] R. S. Mulliken, “Electronic Population Analysis on LCAO[Single Bond]MO Molecular Wave Functions. I,” *J. Chem. Phys.*, vol. 23, no. 10, pp. 1833–1840, 1955.
- [75] J. Kang, D. Sarkar, W. Liu, D. Jena, and K. Banerjee, “A computational study of metal-contacts to beyond-graphene 2D semiconductor materials,” in *IEEE International Electron Devices Meeting*, 2012, pp. 17.4.1–17.4.4.
- [76] J. Kang, W. Liu, D. Sarkar, D. Jena, and K. Banerjee, “Computational Study of Metal Contacts to Monolayer Transition-Metal Dichalcogenide Semiconductors,” *Phys. Rev. X*, vol. 4, no. 3, p. 031005, Jul. 2014.
- [77] S. McDonnell, B. Brennan, A. Azcatl, N. Lu, H. Dong, C. Buie, J. Kim, C. L. Hinkle, M. J. Kim, and R. M. Wallace, “HfO₂ on MoS₂ by Atomic Layer Deposition : Adsorption Mechanisms and Thickness Scalability,” *ACS Nano*, vol. 7, no. 11, pp. 10354–10361, 2013.
- [78] M.-W. Lin, L. Liu, Q. Lan, X. Tan, K. S. Dhindsa, P. Zeng, V. M. Naik, M. M.-C. Cheng, and Z. Zhou, “Mobility enhancement and highly efficient gating of monolayer MoS₂ transistors with polymer electrolyte,” *J. Phys. D: Appl. Phys.*, vol. 45, no. 34, p. 345102, Aug. 2012.

- [79] D. J. Carrad, A. M. Burke, R. W. Lyttleton, H. J. Joyce, H. H. Tan, C. Jagadish, K. Storm, H. Linke, L. Samuelson, and A. P. Micolich, "Electron-beam patterning of polymer electrolyte films to make multiple nanoscale gates for nanowire transistors.," *Nano Lett.*, vol. 14, no. 1, pp. 94–100, Jan. 2014.
- [80] R. H. Boyd, "The dielectric constant of lamellar semicrystalline polymers," *J. Polym. Sci. Polym. Phys. Ed.*, vol. 21, no. 4, pp. 505–514, Apr. 1983.
- [81] D. Sarkar, X. Xie, W. Liu, W. Cao, J. Kang, Y. Gong, S. Kraemer, P. M. Ajayan, and K. Banerjee, "A subthermionic tunnel field-effect transistor with an atomically thin channel," *Nature*, 2015, DOI: 10.1038/nature15387 (in press).
- [82] S. Das, H. Chen, A. V. Penumatcha, and J. Appenzeller, "High Performance Multilayer MoS₂ Transistors with Scandium Contacts," *Nano Lett.*, vol. 13, pp. 100–105, 2013.
- [83] I. Meric, N. Baklitskaya, P. Kim, and K. L. Shepard, "RF performance of top-gated, zero-bandgap graphene field-effect transistors," in *IEEE Transactions on Electron Devices*, 2008, no. c, pp. 513–516.
- [84] M. F. Chang, J. Cong, A. Kaplan, M. Naik, G. Reinman, E. Socher, and S.-W. Tam, "CMP network-on-chip overlaid with multi-band RF-interconnect," in *2008 IEEE 14th International Symposium on High Performance Computer Architecture*, 2008, pp. 191–202.

- [85] X. Li, J. Kang, X. Xie, W. Liu, D. Sarkar, J. Mao, and K. Banerjee, "Graphene inductors for high-frequency applications - design, fabrication, characterization, and study of skin effect," *2014 IEEE Int. Electron Devices Meet.*, pp. 5.4.1–5.4.4, Dec. 2014.
- [86] K. Banerjee, S. Im, N. Srivastava, and S. Barbara, "Interconnect Modeling and Analysis in the Nanometer Era : Cu and Beyond," in *Advanced Metallization Conference (AMC)*, 2005, vol. 1, no. 1, pp. 1–7.
- [87] H. Li and K. Banerjee, "High-Frequency Analysis of Carbon Nanotube Interconnects and Implications for On-Chip Inductor Design," *IEEE Trans. Electron Devices*, vol. 56, no. 10, pp. 2202–2214, 2009.
- [88] L. R. Hanlon, E. R. Falardeau, and J. E. Fischer, "Metallic Reflectance of AsF₅-Graphite Intercalation Compounds," *Solid State Commun.*, vol. 24, pp. 377–381, 1977.
- [89] E. H. Sondheimer, "The mean free path of electrons in metals," *Adv. Phys.*, vol. 50, no. 6, pp. 499–537, Nov. 2010.
- [90] A. H. Wilson, *The Theory of Metals*. Cambridge Univ. Press, 1936.
- [91] G.E.H.Reuter and E. H. Sondheimer, "The Theory of the Anomalous Skin Effect in Metals," *Proc. R. Soc.*, vol. 195, pp. 336–364, 1948.

- [92] “International Technology Roadmap for Semiconductors,”
<http://www.itrs.net/Links/2013ITRS/Home2013.htm>, 2013.
- [93] C. Kittel, *Introduction to Solid State Physics*, 8th ed. John Wiley and Sons, Inc., 2005.
- [94] M. Dresselhaus, “The Novel Nanostructures of Carbon,” *Univ. Tokyo Lect.*, p. Available: www.photon.t.u-tokyo.ac.jp/~maruyama/vi, 2008.
- [95] X. Benedict, V. H. Crespi, S. G. Louie, and M. L. Cohen, “Static conductivity and Superconductivity of Carbon Nanotubes : Relations between Tubes and Sheets,” *Phys. Rev. B*, vol. 52, no. 20, pp. 935–940, 1995.
- [96] H. Li, S. Member, C. Xu, and N. Srivastava, “Carbon Nanomaterials for Next-Generation Interconnects and Passives : Physics , Status , and Prospects,” *IEEE Trans. Electron Devices*, vol. 56, no. 9, pp. 1799–1821, 2009.
- [97] H. M. Greenhouse, “Design of Planar Rectangular Microelectronic Inductors,” *IEEE Trans. Parts, Hybrids. Packag.*, vol. PHP-10, no. 2, pp. 101–109, 1974.
- [98] A. Weisshaar and A. Luoh, “Closed-Form Expressions for the Series Impedance Parameters of On-Chip Interconnects on Multilayer Silicon Substrates,” *IEEE Trans. Adv. Packag.*, vol. 27, no. 1, pp. 126–134, 2004.

- [99] C. Wu, C. Tang, and S. Liu, "Analysis of On-Chip Spiral Inductors Using the Distributed Capacitance Model," *IEEE J. Solid-State Circuits*, vol. 38, no. 6, pp. 1040–1044, 2003.
- [100] K. Gopalakrishnan, P. B. Griffin, and J. D. Plummer, "I-MOS: a novel semiconductor device with a subthreshold slope lower than kT/q ," in *IEEE International Electron Devices Meeting*, 2002, pp. 289–292.
- [101] R. Fritschi, K. Boucart, F. Casset, P. Ancy, and A. M. Ionescu, "Suspended-gate MOSFET: bringing new MEMS functionality into solid-state MOS transistor," in *IEEE International Electron Devices Meeting*, 2005, vol. 00, no. c, pp. 479–481.
- [102] S. Salahuddin and S. Datta, "Use of negative capacitance to provide voltage amplification for low power nanoscale devices," *Nano Lett.*, vol. 8, no. 2, pp. 405–10, Feb. 2008.
- [103] T. Baba, "Proposal for surface tunnel transistors," *Jpn. J. Appl. Phys.*, vol. 31, no. 2, pp. 455–457, 1992.
- [104] H. F. Dadgour and K. Banerjee, "Hybrid NEMS–CMOS integrated circuits: a novel strategy for energy-efficient designs," *IET Comput. Digit. Tech.*, vol. 3, no. 6, p. 593, 2009.

- [105] K. Gopalakrishnan, P. B. Griffin, and J. D. Plummer, "Impact Ionization MOS (I-MOS)—Part I: Device and Circuit Simulations," *IEEE Trans. Electron Devices*, vol. 52, no. 1, pp. 69–76, Jan. 2005.
- [106] K. Gopalakrishnan, R. Woo, C. Jungemann, P. B. Griffin, and J. D. Plummer, "Impact Ionization MOS (I-MOS)—Part II: Experimental Results," *IEEE Trans. Electron Devices*, vol. 52, no. 1, pp. 77–84, Jan. 2005.
- [107] F. Mayer, C. Le Royer, G. Le Carval, C. Tabone, L. Clavelier, and S. Deleonibus, "Comparative study of the fabricated and simulated Impact Ionization MOS (IMOS)," *Solid. State. Electron.*, vol. 51, no. 4, pp. 579–584, Apr. 2007.
- [108] F. Mayer, C. Le Royer, G. Le Carval, L. Clavelier, and S. Deleonibus, "Static and Dynamic TCAD Analysis of IMOS Performance: From the Single Device to the Circuit," *IEEE Trans. Electron Devices*, vol. 53, no. 8, pp. 1852–1857, Aug. 2006.
- [109] W. Y. Choi, J. Y. Song, J. D. Lee, Y. J. Park, and B. Park, "A Novel Biasing Scheme for I-MOS (Impact-Ionization MOS) Devices," *IEEE Trans. Nanotechnol.*, vol. 4, no. 3, pp. 322–325, 2005.
- [110] W. Y. Choi, J. Y. Song, J. D. Lee, Y. J. Park, and B. Park, "100-nm n- / p-Channel I-MOS Using a Novel Self-Aligned Structure," *IEEE Electron Device Lett.*, vol. 26, no. 4, pp. 261–263, 2005.

- [111] W. Y. Choi, J. Y. Song, J. D. Lee, Y. J. Park, and B. Park, "70-nm impact-ionization metal–oxide–semiconductor (I-MOS) devices integrated with tunneling field-effect transistors (TFETs)," in *IEEE International Electron Devices Meeting*, 2005, vol. 6, no. c, pp. 955–958.
- [112] E. Toh, G. H. Wang, G. Lo, N. Balasubramanian, C. Tung, F. Benistant, L. Chan, G. Samudra, and Y. Yeo, "A Novel CMOS Compatible L-shaped Impact-ionization MOS (LI-MOS) Transistor," in *IEEE International Electron Devices Meeting*, 2005, vol. 00, no. c, pp. 951–954.
- [113] E. Toh, G. H. Wang, L. Chan, G. Lo, G. Samudra, and Y. Yeo, "I-MOS Transistor With an Elevated Silicon – Germanium Impact-Ionization Region for Bandgap Engineering," *IEEE Electron Device Lett.*, vol. 27, no. 12, pp. 975–977, 2006.
- [114] C. Onal, R. Woo, H. S. Koh, P. B. Griffin, and J. D. Plummer, "A Novel Depletion-IMOS (DIMOS) Device With Improved Reliability and Reduced Operating Voltage," *IEEE Electron Device Lett.*, vol. 3, no. 1, pp. 64–67, 2008.
- [115] E.-H. Toh, G. H. Wang, L. Chan, G. Samudra, and Y.-C. Yeo, "A Double-Spacer I-MOS Transistor With Shallow Source Junction and Lightly Doped Drain for Reduced Operating Voltage and Enhanced Device Performance," *IEEE Electron Device Lett.*, vol. 29, no. 2, pp. 189–191, Feb. 2008.

- [116] E. Toh, G. H. Wang, D. Weekst, M. Zhu, M. Bauert, J. Speart, L. Chan, S. G. Thomast, G. Samudra, and Y. Yeo, "P-Channel I-MOS transistor featuring silicon nano-wire with multiple-gates, strained Si_{1-y}Cy I-region, in situ doped Si_{1-y}Cy source, and sub-5 mV/decade subthreshold swing," in *International Symposium on VLSI Technology, Systems and Applications*, 2007, vol. 54, no. 10, pp. 24–25.
- [117] W. Y. Choi, J. Y. Song, J. P. Kim, S. W. Kim, J. D. Lee, and B. Park, "Breakdown voltage reduction in I-MOS devices," in *2006 IEEE Nanotechnology Materials and Devices Conference*, 2006, pp. 380–381.
- [118] E.-H. Toh, G. H. Wang, L. Chan, G. Samudra, and Y.-C. Yeo, "Simulation and design of a germanium L-shaped impact-ionization MOS transistor," *Semicond. Sci. Technol.*, vol. 23, no. 1, p. 015012, Jan. 2008.
- [119] U. Abelein, M. Born, K. K. Bhuwarka, M. Schindler, M. Schlosser, T. Sulima, and I. Eisele, "Improved Reliability by Reduction of Hot-Electron Damage in the Vertical Impact-Ionization MOSFET (I-MOS)," *IEEE Electron Device Lett.*, vol. 28, no. 1, pp. 65–67, Jan. 2007.
- [120] C. Charbuillet, S. Monfray, E. Dubois, P. Bouillon, F. Judong, T. Skotnicki, and J. Monnet, "High Current Drive in Ultra-Short Impact Ionization MOS (I-MOS) Devices," in *IEEE International Electron Devices Meeting*, 2009, pp. 1–4.

- [121] C. Shen, J. Lin, E. Toh, K. Changt, P. Bait, C. Heng, G. S. Samudra, and Y. Yeo, "On the Performance Limit of Impact-Ionization Transistors," in *IEEE International Electron Devices Meeting*, 2007, no. 3, pp. 117–120.
- [122] D. Sarkar, N. Singh, and K. Banerjee, "A Novel Enhanced Electric-Field Impact-Ionization MOS Transistor," *IEEE Electron Device Lett.*, vol. 31, no. 11, pp. 1175–1177, 2010. Reprinted with permission from IEEE © 2010.
- [123] S. Balakumar, S. Peng, K. M. Hoe, G. Q. Lo, R. Kumar, N. Balasubramanian, D. L. Kwong, Y. L. Foo, and S. Tripathy, "Fabrication of thick SiGe on insulator (Si_{0.2}Ge_{0.8}OI) by condensation of SiGe/Si superlattice grown on silicon on insulator," *Appl. Phys. Lett.*, vol. 90, no. 19, p. 192113, 2007.
- [124] *MEDICI User Guide Version Z-2007.03*. Synopsys, Inc, 2007.
- [125] S. Millidge, D. C. Herbert, M. Kane, G. W. Smith, and D. R. Wight, "Non-local aspects of breakdown in pin diodes," *Semicond. Sci. Technol.*, vol. 10, pp. 344–347, 1995.
- [126] S. M. Sze and K. K. Ng, *Physics of Semiconductor Devices*. 2008.
- [127] J. J. Quinn and G. Kawamoto, "Subband spectroscopy by surface channel tunneling," *Surf. Sci.*, vol. 73, pp. 190–196, 1978.

- [128] K. K. Bhuvalka, S. Sedlmaier, A. K. Ludsteck, C. Tolksdorf, J. Schulze, and I. Eisele, "Vertical tunnel field-effect transistor," *IEEE Trans. Electron Devices*, vol. 51, no. 2, pp. 279–282, 2004.
- [129] Q. Zhang, W. Zhao, S. Member, and A. Seabaugh, "Low-subthreshold-swing tunnel transistors," *IEEE Electron Device Lett.*, vol. 27, no. 4, pp. 297–300, 2006.
- [130] Y. Khatami and K. Banerjee, "Steep subthreshold slope n- and p-type tunnel-FET devices for low-power and energy-efficient digital circuits," *IEEE Trans. Electron Devices*, vol. 56, no. 11, pp. 2752–2761, Nov. 2009.
- [131] A. M. Ionescu and H. Riel, "Tunnel field-effect transistors as energy-efficient electronic switches.," *Nature*, vol. 479, no. 7373, pp. 329–37, Nov. 2011.
- [132] S. Datta, H. Liu, and V. Narayanan, "Tunnel FET technology: A reliability perspective," *Microelectron. Reliab.*, vol. 54, no. 5, pp. 861–874, May 2014.
- [133] W. Cao, J. Jiang, J. Kang, D. Sarkar, W. Liu, and K. Banerjee, "Designing Band-to-Band Tunneling Field-Effect Transistors with 2D Semiconductors for Next-Generation Low-Power VLSI," in *IEEE International Electron Devices Meeting*, 2015.

- [134] W. Cao, D. Sarkar, Y. Khatami, J. Kang, and K. Banerjee, “Subthreshold-swing physics of tunnel field-effect transistors,” *AIP Adv.*, vol. 4, no. 6, p. 067141, Jun. 2014.
- [135] D. Sarkar, M. Krall, and K. Banerjee, “Electron-hole duality during band-to-band tunneling process in graphene-nanoribbon tunnel-field-effect-transistors,” *Appl. Phys. Lett.*, vol. 97, no. 26, p. 263109, 2010. Reprinted with permission from AIP Publishing LLC © 2010.
- [136] P. M. Solomon, “Inability of single carrier tunneling barriers to give subthermal subthreshold swings in MOSFETs,” *IEEE Electron Device Lett.*, vol. 31, no. 6, pp. 618–620, 2010.
- [137] S. Banerjee, W. Richardson, J. Coleman, and a. Chatterjee, “A new three-terminal tunnel device,” *IEEE Electron Device Lett.*, vol. 8, no. 8, pp. 347–349, Aug. 1987.
- [138] R. B. Fair and H. W. Wivell, “Zener and Avalanche Breakdown in As-Implanted LowVoltage Si n-p Junctions,” *IEEE Trans. Electron Devices*, vol. 23, no. 5, pp. 512–518, 1976.
- [139] K. Boucart and A. M. Ionescu, “Double-Gate Tunnel FET With High- κ Gate Dielectric,” *IEEE Trans. Electron Devices*, vol. 54, no. 7, pp. 1725–1733, 2007.

- [140] M. T. Björk, J. Knoch, H. Schmid, H. Riel, and W. Riess, “Silicon nanowire tunneling field-effect transistors,” *Appl. Phys. Lett.*, vol. 92, no. 19, p. 193504, 2008.
- [141] D. Jiménez, X. Cartoixà, E. Miranda, J. Suñé, F. A. Chaves, and S. Roche, “A drain current model for Schottky-barrier CNT-FETs,” *J. Comput. Electron.*, vol. 5, no. 4, pp. 361–364, Dec. 2006.
- [142] J. Guo, S. Datta, M. Lundstrom, and M. P. Anantam, “Towards Multi-Scale Modeling of Carbon Nanotube Transistors,” *Int. J. Multiscale Comput. Eng.*, vol. 2, no. 2, pp. 257–278, 2004.
- [143] L. Brey and H. Fertig, “Electronic states of graphene nanoribbons studied with the Dirac equation,” *Phys. Rev. B*, vol. 73, no. 23, p. 235411, Jun. 2006.
- [144] D. P. DiVincenzo and E. J. Mele, “Self-consistent effective-mass theory for intralayer screening in graphite intercalation compounds,” *Phys. Rev. B*, vol. 29, no. 4, pp. 1685–1694, 1984.
- [145] K. H. Gundlach and J. G. Simmons, “Range of Validity of the WKB Tunnel Probability, and Comparison of Experimental Data and Theory,” *Solid Film.*, vol. 4, pp. 61–79, 1969.

- [146] D. Sarkar and K. Banerjee, "Proposal for tunnel-field-effect-transistor as ultra-sensitive and label-free biosensors," *Appl. Phys. Lett.*, vol. 100, no. 14, p. 143108, 2012. Reprinted with permission from AIP Publishing LLC © 2012.
- [147] J. L. Moll, "Physics of Semiconductors." McGraw-Hill, New York, p. 249, 1964.
- [148] S. Datta, *Quantum Transport: Atom to Transistor*. Cambridge University Press, 2005.
- [149] E. O. Kane, "Zener Tunneling in Semiconductors," *J. Phys. Chem. Solids*, vol. 12, pp. 181–188, 1959.
- [150] D. Sarkar and K. Banerjee, "Metallic-Nanoparticle Assisted Enhanced Band-to-Band Tunneling Current," *Appl. Phys. Lett.*, vol. 99, no. 13, p. 133116, 2011. Reprinted with permission from AIP Publishing LLC © 2011.
- [151] D. Sarkar, R. Koltun, P. G. Burke, A. C. Gossard, C. J. Palmstrom, and K. Banerjee, "Improvement Band-to-Band Tunneling Current through Incorporation of Semi-metallic Nanoparticles," (to be submitted).
- [152] D. Driscoll, M. P. Hanson, E. Mueller, and A. C. Gossard, "Growth and microstructure of semimetallic ErAs particles embedded in an In_{0.53}Ga_{0.47}As matrix," *J. Cryst. Growth*, vol. 251, no. 1–4, pp. 243–247, Apr. 2003.

- [153] T. E. Buehl, J. M. LeBeau, S. Stemmer, M. a. Scarpulla, C. J. Palmstrøm, and A. C. Gossard, "Growth of embedded ErAs nanorods on (411)A and (411)B GaAs by molecular beam epitaxy," *J. Cryst. Growth*, vol. 312, no. 14, pp. 2089–2092, Jul. 2010.
- [154] M. P. Hanson, D. C. Driscoll, E. Muller, and a. C. Gossard, "Microstructure and electronic characterization of InGaAs containing layers of self-assembled ErAs nanoparticles," *Phys. E Low-dimensional Syst. Nanostructures*, vol. 13, no. 2–4, pp. 602–605, Mar. 2002.
- [155] D. O. Klenov and J. M. O. Zide, "Structure of the InAlAs/InP interface by atomically resolved energy dispersive spectroscopy," *Appl. Phys. Lett.*, vol. 99, no. 14, p. 141904, 2011.
- [156] J. Tersoff, "Schottky Barriers and Semiconductor Band Structures," *Phys. Rev. B*, vol. 32, no. 10, pp. 6968–6971, 1985.
- [157] B. D. Schultz and C. J. Palmstrøm, "Embedded assembly mechanism of stable metal nanocrystals on semiconductor surfaces," *Phys. Rev. B*, vol. 73, no. 24, p. 241407, Jun. 2006.
- [158] P. R. Srinivas, B. S. Kramer, and S. Srivastava, "Trends in biomarker research for cancer detection," *Lancet Oncol.*, vol. 2, pp. 696–704, 2001.

- [159] D. Galasko, "Biomarkers for Alzheimer's disease – Clinical needs and application," *J. Alzheimer's Dis.*, vol. 8, pp. 339–346, 2005.
- [160] D. de Jong, B. P. H. Kremer, M. G. M. Olde Rikkert, and M. M. Verbeek, "Current state and future directions of neurochemical biomarkers for Alzheimer's disease," *Clin. Chem. Lab. Med.*, vol. 45, no. 11, pp. 1421–34, Jan. 2007.
- [161] J. M. Barletta, D. C. Edelman, and N. T. Constantine, "Lowering the Detection Limits of HIV-1 Viral Load Using Real-Time Immuno-PCR for HIV-1 p24 Antigen," *Am. J. Clin. Pathol.*, vol. 122, no. 1, pp. 20–27, Jul. 2004.
- [162] P. Bergveld, "Development of an Ion-Sensitive Solid-State Device for Neurophysiological Measurements," *IEEE Trans. Biomed. Eng.*, vol. 17, pp. 70–71, 1970.
- [163] S. Caras and J. Janata, "Field effect transistor sensitive to penicillin," *Anal. Chem.*, vol. 52, pp. 1935–1937, 1980.
- [164] E. Souteyrand, J. P. Cloarec, J. R. Martin, C. Wilson, I. Lawrence, S. Mikkelsen, M. F. Lawrence, L. De Physicochimie, E. C. De Lyon, and E. Cedex, "Direct Detection of the Hybridization of Synthetic Homo-Oligomer DNA Sequences by Field Effect," *J. Phys. Chem. B*, vol. 101, pp. 2980–2985, 1997.

- [165] Y. Cui, Q. Wei, H. Park, and C. M. Lieber, “Nanowire nanosensors for highly sensitive and selective detection of biological and chemical species,” *Science* (80-.), vol. 293, pp. 1289–1292, Aug. 2001.
- [166] W. Yang, K. R. Ratinac, S. P. Ringer, P. Thordarson, J. J. Gooding, and F. Braet, “Carbon nanomaterials in biosensors: should you use nanotubes or graphene?,” *Angew. Chem. Int. Ed. Engl.*, vol. 49, no. 12, pp. 2114–38, Mar. 2010.
- [167] X. Li, Z. Chen, N. Shen, D. Sarkar, and S. Member, “Vertically Stacked and Independently Controlled Twin-Gate MOSFETs on a Single Si Nanowire,” *IEEE Electron Device Lett.*, vol. 32, no. 11, pp. 1492–1494, 2011.
- [168] M. S. Makowski and A. Ivanisevic, “Molecular analysis of blood with micro-/nanoscale field-effect-transistor biosensors,” *Small*, vol. 7, no. 14, pp. 1863–75, Jul. 2011.
- [169] P. K. Ang, W. Chen, A. T. S. Wee, and K. P. Loh, “Solution-gated epitaxial graphene as pH sensor,” *J. Am. Chem. Soc.*, vol. 130, no. 44, pp. 14392–3, Nov. 2008.
- [170] Y. Ohno, K. Maehashi, Y. Yamashiro, and K. Matsumoto, “Electrolyte-Gated Graphene Field-Effect Transistors for Detecting pH and Protein Adsorption,” *Nano Lett.*, vol. 9, no. 9, pp. 3318–3322, 2009.

- [171] Y. Ohno, K. Maehashi, and K. Matsumoto, "Label-free biosensors based on aptamer-modified graphene field-effect transistors," *J. Am. Chem. Soc.*, vol. 132, no. 51, pp. 18012–3, Dec. 2010.
- [172] M. Dankerl, M. V. Hauf, A. Lippert, L. H. Hess, S. Birner, I. D. Sharp, A. Mahmood, P. Mallet, J.-Y. Veuillen, M. Stutzmann, and J. a. Garrido, "Graphene Solution-Gated Field-Effect Transistor Array for Sensing Applications," *Adv. Funct. Mater.*, vol. 20, no. 18, pp. 3117–3124, Sep. 2010.
- [173] H. Wu, R. Yang, B. Song, Q. Han, J. Li, Y. Zhang, Y. Fang, and R. Tenne, "Biocompatible Inorganic Fullerene- Nanoparticles Produced by Pulsed Laser Ablation in Water," *ACS Nano*, vol. 5, no. 2, pp. 1276–1281, 2011.
- [174] O. Lopez-Sanchez, D. Lembke, M. Kayci, A. Radenovic, and A. Kis, "Ultrasensitive photodetectors based on monolayer MoS₂," *Nat. Nanotechnol.*, vol. 8, no. 7, pp. 497–501, Jul. 2013.
- [175] C. Zhu, Z. Zeng, H. Li, F. Li, C. Fan, and H. Zhang, "Single-Layer MoS₂ Based Nanoprobes for Homogeneous Detection of Biomolecules," *J. Am. Chem. Soc.*, vol. 135, pp. 5998–6001, 2013.
- [176] Q. He, Z. Zeng, Z. Yin, H. Li, S. Wu, X. Huang, and H. Zhang, "Fabrication of flexible MoS₂ thin-film transistor arrays for practical gas-sensing applications.," *Small*, vol. 8, no. 19, pp. 2994–9, Oct. 2012.

- [177] S. Z. Bajwa, G. Mustafa, R. Samardzic, T. Wangchareansak, and P. a Lieberzeit, "Nanostructured materials with biomimetic recognition abilities for chemical sensing.," *Nanoscale Res. Lett.*, vol. 7, no. 1, p. 328, Jan. 2012.
- [178] S. Wu, Z. Zeng, Q. He, Z. Wang, S. J. Wang, Y. Du, Z. Yin, X. Sun, W. Chen, and H. Zhang, "Electrochemically reduced single-layer MoS₂ nanosheets: characterization, properties, and sensing applications.," *Small*, vol. 8, no. 14, pp. 2264–70, Jul. 2012.
- [179] M. J. Deen, M. W. Shinwari, J. C. Ranuárez, and D. Landheer, "Noise considerations in field-effect biosensors," *J. Appl. Phys.*, vol. 100, no. 7, p. 074703, 2006.
- [180] A. Castellanos-Gomez, N. Agrait, and G. Rubio-Bollinger, "Optical identification of atomically thin dichalcogenide crystals," *Appl. Phys. Lett.*, vol. 96, no. 21, p. 213116, 2010.
- [181] S. Bertolazzi, J. Brivio, and A. Kis, "Stretching and breaking of ultrathin MoS₂," *ACS Nano*, vol. 5, no. 12, pp. 9703–9, Dec. 2011.
- [182] S. Liu and X. Guo, "Carbon nanomaterials field-effect-transistor-based biosensors," *NPG Asia Mater.*, vol. 4, no. 8, pp. 1–10, Aug. 2012.

- [183] J. a Streifer, H. Kim, B. M. Nichols, and R. J. Hamers, “Covalent functionalization and biomolecular recognition properties of DNA-modified silicon nanowires,” *Nanotechnology*, vol. 16, no. 9, pp. 1868–1873, Sep. 2005.
- [184] Y. L. Bunimovich, Y. S. Shin, W. Yeo, M. Amori, G. Kwong, and J. R. Heath, “Quantitative Real-Time Measurements of DNA Hybridization with Alkylated Nonoxidized Silicon Nanowires in Electrolyte Solution,” *J. Am. Chem. Soc.*, vol. 128, pp. 16323–16331, 2006.
- [185] S. Banerjee, T. Hemraj-Benny, and S. S. Wong, “Covalent Surface Chemistry of Single-Walled Carbon Nanotubes,” *Adv. Mater.*, vol. 17, no. 1, pp. 17–29, Jan. 2005.
- [186] S. Liu, Q. Shen, Y. Cao, L. Gan, Z. Wang, M. L. Steigerwald, and X. Guo, “Chemical functionalization of single-walled carbon nanotube field-effect transistors as switches and sensors,” *Coord. Chem. Rev.*, vol. 254, no. 9–10, pp. 1101–1116, May 2010.
- [187] X. Zhou, J. M. Moran-Mirabal, H. G. Craighead, and P. L. McEuen, “Supported lipid bilayer/carbon nanotube hybrids,” *Nat. Nanotechnol.*, vol. 2, no. 3, pp. 185–90, Mar. 2007.
- [188] M. T. Martinez, Y.-C. Tseng, N. Ormategui, I. Loinaz, R. Eritja, and J. Bokor, “Label-Free DNA Biosensors Based on Functionalized Carbon Nanotube Field Effect Transistor,” *Nano*, vol. 9, no. 2, pp. 530–536, 2009.

- [189] W. Fu, C. Nef, O. Knopfmacher, A. Tarasov, M. Weiss, M. Calame, and C. Schonenberger, "Graphene Transistors Are Insensitive to pH Changes in Solution," *Nano Lett.*, vol. 11, pp. 3597–3600, 2011.
- [190] I. Heller, A. M. Janssens, J. Ma, E. D. Minot, S. G. Lemay, and C. Dekker, "Identifying the Mechanism of Biosensing with Carbon Nanotube Transistors," *Nano Lett.*, vol. 8, no. 2, pp. 591–595, 2008.
- [191] D. R. Kauffman and A. Star, "Electronically monitoring biological interactions with carbon nanotube field-effect transistors," *Chem. Soc. Rev.*, vol. 37, no. 6, pp. 1197–206, Jun. 2008.
- [192] M. N. Tahir, N. Zink, M. Eberhardt, H. a Therese, U. Kolb, P. Theato, and W. Tremel, "Overcoming the insolubility of molybdenum disulfide nanoparticles through a high degree of sidewall functionalization using polymeric chelating ligands.," *Angew. Chemie*, vol. 45, no. 29, pp. 4809–15, Jul. 2006.
- [193] A. Ortiz-Conde, F. J. G. Sanchez, J. J. Liou, A. Cerdeira, M. Estrada, and Y. Yue, "A review of recent MOSFET threshold voltage extraction methods," *Microelectron. Reliab.*, vol. 42, pp. 583–596, 2002.
- [194] P. Bergveld, R. E. G. van Hal, and J. C. T. Eijkel, "The remarkable similarity between the acid-base properties of ISFETs and proteins and the consequences for the design of ISFET biosensors," *Biosens. Bioelectron.*, vol. 10, no. 5, pp. 405–414, Jan. 1995.

- [195] S. Zafar, C. D'Emic, A. Afzali, B. Fletcher, Y. Zhu, and T. Ning, "Optimization of pH sensing using silicon nanowire field effect transistors with HfO₂ as the sensing surface," *Nanotechnology*, vol. 22, no. 40, p. 405501, Oct. 2011.
- [196] X. P. a Gao, G. Zheng, and C. M. Lieber, "Subthreshold regime has the optimal sensitivity for nanowire FET biosensors.," *Nano Lett.*, vol. 10, no. 2, pp. 547–52, Feb. 2010.
- [197] R. K. Her, "The Chemistry of Silica." New York et al.: Wiley, 1979.
- [198] F. Seker, K. Meeker, T. F. Kuech, and A. B. Ellis, "Surface Chemistry of Prototypical Bulk II–VI and III–V Semiconductors and Implications for Chemical Sensing," *Chem. Rev.*, vol. 100, no. 7, pp. 2505–2536, Jul. 2000.
- [199] E. Stern, J. F. Klemic, D. a Routenberg, P. N. Wyrembak, D. B. Turner-Evans, A. D. Hamilton, D. a LaVan, T. M. Fahmy, and M. a Reed, "Label-free immunodetection with CMOS-compatible semiconducting nanowires.," *Nature*, vol. 445, no. 7127, pp. 519–22, Feb. 2007.
- [200] E. Stern, A. Vacic, N. K. Rajan, J. M. Criscione, J. Park, B. R. Ilic, D. J. Mooney, M. a Reed, and T. M. Fahmy, "Label-free biomarker detection from whole blood.," *Nat. Nanotechnol.*, vol. 5, no. 2, pp. 138–42, Feb. 2010.

- [201] F. Schedin, a. K. Geim, S. V. Morozov, E. W. Hill, P. Blake, M. I. Katsnelson, and K. S. Novoselov, "Detection of individual gas molecules adsorbed on graphene," *Nat. Mater.*, vol. 6, no. 9, pp. 652–655, Jul. 2007.
- [202] X. Guo, J. P. Small, J. E. Klare, Y. Wang, M. S. Purewal, I. W. Tam, B. H. Hong, R. Caldwell, L. Huang, S. O. Brien, J. Yan, R. Breslow, S. J. Wind, J. Hone, P. Kim, and C. Nuckolls, "Covalently Bridging Gaps in with Conducting Molecules," *Science (80-.)*, vol. 311, pp. 356–359, 2006.
- [203] B. R. Goldsmith, J. G. Coroneus, V. R. Khalap, A. A. Kane, G. A. Weiss, and P. G. Collins, "Conductance-Controlled Point Functionalization of Single-Walled Carbon Nanotubes," *Science (80-.)*, vol. 315, pp. 77–81, 2007.
- [204] F. Patolsky, G. Zheng, O. Hayden, M. Lakadamyali, X. Zhuang, and C. M. Lieber, "Electrical detection of single viruses," *Proc. Natl. Acad. Sci. U. S. A.*, vol. 101, no. 39, pp. 14017–22, Sep. 2004.
- [205] N. Mohanty and V. Berry, "Resolution Biodevice and DNA Transistor : Interfacing Graphene Derivatives with Nanoscale and Microscale Biocomponents," *Nano Lett.*, vol. 8, no. 12, pp. 4469–4476, 2008.
- [206] P. R. Nair, S. Member, and M. A. Alam, "Design Considerations of Silicon Nanowire Biosensors," *IEEE Trans. Electron Devices*, vol. 54, no. 12, pp. 3400–3408, 2007.

- [207] M. J. Heller, A. H. Forster, and E. Tu, "Active microelectronic chip devices which utilize controlled electrophoretic fields for multiplex DNA hybridization and other genomic applications Nucleic acids," *Electrophoresis*, vol. 21, pp. 157–164, 2000.
- [208] D. L. Graham, H. Ferreira, J. Bernardo, P. P. Freitas, and J. M. S. Cabral, "Single magnetic microsphere placement and detection on-chip using current line designs with integrated spin valve sensors: Biotechnological applications," *J. Appl. Phys.*, vol. 91, no. 10, p. 7786, 2002.
- [209] M. Acik and Y. J. Chabal, "A Review on Reducing Graphene Oxide for Band Gap Engineering," *J. Mater. Sci. Res.*, vol. 2, no. 1, p. 5539, Dec. 2012.
- [210] D. Sarkar and K. Banerjee, "Fundamental limitations of conventional-FET biosensors: Quantum-mechanical-tunneling to the rescue," in *70th Device Research Conference*, 2012, pp. 83–84.
- [211] D. Sarkar, H. Gossner, W. Hansch, and K. Banerjee, "Tunnel-field-effect-transistor based gas-sensor: Introducing gas detection with a quantum-mechanical transducer," *Appl. Phys. Lett.*, vol. 102, no. 2, p. 023110, 2013.
Reprinted with permission from AIP Publishing LLC © 2013.
- [212] D. Sarkar, H. Gossner, W. Hansch, and K. Banerjee, "Impact-ionization field-effect-transistor based biosensors for ultra-sensitive detection of

biomolecules,” *Appl. Phys. Lett.*, vol. 102, no. 20, p. 203110, 2013. Reprinted with permission from AIP Publishing LLC © 2013.

- [213] B. K. Miremadi, R. C. Singh, S. R. Morrison, and K. Colbow, “A highly sensitive and selective hydrogen gas sensor from thick oriented films of MoS₂,” *Appl. Phys. A Mater. Sci. Process.*, vol. 63, no. 3, pp. 271–275, Sep. 1996.
- [214] D. Sarkar and K. Banerjee, “Fundamental limitations of conventional-FET biosensors: Quantum-mechanical-tunneling to the rescue,” in *70th Device Research Conference*, 2012, pp. 83–84.
- [215] P. R. Nair and M. a Alam, “Screening-limited response of nanobiosensors,” *Nano Lett.*, vol. 8, no. 5, pp. 1281–5, May 2008.
- [216] D. McQuarrie, “Statistical Mechanics.” New York: Harper & Row, 1976.
- [217] P. R. Nair and M. a. Alam, “Performance limits of nanobiosensors,” *Appl. Phys. Lett.*, vol. 88, no. 23, p. 233120, 2006.
- [218] P. E. Sheehan and L. J. Whitman, “Detection Limits for Nanoscale Biosensors,” *Nano Lett.*, vol. 5, no. 4, pp. 803–807, 2005.
- [219] Z. Lu, N. Collaert, M. Aoulaiche, B. De Wachter, A. De Keersgieter, J. G. Fossum, L. Altimime, and M. Jurczak, “Realizing super-steep subthreshold

slope with conventional FDSOI CMOS at low-bias voltages,” in *2010 International Electron Devices Meeting*, 2010, pp. 16.6.1–16.6.3.

- [220] A. Salomonsson, M. Eriksson, and H. Dannelun, “Hydrogen interaction with platinum and palladium metal–insulator–semiconductor devices,” *J. Appl. Phys.*, vol. 98, no. 1, p. 014505, 2005.
- [221] I. Lundström, S. Shivaraman, C. Svensson, and L. Lundkvist, “A hydrogen–sensitive MOS field–effect transistor,” *Appl. Phys. Lett.*, vol. 26, no. 2, p. 55, 1975.
- [222] J. Fogelberg, M. Eriksson, H. Dannelun, and L.-G. Petersson, “Kinetic modeling of hydrogen adsorption/absorption in thin films on hydrogen-sensitive field-effect devices: Observation of large hydrogen-induced dipoles at the Pd-SiO₂ interface,” *J. Appl. Phys.*, vol. 78, no. 2, p. 988, 1995.
- [223] J. Janata and M. Josowicz, “Chemical Modulation of Work Function as a Transduction Mechanism for Chemical Sensors,” *Acc. Chem. Res.*, vol. 31, no. 5, pp. 241–248, May 1998.
- [224] J. Janata, “Potentiometry in gas phase,” *Collect. Czechoslov. Chem. Commun.*, vol. 74, no. 11–12, pp. 1623–1634, Jan. 2009.
- [225] J. Fogelberg and L.-G. Petersson, “Kinetic modelling of the H₂□O₂ reaction on Pd and of its influence on the hydrogen response of a hydrogen sensitive Pd

metal-oxide-semiconductor device,” *Surf. Sci.*, vol. 350, no. 1–3, pp. 91–102, Apr. 1996.

- [226] M. Born, K. K. Bhuiwarka, M. Schindler, U. Abelein, M. Schmidt, T. Sulima, and I. Eisele, “Tunnel FET: A CMOS Device for high Temperature Applications,” in *25th International Conference on Microelectronics*, 2006, pp. 124 – 127.
- [227] C.-H. Lee, G.-H. Lee, A. M. van der Zande, W. Chen, Y. Li, M. Han, X. Cui, G. Arefe, C. Nuckolls, T. F. Heinz, J. Guo, J. Hone, and P. Kim, “Atomically thin p–n junctions with van der Waals heterointerfaces,” *Nat. Nanotechnol.*, vol. 9, no. 9, pp. 676–681, Aug. 2014.
- [228] S. Das, A. Prakash, R. Salazar, and J. Appenzeller, “Toward low-power electronics: tunneling phenomena in transition metal dichalcogenides,” *ACS Nano*, vol. 8, no. 2, pp. 1681–9, Feb. 2014.
- [229] T. Roy, M. Tosun, X. Cao, H. Fang, D. Lien, P. Zhao, Y.-Z. Chen, Y.-L. Chueh, J. Guo, and A. Javey, “Dual-Gated MoS₂ /WSe₂ van der Waals Tunnel Diodes and Transistors,” *ACS Nano*, vol. 9, no. 2, pp. 2071–2079, 2015.
- [230] L. Britnell, R. V Gorbachev, R. Jalil, B. D. Belle, F. Schedin, A. Mishchenko, T. Georgiou, M. I. Katsnelson, L. Eaves, S. V Morozov, N. M. R. Peres, J. Leist, a K. Geim, K. S. Novoselov, and L. a Ponomarenko, “Field-effect

tunneling transistor based on vertical graphene heterostructures.,” *Science*, vol. 335, no. 6071, pp. 947–50, Feb. 2012.

[231] T. Georgiou, R. Jalil, B. D. Belle, L. Britnell, R. V Gorbachev, S. V Morozov, Y.-J. Kim, A. Gholinia, S. J. Haigh, O. Makarovskiy, L. Eaves, L. a Ponomarenko, A. K. Geim, K. S. Novoselov, and A. Mishchenko, “Vertical field-effect transistor based on graphene-WS₂ heterostructures for flexible and transparent electronics.,” *Nat. Nanotechnol.*, vol. 8, no. 2, pp. 100–3, Feb. 2013.

[232] D. Sarkar, J. Kang, R. Koltun, C. Palmstrom, and K. Banerjee, “Tunable Van der Waal’s Heterostructures with High Band-to-Band Tunneling as Building Blocks for Green Electronics,” (under preparation).

[233] H. Xu, S. Fathipour, E. W. Kinder, A. C. Seabaugh, and S. K. Fullerton-Shirey, “Reconfigurable Ion Gating of 2H-MoTe₂ Field-Effect Transistors Using Poly(ethylene oxide)-CsClO₄ Solid Polymer Electrolyte,” *ACS Nano*, vol. 9, no. 5, pp. 4900–4910, 2015.

[234] H.-M. Li, D. Lee, D. Qu, X. Liu, J. Ryu, A. Seabaugh, and W. J. Yoo, “Ultimate thin vertical p-n junction composed of two-dimensional layered molybdenum disulfide.,” *Nat. Commun.*, vol. 6, p. 6564, Jan. 2015.

[235] B. W. H. Baugher, H. O. H. Churchill, Y. Yang, and P. Jarillo-Herrero, “Optoelectronic devices based on electrically tunable p-n diodes in a

- monolayer dichalcogenide.,” *Nat. Nanotechnol.*, vol. 9, no. 4, pp. 262–967, Apr. 2014.
- [236] J. H. Yu, H. R. Lee, S. S. Hong, D. Kong, H.-W. Lee, H. Wang, F. Xiong, S. Wang, and Y. Cui, “Vertical heterostructure of two-dimensional MoS₂ and WSe₂ with vertically aligned layers.,” *Nano Lett.*, vol. 15, no. 2, pp. 1031–1035, Feb. 2015.
- [237] R. Yan, S. Fathipour, Y. Han, B. Song, S. Xiao, M. Li, N. Ma, V. Protasenko, D. A. Muller, D. Jena, and H. G. Xing, “Esaki diodes in van der Waals heterojunctions with broken-gap energy band alignment,” *arxiv*, pp. 1–26.
- [238] W. Feng, W. Zheng, X. Chen, G. Liu, W. Cao, and P. Hu, “Solid-State Reaction Synthesis of a InSe/CuInSe₂ Lateral p–n Heterojunction and Application in High Performance Optoelectronic Devices,” *Chem. Mater.*, vol. 27, no. 3, pp. 983–989, Feb. 2015.
- [239] Y. Deng, Z. Luo, N. J. Conrad, H. Liu, Y. Gong, S. Najmaei, P. M. Ajayan, J. Lou, X. Xu, and P. D. Ye, “Black Phosphorous-Monolayer M oS₂ van der Waals Heterojunction p-n Diode,” *ACS Nano*, vol. 8, no. 8, pp. 8292–8299, 2014.
- [240] S. O. Koswatta, S. J. Koester, and W. Haensch, “On the Possibility of Obtaining MOSFET-Like Performance and Sub-60-mV / dec Swing in 1-D

- Broken-gap Tunnel Transistors,” *IEEE Trans. Electron Devices*, vol. 57, no. 12, pp. 3222–3230, 2010.
- [241] S. Najmaei, Z. Liu, W. Zhou, X. Zou, G. Shi, S. Lei, B. I. Yakobson, J. Idrobo, P. M. Ajayan, and J. Lou, “Vapour phase growth and grain boundary structure of molybdenum disulphide atomic layers,” *Nat. Mater.*, vol. 12, no. 8, pp. 754–759, 2013.
- [242] H. Liu, J. Gu, P. D. Ye, and S. Member, “MoS2 nanoribbon transistors : transition from depletion mode to enhancement mode by channel-width trimming,” *IEEE Electron Device Lett.*, vol. 33, no. 9, pp. 1273–1275, 2012.
- [243] J. Kang, W. Liu, and K. Banerjee, “High-performance MoS2 transistors with low-resistance molybdenum contacts,” *Appl. Phys. Lett.*, vol. 104, no. 9, p. 093106, Mar. 2014.
- [244] W. S. Mos, Y. Gong, J. Lin, X. Wang, G. Shi, S. Lei, Z. Lin, X. Zou, G. Ye, R. Vajtai, B. I. Yakobson, H. Terrones, M. Terrones, K. Tay, J. Lou, S. T. Pantelides, Z. Liu, W. Zhou, and P. M. Ajayan, “Vertical and in-plane heterostructures from WS2/MoS2 monolayers,” *Nat. Mater.*, vol. 13, no. September, pp. 1135–1142, 2014.
- [245] J. L. Alay, M. Fukuda, C. H. Bjorkman, K. Nakagawa, S. Yokoyama, S. Sasaki, and M. Hirose, “Determination of valence band alignment at ultrathin

- SiO₂ / Si interfaces by high-resolution x-ray photoelectron spectroscopy,” *Jpn. J. Appl. Phys.*, vol. 34, no. 2, pp. 653–656, 1995.
- [246] Y. Khatami, J. Kang, and K. Banerjee, “Graphene nanoribbon based negative resistance device for ultra-low voltage digital logic applications,” *Appl. Phys. Lett.*, vol. 102, no. 4, p. 043114, 2013.
- [247] A. Mallik and A. Chattopadhyay, “Drain-dependence of tunnel field-effect transistor characteristics : the role of the channel,” *IEEE J. Electron Devices Soc.*, vol. 58, no. 12, pp. 4250–4257, 2011.
- [248] K. Boucart and A. M. Ionescu, “A new definition of threshold voltage in tunnel FETs,” *Solid. State. Electron.*, vol. 52, no. 9, pp. 1318–1323, Sep. 2008.
- [249] S. Mookerjea, R. Krishnan, S. Datta, and V. Narayanan, “Effective capacitance and drive current for Tunnel FET (TFET) CV/I estimation,” *IEEE Trans. Electron Devices*, vol. 56, no. 9, pp. 2092–2098, 2009.
- [250] A. S. Verhulst, W. G. Vandenberghe, K. Maex, and G. Groeseneken, “Tunnel field-effect transistor without gate-drain overlap,” *Appl. Phys. Lett.*, vol. 91, no. 5, p. 053102, 2007.
- [251] R. Narang, M. Saxena, R. S. Gupta, and M. Gupta, “Device and circuit level performance comparison of tunnel FET architectures and impact of

- heterogeneous gate dielectric,” *J. Semicond. Technol. Sci.*, vol. 13, no. 3, pp. 224–236, 2013.
- [252] K. Tomioka, M. Yoshimura, and T. Fukui, “Steep-slope tunnel field-effect transistors using III-V nanowire / Si heterojunction,” in *Symposium on VLSI Technology*, 2012, no. 2010, pp. 47–48.
- [253] R. Gandhi, Z. Chen, N. Singh, S. Member, K. Banerjee, and S. Lee, “Vertical Si-nanowire n -type tunneling FETs with low subthreshold swing (≤ 50 mV/decade) at room temperature,” *IEEE Electron Device Lett.*, vol. 32, no. 4, pp. 437–439, 2011.
- [254] R. Gandhi, Z. Chen, N. Singh, S. Member, K. Banerjee, and S. Lee, “CMOS-compatible vertical-Silicon-nanowire gate-all-around p-type tunneling FETs with ≤ 50 -mV / decade subthreshold swing,” *IEEE Electron Device Lett.*, vol. 32, no. 11, pp. 1504–1506, 2011.
- [255] K. Jeon, W. Loh, P. Patel, C. Y. Kang, J. Oh, A. Bowonder, C. Park, C. S. Park, C. Smith, P. Majhi, H. Tseng, R. Jammy, T. K. Liu, and C. Hu, “Si tunnel transistors with a novel silicided source and 46mV / dec swing,” in *Symposium on VLSI Technology*, 2010, vol. 1, no. 2009, pp. 2009–2010.
- [256] S. H. Kim, H. Kam, C. Hu, and T. K. Liu, “Germanium-source tunnel field effect transistors with record high I_{ON} / I_{OFF} ,” in *Symposium on VLSI Technology*, 2009, pp. 178–179.

- [257] F. Mayer, C. Le Royer, J.-F. Damlencourt, K. Romanjek, F. Andrieu, C. Tabone, B. Previtali, and S. Deleonibus, "Impact of SOI, Si_{1-x}Ge_xOI and GeOI substrates on CMOS compatible tunnel FET performance," in *2008 IEEE International Electron Devices Meeting*, 2008, vol. 4, pp. 1–5.
- [258] W. Y. Choi, B. Park, J. D. Lee, and T. K. Liu, "Tunneling Field-Effect Transistors (TFETs) with subthreshold swing (SS) less than 60 mV/dec," *IEEE Electron Device Lett.*, vol. 28, no. 8, pp. 743–745, Aug. 2007.
- [259] J. Appenzeller, Y.-M. Lin, J. Knoch, and P. Avouris, "Band-to-band tunneling in carbon nanotube field-effect transistors," *Phys. Rev. Lett.*, vol. 93, no. 19, p. 196805, Nov. 2004.
- [260] L. Knoll, Q. Zhao, A. Nichau, S. Trellenkamp, S. Richter, A. Schäfer, D. Esseni, L. Selmi, K. K. Bourdelle, and S. Mantl, "Inverters with strained Si nanowire complementary tunnel field-effect transistors," *IEEE Electron Device Lett.*, vol. 34, no. 6, pp. 813–815, 2013.
- [261] T. Krishnamohan, D. Kim, S. Raghunathan, and K. Saraswat, "Double-gate strained-Ge heterostructure Tunneling FET (TFET) with record high drive currents and <60mV/dec subthreshold slope," in *IEEE International Electron Devices Meeting*, 2008, vol. 67, no. May 2006, pp. 7–9.
- [262] Q. Huang, R. Huang, C. Wu, H. Zhu, C. Chen, J. Wang, L. Guo, R. Wang, L. Ye, and Y. Wang, "Comprehensive performance reassessment of TFETs with a

novel design by gate and source engineering from device / circuit perspective,” in *IEEE International Electron Devices Meeting*, 2014, pp. 335–338.

- [263] A. Villalon, C. Le Royer, M. Cassé, D. Cooper, B. Prévitali, C. Tabone, J. Hartmann, P. Perreau, P. Rivallin, J. Damlencourt, F. Allain, F. Andrieu, O. Weber, O. Faynot, and T. Poiroux, “Strained Tunnel FETs with record I ON : First demonstration of ETSOI TFETs with SiGe channel and RSD,” in *Symposium on VLSI Technology*, 2012, vol. 044510, no. 2011, pp. 2011–2012.
- [264] B. Ganjipour, J. Wallentin, M. T. Borgstro, L. Samuelson, and C. Thelander, “Tunnel field-effect transistors based on InP-GaAs heterostructure nanowires,” *ACS Nano*, vol. 6, no. 4, pp. 3109–3113, 2012.
- [265] M. Kim, Y. Wakabayashi, R. Nakane, M. Yokoyama, M. Takenaka, and S. Takagi, “High I on / I off Ge-source ultrathin body strained-SOI Tunnel FETs - impact of channel strain , MOS interfaces and back gate on the electrical properties,” in *IEEE International Electron Devices Meeting*, 2014, pp. 331–334.
- [266] G. Dewey, B. Chu-Kung, J. Boardman, J. M. Fastenau, J. Kavalieros, R. Kotlyar, W. K. Liu, D. Lubyshev, M. Metz, N. Mukherjee, P. Oakey, R. Pillarisetty, M. Radosavljevic, H. W. Then, and R. Chau, “Fabrication, characterization, and physics of III–V Heterojunction Tunneling Field Effect

Transistors (H-TFET) for steep sub-threshold swing,” *2011 Int. Electron Devices Meet.*, vol. 3, pp. 33.6.1–33.6.4, Dec. 2011.

[267] S. Agarwal and E. Yablonovitch, “Pronounced Effect of pn-Junction Dimensionality on Tunnel Switch Sharpness,” *arXiv:1109.0096*, 2012.